

**The Dissertation Committee for Zhaohe Dai Certifies that this is the approved version of
the following Dissertation:**

Mechanics of Bubbles and Tents Formed by 2D Materials

Committee:

Nanshu Lu, Supervisor

Filippo Mangolini

Rui Huang

Krishnaswa Ravi-Chandar

Kenneth M. Liechti

Mechanics of Bubbles and Tents Formed by 2D Materials

by

Zhaohe Dai

Dissertation

Presented to the Faculty of the Graduate School of

The University of Texas at Austin

in Partial Fulfillment

of the Requirements

for the Degree of

Doctor of Philosophy

The University of Texas at Austin

May 2020

This dissertation is dedicated to friends, teachers, and professors who have provided me with guidance and equipped me with knowledge for opportunities I want to pursue.

Acknowledgements

First and foremost, I must express my gratitude to Prof. Nanshu Lu, my supervisor, for her guidance and financial support. The collaborative and interdisciplinary culture of Lu group has inspired this dissertation in various ways.

I am grateful to Prof. Rui Huang for many discussions and his mechanics insight. These have been highly encouraging and very helpful in shaping my research in and beyond this dissertation.

I would like to thank Daniel Sanchez, Luqi Liu, Yuan Hou, Guorui Wang, Christopher Brennan for providing me with the raw experimental data about 2D material bubbles and tents. These AFM images are beautiful and inspiring! I also thank Peng Wang for supporting my theoretical analysis in Chapter 6 with MD simulations and sharing his finite difference code on the bubble problem; a modified version was used in Chapter 5 to study the effect of edge slippage in both tent and bubble problems.

Nanshu Lu, Rui Huang, Luqi Liu, Dominic Vella, Wei Gao, Zhiping Xu, Shutao Qiao, Guorui Wang, Daniel Sanchez, Kuan Zhang, Liu Wang, Yinbo Zhu, Shan Tang, Zhong Zhang, Yueguang Wei, and Zhuping Huang have made useful comments when I discussed with them about my research details/slides via individual, group, or Skype meetings etc. Thank y'all for the questions and criticism (many of which are constructive to this dissertation) as well as the positive comments.

Sincere thanks go to the faculty of Engineering Mechanics as well as Roger Bonnez of Chemical Engineering for training me with great mechanics lectures and to members on my committee, Professor K. Ravi-Chandar, Filippo Mangolini, Rui Huang, Kenneth Liechti for their commitment and help. I also thank Filippo Mangolini for sharing

his MSCA application materials and experience. I am grateful to Kenneth Liechti for making many useful comments and suggestions on an earlier draft of this dissertation.

It has been a privilege to share so many moments with my officemates and labmates and graduate students in Engineering Mechanics. I would like to send my thanks to Daniel Sanchez for providing many useful suggestions on my research, paper writing, and interview, Liu Wang for critical comments on things I am proud of and a number of dinners, and Yifan Rao for the coffee and milk tea time.

Financial support from US NSF (Grant No. 1351875; PI: Nanshu Lu) is gratefully acknowledged. I thank Professor Chad Landis, Rui Huang, Gregory Rodin, Nanshu Lu, Mark Mear for offering me TA during Fall 2016 to Spring 2019. I also thank UT Austin Graduate Continuing Fellowship for supporting my fourth year, Global Research Fellowship for supporting my collaborative research with Luqi Liu during the 2017 winter, several travel awards provided by UT Austin and CMSSM, as well as the generous Warren A. and Alice L. Meyer Endowed Scholarship and Eric Baker Becker III Memorial Graduate Scholarship.

Finally, I am indebted to my parents and my wife, who have always been there for me.

Abstract

Mechanics of Bubbles and Tents Formed by 2D Materials

Zhaohe Dai, Ph.D.

The University of Texas at Austin, 2020

Supervisor: Nanshu Lu

Poking and bulging have been standard methods for characterizing the mechanics of thin solids, including biological, metallic, and elastomeric membranes, as well as emergent atomically thin 2D materials. We call the poked and bulged thin solids tents and bubbles, respectively. Besides their broad uses for fundamental mechanics metrologies, 2D material bubbles and tents have seen a surge of interest in the field of condensed matter physics. The interest is triggered by the fact that the out-of-plane deformation associated with bubbles and tents can produce self-sustained, non-uniform in-plane strains, based on which exciting strain-coupled physics (e.g., bandgap engineering and pseudomagnetic fields) and unique quantum applications have been extensively demonstrated.

The deterministic control of these experiments brings the necessity to elucidate the kinematics of 2D material bubbles and tents as well as how the geometry is selected by the elasticity and the film-substrate adhesive interaction. However, there are significant gaps between experimental observations and theoretical understanding of these systems, due to the under-appreciation of the atomically smooth/lubricated nature of 2D materials. In particular, 2D material-substrate interfaces are extremely susceptible to shear, while bubbles and tents have been frequently modeled with clamped boundary conditions that

prohibit any motions of their edges. In striking contrast, experimental observations have revealed subtle wrinkling instabilities near the edge of 2D material bubbles and tents (even at small deflections before further edge delamination occurs). This gives concrete evidence for the existence of inward slippage/shear of these atomic sheets on their supporting substrates, on which our quantitative understanding has been lacking.

As a consequence, many questions arise that are of vital importance to both metrology and functionality applications of 2D material bubbles and tents. How does the shear of 2D material interfaces and the formation of elastic instabilities modify the mechanical responses of the sheet to point and distributed transverse loads on tents or bubbles? How are the strain fields modified? Besides, in many scenarios, 2D material bubbles and tents form spontaneously by trapping liquids and nanoparticles at the 2D material-substrate interfaces, respectively. A natural question is how the elasticity of the 2D material, together with its adhesive and shear interactions with the substrate, select the geometry of those spontaneous bubbles and tents. Notably, the geometry may include not only the global out-of-plane profiles but also local features such as the extent of the elastic instabilities due to edge slippages.

This dissertation aims to answer these questions concerning the mechanics of 2D material bubbles and tents. We study a collection of problems in this area with a particular emphasis on the role of the shear deformations associated with the atomic-level interfaces. With the understanding of these questions, we proceed to discuss a number of useful implications for the elasticity and interface metrology of 2D materials as well as the rational design of bubbles and tents for a range of applications with the instabilities being either avoided or exploited.

Table of Contents

List of Tables	xv
List of Figures	xvi
Chapter 1: Introduction	1
1.1 2D Materials	2
1.2 van der Waals structures	3
1.3 Elasto-intermolecular phenomena	4
1.3.1 In-plane tension/shear	5
1.3.2 Out-of-plane bending	9
1.3.3 Out-of-plane stretching	14
1.4 Motivation	16
1.4.1 2D material interfaces	17
1.4.2 Spontaneous bubbles and tents	19
1.4.3 Indentation and bulge tests	19
1.4.4 Questions to be answered	20
1.5 Structure of the dissertation	22
Chapter 2: Theory	25
2.1 Introduction	26
2.2 Problem description	28
2.2.1 Föppl–von Kármán equations	28
2.2.2 Clamped boundary conditions	30
2.2.3 Non-dimensionlization	31
2.3 Radial slippage and occurrence of instabilities	32

2.3.1 Experimental observations.....	32
2.3.2 Three cases.....	34
2.4 Case I: the base state.....	35
2.4.1 Inside the tent.....	36
2.4.2 Outside the tent	36
2.4.3 Boundary and matching conditions	37
2.5 Case II: wrinkling without buckling delamination	37
2.5.1 Unwrinkled/unbuckled regions.....	38
2.5.2 Wrinkled region	38
2.5.3 Boundary and matching conditions	39
2.6 Case III: wrinkling with buckling delamination	40
2.6.1 Buckled region.....	40
2.6.2 Boundary and matching conditions	40
2.7 Bubbles	41
2.8 Conclusions.....	42
Chapter 3: Stretching	44
3.1 Introduction.....	45
3.2 Poking tests	46
3.3 Tents without instabilities.....	49
3.3.1 Effect of \mathcal{T}	49
3.3.2 Sliding number \mathcal{S}	51
3.4 Tents with instabilities	53
3.4.1 Wrinkling and no buckling delamination	53

3.4.2 Wrinkling with buckling delamination	56
3.5 Implications for indentation tests.....	59
3.6 Bulge tests.....	60
3.6.1 Experiments in the literature.....	61
3.6.3 Numerical results	63
3.7 Implications for bulge tests.....	67
3.8 Conclusions.....	68
3.9 Appendix.....	69
Chapter 4: Bending	71
4.1 Introduction.....	72
4.2 Current understanding of 2D material bending	75
4.3 Theory of bulging	77
4.3.1 FvK equations	78
4.3.2 $h \ll \ell_c$	80
4.3.3 $h \gg \ell_c$	80
4.3.4 An approximate solution.....	81
4.4 Experiments of bulging.....	84
4.4.1 Set-up.....	84
4.4.2 Determination of the layer numbers	85
4.4.3 Shape: plate or membrane.....	86
4.4.4 Pressure-deflection relation	88
4.4.4 Young's modulus and Bending rigidity.....	90
4.5 Discussion.....	92

4.5.1 Two theoretical limits	94
4.5.2 Experimental results	95
4.6 Error sources	95
4.6.1 Edge slippage.....	95
4.6.2 Pretension.....	96
4.6.3 “Sag” effect.....	98
4.6.4 Summary.....	99
4.7 Conclusions.....	100
Chapter 5: Strain	102
5.1 Introduction.....	103
5.2 Shape of bubbles and tents.....	105
5.3 Theoretical setting.....	108
5.3.1 Analytical solutions	109
5.3.2 Numerical verification	111
5.4 Experimental validation.....	113
5.4.1 Pressurized bubbles.....	113
5.4.2 Strain at the bubble center	115
5.4.3 Strain distributions.....	118
5.5 Discussion.....	120
5.5.1 Strain distributions near the edge.....	120
5.5.2 Strain distributions at the center	121
5.5.3 Experiments about tents in the literature	123
5.6 Strain engineering applications.....	124

5.7 Conclusions.....	126
5.8 Appendix.....	127
5.A Experimental section.....	127
5.B Numerical section.....	129
Chapter 6: Elasto-capillarity	132
6.1 Introduction.....	133
6.2 Aspect ratio of bubbles	135
6.3 Analytical expressions	139
6.3.1 Scaling	140
6.3.2 An energy-based membrane analysis	142
6.3.3 Finite sheet size in simulations	146
6.4 Aspect ratios of various blisters.....	147
6.5 Hencky's analysis	152
6.5.1 Finite shear.....	152
6.5.2 Finite sheet size in experiments	158
6.6 MD simulations.....	160
6.6.1 Comparison with analytical results.....	160
6.6.2 Breakdown of the continuum model.....	163
6.7 Useful implications	166
6.7.1 Adhesion metrology.....	166
6.7.2 Applications of 2D material blisters	172
6.8 Conclusions.....	173

Chapter 7: Buckles	175
7.1 Introduction.....	176
7.2 Experiments	178
7.2.1 Sample preparation	178
7.2.2 Shapes	180
7.2.3 1D analysis.....	182
7.2.4 Formation mechanism of radial buckles	184
7.4 Near-threshold modeling	187
7.4.1 General theory.....	187
7.4.2 Non-dimensionalization.....	188
7.4.3 Analytical results: outside the tent.....	189
7.4.4 Analytical results: inside the tent.....	190
7.4.5 A composite parameter	192
7.5 Parametric studies based on near-threshold modeling.....	193
7.5.1 Effect of \mathcal{S}	193
7.5.2 Effect of \mathcal{T}	195
7.5.3 Effect of ρ_{out}	197
7.5.4 Effect of ρ_{in}	199
7.6 Far-from-threshold modeling.....	201
7.7 Parametric studies based on far-from-threshold modeling.....	204
7.7.1 Extent of the buckled and wrinkled region.....	205
7.7.2 NT and FFT modeling	206
7.7.3 Finite pillar radius.....	208

7.8 Implications for 2D material applications	210
7.8.1 Estimation of interface adhesion.....	210
7.8.2 Estimation of interface friction (FFT)	213
7.8.3 Estimation of interface friction (NT)	215
7.8.4 Guidelines for fabricating arrays of 2D material tents	217
7.9 Conclusions.....	220
7.10 Appendix.....	221
7.A Pretension (NT).....	221
7.B Finite sheet size (NT)	221
7.C Finite pillar radius (NT)	222
7.D The composite parameter (FFT)	224
7.E Finite pillar radius (FFT).....	224
Chapter 8: Epilogue	226
8.1 Conclusions.....	227
8.2 Future work.....	230
8.3 Discussion.....	233
Bibliography	235

List of Tables

Table 4.1:	Summary of the thickness, Young's modulus and bending rigidity for three 2D materials, including the measurement errors. *Lack of error bar because only one measurement was achieved in this case.	100
Table 6.1:	The prefactor ϕ that determines the aspect ratio by $\Delta\gamma/E_{2D}$ in (6.4).....	152
Table 6.2:	Shear stress at 2D material interfaces.	167
Table 6.3:	In-plane stiffness of 2D materials.	168
Table 6.4:	Water contact angle (WCA) for 2D materials and substrates used in Figure 6.14 and Table 6.5.	168
Table 6.5:	Adhesion energies of 2D material interfaces obtained in this work and in literature.	171

List of Figures

Figure 1.1:	2D materials with various atomic structures and increasing bandgap from left to right. Adapted with permission from (Liu et al., 2016).....	2
Figure 1.2:	(a) Schematic and (b) transmission electron microscope (TEM) cross section of a graphene/hBN heterostructure. Adapted with permission from (Novoselov et al., 2016).....	3
Figure 1.3:	Domain walls in bilayer graphene. (a) Near-field infrared image of a sharp L-shape domain wall containing horizontal shear-type and vertical tensile-type solitons. Schematic illustrations of the shear- (b) and tensile-type (c) strain solitons. (a-c) are adapted with permission from (Jiang et al., 2016). (d) Dark-field TEM image of bilayer graphene with electrons selected from the $[-1010]$ family of diffraction angles that helps to distinguish AB (gray) from BA (black) domains. Adapted with permission from (Alden et al., 2013). (e) Dark-field TEM image of bilayer graphene with a uniform twisting angle of 0.1 degree. Adapted with permission from (Yoo et al., 2019).....	5
Figure 1.4:	Introduction of in-plane strain into 2D materials. (a) CVD growth of 2D materials on a substrate with a mismatched lattice. (b) Tensile or compressive residual strain could be achieved by exploiting the thermal-expansion mismatch between the 2D material and its substrate. Adapted with permission from (Ahn et al., 2017). (c) Schematic of straining a 2D material by deforming its supporting substrate. Adapted with permission from (Mohiuddin et al., 2009).....	8

Figure 1.5: Scrolls and folds. (a) Schematic of the spontaneous rolling of a CVD-grown TMD monolayer. Adapted with permission from (Cui et al., 2018). (b) AFM images of self-folding of bilayer graphene ribbons with different initial width. Adapted with permission from (Annett and Cross, 2016).10

Figure 1.6: 2D material buckles and wrinkles. Schismatic of 2D material buckles and wrinkles stemming from different origins: (a) the compression or pre-stretch of the substrate, (b) shrinking of the 2D material/substrate system due to a temperature change, and (c) heterostructures with an intrinsic lattice mismatch between layers. (d) Scanning electron microscope (SEM) image of a MoS₂ flake buckling on an elastomeric substrate. Adapted with permission from (Castellanos-Gomez et al., 2013). (e) PL intensity image of a triangle monolayer WS₂ where edge buckle delamination occurs due to the thermal residual strain. Adapted with permission from (Ly et al., 2017). (f) SEM images of buckle delamination at edges of Bi₂Se₃/Bi₂Te₃ heterojunctions where the bottom layer is compressed by the top layer due to the ~5.9% lattice mismatch. Adapted with permission from (Lou et al., 2018). (g) Optical image of a multilayer black phosphorus wrinkling on an elastomer. The inset shows a sketch of the crystal lattice orientation. Adapted with permission from (Quereda et al., 2016). (h) SEM image of a wrinkled graphene grown on copper as this system cools. Adapted with permission from (Meng et al., 2013a). (i) SEM images of WS₂/WSe₂ superlattices with wrinkled/rippled structures at edges (greyish regions). Adapted with permission from (Xie et al., 2018).13

Figure 1.7:	2D materials with large out-of-plane deformations. (a) SEM image of a MoS ₂ layer fully conforming on a dome-patterned substrate. Adapted with permission from (Li et al., 2015). (b) AFM image of spontaneously formed graphene bubbles on bulk hBN. Adapted with permission from (Khestanova et al., 2016). (c) SEM image of tents formed by transferring a graphene sheet onto pillar-patterned silicon substrate. Adapted with permission from (Reserbat-Plantey et al., 2014).	15
Figure 1.8:	Suspended 2D materials under a point load or pressure. Schematic depiction of the indentation experiment (a) and blister test (b) on 2D materials. (a) and (b) are adapted with permission from (Bertolazzi et al., 2011) and (Koenig et al., 2011), respectively.	20
Figure 2.1:	Free body diagrams of the base state of a 2D material tent and bubble.	28
Figure 2.2:	AFM amplitude images of a spontaneous multilayer graphene tent (left, courtesy of Daniel Sanchez) and a gas-pressurized bilayer graphene bubble (right, courtesy of Guorui Wang).....	33
Figure 2.3:	(a-c) Schematics for three possible deformed configurations when the sheet is allowed to slide over its supporting substrate. (d) Schematic illustration of Case III (top view) where the thin sheet wrinkles in $[\rho_w, 1]$ and delaminates in $[1, \rho_o]$	34
Figure 2.4:	(a-c) Schematics for three possible deformed configurations of bubbles when the sheet is allowed to slide over its supporting substrate.....	41
Figure 3.1:	Schematic illustrations of indentation tests on freestanding thin sheets with a fixed edge (a) and a vdW-glued edge (b). (c) Rescaled indentation force-depth relation measured on monolayer graphene in the literature. (a) is adapted from (Ozaki et al., 2018)	46

Figure 3.2:	(a) Numerical indentation force-depth curves for thin sheets with various interfacial shear tractions to their substrates. (b) The dependency of the size of the sliding zone on the center deflection (i.e., indentation depth) for various interfacial shear tractions.....	50
Figure 3.3:	The dependency on the sliding number of the effective stiffness (a) and the size of the sliding zone (b).	52
Figure 3.4:	The dependency on the sliding number of the effective stiffness of poking a wrinkled sheet.	54
Figure 3.5:	The dependency on the sliding number of the size of the sliding zone (a) and the size of the wrinkling zone (b).....	55
Figure 3.6:	The dependency on the sliding number of the effective stiffness.....	57
Figure 3.7:	The dependency on the sliding number of the size of the sliding zone (a) and the size of the wrinkling zone (b).....	58
Figure 3.8:	The effective stiffness of the thin sheet under poking for three possible deformed configurations, which are further illustrated in the right panel.	59
Figure 3.9:	(a) Schematic illustrations of bulge tests on an aluminum alloy plate, the edge of which is constrained via the friction enhanced mechanically by draw beads. The top panel shows the photo of a plate after the test (Chen et al., 2018). (b) AFM amplitude images of a gas-pressurized bilayer graphene bubble (right, courtesy of Guorui Wang). (c) Rescaled pressure-deflection relation measured on monolayer graphene in the literature.	62

Figure 3.10: (a) The pressure-deflection curves for thin sheets with various interfacial shear tractions to their substrates. (b) The dependency of the size of the sliding zone on the center deflection for various interfacial shear tractions.....	63
Figure 3.11: The dependency on the sliding number of the effective stiffness (a) and the size of the sliding zone (b).	64
Figure 3.12: The dependency on the sliding number of the effective stiffness.....	65
Figure 3.13: The dependency on the sliding number of the effective stiffness.....	66
Figure 3.14: The effective stiffness of the thin sheet under poking for three possible deformed configurations, which are further illustrated in the right panel. ...	67
Figure 3.A1: The dependency on the sliding number of the size of the sliding zone (a) and the size of the wrinkling zone (b) in the bulge test. Markers are numerical results based on Case II of the bulging problem; black solid curves are based on Case I of the bulging problem (no instabilities); brown dashed lines are guessed according to our studies on Case II of the poking problem in section 3.4.....	69
Figure 3.A2: The dependency on the sliding number of the size of the sliding zone (a) and the size of the wrinkling zone (b) in the bulge test. Markers are numerical results based on Case III of the bulging problem; black solid curves are based on Case I of the bulging problem (no instabilities); brown dashed lines are guessed according to our studies on Case III of the poking problem in section 3.4.....	70

Figure 4.1:	The schematics (a) and corresponding electron microscope images (b) illustrate various deformation modes. (Reproduced with permission from Ref. (Bao et al., 2009; Lee et al., 2015; Lopez-Bezanilla et al., 2012; Yang et al., 2015; Zhang et al., 2013b). Panels (c) and (d) illustrate the microstructural deformation upon bending of multilayer 2D materials with perfectly glued (c) and ultra-lubricated (d) interfaces.	72
Figure 4.2:	Bending of multilayer 2D materials. (a) Schematic of a bent multilayer where interlayer interfaces are glued (top panel) and lubricated (bottom panel) (Han et al., 2019). (b) Bright-field STEM image of 12-layer graphene bent to 12° , where the number of atomic columns in the arc is provided for layers at three different locations (Han et al., 2019).	75
Figure 4.3:	The pressure-deflection relation of a clamped, circular sheet subject to a uniform pressure. Markers denote numerical results, and the solid curve is based on (4.22)	83
Figure 4.4:	Shape of a clamped, circular sheet subject to a uniform pressure when the deflection is relatively small (a) and large (b). Markers denote numerical results based on $\mathcal{K} = 10^3$	83
Figure 4.5:	(a) An optical image of 2D materials suspended over the cavities with diameters of 0.5-1.5 μm on SiO_2/Si substrate. (b) Schematic illustration of the bubbling device with pressure difference applied across the 2D sheet. Bending of multilayer 2D materials. (c) The schematic of pressurized bubbles with two distinct shape characteristics at small and large deflections.	84

- Figure 4.6: Optical images of (a) graphene, (c) hBN and (e) MoS₂ sheets with various layer numbers. The magnified views of the rectangular regions are shown in AFM images for (b) graphene, (d) hBN and (f) MoS₂, respectively. The insets give the height profiles along the red dashed lines, where the interlayer distance was found to be around 0.34 nm, 0.35 nm and 0.69 nm for graphene, hBN, and MoS₂, respectively. The relatively high thickness of the bottom layer (0.7 nm for graphene and hBN, and 1.2 nm for MoS₂) was typically attributed to the instrumental scanning offset from the substrate to the 2D materials.85
- Figure 4.7: (a) Normalized deflection profiles measured from two sets of 0.5- μ m-radius bubbles. We observed a membrane-like shape with a kinked edge for $h/t \gtrsim 2$ (orange markers) and a plate-like shape with a smooth edge for $h/t \lesssim 1.5$ (blue markers). (b,c) Critical ratios of bubble height to the thickness (h/t) to discriminate shapes dominated by the plate or membrane for graphene, hBN, and MoS₂.87
- Figure 4.8: pa^4/h^3t as a function of h/t for graphene (a), hBN (b) and MoS₂ (c), respectively. The solid lines represent the idealized nonlinear plate solution, and horizontal dot-dashed lines are the membrane solution. In the color system, darker symbols denote the thicker samples.89
- Figure 4.9: Extracted Young's modulus (a) and bending rigidity (b) as a function of thickness. At a given thickness, AFM measurements of up to 17 different bubbles produce the results plotted as symbols. The dash-dotted lines in (a) indicate the average values, while the dashed and solid lines in (b) are the theoretical predictions for the perfectly glued ($D \sim N^3$) and ultra-lubricated ($D \sim N$) cases, respectively.91

Figure 4.10: The layer-dependent function to measure the effect of interlayer coupling on the bending rigidity of multilayered graphene, hBN, and MoS ₂ . The black lines are theoretical predictions of the limiting cases for graphene. Our experimental results are denoted by colored markers, sitting between the two limits.	93
Figure 4.11: The Raman contour map of G (E _{2g}) peak positions for (a) graphene, (b) hBN and (c) MoS ₂ at $h = 33$ nm, 37 nm, 45 nm, respectively.	95
Figure 4.12: pa^4/h^3t as a function of h/t for graphene with various thicknesses (a-d). Though these data were measured from bubbles with different radii, they can collapse to the radius-independent master curve predicted by (4.25).	97
Figure 4.13: Initial surface morphology of three different 2D materials with (a-c) low and (d-f) high thickness. The white dashed circle indicates the perimeter of the hole with the diameter of 1 μ m and the height profiles of suspended region along with the yellow dash-dotted lines are also shown in the insets. (g) Initial sag depth of three 2D materials at different thicknesses.	98

- Figure 5.1: From top to bottom: Optical/SEM images, AFM amplitude and height images of spontaneously formed graphene bubbles on SiO₂ (a), a multilayer graphene tent on SiO₂ (b), and a CVD-MoS₂ tent on gold film (c). (d) From left to right: optical image of graphene flakes exfoliated on pre-patterned SiO₂ with micro-cavities, AFM height images of a monolayer graphene bubble, and a 4-layer MoS₂ bubble. Note that (S) represents bubbles or tents formed spontaneously while (P) represents those formed by controllable air pressurization. The scale bars represent 4 μm in (a), 2 μm in (b), 200 nm in (c), and 10 μm , 1 μm and 500 nm in (d) left, middle and right panels, respectively.....106
- Figure 5.2: Universal shape characteristics of 2D material bubbles and tents. (a) Normalized bubble profiles measured by our experiments and collected from the literature. Note that samples from (Khestanova et al., 2016) feature atomically smooth interfaces, are labeled by *. (b) Normalized tent profiles measured by our experiments and simulation results in the literature. The simulation data about graphene and MoS₂ is from (Feng et al., 2012; Zhu et al., 2014).107
- Figure 5.3: Normalized strain distribution curves predicted by our analytical solution (solid lines) and solved by numerical analysis (markers) in bubbles (a) and tents (b), subjected to both clamped (strong interface) and frictionless (sliding interfaces) boundary conditions. The strain is normalized by h^2/a^2 , giving rise to deflection-independent curves. The numerical results are solved for a monolayer graphene with aspect ratios ranging $0.02 < h/a < 0.2$112

Figure 5.4: Schematics of the graphene drumheads formed on a SiO ₂ substrate (a) and on a graphene-covered SiO ₂ substrate (b).....	114
Figure 5.5: Representative Raman spectra measured at the center of the graphene bubble under different levels of deformation (h/a). (a) SiO ₂ -supported graphene bubbles. (b) Graphene-supported graphene bubbles. We note that when subjected to equal deformation level, SiO ₂ -supported graphene bubbles exhibit much more significant G and 2D band shifts than graphene-supported graphene bubbles. Specifically, when the $h/a \cong 0.1$, the G band downshifted by 53 and 34 cm ⁻¹ for the SiO ₂ -supported and the graphene-supported graphene bubble, respectively. And the 2D band downshifted by 102 and 84 cm ⁻¹ for the SiO ₂ -supported and the graphene-supported graphene bubble, respectively. This fact implies that the sliding behavior of the graphene-graphene interface at the edge can considerably reduce the strain magnitude in the bubble.....	116
Figure 5.6: Raman shifts of the G band predicted by our analytical solution (solid curves) and measured by our experiments (markers) at the center of graphene bubbles.	117

- Figure 5.7: Line mapping of Raman G band frequency. (a) SiO₂-supported graphene bubbles. (b) Graphene-supported graphene bubbles. Unsurprisingly, the Raman G band shifts increase with the applied out-of-plane deformation. Also, the shifts decrease from the center ($r/a = 0$) to the edge ($r/a = 1$) of the bubble, implying that the “strain” increases from the edge to the center. When approaching the edge, the curves of Raman G band shift (as functions of the radial position) behave differently between SiO₂-supported and graphene-supported graphene bubbles. One possible reason likely comes from the different doping levels by the substrate, which is SiO₂ for (a) and few-layer graphene for (b). For instance, we found the upshifting of G band with 2-4 cm⁻¹ by the SiO₂ doping while the downshifting of G band with 0-2 cm⁻¹ by the hybrid substrate doping (few-layer graphene on SiO₂).118
- Figure 5.8: Normalized Raman shifts of the G band ($\Delta\omega_G a^2 / \omega_0 h^2$) as functions of the normalized radial position (r/a) for monolayer graphene bubbles.119
- Figure 5.9: Line mapping of the width of Raman G band. For a SiO₂-supported graphene bubble at $h/a = 0.074$, a series of Raman spectra (G band) are stacked vertically in the direction of the line scan. The x is defined by the distance to the center of the hole (the bubble). Substantial variations in both the frequency and the full width at half-maximum (FWHM) can be detected. The apparent downshift of Raman G band has been shown in Figure 5.7. The peak broadening at the edge ($x \rightarrow 2.5 \mu\text{m}$) and the sharpening at the center ($x \rightarrow 0 \mu\text{m}$) of the hole are highlighted.120

Figure 5.10: Dependency of the strain at the bubble center on the aspect ratio of the bubble.....	122
Figure 5.11: (a) Raman shifts of the 2D band of a multilayer graphene tent as a function of r/a (from (Elibol et al., 2016)). Like that in bubbles, r is defined by the distance to the center of the tent and a is the radius of the tent. (b) Normalized Raman shifts predicted by our analytical solution (solid curves) and measured by experiments (Elibol et al., 2016).....	123
Figure 5.12: Analytically predicted pseudomagnetic fields (PMFs) in graphene bubbles and tents under strong- and weak-shear. A circular monolayer graphene drumhead of a 25-nm-radius is pressurized (a, b) or poked (c, d) with 1 nm deflection. Solid circles represent the edges of these blisters. The PMF outside the tent in (d) is magnified four times in efforts to show the sliding effects.	125
Figure 6.1: (a) Liquid-filled bubbles between graphene and a silicon substrate (AFM amplitude image, courtesy of Daniel Sanchez). (b) Satellite bubbles can be observed by zooming in on the boxed region in (a).	135
Figure 6.2: (a) By extracting the height profile of each blister, the height and radius is calculated by curve fitting a parabolic function. (b) Blisters for a specific interface show a consistent aspect ratio that is independent of volume.....	136
Figure 6.3: Aspect ratio of 2D material blisters in literature. The top panel shows data from the case of 2D materials on regular substrates; the bottom shows the blisters formed between 2D materials.....	137
Figure 6.4: Schematic illustration of an axisymmetric bubble.....	142

Figure 6.5: Effect of the finite membrane size in MD simulations on the blister radius a and the coefficient ϕ in the height-to-radius ratio equation (6.19).	146
Figure 6.6: The radius ratio ρ of the interfacial sliding zone (black lines) and Hencky constant b_0 (blue lines) as a function of ξ .	155
Figure 6.7: The dimensionless pressures as a function of height/radius ratio under various shear stress. Blue and red dots are from the analysis based on Section 5.3.	156
Figure 6.8: The dependency of the aspect ratio on $\Delta\gamma/E_{2D}$ for different shear stress. Blue and red dots are from the simple analysis.	158
Figure 6.9: The aspect ratio as a function of ρ_0 . The shear stress used for this demonstration is $\tau = 10^{-5}$, with which interface is more sensitive to the lateral size compared that with strong shear.	160
Figure 6.10: MD simulation of a graphene blister with 2700 water molecules. The adhesion energy was $\Gamma_{GS} = 0.242 \text{ J/m}^2$, while the water contact angles were 60° and 40° for graphene and the substrate, respectively. (a) A top view snapshot of the blister, with color contour for the z -position of the carbon atoms in graphene; (b) A height profile along a line scan (dashed line in a) across the blister; (c) A cross-sectional view of the blister, showing the water molecules (oxygen in red and hydrogen in white) between graphene (carbon in gray) and the substrate surface (blue line).	161

Figure 6.11: Modeling and MD simulations of water-filled blisters. MD simulation results (circular markers) best agree with our simplified model assuming a frictionless, sliding interface (modified weak shear). The deviations, especially under small height or aspect ratio, is attributed to the size limitation of MD, which can induce discrete behaviors. The figures in the top panel demonstrate how the shape of the blister changes for different values of the work of adhesion.....	162
Figure 6.12: (a) The height of graphene blister as a function of the number of water molecules, predicted by the continuum model for $\Gamma_{GS} = 0.1 \text{ J/m}^2$ and 0.242 J/m^2 , where the dashed line indicates the critical height for the continuum model. (b) The breakdown limit for the continuum model, in terms of the adhesion energy Γ_{GS} and the number of water molecules N with the water contact angles being 60° and 40° for graphene and the substrate, respectively.	164
Figure 6.13: Blister aspect ratio for different numbers of water molecules, for $\Gamma_{GS} = 0.242 \text{ J/m}^2$ (a) and 0.1 J/m^2 (b) with water contact angles being 60° and 40° for graphene and the substrate, respectively. The dashed line is predicted by the continuum model. The breakdown of the continuum model is predicted at $N = 1690$ for $\Gamma_{GS} = 0.242$ (dotted vertical line in a) and $N = 7640$ for $\Gamma_{GS} = 0.1 \text{ J/m}^2$	164
Figure 6.14: Work of adhesion values for various 2D material interfaces estimated according to blister profiles, including many interfaces found in 2D heterostructures. Solid markers indicate our own experiments while open markers are for blisters reported in the literature.....	170

Figure 7.1: (a) A schematic of transferring graphene over a pillared substrate. (b) A schematic of radial buckles (blue arrows) surrounding a graphene tent formed over an Au pillar (red arrow). (c) Scanning electron microscope (SEM) image of monolayer graphene covering a periodic array of nanopillars. Each nanopillar has a height of about 260 nm and an apex radius of 20 nm – 50 nm. The pillar pitch is 1.4 μm . Source: Figures adapted from (Xu et al., 2016) (a and b) and (Reserbat-Plantey et al., 2014) (c).....177

Figure 7.2: (a) AFM images of a multilayer graphene tent and a monolayer MoS_2 tent. The vertical scales indicate the height of the tents. Radial buckles can be found at the substrate-supported regime outside the tent, and their profiles can be obtained by taking scans transverse to the buckles in the AFM height image. (b) Normalizing these AFM scans gives the characteristic buckle profile, which is well fitted by the cosine function given by (7.1) (black curve). This fit can yield the buckle wavelength λ and height δ . Different colors of the markers represent scans at different radial locations in the MoS_2 tent while these profiles are normalized by their fitted wavelength and height. (c) The wavelength (λ) of the multilayer graphene and monolayer MoS_2 buckles as a function of their height (δ) in a log-log plot. Colored markers are used to differentiate different buckles surrounding the same tent. The black lines correspond to a power-law fit with an exponent of $1/2$180

- Figure 7.3: (a) A schematic of a 1D buckle where Δ represents the compressive displacement. (b) Schematic illustration of radial buckles at the periphery of a tent. r represents the radial position. κ_θ and κ_r denote the buckle crest curvature in the hoop and radial direction, respectively. Δ represents the compressive displacement in the hoop direction which varies with r . (c) Experimentally measured δ^2/λ , λ^2/δ , λ , δ of the buckles formed by the monolayer MoS₂ tent as a function of the radial position. Solid lines are based on the scaling law given in (7.7), and the dashed lines represent the best fitting.185
- Figure 7.4: Notations for the analysis of an axisymmetric tent where a finite zone in the substrate-supported regime $R < r < R_o$ undergoes hoop compression caused by interface sliding. R is the edge of the tent, R_o is the edge of the compression zone, and R_{out} is the outer radius of consideration. τ is the membrane-substrate interface shear traction and t_{pre} is the pretension in the membrane.187
- Figure 7.5: (a) Hoop compressive displacement along the radial direction for various interfacial shear tractions. Solid curves denote tents with a center height $H = 0.2$ while dashed curves denote $H = 0.02$. (b) The size of the compression zone versus the center height of the tent for various interfacial shear tractions. (c) The dependency on \mathcal{S} of the hoop compressive displacement at the edge of the tent. (d) The dependency on \mathcal{S} of the size of the compression zone. All quantities are normalized quantities in this figure.....194

Figure 7.6: (a) Hoop compressive displacement along the radial direction for different values of pretension. Solid curves denote tents with a center height $H = 0.3$ while dashed curves denote $H = 0.03$. Note that for the cases of $T_{pre} = 10^{-3}$ and 10^{-2} , the tent of $H = 0.03$ shows hoop tension across the entire membrane indeed. (b) The size of the compression zone versus the center height of the tent for different values of pretension. The dashed line shows that a critical center deflection is required for the onset of a compression zone outside the tent due to the existence of pretension. (c) The dependency on $\mathcal{T} = T_{pre}/H^2$ of the compressive displacement at the edge of the tent. (d) The dependency on \mathcal{T} of the size of the compression zone. All quantities are normalized quantities in this figure.196

Figure 7.7: (a) Hoop compressive displacement along the radial direction for tents with various center heights. Solid curves denote tents with an outer radius $\rho_{out} = 3$ while dashed curves denote the case where the membrane size is sufficiently large. Note that when the center height is small (i.e. $H = 0.04$ and 0.06), the solid and dashed curves overlap because $\rho_o \leq \rho_{out}$. (b) The dependency on T/H^2 of the normalized compressive displacement at the edge of the tent.198

Figure 7.8: Contour plots for the normalized compressive displacement at the edge of the tent Δ_1/H^2 (a) and the size of the compression zone ρ_o (b) as a function of two governing parameters: ρ_{in} and \mathcal{S}200

Figure 7.9: Schematic illustration of the difference between near-threshold (NT) and far-from-threshold (FFT) modeling of a thin sheet tent.201

Figure 7.10: (a) The dependency on T/H^2 of the extent of the buckled region ρ_b (black solid curve, predicted by FFT analysis) and the size of the compression zone ρ_0 (black solid curve predicted by FFT analysis and red dashed curve predicted by NT analysis). (b) The dependency on T/H^2 of the extent of the wrinkled region ρ_w in the suspended region of the tent (predicted by FFT analysis).	206
Figure 7.11: (a) Hoop compressive displacement along the radial direction for various interfacial shear tractions. Solid curves denote tents with a center height $H = 0.2$ while dashed curves denote $H = 0.02$. The markers are from NT modeling in Figure 7.5a. (b) The dependency on \mathcal{S} of the compressive displacement at the edge of the tent. The red dashed curve is from NT modeling in Figure 7.5c.	207
Figure 7.12: Contour plots for the extent of the buckled region ρ_b outside the tent (a) and the extent of the wrinkled region ρ_w inside the tent (b) as a function of two governing parameters: ρ_{in} and \mathcal{S}	209
Figure 7.13: (a) The estimated adhesion energy between CVD-grown monolayer MoS ₂ and the Al ₂ O ₃ substrate. This estimation is enabled by measuring the buckle profiles at different radial locations, which are offered in Figure 7.3c. Blue markers are based on gas-filled buckles and solid markers are based on water-filled buckles. (b) The SEM image of the monolayer MoS ₂ tent in Figure 7.2a. The solid white circle highlights the edge of the tent.	211

Figure 7.14: AFM height (a) and amplitude (b) images of a monolayer MoS ₂ tent, based on which ρ_{in} , H , ρ_b and ρ_w are extracted (These two are the same with the Figure 1c in (Dai et al., 2018)). The extent of the buckled region (c) and wrinkled region (d) depends on the interface shear traction T , the height of the tent H , and the radius of the pillar ρ_{in}	214
Figure 7.15: AFM height (a) and amplitude (b) images of a ~15-layer graphene tent, based on which ρ_{in} , H , and ρ_o are extracted (These two are the same with the Figure 7.1b in (Dai et al., 2018)). (c) The radius of the compression zone outside the tent depends on the interface shear traction T , the height of the tent H , and the radius of the pillar ρ_{in}	216
Figure 7.16: (a) Schematic of an array of 2D material tents. (b) SEM image of CVD- grown monolayer graphene on silicon pillars (Reserbat-Plantey et al., 2014). (c) SEM image of CVD-grown monolayer graphene on lift-off resist nanopillars (Tomori et al., 2011). (c) AFM image of the topography of an exfoliated monolayer WSe ₂ flake on top of negative resist nanopillars (Branny et al., 2017). (e) A Phase diagram of three configurations of 2D material tent arrays.	219
Figure 8.1: AFM amplitude images of a spontaneous multilayer graphene tent (a, courtesy of Daniel Sanchez) and a gas-pressurized bilayer graphene bubble (b, courtesy of Guorui Wang). (c) Schematics for case II of the tent problem (top panel) and the bubble problem (bottom panel) when the sheet is allowed to slide over its supporting substrate and wrinkling forms. (d) The dependency of the extent of the wrinkling zone on the sliding number from bubbles and tents.	232

Chapter 1: Introduction¹

In this chapter, we first briefly introduce the thin solid objects that this dissertation focuses on: a class of atomically thin films, termed two-dimensional (2D) materials, and their layered assemblies, termed vdW structures. We summarize an immense variety of mechanical phenomena seen in electronic devices based on 2D materials and vdW structures. These phenomena, though lead to structures across scales ranging from a few nanometers to a few microns, share a similar physical principle – their geometrical characteristics are controlled by the complex interplay between the elasticity of the 2D material and the interfacial interactions with its substrate. Such fact motivates this dissertation to explore how the elasticity and interface interactions associated with the thin sheets can be characterized, particularly with these mechanical phenomena being utilized. To this end, we focus on 2D material bubbles and tents that can be seen ubiquitously in 2D material devices or in standard indentation and bulge tests.

¹Part of the content in this Chapter would also be found in:

Z. Dai, R. Huang, K. M. Liechti, N. Lu. *Mechanics at the Interfaces of 2D Materials: Challenges and Opportunities*. Current Opinions in Solid State and Material Science 2020. (Z.D. wrote the draft for the 2D-2D part.)

Z. Dai, L. Liu, Z. Zhang. *Strain Engineering of Two-Dimensional Materials: Issues and Opportunities at the Interface*. Advanced Materials 2019, 31, 1805417. (Z.D. wrote the draft of this perspective.)

1.1 2D MATERIALS

2D materials are a relatively new class of thin materials consisting of a single layer of covalently bonded atoms (Geim and Grigorieva, 2013; Liu et al., 2016; Novoselov et al., 2016). Graphene is the first 2D material to be isolated in nature and consists of a layer of carbon atoms arranged in a hexagonal lattice (Neto et al., 2009; Novoselov et al., 2004). In the last decade, graphene research has seen a surge of interest in the fields of physics, chemistry, materials science, engineering, and biology. This interest has led to the emergence of a variety of other 2D materials with diverse electronic properties (Figure 1.1) (Geim and Grigorieva, 2013; Liu et al., 2016; Novoselov et al., 2016), such as insulative hexagonal boron nitride (hBN), semi-conductive transition metal dichalcogenide (TMD), and metallic two-dimensional inorganic compounds (MXenes), and so on.

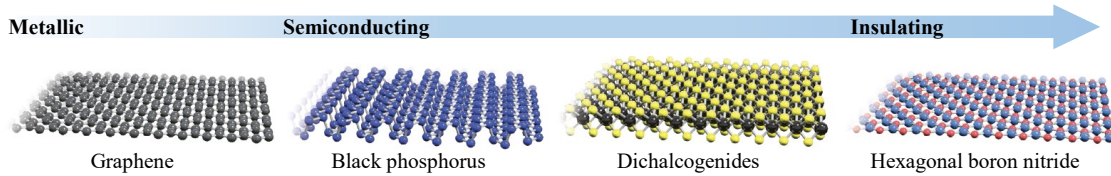


Figure 1.1: 2D materials with various atomic structures and increasing bandgap from left to right. Adapted with permission from (Liu et al., 2016).

As their dimension approaches the atomic limit, 2D materials not only show fundamental mechanical and thermal properties that are superior to conventional materials but also enable a number of electronic structures that cannot be seen at the bulk scale (some of them only exist theoretically). For example, graphene has been touted as the strongest material ever measured and may lead to the next generation of high-performance nanocomposites (Dai et al., 2019b; Lee et al., 2008). In general, 2D materials exfoliated from bulk crystals can sustain much larger deformation before fracture than their bulk counterparts (Akinwande et al., 2017; Androulidakis et al., 2018; Lee et al., 2008; Meng et

al., 2017). They also show excellent electronic properties because of a non-existent (overlapping) and direct bandgap between the electronic states of the bonded atoms (Geim and Grigorieva, 2013; Liu et al., 2016; Novoselov et al., 2016). The combination of unique electronic and mechanical properties of 2D materials has lent them well to many technology-focused applications, in particular atomically thin electronic and optoelectronic devices (Geim and Grigorieva, 2013; Liu et al., 2016; Novoselov et al., 2016).

1.2 VAN DER WAALS STRUCTURES

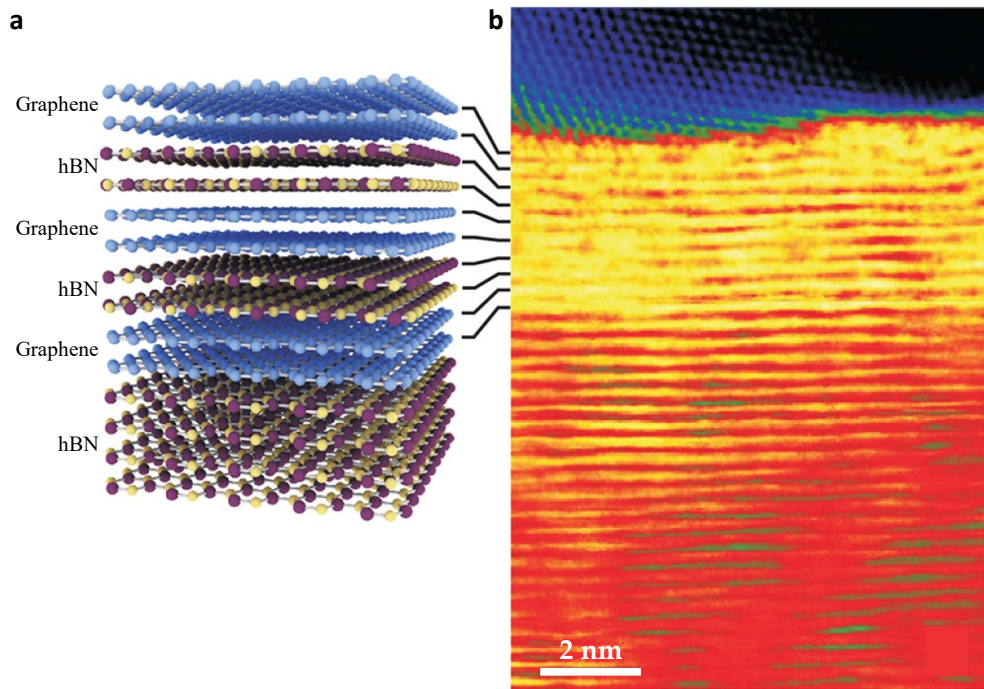


Figure 1.2: (a) Schematic and (b) transmission electron microscope (TEM) cross section of a graphene/hBN heterostructure. Adapted with permission from (Novoselov et al., 2016).

While the fundamental physics of individual 2D materials is intriguing, a more intriguing paradigm can be achieved by stacking different 2D materials on top of each other for the material design in a bottom-up manner (Geim and Grigorieva, 2013; Liu et al., 2016;

Novoselov et al., 2016). The resulting layered structures, often called vdW heterostructures, feature strong intra-layer covalent bonding and weak interlayer vdW interactions (Figure 1.2). This unique anisotropy provides vdW structures with tunable collective properties via the vertical stacking sequence and the twisting angle between stacked 2D materials (Cao et al., 2018a; Cao et al., 2018b; Jin et al., 2019; Lu et al., 2019; Ribeiro-Palau et al., 2018; Seyler et al., 2019; Sunku et al., 2018; Yankowitz et al., 2019a). Furthermore, a plethora of opportunities appear by adding mechanical loads to the structure, including bending, stretching, and hydrostatic pressure (Burch et al., 2018; Levy et al., 2010; Yankowitz et al., 2019a; Yankowitz et al., 2018; Yankowitz et al., 2019b). Such unprecedented tunability has led to several observations of new physics (e.g. ‘magic-angle’ superconductivity (Cao et al., 2018b) and pseudomagnetic fields (Burch et al., 2018)) and a host of applications (e.g. phototransistors, light-emitting diodes and so on) (Geim and Grigorieva, 2013; Liu et al., 2016; Novoselov et al., 2016).

1.3 ELASTO-INTERMOLECULAR PHENOMENA

Complementary to these research activities in condensed-matter physics, research on mechanics of these 2D materials and their vdW structures has emerged recently (Akinwande et al., 2017; Androulidakis et al., 2018; Dai et al., 2019a; Liechti, 2019; Wei and Yang, 2018; Xu and Zheng, 2018). A particular finding at such atomic levels is that the area-related surface and interface forces start to dominate and interact tightly with the volume-related elastic forces. Such interaction has been the source of a variety of interesting mechanical behaviors of 2D materials and vdW structures in their functional devices; we term this class of mechanical behaviors *elasto-intermolecular* phenomena.

1.3.1 In-plane tension/shear

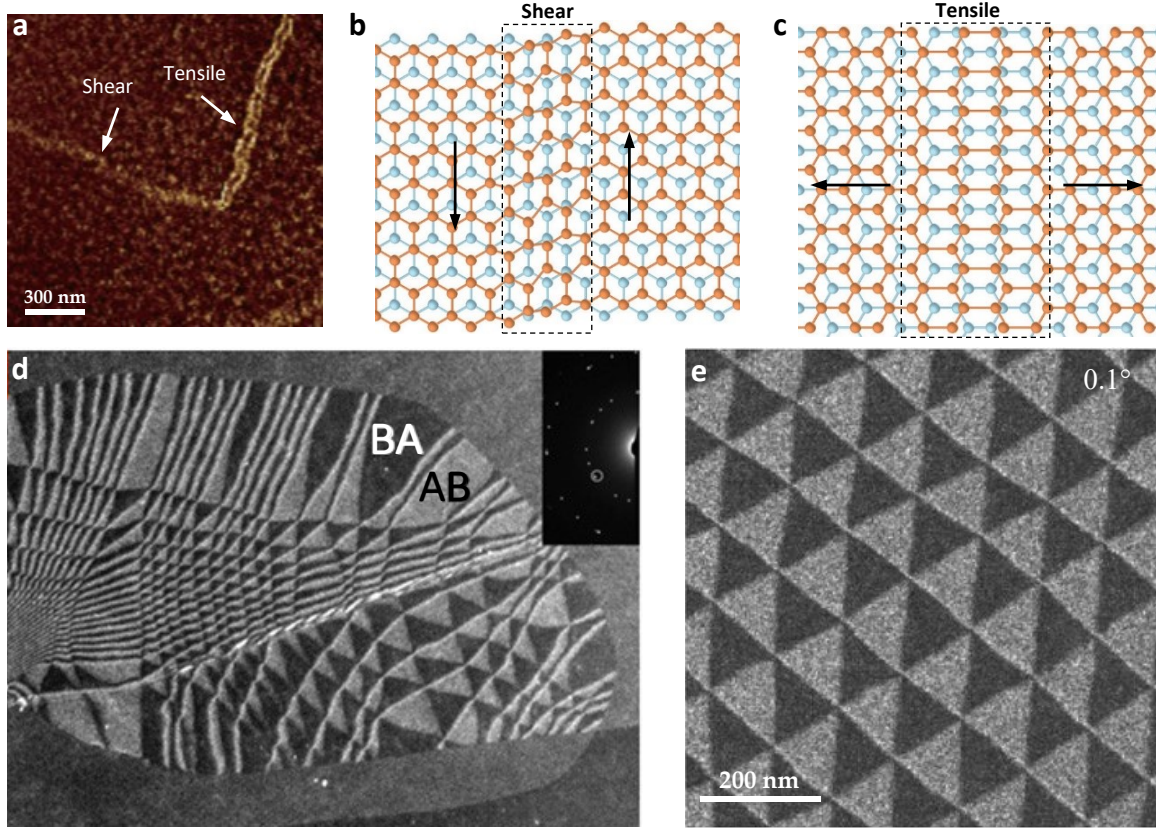


Figure 1.3: Domain walls in bilayer graphene. (a) Near-field infrared image of a sharp L-shape domain wall containing horizontal shear-type and vertical tensile-type solitons. Schematic illustrations of the shear- (b) and tensile-type (c) strain solitons. (a-c) are adapted with permission from (Jiang et al., 2016). (d) Dark-field TEM image of bilayer graphene with electrons selected from the $[-1010]$ family of diffraction angles that helps to distinguish AB (gray) from BA (black) domains. Adapted with permission from (Alden et al., 2013). (e) Dark-field TEM image of bilayer graphene with a uniform twisting angle of 0.1 degree. Adapted with permission from (Yoo et al., 2019).

A direct example comes from strain solitons in bilayer graphene (Butz et al., 2014), where two commensurate stacking orders (i.e., AB and BA, or collectively called Bernal stacking) exist in bilayer graphene (Yankowitz et al., 2014). One can transit to the other through a dislocation vector along the armchair direction of the graphene (Alden et al.,

2013; Kumar et al., 2016; Pochet et al., 2017). It often happens in experiments that two graphene layers are not perfectly Bernal-stacked. Then domains, where graphene layers are commensurate, are separated by 1D domain walls, where graphene layers are subject to mechanical strains and the stacking order changes rapidly in space (Figure 1.3a) (Jiang et al., 2016; Jiang et al., 2018; Woods et al., 2014). Domain walls in bilayer graphene are typically nanometer-wide and called shear-type or tensile-type solitons (Figure 1.3b&c), depending on whether the soliton is parallel to or perpendicular to the dislocation vector (Alden et al., 2013). The subtle strain solitons in bilayer graphene have provided a platform for the studies of novel electronic states (Alden et al., 2013) and fascinating electrical and optical properties according to theoretical predictions and recent experimental demonstrations (Ju et al., 2015; Yao et al., 2009; Zhang et al., 2011c).

More broadly, strain solitons and domain walls are common topological features of bilayer 2D material systems due to the periodic interlayer interaction potential (Ni et al., 2019; Woods et al., 2014). Such topology can evolve under thermal annealing (Figure 1.3d). For example, Alden et al. found that solitons in bilayer graphene became shorter and straighter during in situ heating above 1,000 °C, implying that AB and BA domains energetically favor regular structures (Alden et al., 2013). The example in Figure 1.3e shows triangular patterns of solitons and commensurate domains in 0.1°-twisted bilayer graphene that were found to correlate to moiré patterns (Yoo et al., 2019).

Under thermal stimuli, motions of localized solitons could accumulate and result in discernable global motions between two layers towards an interface-favored state (Wang et al., 2016a; Wang et al., 2015b; Woods et al., 2016). For example, Wang et al. observed a critical angle ($\sim 12^\circ$) for the rotation of a monolayer graphene on hBN, below which graphene tends to rotate towards a relative twisting angle of $\sim 0^\circ$ (most stable) with hBN, and $\sim 30^\circ$ (metastable) otherwise (Wang et al., 2016a). This interface-driven motion was

also found for graphene flakes of tens of micrometers with a translation or rotation of up to a few micrometers (Wang et al., 2015b; Woods et al., 2016). The fabrication of vdW structures and devices has benefitted from this unique self-rotation behavior; for example, a 2D material heterostructure can be aligned automatically by heating though it might be assembled with a random orientation of each layer initially (Wang et al., 2015b; Wang et al., 2013a).

Besides these spontaneous deformations, extensive efforts in the literature have focused on how in-plane strain could be applied to 2D materials controllably. The main motivation is that mechanical strains can tune the electronic and photonic properties of 2D materials and may ultimately give rise to high-performance devices (Dai et al., 2019a; Deng et al., 2018; Roldán et al., 2015; Sun and Liu, 2019). This principle is termed *strain engineering*; it has been leveraged extensively as a mechanical treatment to traditional semiconductors, for example, to reduce inter-valley scattering, increase mobility in Si transistors, and reduce the hole effective mass in III–V semiconductor lasers (Del Alamo, 2011). As an old technique developed for traditional semiconductors (Freund and Suresh, 2004), epitaxial growth on a substrate with a controlled lattice mismatch is still useful to 2D materials (Ahn et al., 2017; Akinwande et al., 2014; Amani et al., 2014; Liu et al., 2014), as illustrated in Figure 1.4a. Recent advances have advanced this technique for TMD heterojunctions containing multiple vertically or laterally connected TMD layers (Han et al., 2018; Xie et al., 2018; Zhang et al., 2018a; Zhao et al., 2015).

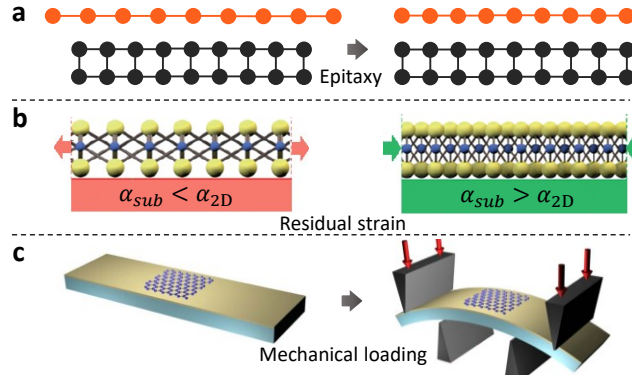


Figure 1.4: Introduction of in-plane strain into 2D materials. (a) CVD growth of 2D materials on a substrate with a mismatched lattice. (b) Tensile or compressive residual strain could be achieved by exploiting the thermal-expansion mismatch between the 2D material and its substrate. Adapted with permission from (Ahn et al., 2017). (c) Schematic of straining a 2D material by deforming its supporting substrate. Adapted with permission from (Mohiuddin et al., 2009).

The epitaxial growth of 2D materials typically involves an elevated temperature. After cooling, compressive or tensile strain can be deterministically achieved in the 2D material by selecting the substrate with different coefficients of thermal expansion (Figure 1.4b) (Freund and Suresh, 2004; Wang et al., 2017g). For example, Ahn et al. demonstrated stable built-in strains ranging from 1% tension to 0.2% compression by growing WSe₂ (9.5 ppm) on substrates with coefficients of thermal expansion ranging from 0.55 ppm to 12 ppm (Ahn et al., 2017). Notably, besides the growth method, post-heating/cooling of the 2D material-substrate system could offer a controllable way to introduce the thermal strain (Plechinger et al., 2015; Wang et al., 2015a). In this case, substrates could be arbitrary (not limited to be crystalline); and intricate strain patterns can be achieved in the 2D material by heating the substrate locally, such as with a focused laser (Plechinger et al., 2015).

2D materials are much more deformable than traditional silicon-based semiconductors and they can be readily transferred onto a flexible substrate (e.g., elastomer) (Jang et al., 2020; Papageorgiou et al., 2017). To develop mechanical strains in

2D materials, a natural way comes from direct tension/compression or bending of the substrate (Figure 1.4c) (Gong et al., 2010; He et al., 2013; Liang et al., 2017; Ni et al., 2008; Raju et al., 2014; Sarwat et al., 2018; Wu et al., 2018; Yang et al., 2017; Yang et al., 2015). This strategy allows for incremental tuning of the mechanical strain and simultaneous characterization of Raman and photoluminescence (PL) responses of 2D materials (Androulidakis et al., 2019; Dai et al., 2016b; Dou et al., 2018; Gong et al., 2010; Jiang et al., 2014; Wang et al., 2016b; Wang et al., 2017e; Xu et al., 2015; Xu et al., 2016). Such advantage has given rise to well-established relations between mechanical strains and electronic structures (e.g., bandgap) in monolayer and multilayer 2D materials, especially TMDs (He et al., 2013; Wu et al., 2018). Alternatively, once the Raman and PL response of the 2D material to the strain is calibrated, their monolayer nature makes 2D materials particularly promising for applications as conformable wireless strain sensors (Raju et al., 2014). Central to these applied in-plane strains is the interface mechanics between the 2D material and its substrate, particularly the tangential interfacial interactions (Dai et al., 2016b; Gong et al., 2010; Guo and Zhu, 2015; Jiang et al., 2014). The atomic smoothness of 2D materials renders their interfaces susceptible to slippage that limits the stress transfer efficiency from the substrate to the sheet. The interfacial shear stress during slippage has been modeled with a nonlinear shear lag model to explain the strain/Raman band gradient revealed in experiments (Dai et al., 2016b; Gong et al., 2010; Guo and Zhu, 2015; Jiang et al., 2014; Na et al., 2016).

1.3.2 Out-of-plane bending

In addition to in-plane deformations and rotations/translations, a range of out-of-plane deformations of 2D materials may interplay with interfacial interactions (Dai et al., 2019a; Deng and Berry, 2016; Kushima et al., 2015). As we mentioned in Section 1.3.1,

the CVD growth of 2D materials typically requires a high temperature, and a mechanical strain (either compressive or tensile) can be generated after cooling (Ahn et al., 2017; Dai et al., 2019a). Cui et al demonstrated the spontaneous formation of nanoscrolls by CVD-grown TMDs (Figure 1.5a), which was triggered by an ethanol droplet and energetically favored by the release of the residual strain and the formation of 2D-2D interfaces (Cui et al., 2018).

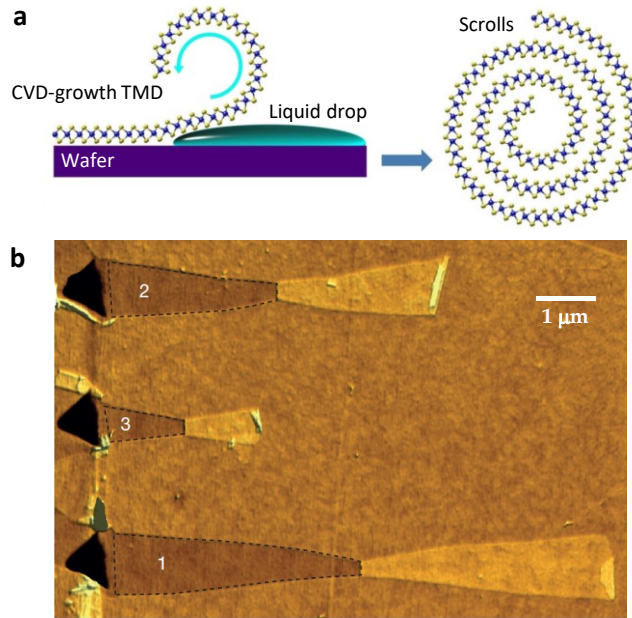


Figure 1.5: Scrolls and folds. (a) Schematic of the spontaneous rolling of a CVD-grown TMD monolayer. Adapted with permission from (Cui et al., 2018). (b) AFM images of self-folding of bilayer graphene ribbons with different initial width. Adapted with permission from (Annett and Cross, 2016).

2D material folds have been frequently observed with a nanoscale curvature (Hallam et al., 2014; Ortolani et al., 2012; Shenoy and Gracias, 2012) in 2D material devices, reminiscent of carbon nanotube folds (Buehler et al., 2006; Mikata, 2010; Tawfick et al., 2011). By electron diffraction, Zhang et al. examined the edge structure of ~ 100 suspended graphene folds and found that about $\sim 1/3$ were armchair (global energy

minimum) and $1/3$ were zigzag (local energy minimum) (Zhang et al., 2010). More recently, Annett and Cross pierced a graphene layer on a substrate by an indenter and found that small tabs of folded-over graphene initiated and grew with spontaneous sliding, peeling, and tearing over time (Figure 1.5b) (Annett and Cross, 2016). This finding highlights the remarkable driving force provided by the 2D-2D interactions that can overwhelm both the edge energy of the sheet and the 2D material-substrate adhesion. Though folds are undesirable from the point of view of the device reliability, this type of out-of-plane deformation could be useful in mechanical metrologies (Chen et al., 2015; Han et al., 2019; Qu et al., 2019; Zhao et al., 2015), vdW structure fabrications (Rode et al., 2018; Schmidt et al., 2014), 2D material-based 3D origami and composites (Akius and van Ruitenbeek, 2018; Wang et al., 2019a; Wang et al., 2018; Xu et al., 2017). Extensive efforts have focused on controlling the folding and unfolding of these atomically thin sheets, and hence the physical properties of folds (Akius and van Ruitenbeek, 2018; Chang et al., 2018; Chen et al., 2019; Schniepp et al., 2008; Wang et al., 2017a; Yi et al., 2019). For example, Chen et al. used scanning tunneling microscope tips to tune the folding directions of monolayer graphene such that the folded, tubular edge can be precisely designed with specified chirality and thus 1D electronic properties (similar to those of carbon nanotubes) (Chen et al., 2019).

Another type of bending-dominated deformations arises from elastic instabilities when a compressive strain appears in the 2D material/substrate system (Dai et al., 2019a; Dai et al., 2020). As illustrated in Figure 1.6a-c. The compressive strain could come from several origins, including the compression or pre-tension of the substrate, thermal residual stress, and the growth or transfer of 2D materials on substrates (including other 2D materials) with a relatively smaller lattice constant. In general, when the substrate is relatively stiff, buckle delamination is typically observed (Figure 1.6d-f) (Carbone et al.,

2019; Castellanos-Gomez et al., 2013; Hattab et al., 2012; Lou et al., 2018; Ly et al., 2017; Yang et al., 2015); When the substrate is relatively compliant, wrinkles are more likely to occur (Figure 1.6g-i) (Chen et al., 2016b; Hattab et al., 2012; Meng et al., 2013a; Quereda et al., 2016; Sampathkumar et al., 2019; Xie et al., 2018). In some systems, wrinkles and buckle delamination can co-exist and co-evolve with the magnitude of the applied/existing compressive strain (Brennan et al., 2015; Pan et al., 2014). Of particular interest is the localized strain at the crest of these buckles and wrinkles, where the curvature reaches the maximum. Recent works have shown that such localized strain could alter the electronic and optical properties of 2D materials remarkably, such as effective reduction of the direct bandgap in MoS₂ multilayers and 0.7-eV shift of the absorption edge in black phosphorus flakes (Castellanos-Gomez et al., 2013; Quereda et al., 2016). In addition, the wavelength of wrinkles and the crest curvature of buckles have been used for measuring Young's modulus of 2D materials (Iguñiz et al., 2019) and 2D material-substrate adhesion (Dai et al., 2019a; Deng and Berry, 2016), respectively.

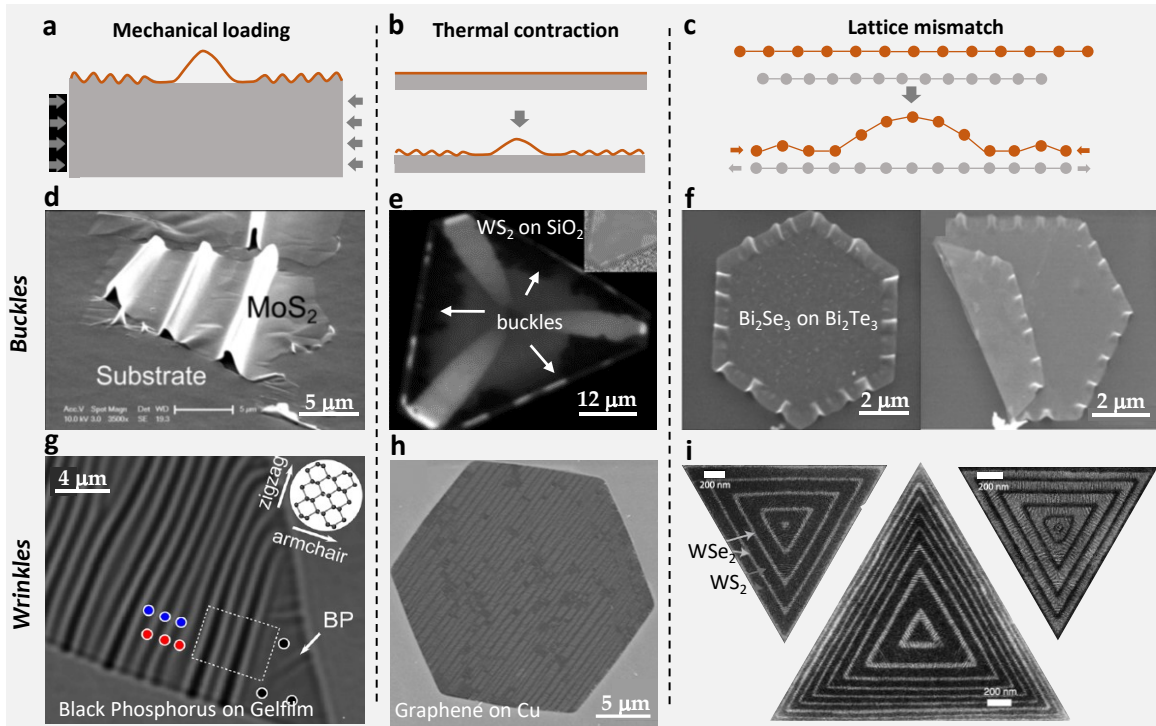


Figure 1.6: 2D material buckles and wrinkles. Schismatic of 2D material buckles and wrinkles stemming from different origins: (a) the compression or pre-stretch of the substrate, (b) shrinking of the 2D material/substrate system due to a temperature change, and (c) heterostructures with an intrinsic lattice mismatch between layers. (d) Scanning electron microscope (SEM) image of a MoS₂ flake buckling on an elastomeric substrate. Adapted with permission from (Castellanos-Gomez et al., 2013). (e) PL intensity image of a triangle monolayer WS₂ where edge buckle delamination occurs due to the thermal residual strain. Adapted with permission from (Ly et al., 2017). (f) SEM images of buckle delamination at edges of Bi₂Se₃/Bi₂Te₃ heterojunctions where the bottom layer is compressed by the top layer due to the $\sim 5.9\%$ lattice mismatch. Adapted with permission from (Lou et al., 2018). (g) Optical image of a multilayer black phosphorus wrinkling on an elastomer. The inset shows a sketch of the crystal lattice orientation. Adapted with permission from (Quereda et al., 2016). (h) SEM image of a wrinkled graphene grown on copper as this system cools. Adapted with permission from (Meng et al., 2013a). (i) SEM images of WS₂/WSe₂ superlattices with wrinkled/rippled structures at edges (greyish regions). Adapted with permission from (Xie et al., 2018).

1.3.3 Out-of-plane stretching

Although these 2D material folds, scrolls, wrinkles, and buckles experience large out-of-plane deformations, their material length is almost preserved, and the gross Gaussian curvature of the structure nearly remains zero in the deformation configurations (Audoly and Pomeau, 2000; Holmes, D.P., 2019; Vella, 2019). Another class of out-of-plane deformation arises when a Gaussian curvature of the deformed sheet changes.

The excellent flexibility of 2D materials, together with their strong vdW interactions to substrates, usually guarantees an excellent conformability. As a consequence, the Gaussian curvature change of 2D materials can be naturally achieved by transferring them onto pre-patterned substrates (Li et al., 2016b; Reserbat-Plantey et al., 2014; Shin et al., 2016; Zhang et al., 2018b). Recently, a variety of substrate patterns have been demonstrated, along with technical strategies for the transfer of 2D materials onto such patterns (Choi et al., 2015; Li et al., 2015; Li et al., 2016a; Li et al., 2016b; Nemes-Incze et al., 2017). The resulted configurations have been practically useful in many situations, where the mechanical strains in the 2D materials couple with interface chemistry and physics. For example, Zheng et al. transferred MoS₂ to SiO₂ nano-domes with the aid of capillary pressures (Figure 1.7a) and demonstrated the applications of the strained structure in hydrogen evolution and bandgap engineering (Li et al., 2015; Li et al., 2016a; Li et al., 2016b). Notably, Choi et al. proposed a ‘three-step’ graphene integration technique that essentially allows arbitrary 3D graphene patterns; elongated pyramids, rectangular pillars, and inverse pyramids were demonstrated in (Choi et al., 2015).

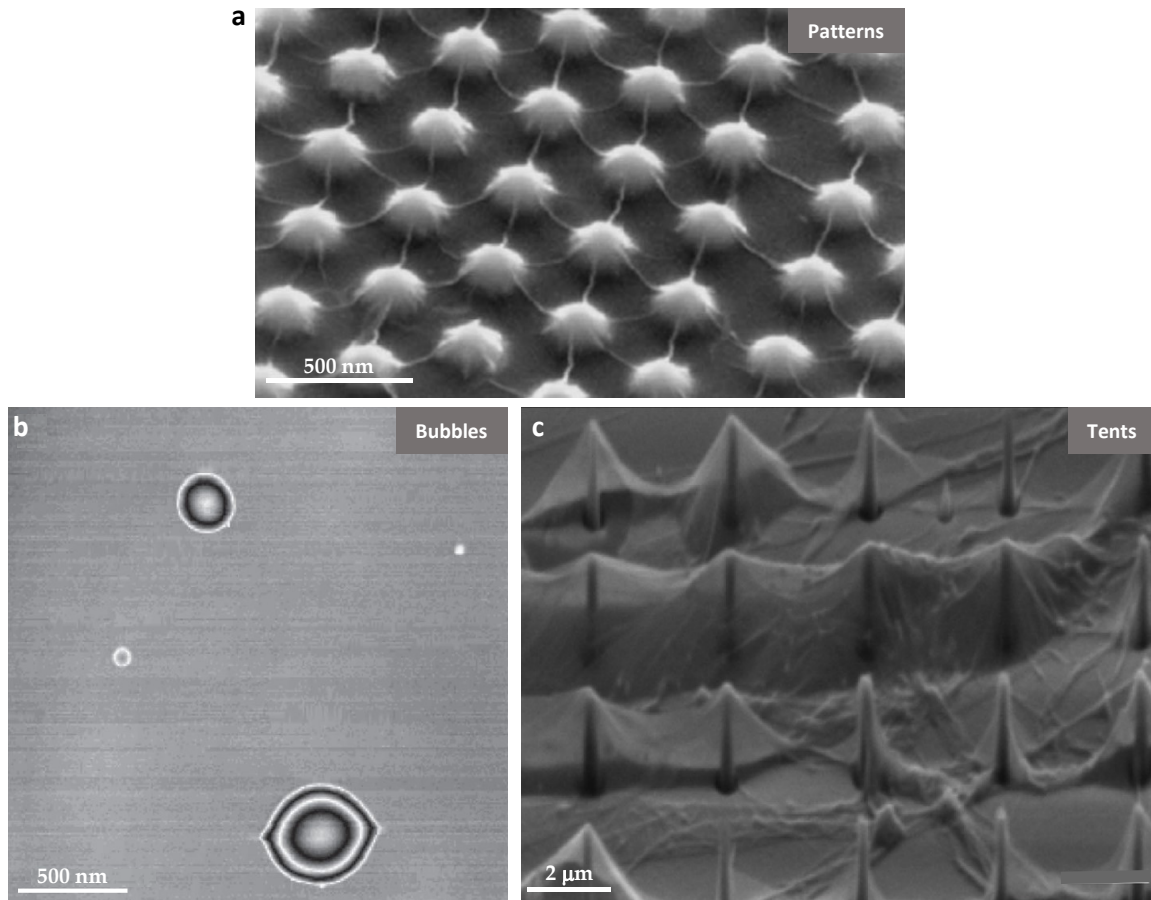


Figure 1.7: 2D materials with large out-of-plane deformations. (a) SEM image of a MoS₂ layer fully conforming on a dome-patterned substrate. Adapted with permission from (Li et al., 2015). (b) AFM image of spontaneously formed graphene bubbles on bulk hBN (Khestanova et al., 2016). (c) SEM image of tents formed by transferring a graphene sheet onto pillar-patterned silicon substrate. Adapted with permission from (Reserbat-Plantey et al., 2014).

Applications of 2D materials and their vdW structures have to involve multiple transfer process of 2D materials. *2D material bubbles and tents* frequently form due to the trapping of fluids (e.g., water, gas, hydrocarbons) and solid nanoparticles at the interface (Figure 1.7b&c) (Ghorbanfekr-Kalashami et al., 2017; Khestanova et al., 2016; Vasu et al., 2016; Yoshida et al., 2018; Zamborlini et al., 2015). Initially, those circular blisters have been viewed as an inconvenience for device applications (Kretinin et al., 2014; Pizzocchero

et al., 2016). However, recent studies showed that the considerable in-plane strain associated with these bubbles and tents could, in turn, create opportunities for the study of new fundamental physics and applications of 2D materials emerging at large strain levels (Branny et al., 2017; Klimov et al., 2012; Levy et al., 2010; Settnes et al., 2016). Alternatively, many 2D material bubbles and tents are designedly created by confining interface liquids or gas (Chen et al., 2017; Ghorbanfekr-Kalashami et al., 2017; Jia et al., 2019; Tedeschi et al., 2019) or pre-patterning substrates with pillars (Figure 1.7c) (Branny et al., 2017; Jiang et al., 2017; Reserbat-Plantey et al., 2014). Applications include strain-caused pseudo-magnetic fields (up to 300 T) in graphene bubbles and tents (Jiang et al., 2017; Klimov et al., 2012) as well as large-scale quantum emitters enabled by draping 2D semiconductors over an array of micropillars (Branny et al., 2017).

1.4 MOTIVATION

These interesting elasto-intermolecular phenomena could be understood as a result of the balance between elastic and surface/interface forces. In fact, a qualitatively similar class of problems concerning the deformation of solids caused by surface forces (mainly from liquids) have been widely studied at sub-millimetric scales and frequently referred to as elasto-capillarity (Andreotti and Snoeijer, 2019; Bico et al., 2018; Style et al., 2017). Distinctively, the unique combination of the atomic thinness of 2D materials and the rich behaviors at 2D material interfaces make these small-scale elasto-intermolecular phenomena particularly interesting. There are natural needs to achieve a mechanistic understanding of such phenomena. In this context, extensive efforts have been reported in the literature; however, the atomically smooth nature of 2D material interfaces has been largely under-appreciated (see further discussion in Chapters 2-7), which motivates this dissertation. In the following, the features of 2D material interfaces will be briefly

reviewed. We then highlight bubbles and tents that could be powerful tools for the characterization of the mechanics of 2D materials and their interfaces.

1.4.1 2D material interfaces

Clearly, normal interfacial tractions at 2D material interfaces could be “strong” (Boddeti et al., 2013a; Boddeti et al., 2013b; Koenig et al., 2011), relatively to elastic forces. We have reviewed that the interfacial adhesion can compete with the elastic energies associated with the bending and stretching of 2D materials. The competition typically gives rise to a characteristic length scale or geometry for the deformed 2D materials. Examples include the curvature for graphene scrolls (Li et al., 2018; Zhang et al., 2018c) and folds (Meng et al., 2013b; Zhang et al., 2010; Zhao et al., 2015) as well as 2D material buckles (Dai et al., 2019a; Deng and Berry, 2016; Vella et al., 2009), the lateral size of strain solitons (Braun and Kivshar, 2013), the tapering angle (Fonseca and Galvão, 2019; Gao et al., 2018) and final width of self-torn graphene (Annett and Cross, 2016; He et al., 2018), and the aspect ratios of 2D material bubbles and tents (Dai et al., 2018; Jia et al., 2019; Khestanova et al., 2016; Lyublinskaya et al., 2019; Sanchez et al., 2018; Tedeschi et al., 2019). Besides, adhesion energies between 2D materials and substrates (including 2D materials themselves) play an essential role in the fabrication of 2D material devices and vdW structures. For instance, the manufacturing typically involves extensive transfer processes (Frisenda et al., 2018), such as the exfoliation of 2D materials from their bulk crystals and (multiple) deliveries from donor substrates to target substrates. A so-called vdW pick-up transfer method has been developed that used an hBN flake (instead of elastomer) as the stamp to grab the 2D material from its substrate (Frisenda et al., 2018; Pizzocchero et al., 2016; Wang et al., 2013a), which essentially leveraged the strong vdW interactions between atomically smooth sheets,

On the other hand, the tangential interfacial tractions are relatively “weak” (Hod et al., 2018a; Song et al., 2018; Wang et al., 2017b) that facilitate the shear deformation of 2D-material-based interfaces. Examples include the slippage at 2D material-polymer interfaces (Dai et al., 2016b; Jiang et al., 2014), self-peeling/folding of graphene sheets (Annett and Cross, 2016), self-rotation of vdW structures (Wang et al., 2016a; Wang et al., 2015b; Woods et al., 2016), and thermal motion of strain solitons (Alden et al., 2013). The weakness of 2D material interfaces in shear could also degrade the stretching and bending resistance of multilayer 2D materials (Liu et al., 2011; Nazemnezhad et al., 2014; Pan et al., 2019; Ruiz et al., 2015; Shen and Wu, 2012). The weak shear interaction between 2D materials can also be indicated by the softened bending rigidity of multilayer 2D materials – a crucial parameter controlling their out-of-plane behavior (e.g., scrolling, folding, wrinkling, and so on) (Chen et al., 2015; Han et al., 2019; Qu et al., 2019; Zhao et al., 2015). For example, a limiting case comes from classical plate theory that assumes perfectly glued interfaces between layers and leads to a bending rigidity proportional to N^3 for a N -layer 2D material (Gao and Huang, 2011). However, when the interface is ultra-lubricated, another limiting case is that each layer would bend independently so that the overall bending rigidity of a multilayer would scale linearly with N . The actual bending rigidity of a number of 2D materials has been found to close to the lower limit (Wang et al., 2019b).

These examples again indicate the importance of understanding the interfacial properties as well as the mechanical properties of 2D materials. The understanding would be highly beneficial to the control of the overall structural and mechanical behavior of 2D material devices and vdW structures, the optimization of fabrication methods, and the design of their functionalities. Numerous techniques have been developed to characterize

these properties (Akinwande et al., 2017; Liechti, 2019), among which 2D material bubbles and tents that can form either spontaneously or designedly stand out as versatile platforms.

1.4.2 Spontaneous bubbles and tents

Due to the extremely high surface-to-volume ratio of 2D materials, ambient contaminants such as water molecules and hydrocarbons are inevitably absorbed on the surface of 2D materials. The fabrication of 2D material devices and vdW structures involves intensive transfer processes. Consequently, bubbles (also called blisters, pockets) are frequently formed at the 2D material-substrate interfaces as the interfacial interactions can lump adsorbed molecules together (Khestanova et al., 2016; Novoselov et al., 2016; Sanchez et al., 2018). At first, interfacial bubbles were viewed as a result of the self-cleansing of the interfaces (Novoselov et al., 2016). They have been used as indicators of good adhesion between the constituents of vdW heterostructures. In essence, bubbles are energetically favorable only when the adhesion between layers is substantial enough to drive the cleansing (Novoselov et al., 2016). Similarly, when the contaminants are nanoparticles, 2D material tents can form spontaneously as the sheet comes into contact with the substrate and drapes over the nanoparticles (Gao et al., 2017; Zong et al., 2010). Based on the deformed configuration of graphene tents, Zong et al. achieved the first estimation of adhesion energy ($\sim 0.15 \text{ J/m}^2$) between graphene and silicon oxide (Zong et al., 2010).

1.4.3 Indentation and bulge tests

More detailed information about the mechanical properties of 2D materials and their adhesion to substrates can be provided by 2D material bubbles and tents created by controlled loading (Figure 1.8) (Cao and Gao, 2019; Cao, 2015; Cao et al., 2015, 2016;

Cao et al., 2014; Wang et al., 2013b; Yue et al., 2012). For example, nanoindentation of 2D material drumheads represents a common type of inverse tents and now has been widely used for the stiffness and strength measurements of various 2D materials (Bertolazzi et al., 2011; Castellanos-Gomez et al., 2012; Dai et al., 2019b; Lee et al., 2008; Lipatov et al., 2018; Tu et al., 2018; Xu et al., 2018). Bunch and co-workers invented gas-pressurized graphene bubbles with controlled sealed gas molecules (Boddeti et al., 2013a; Boddeti et al., 2013b; Koenig et al., 2011). This set-up has not only detected the stiffness of the sheets but also achieved stable sheet-substrate contacting and separating that led to systematic studies of the normal interfacial interactions between graphene and silicon oxide (Liu et al., 2013; Lloyd et al., 2017; Lloyd et al., 2016). Liechti and co-workers developed the graphene bubbles with associated analysis to characterize the mixed-mode traction-separation relations between graphene and copper (Cao, 2015; Cao et al., 2015, 2016; Cao et al., 2014).

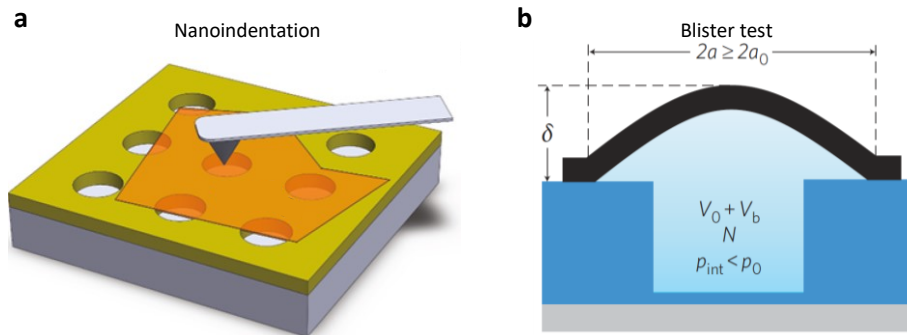


Figure 1.8: Suspended 2D materials under a point load or pressure. Schematic depiction of the indentation experiment (a) and blister test (b) on 2D materials. (a) and (b) are adapted with permission from (Bertolazzi et al., 2011) and (Koenig et al., 2011), respectively.

1.4.4 Questions to be answered

These experiments have demonstrated the potential of bubbles and tents to establish themselves as standard methods for characterizing the rich mechanics of 2D materials as well as 2D material interfaces. Besides, 2D material bubbles and tents have found extensive opportunities and applications in strain engineering: the associated in-plane strains have been exploited in a range of exciting strain-coupled physics (e.g., bandgap engineering and pseudomagnetic fields) and unique quantum applications.

Surprisingly, a key feature of 2D material interfaces has been neglected in the modeling of these systems – the weak resistance to tangential shear. Such shear can even vanish at incommensurate 2D-2D interfaces, which is called structural superlubricity. However, bubbles and tents have been frequently modeled with a clamped boundary that prohibits any shear motions of the tangentially weak sheet-substrate interface. In striking contrast to such modeling, experimental observations have revealed subtle instabilities at the edge of 2D material bubbles and tents, even at deflections far from the occurrence of vertical interfacial delamination (see details in Figure 2.2 in Chapter 2). These instabilities take the form of wrinkling in the suspended region and buckling delamination in the supported (if occurs). Essentially, they result from the radially inward sliding of the bubble/tent boundary or the 2D material atop its substrate (Dai et al., 2018; Huang and Zhang, 2011).

It is natural to ask how the shear of 2D material interfaces and the formation of elastic instabilities modify the mechanical resistance of the sheet to applied point loads or pressure. The answer would help to precisely characterize the elastic properties of 2D materials in those indentation and blister tests (Akinwande et al., 2017). Also, the strain in bubbles and tents seems useful to tune the physical and chemical properties of the atomic

sheet (Dai et al., 2019a). It is, therefore, vital to know how strain fields are modified as well so that the strain engineering of 2D materials can be guided in a deterministic way.

These monolayers have to contact substrates to realize the promised functionalities. Adhesion energies between 2D materials and various surfaces would play an important role. The task of detecting the adhesion of each interface is highly challenging due to both technical issues associated with the atomic dimension of 2D materials and the fact that over 100 different materials in principle can be isolated into atomic monolayers. However, spontaneously formed bubbles and tents would be useful for quick estimations of the 2D material/substrate adhesion, particularly given their ubiquitous appearance in 2D material devices (Sanchez et al., 2018). To this end, we need to answer a general question about how the elasticity of the 2D material (together with its adhesive and shear interactions to the substrate) selects the bubble and tent geometry. This general question can raise several specific questions: What is the role of the trapped substances (especially the liquids trapped by bubbles) at the small scales in addition to providing a geometrical constraint? What are governing equations for regimes with and without instabilities in these spontaneous bubbles and tents? What are the conditions to match different regimes?

1.5 STRUCTURE OF THE DISSERTATION

This dissertation aims to answer these questions concerning the mechanics of 2D material bubbles and tents. We study a collection of problems in this area with a particular emphasis on the role of the shear deformation associated with atomically smooth interfaces.

In Chapter 2, we present the theoretical framework for point-loaded and pressurized circular elastic sheets. We consider the previously mysterious *edge slippage* of 2D material sheets upon loading as the sheet-substrate vdW interactions allow the sheet edges to move inward. Furthermore, such edge slippage can cause interesting elastic instabilities of those

highly bendable sheets. Based on the observation of deformed thin sheets that are revealed in experiments, we consider three possible situations where instabilities perturb the instability-free base state to different degrees.

The numerical analysis of the three possible cases discussed in Chapter 2 is presented and discussed in Chapter 3. The results include the effective stiffness of the sheet and the extent of the wrinkling in the suspended region as well as the buckling (if any) in the supported area. We identify a single parameter for the system, *sliding number*, which compares tractions due to interfacial friction and sheet stretching. We discuss how this single parameter controls the growth of the wrinkling or buckling region as well as the softening of the effective stiffness of the sheet under poking and bulging.

In Chapter 4, we focus on a particular case of the bulge test of 2D materials when the *bending* contribution to the vertical loading is considerable. We start with theoretical modeling of a pressurized thin sheet with bending rigidity that is independent of Young's modulus – a unique property of 2D materials or 2D-material-based structures. We suggest the signatures of the bending effect being dominant and a simple analytical formula with excellent approximation across two asymptotic regimes (i.e., bending-dominated and stretching-dominated). This understanding helps the design of experiments and the interpretation of experimental data, which eventually leads to direct measurements of the bending rigidity of three types of multilayer 2D materials, say graphene, molybdenum disulfide (MoS_2), and hexagonal boron nitride (hBN).

In Chapter 5, we provide the *analytical* solution to the strain fields in blisters, including bubbles and tents formed by 2D materials. We are motivated by their uses for strain engineering of 2D materials. We first show recent experiments that inspired us to characterize a simple and unified power law for the profiles of a variety of 2D material bubbles and tents. Using membrane theory, we draw an analytical relation between the in-

plane strains of these blisters and their shape and interface characteristics (i.e., friction and adhesion). We offer direct ties between the aspect ratio (height-to-radius ratio) of a 2D material blister and the strain fields in it.

Previous chapters have revealed the crucial role of the aspect ratio of 2D material bubbles and tents in controlling their strain fields as well as the edge slippage and elastic instabilities. In Chapter 6, we further show that the aspect ratio often appears constant in experiments, which could be understood as a result of the balance of elastic and surface/interface forces in the system. 2D material bubbles are the focus of this chapter though the underlying physical idea discussed here also applies to 2D material tents. We develop a simple scaling law and a rigorous theoretical model for liquid-filled bubbles, predicting that the fourth power of the aspect ratio of the blister is related to the interfacial work of adhesion and the surface tension of the liquid. This prediction is further used to estimate the adhesion between the 2D material and its substrate.

Unlike previous chapters where we have mainly studied buckle-delamination-free blisters, Chapter 7 presents the discussion on microscale tents that are formed when 2D materials are transferred over nanoparticles or nanopillars – in the periphery of which radial buckle delamination has been often observed. We obtain theoretical predictions for the extent of those buckles by exact closed-form solutions to Föppl–von Kármán (FvK) equations in this chapter. Analytical solutions to both near-threshold and far-from-threshold conditions are provided.

Chapter 8 summarizes our findings and discusses a number of avenues for further research as well as several important questions that remain unanswered in this dissertation.

The theoretical setting for Chapter 3 relies on the framework and notation developed in Chapter 2. Otherwise, the chapters are self-contained and include an introduction to relevant research areas.

Chapter 2: Theory¹

Motivated by the vast uses of indentation and bulge tests on small-scale thin sheets, we present theoretical modeling of point-loaded and pressurized circular elastic sheets. We consider the edge slippage of the sheet upon loading as the sheet edges are usually held by the sheet-substrate vdW interactions that are extremely susceptible to shear deformations. Furthermore, such edge slippage involves interesting elastic instabilities of those highly flexible sheets. Based on the deformed configurations of thin sheets revealed in our experiments, we discuss the following three situations to different extents to which the instabilities perturb the base state. Case I describes the base state where the applied load causes the interfacial slippage inward radially, but elastic instabilities are suppressed (though unrealistic for 2D materials). Case II allows the formation of wrinkles in the suspended region to release any (hoop) compression while assumes that instabilities are suppressed by the strong interfacial adhesion in the supported region. In Case III, elastic instabilities are permitted in both the suspended region (in the form of wrinkling) and the supported region (in the form of buckling delamination). These results are the basis of the membrane analysis performed in Chapter 3 and the nonlinear plate analysis undertaken in Chapter 4.

¹A paper will be prepared based on the work in this Chapter and Chapter 3:
Z. Dai, N. Lu. *Poking and Bulging of Ultrathin Elastic Sheets: Edge Slippage and Instabilities*. (The manuscript is in preparation.)

2.1 INTRODUCTION

2D materials are frequently deformed by forces in the 3rd dimension. In particular, *poking* by indentation (Bertolazzi et al., 2011; Castellanos-Gomez et al., 2012; Dai et al., 2019b; Lee et al., 2008; Lipatov et al., 2018; Tu et al., 2018; Wang et al., 2017d; Xu et al., 2018) and *bulging* by pressurization (Boddeti et al., 2013a; Boddeti et al., 2013b; Cao et al., 2015, 2016; Koenig et al., 2011; Liu et al., 2013; Lloyd et al., 2017; Lloyd et al., 2016; Wang et al., 2017b; Wang et al., 2013b; Yue et al., 2012) have been popular tools with which to characterize the mechanics of a variety of 2D materials and their interfaces. In this dissertation, we call the deformed configurations of the sheet upon indentation and pressurization tents and bubbles, respectively, to underline their shape characteristics. Both are also frequently referred to as blisters in the literature. Tents and bubbles are also ubiquitous in a range of 2D material devices due to the spontaneous trapping of solids, gases, or liquids at the material interfaces. The trapped substances are typically absorbed from the ambient during device fabrication processes; More recently, extensive experimental efforts have focused on controlling the types and amounts of these interfacial substances for desired functionalities (Branny et al., 2017; Chen et al., 2017; Gao et al., 2017; Ghorbanfekr-Kalashami et al., 2017; Jia et al., 2019; Jiang et al., 2017; Khestanova et al., 2016; Kretinin et al., 2014; Novoselov et al., 2016; Pizzocchero et al., 2016; Reserbat-Plantey et al., 2014; Sanchez et al., 2018; Tedeschi et al., 2019; Vasu et al., 2016; Yoshida et al., 2018; Zamborlini et al., 2015; Zong et al., 2010).

Mathematical modeling of blisters usually assumes an edge-clamped, moderately deformed, linearly elastic thin sheet subjected to a point force for a tent or a uniform pressure for a bubble (Begley and Mackin, 2004; Komaragiri et al., 2005; Vella and Davidovitch, 2017; Wan et al., 2003). These assumptions largely simplify the modeling and give rise to analytical formulae that have been widely used for the analysis and

interpretation of experimental data (Bertolazzi et al., 2011; Castellanos-Gomez et al., 2012; Dai et al., 2019b; Freund and Suresh, 2004; Lee et al., 2008; Lipatov et al., 2018; Mansfield, 2005; Tu et al., 2018; Xu et al., 2018). However, issues appear if we consider the subtle nature of the 2D material-to-substrate interface. Mainly, the atomic smoothness and flexibility of the sheet render a robust vertical contact with its substrate (Boddeti et al., 2013a; Boddeti et al., 2013b; Koenig et al., 2011) but a quite weak tangential resistance of the interface to shear deformations (Hod et al., 2018a; Song et al., 2018; Wang et al., 2017b). As a result, the sheet could be readily pulled to slide over its substrate by the vertical load, even when the deflection is small, and the vertical interfacial contact remains intact (Dai et al., 2020; Kitt et al., 2013; Wang et al., 2017b). These important subtleties have been hidden in the modeling based on clamped boundary assumptions (Begley and Mackin, 2004; Komaragiri et al., 2005; Vella and Davidovitch, 2017; Wan et al., 2003). We thus pose a question of how the interfacial slippage modifies the mechanical responses of 2D material to out-of-plane loading, which remains unanswered despite extensive theoretical and experimental studies of the 2D material blisters for more than a decade.

In this chapter, we present a theoretical framework for the point-loaded and pressurized circular sheets, in which the annulus edges of the sheets are allowed to slide on the supporting substrate to account for the shear behavior of 2D material interfaces. Without loss, we assume a finite, constant interfacial shear/sliding resistance. Since such interfacial slippage would compress a material circle circumferentially, our theoretical framework involves the analysis of radial elastic instabilities of thin sheets in the suspended and supported regions.

2.2 PROBLEM DESCRIPTION

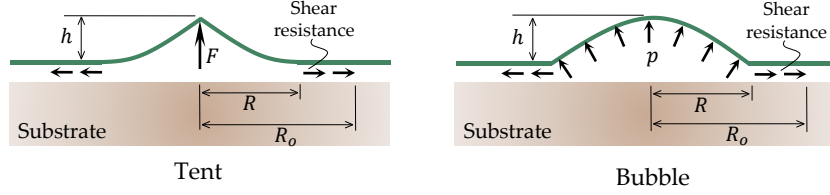


Figure 2.1: Free body diagrams of the base state of a 2D material tent and bubble.

Figure 2.1 shows the diagrams of the point-loaded and pressurized thin sheet. The thin sheet is suspended in $[0, R]$ while supported by the substrate in $[R, \infty]$. Typically, the radius R is prescribed in indentation and bulge tests, for example, by the patterned geometry on the substrate. When delamination occurs or for spontaneously formed blisters, the radius becomes unknown, while we will show in Chapter 6 that it could be related to other given geometrical or mechanical quantities. Interfacial slippage is assumed to take place in $[R, R_o]$, where R_o is not known *a priori*.

2.2.1 Föppl–von Kármán equations

We first discuss the force equilibrium in the suspended region of a blister. In the vertical direction, the load $q(r)$, which is $F\delta(r)/2\pi r$ for the point load and p for the pressure, is balanced by the bending and stretching of the sheet (Mansfield, 2005),

$$\nabla^2(B\nabla^2 w) - (N_{rr}\kappa_{rr} + N_{\theta\theta}\kappa_{\theta\theta}) - q(r) = 0, \quad (2.1)$$

where B is the bending stiffness of the sheet, N_{rr} and $N_{\theta\theta}$ are the radial and hoop stress resultants, respectively, w represents the out-of-plane deflection of the sheet. We assume moderate rotation, linear elasticity, and axisymmetry such that $\nabla^2 f = d^2 f/dr^2 + r^{-1}df/dr$ and the curvatures can be approximated by

$$\kappa_{rr} \approx \frac{d^2 w}{dr^2} \text{ and } \kappa_{\theta\theta} \approx \frac{dw}{rdr}. \quad (2.2)$$

The in-plane force balance leads to

$$\frac{d}{dr}(rN_{rr}) - N_{\theta\theta} = 0. \quad (2.3)$$

The equilibrium equations with linearized curvatures are often called Föppl–von Kármán (FvK) equations. It is convenient for numerical computations in Chapters 3 and 4 to introduce the Airy stress function. By this, the in-plane equilibrium can be satisfied automatically by setting the radial and circumferential stress resultants as

$$N_{rr} = \frac{d\phi}{rdr} \text{ and } N_{\theta\theta} = \frac{d^2\phi}{dr^2}. \quad (2.4)$$

FvK equations can then be rewritten in terms of Airy stress function and the out-of-plane deflection (Mansfield, 2005),

$$\nabla^2(B\nabla^2w) - [\phi, w] - q(r) = 0 \quad (2.5)$$

and

$$\nabla^4\phi + \frac{1}{2}E_{2D}[w, w] = 0, \quad (2.6)$$

where E_{2D} is the in-plane stiffness of the membrane, $[f, g] = r^{-1}d\left(\frac{df}{dr}\frac{dg}{dr}\right)/dr$, and $\nabla^4 = \nabla^2\nabla^2$. Equations (2.5) and (2.6) are invariant under $w \rightarrow -w$, $q(r) \rightarrow -q(r)$; the equilibrium, therefore, is identical to the cases of pushing downward and pulling upward.

It is advantageous to write FvK equations in terms of vertical and horizontal displacements if one of them could be analytically expressed (or approximated), for instance, in the experimental observations in Chapter 5. To this end, the stresses in (2.1) are linked to strains according to Hooke's law (linear elasticity) that are further presented regarding displacements based on nonlinear kinematics (moderate rotation). The vertical and horizontal equilibrium now become (Timoshenko and Woinowsky-Krieger, 1959; Wang et al., 2013b)

$$B\left(\frac{d^3w}{dr^3} + \frac{1}{r}\frac{d^2w}{dr^2} - \frac{1}{r^2}\frac{dw}{dr}\right) + \frac{E_{2D}}{1-\nu^2}\frac{dw}{dr}\left[\frac{du}{dr} + \nu\frac{u}{r} + \frac{1}{2}\left(\frac{dw}{dr}\right)^2\right] - \frac{1}{r}\int_0^r q r dr = 0 \quad (2.7)$$

and

$$\frac{d^2u}{dr^2} + \frac{1}{r} \frac{du}{dr} - \frac{u}{r} + \frac{1-\nu}{2r} \left(\frac{dw}{dr} \right)^2 + \frac{dw}{dr} \frac{d^2w}{dr^2} = 0, \quad (2.8)$$

respectively, where ν is the Poisson's ratio of the sheet, and we integrated (2.1) once to obtain (2.7). The integration constant over the domain $[0, r]$ is set to be zero to satisfy the vertical shear force balance (Timoshenko and Woinowsky-Krieger, 1959).

2.2.2 Clamped boundary conditions

Numerical calculations could be performed based on either (2.5) and (2.6) or (2.7) and (2.8). For the latter, five boundary conditions are required; they are straightforward when the edge of the sheet is clamped. Specifically, we have, at the center of the blister,

$$\left(\frac{dw}{dr} \right)_{r=0} = u(0) = 0 \quad (2.9)$$

and, at the edge of the sheet,

$$w(R) = \left(\frac{dw}{dr} \right)_{r=R} = 0, \quad u(R) = u_{pre}, \quad (2.10)$$

where u_{pre} is caused by the pretension, t_{pre} , in the sheet and can be calculated according to Hooke's law

$$\frac{u_{pre}}{R} = (1 - \nu) \frac{t_{pre}}{E_{2D}}. \quad (2.11)$$

Seemingly, (2.5) and (2.6) could be solved along with eight boundary conditions. However, physical considerations, i.e., the equilibrium of the vertical shear force and the absence of shear components in the applied load, would reduce the order of (2.5) and (2.6) by integrating them over $[0, r]$ once with zero integration constants. In addition to the five conditions in (2.9) and (2.10), the missing boundary condition comes from the fact that only ϕ' can change the stress field; we thus can have an arbitrary choice of ϕ at a given r (Box et al., 2017); here we take,

$$\phi(0) = 0. \quad (2.12)$$

2.2.3 Non-dimensionlization

In the following chapters except Chapter 5, our calculations will be based on FvK equations in terms of Airy stress function and out-of-plane deflection, i.e., (2.5) and (2.6). The stiffness E_{2D} is typically fixed under the linear elasticity assumption, the blister radius R is frequently prescribed by the dimension of holes patterned on the substrate. We thus use these two quantities to normalize the variables

$$\rho = \frac{r}{R}, \rho_o = \frac{R_o}{R}, W = \frac{w}{R}, H = \frac{h}{R}, u = \frac{u}{R}, \mathcal{F} = \frac{F}{E_{2D}R}, P = \frac{pR}{E_{2D}}, \Phi = \frac{\phi}{E_{2D}R^2}. \quad (2.13)$$

The FvK equations can then be rewritten in a dimensionless form

$$\nabla^2(\mathcal{K}^{-1}\nabla^2W) - [\Phi, W] - Q = 0 \quad (2.14)$$

and

$$\nabla^4\Phi + \frac{1}{2}[W, W] = 0, \quad (2.15)$$

where Q is $\frac{\mathcal{F}\delta(\rho)}{2\pi\rho}$ for a point load and P for a pressure, and

$$\mathcal{K} = \frac{E_{2D}R^2}{B} \quad (2.16)$$

is often referred to as FvK number (Blees et al., 2015). \mathcal{K} can also be thought of as the bendability of a thin sheet since sheets with higher numbers are more comfortable to bend than to stretch.

For classical plates, the bendability simply compares the blister radius with plate thickness, scaling as $(R/t)^2$. Along with this line, monolayer 2D materials are expected to be highly bendable due to their atomic thinness. However, the thickness of a monolayer 2D material is not well defined, though the interlayer distance, d_{spacing} , is frequently used as the nominal thickness. Instead, we assess the bendability of a monolayer 2D material via its bending stiffness and in-plane tensile stiffness directly. In particular, unlike classical plates that resist bending deformations via tension and compression across the neutral plane, 2D materials resist stretching by the strong in-plane covalent bonds and bending by a different physical origin (i.e., weak out-of-plane π bonds) (Zhang et al., 2011). This leads

to a much smaller bending stiffness for 2D materials than the prediction of classical plate theory and, thus, an extremely high bendability for 2D material blister problems (Wang et al., 2019b). For example, \mathcal{K} of a monolayer graphene in a blister with a radius of ~ 100 nm is $\sim 10^7$ (Androulidakis et al., 2018).¹ By contrast, $W \sim \mathcal{O}(10^{-1})$ and $\Phi \gtrsim 10^{-3}$ in experiments.

The high bendability of 2D materials motivates us to clarify the condition that the bending contribution in the vertical equilibrium can be neglected. We consider a scaling analysis: the compatibility equation (2.15) indicates that $\Phi \sim W^2 \sim H^2$, and hence stretching of the sheet dominates in (2.14) when $\mathcal{K}^{-1}H \ll H^3$. In other words, the bending effect of a sheet becomes negligible when $H \gg \mathcal{K}^{-1/2}$ or $h \gg Nd_{\text{spacing}} \gg (B/E_{2D})^{-1/2}$, where N is the layer number of the 2D material. In Chapter 4, we will show a particular case of slightly pressurized multilayer 2D materials on a small hole with N ranging from 7 to 70. In this case, the bending of the 2D material will contribute to the pressure in a nontrivial manner so that the bending stiffness could be measured. In general, however, in most 2D material (including multilayer) blister experiments, the criterion of $h \gg Nd_{\text{spacing}}$ can be readily satisfied. Therefore, in the remainder of this dissertation except Chapter 4, our primary interest will be to discuss the deformation of 2D materials without considering the bending term in (2.15); such treatment is often referred to as the membrane limit of FvK equations (Vella and Davidovitch, 2017).

2.3 RADIAL SLIPPAGE AND OCCURRENCE OF INSTABILITIES

2.3.1 Experimental observations

Clamped conditions at the edge of a blister hide rich behaviors in the substrate-supported region that have been recently observed (Figure 2.2). For example, Kitt et al.

¹ See details about the mechanical properties of other 2D materials in <http://2dmechanics.com/>.

(Kitt et al., 2013) and Wang et al. (Wang et al., 2017b) found a strain gradient (equivalently, Raman G-band position gradient) in the annulus region outside the graphene bubbles. The mechanism is attributed to the shear stress associated with the relative slip between the sheet and the substrate, acting as an in-plane body force on the sheet.

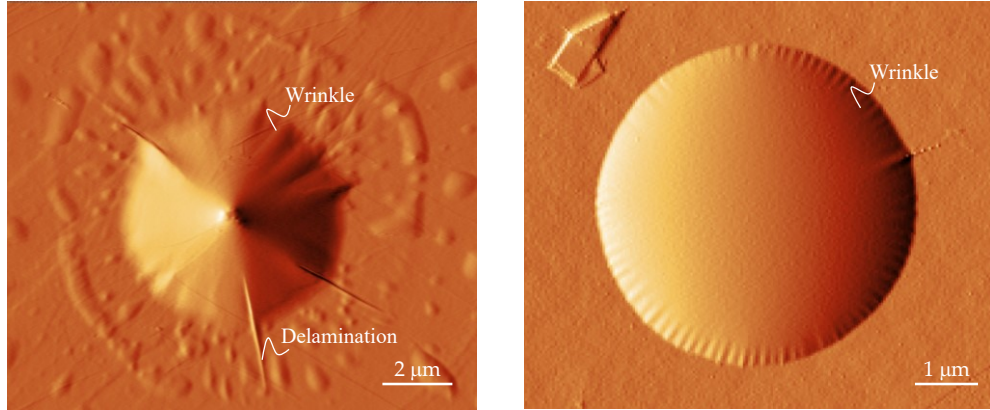


Figure 2.2: AFM amplitude images of a spontaneous multilayer graphene tent (left, courtesy of Daniel Sanchez) and a gas-pressurized bilayer graphene bubble (right, courtesy of Guorui Wang).¹

Furthermore, the inward sliding could compress the thin sheet circumferentially. Thin sheets usually relieve the compression by the formation of elastic instabilities, as evidenced in AFM images of a point-loaded few-layer graphene tent and a pressurized bilayer graphene bubbles in Figure 2.2. The instability typically takes the form of wrinkling in the suspended region and buckle delamination in the supported region. Notably, the delamination may be absent when the interfacial sliding is not substantial enough to overcome the substrate adhesion (e.g., in the right panel of Figure 2.2).

¹ These two images are also adapted for the Graphic illustration in Phys. Rev. Lett. 121, 266101 (2018) <https://journals.aps.org/prl/issues/121/26>.

2.3.2 Three cases

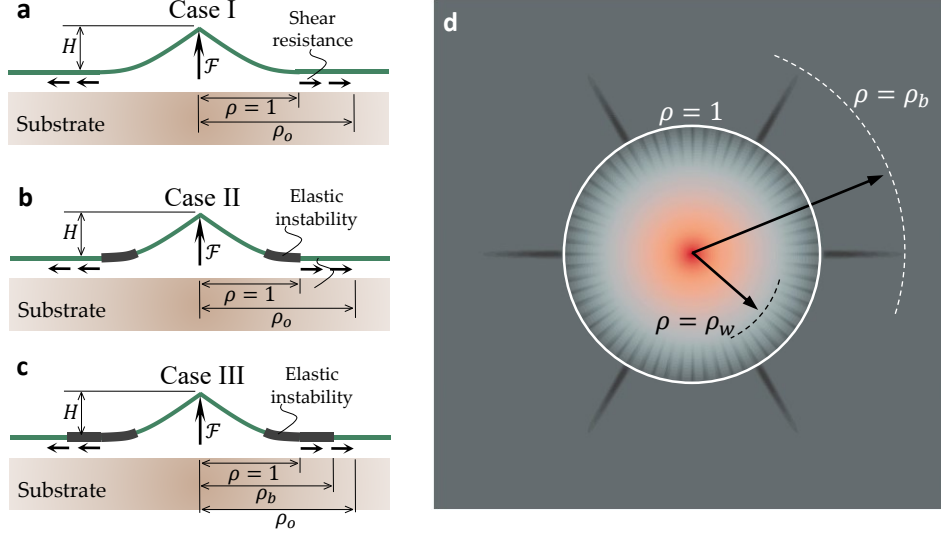


Figure 2.3: (a-c) Schematics for three possible deformed configurations when the sheet is allowed to slide over its supporting substrate. (d) Schematic illustration of Case III (top view) where the thin sheet wrinkles in $[\rho_w, 1]$ and delaminates in $[1, \rho_o]$.

We release the clamped boundary conditions at the blister edges and consider a finite shear stress at the sheet-substrate interface (Kitt et al., 2013; Wang et al., 2017b). The interface then behaves like an ideal plastic “material” (Dai et al., 2019a; Gong et al., 2010; Jiang et al., 2014) and how large the sliding zone can grow under a given pressure or point load would be the question we aim to answer. The geometrical parameters (e.g., the blister radius and the center deflection) and the mechanical properties (e.g., the stiffness of the 2D material and the friction/adhesion of the sheet to the substrate) would work together as controlling factors. The essence of this problem may be thought of to clarify how the extent of instabilities in the deformed sheet alters the size of the domain where regular FvK theories apply. Motivated by the full propagation of the indentation test for measuring the mechanical behavior of 2D materials, we focus on point-loaded sheets

(tents) and discuss three possible configurations in the following sections. We will conclude in Section 2.7 by discussing that the formulations for tents can be readily extended for bubbles (i.e., pressurized sheets).

Before proceeding, we introduce several useful parameters and their dimensionless forms. The shear stress, τ , is assumed to be constant, arising within $[R, R_o]$ (see Figure 2.3), where the slippage takes place, and the in-plane displacement is negative (we thus term this domain to be the sliding zone). In Cases II and III, wrinkling occurs in the domain of $[R_w, R]$; in Case III, the buckle delamination is in $[R, R_b]$ where $R_b \leq R_o$ when $\nu \geq 0$. Along with the line of non-dimensionlization in (2.13), we adopt

$$\rho_w = \frac{R_w}{R}, \rho_b = \frac{R_b}{R}, T = \frac{\tau R}{E_{2D}}, \tilde{N}_\rho = \frac{N_{rr}}{E_{2D}}, \tilde{N}_\theta = \frac{N_{\theta\theta}}{E_{2D}}. \quad (2.17)$$

We expect there to be a $\sim \rho^{-1/3}$ singularity in the stresses for point-loaded tents as $\rho \rightarrow 0$, according to Schwerin's solution (Schwerin, 1929), though the edge sliding may slightly ameliorate this singularity. It is convenient for numerical computations to introduce

$$\Psi = \rho \Phi', \tilde{N}_\rho = \frac{\Psi}{\rho^2} \text{ and } \tilde{N}_\theta = \frac{\Psi'}{\rho} - \frac{\Psi}{\rho^2}. \quad (2.18)$$

such that the variable corresponding to stresses (i.e., Ψ) becomes regular, where $(\)'$ denotes differentiation with respect to ρ .

2.4 CASE I: THE BASE STATE

We begin by discussing the base state of a point-loaded thin sheet whose edge is allowed to slide inward. At the same time, the elastic instability is prohibited such that hoop compressive stress, if any, remains. The assumption for this limiting case would be appropriate only when the instability is absent or in its very early stage so that the stresses in the base state are not significantly perturbed. We suggest that this situation is more likely to be true for thick plates or thin sheets with strong adhesion to their substrate under a small center deflection.

2.4.1 Inside the tent

With (2.18), the dimensionless form of the membrane limit of FvK equations for a tent reads

$$\Psi W' = -\frac{\rho \mathcal{F}}{2\pi} \quad (2.19)$$

and

$$\Psi'' - \frac{\Psi'}{\rho} = -\frac{1}{2} W'^2, \quad (2.20)$$

where we integrated (2.14) and (2.15) once. For a given load \mathcal{F} , the equations are to be solved with three boundary conditions; the zero in-plane deformation at the tent center and out-of-plane deformation at the tent edge give

$$\lim_{\rho \rightarrow 0} u(\rho) = 0 \text{ and } W(1) = 0, \quad (2.21)$$

respectively. The third condition should match the continuity of the displacement across the tent edge, which needs a bit of thought. We thus move on to the supported region.

2.4.2 Outside the tent

Within the supported domain, i.e., $r \in [1, \rho_o]$, the only equilibrium equation comes from the in-plane force balance (Kitt et al., 2013; Wang et al., 2017b),¹

$$\frac{d}{d\rho}(\rho \tilde{N}_\rho) - \tilde{N}_\theta + T\rho = 0. \quad (2.22)$$

Assuming a constant interfacial shear stress as well as linear elasticity and kinematics for this flat region, we can rewrite (2.22) in terms of \tilde{N}_ρ ,

$$\rho \tilde{N}_\rho'' + 3\tilde{N}_\rho' + (2 + \nu)T = 0. \quad (2.23)$$

We obtain the exact solution to the plane-stress problem (2.23) when pretension is neglected such that both stresses become zero at $\rho \rightarrow \rho_o$,

$$\tilde{N}_\rho = T \left[(2 + \nu) \left(-\frac{1}{3} \rho - \frac{\nu-1}{6(2+\nu)} \rho_o^3 \rho^{-2} \right) + \frac{1+\nu}{2} \rho_o \right], \quad (2.24)$$

¹ This statement is true for vanishing pretension. When the sheet undergoes a uniform pretension, three domains should be considered for the supported region: the interfacial shear stress in the inner one is outwards to resist the inwards pulling of the sheet; the shear stress in the middle one is inwards such that the displacement is outwards and both stresses develop to the uniform solution in the outermost domain.

which, together with (2.22), further gives rise to

$$\tilde{N}_\theta = T \left[(2 + \nu) \left(-\frac{1+2\nu}{3(2+\nu)} \rho + \frac{\nu-1}{6(2+\nu)} \rho_o^3 \rho^{-2} \right) + \frac{1+\nu}{2} \rho_o \right]. \quad (2.25)$$

The clamped boundary condition is a special case of (2.24) and (2.25) with vanishing sliding zone, i.e., $\rho_o \rightarrow 1$. In this case, we find $\lim_{\rho_o \rightarrow 1} \tilde{N}_\theta(1^+)/\tilde{N}_\rho(1^+) = \nu$, implying zero circumferential strain or zero in-plane displacement, which is consistent with the clamped condition.

2.4.3 Boundary and matching conditions

Naturally, the radial stress and in-plane displacement are continuous at the tent edge, leading to

$$\Psi(1) = T \left(\frac{1-\nu}{6} \rho_o^3 + \frac{1+\nu}{2} \rho_o - \frac{2+\nu}{3} \right) \quad (2.26)$$

and

$$\Psi'(1) - (1 + \nu)\Psi(1) = \frac{T}{6} (\nu^2 - 1)(\rho_o - 1)^2(\rho_o + 2). \quad (2.27)$$

With a prescribed point load and given interfacial shear stress, the ODEs (2.19) and (2.20) as well as the size of the sliding zone ρ_o can be solved with 4 conditions provided by (2.21), (2.26), and (2.27).

2.5 CASE II: WRINKLING WITHOUT BUCKLING DELAMINATION

We consider that the hoop compressive stress in the sheet is released completely by the wrinkling in the suspended region but is maintained in the supported area. We suggest that this limiting case often happens in nanoindentation tests where the center deflection is moderate ($H \lesssim 0.3$), and the sheet-substrate adhesion can suppress the buckle delamination.

2.5.1 Unwrinkled/unbuckled regions

Due to wrinkling, the domain where regular FvK equations apply shrinks to be $\rho \in [0, \rho_w]$. The solutions to the plane stress problem in the supported region still hold as we assumed no buckled delamination. A natural question is what sets the extent of the wrinkled region. We may expect that the propagation of the wrinkling zone is a process of releasing elastic strain energies; hence the wrinkling extent would be determined based on the energetic minimization with respect to this length. However, we will show later that this energetic argument is equivalent to the continuity of hoop stress across the movable wrinkling tip.

2.5.2 Wrinkled region

We adopt the tension field theory (TFT) to describe the stress state in the wrinkling zone $[\rho_w, 1]$. Accordingly, unlike Case I, the hoop compression in this domain is released, and a zero hoop stress replaces the second FvK equation concerning the compatibility. The vertical force balance in (2.5) becomes

$$(\Phi'W')' = 0. \quad (2.28)$$

The exact solutions to (2.28), together with the in-plane force balance (2.3) with $\tilde{N}_\theta = 0$, can be derived as

$$\Phi' = C_N \text{ and } W = C_W(1 - \rho). \quad (2.29)$$

Equation (2.29) suggests a linear out-of-plane profile, implying that the wrinkling renders a preserved Gaussian curvature ($G \equiv 0$ in our case) (Audoly and Pomeau, 2000). The problem now is to solve the regular FvK equations with 4 unknown constants (i.e., ρ_w, C_N, C_W , and ρ_o), which requires 7 boundary or matching conditions.

2.5.3 Boundary and matching conditions

Besides the state of zero in-plane displacement at the tent center, the continuity conditions at the inner and outer edge of the wrinkling sheet should be enforced,

$$\lim_{\rho \rightarrow 0} u = 0 \text{ and } [W]_{\rho_w^+}^{\rho_w^+} = [W']_{\rho_w^+}^{\rho_w^+} = [\tilde{N}_\rho]_{\rho_w^+}^{\rho_w^+} = [\tilde{N}_\rho]_{1^-}^{1^+} = 0, \quad (2.30)$$

where $[x]^\pm = x^+ - x^-$ and $W(1) = 0$ has been implied in (2.29). The hoop stress in the wrinkled region $[\rho_w, 1]$ would provide an additional condition where TFT predicts $\tilde{N}_\theta(\rho) = 0$. As the hoop compression is maintained in the supported region, we expect a jump of hoop stress across the tent edge. However, such jump vanishes at the inner edge of the wrinkling zone, leading to

$$[\tilde{N}_\theta]_{\rho_w^+}^{\rho_w^+} = 0 \text{ and } [\tilde{N}_\theta]_{1^-}^{1^+} \neq 0. \quad (2.31)$$

Note that the hoop stress continuity in the suspended region has been proved mathematically in similar problems (Davidovitch et al., 2011; King et al., 2012), to be equivalent to the minimization of total elastic energy when varying ρ_w . The final condition arises from the continuity of the in-plane displacement, whose solution in unwrinkled regions can be related to the stress states but has been missing in the wrinkled sheet. We then use the kinematics and Hooke's law in the wrinkling region,

$$\epsilon_\rho = u' + \frac{1}{2}(W')^2 = \tilde{N}_\rho - \nu \tilde{N}_\theta, \quad (2.32)$$

to show that

$$u(\rho_w^+) - u(1^-) = C_N \ln \rho_w + \frac{1}{2} C_W^2 (1 - \rho_w), \quad (2.33)$$

where we used (2.29). The displacements on the right side of (2.33) can be calculated according to the stress states in the unwrinkled regions since $[u]_{\rho_w^+}^{\rho_w^+} = [u]_{1^-}^{1^+} = 0$.

Equations (2.30), (2.31), and (2.33) complete the 7 conditions that are required to solve the problem in Case II.

2.6 CASE III: WRINKLING WITH BUCKLING DELAMINATION

We consider that any (hoop) compression is released in both suspended and supported regions. A similar phenomenon has been observed in pillar-supported 2D material tents where buckle delamination in the supported region could even develop a network. Note that the formation process of tents is spontaneous as the 2D material comes into contact with the pillar-patterned substrate via the sheet-substrate vdW interactions.

2.6.1 Buckled region

Both the wrinkled and unwrinkled theories in Case II still apply in the suspended domain. However, the occurrence of buckle delamination would modify the plane stress problem in the supported domain. Specifically, due to the Poisson effect, though the thin sheet slides over the substrate in $[1, \rho_o]$, the hoop stress appear negative only when the size of the sliding zone is large enough (we will show in Chapter 3 that what is meant by large is $\rho_o \gtrsim 1.36$ for graphene with $\nu = 0.165$) and the buckling occurs within $[1, \rho_b]$, where $\rho_b \leq \rho_o$ for a thin sheet with a non-negative Poisson's ratio (e.g., $\rho_b \cong \rho_o/1.36$ for graphene). In the intact region $[\rho_b, \rho_o]$, equations (2.24) and (2.25) hold while, in the delaminated region, we rewrite the in-plane force balance equation (2.23) with $\tilde{N}_\theta = 0$:

$$\frac{d}{d\rho}(\rho\tilde{N}_\rho) + T\rho = 0. \quad (2.34)$$

As a consequence, the simplified problem is to solve the regular FvK equations and (2.34) with 5 unknowns (i.e., ρ_w, C_N, C_W, ρ_b , and ρ_o) that requires 9 boundary or matching conditions.

2.6.2 Boundary and matching conditions

According to the condition of zero in-plane displacement at the tent center and the continuity conditions, we have

$$\lim_{\rho \rightarrow 0} u = 0,$$

and

$$[W]_{\rho_w^+}^{\rho_w^+} = [W']_{\rho_w^+}^{\rho_w^+} = [\tilde{N}_\rho]_{\rho_w^+}^{\rho_w^+} = [\tilde{N}_\theta]_{\rho_w^+}^{\rho_w^+} = [\tilde{N}_\rho]_{1^-}^{1^+} = [\tilde{N}_\rho]_{\rho_b^-}^{\rho_b^+} = [\tilde{N}_\theta]_{\rho_b^-}^{\rho_b^+} = 0. \quad (2.35)$$

We note that $[\tilde{N}_\theta]_{1^-}^{1^+} = 0$ is satisfied automatically as we assume the hoop compression is released by wrinkling and buckling, i.e., $\tilde{N}_\theta = 0$ throughout $[\rho_w, \rho_b]$, where $\rho_w \leq 1 \leq \rho_b$. Again, the last condition comes from the continuity of the in-plane displacement across the wrinkling and buckling instability region,

$$u(\rho_w^+) - u(\rho_b^+) = C_N \ln \rho_w + \frac{1}{2} C_W^2 (1 - \rho_w) - \int_{\rho_b^+}^1 (\tilde{N}_\rho - v \tilde{N}_\theta) d\rho, \quad (2.36)$$

where the displacements on the right side of (2.36) can be calculated according to the stress states in the unwrinkled/unbuckled regions since $[u]_{\rho_w^+}^{\rho_w^+} = [u]_{\rho_b^-}^{\rho_b^+} = 0$. Equations (2.35) and (2.36) complete the 9 conditions with which to solve the problem in Case III.

2.7 BUBBLES

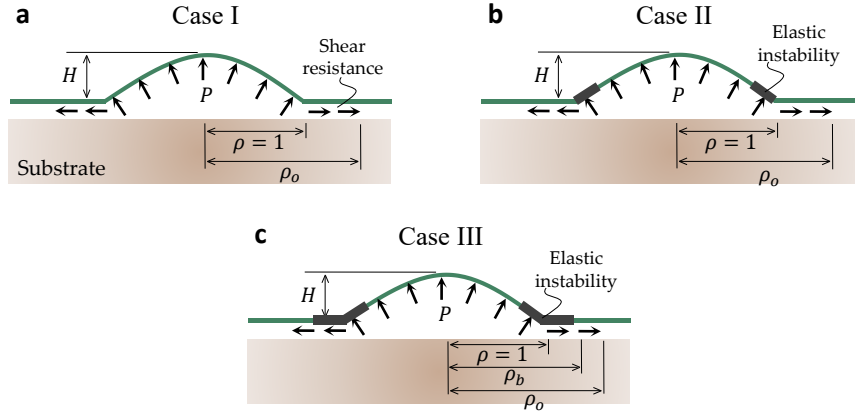


Figure 2.4: (a-c) Schematics for three possible deformed configurations of bubbles when the sheet is allowed to slide over its supporting substrate.

We may perform the analysis for pressurized bubbles following the same techniques outlined in Sections 2.4-2.6. The force balance would be identical in the supported region while it needs modifications to switch from a point force for tents to a

uniform pressure for bubbles. The regular membrane limit of FvK equations, according to (2.5), could be written as

$$\Phi W' = -\frac{1}{2} P \rho^2 \quad (2.37)$$

and

$$\rho \Phi'' + \Phi' - \frac{\Phi}{\rho} = -\frac{1}{2} W'^2, \quad (2.38)$$

where we used Φ to substitute Φ' for convenience, and we can obtain

$$\tilde{N}_\rho = \Phi/\rho \text{ and } \tilde{N}_\theta = \Phi'. \quad (2.39)$$

Equations (2.37) and (2.38) hold in $[0, \rho_w]$ (though $\rho_w = 1$ in Case I). In the wrinkled region in Cases II and III, i.e., $[\rho_w, 1]$, the hoop compression vanishes due to the wrinkling and the vertical force balance in (2.5) becomes

$$(\Phi W')' = -P\rho. \quad (2.40)$$

The exact solutions to (2.40), together with the in-plane force balance (2.3) with $\tilde{N}_\theta = 0$, can be derived

$$\Phi = C_N \text{ and } W = \frac{P}{6C_N} (1 - \rho^3), \quad (2.41)$$

where we enforced $W(1) = 0$ and the continuity of W' at $\rho = \rho_w$. Unlike (2.29) in the tent problem where the deformed profile appears linear, (2.41) presents a nonlinear shape for the wrinkled bubble.

2.8 CONCLUSIONS

We have completed the governing equations and the associated boundary and matching conditions for a thin sheet with a sliding boundary under a point load or pressure. Three cases with different extents of elastic instabilities have been discussed here, which may cover all possible scenarios in experiments. This theoretical setting is built for 2D materials sticking to a substrate via “weak” vdW interactions. However, the underlying physics would also apply for larger-scale systems such as pulling of polymeric sheets from

a liquid-lubricated substrate. Numerical calculations on these problems are the focus of Chapter 3. We will show exact analytical solutions to the tent systems, though tedious, in Chapter 7.

Chapter 3: Stretching¹

Indentation and pressurization experiments have been developed as the standard tests for characterizing the in-plane elastic properties of a variety of 2D materials. In such experiments, the set-up often suspends the sheet over a hole-patterned substrate to form a drumhead; the widely used theoretical model typically assumes a clamped sheet-substrate interface when the poking force or the bulging pressure is applied to the suspended drumhead. However, the atomically smooth nature of 2D materials challenges this assumption. In this Chapter, we solve the theory developed in Chapter 2 that allows the vertical load to drive the radially inward sliding of 2D materials on the substrate as well as the formation of elastic instabilities due to the sliding-caused hoop compression. We focus on the effective stiffness of the sheet and the extent of the wrinkling in the suspended region and buckling (if any) in the supported region. We identify a single parameter (\mathcal{S}) for these quantities, comparing the forces due to the interfacial friction and sheet stretching. We discuss how this single parameter controls the growth of the wrinkling/buckling region as well as the effective stiffness of the sheet under poking and bulging.

¹A paper will be written based on the work in this Chapter and Chapter 2:
Z. Dai, N. Lu. *Poking and Bulging of Ultrathin Elastic Sheets: Edge Slippage and Instabilities*. (The manuscript is in preparation.)

3.1 INTRODUCTION

The measurement of the in-plane elasticity of thin sheets, including metallic, polymeric, and biomedical membranes and the emerging atomically thin 2D materials, often leverage “out-of-plane” methodologies, such as bulge and indentation tests (Koenig et al., 2011; Lee et al., 2008). The experimental task is to detect the deformed configuration of the thin sheet upon applied force/pressure. The analysis and interpretation of those experimental data is always a nontrivial task, even for linearly elastic isotropic thin sheets, due to the inherent nonlinearity of the deformed geometry. More recently, extensive experiments (indentation tests, in particular) on a variety of 2D sheets with axisymmetry have been carried out in the past decade (Bertolazzi et al., 2011; Dai et al., 2019b; Lee et al., 2008; Tu et al., 2018). The in-plane stiffness of these atomically thin sheets has been estimated by fitting experimental data with an oversimplified formula that composites the asymptotic expressions for small (pretension-controlled) and large (stretch-controlled) deflections under clamped boundary conditions. Such formula, however, has been proved to produce significant errors, up to $\sim \mathcal{O}(1)$, according to a recent mathematical modeling work by D. Vella and B. Davidovitch (2017). The error becomes negligible only when the deflection is sufficiently large so that the large-deflection solution dominates (Vella and Davidovitch, 2017). A similar situation should also be expected for the bulge test.

The accuracy of the application of the simple analytical expressions needs deep indentations or large pressurizations. Under this circumstance, a number of material subtleties arise, such as the nonlinear and anisotropic elasticity, (Wei et al., 2009; Wei and Kysar, 2012) and ruin any analytical efforts. For 2D materials, an additional issue comes from the sheet edge, which is held by the vdW interaction between the sheet and the supporting substrate. This spontaneous interaction is extremely susceptible to tangential shear deformations when the vertical load is applied, due to the atomic-level smoothness

of 2D material. As a result, a dilemma appears when designing indentation and bulge tests on 2D materials that we discuss in detail as follows.

3.2 POKING TESTS

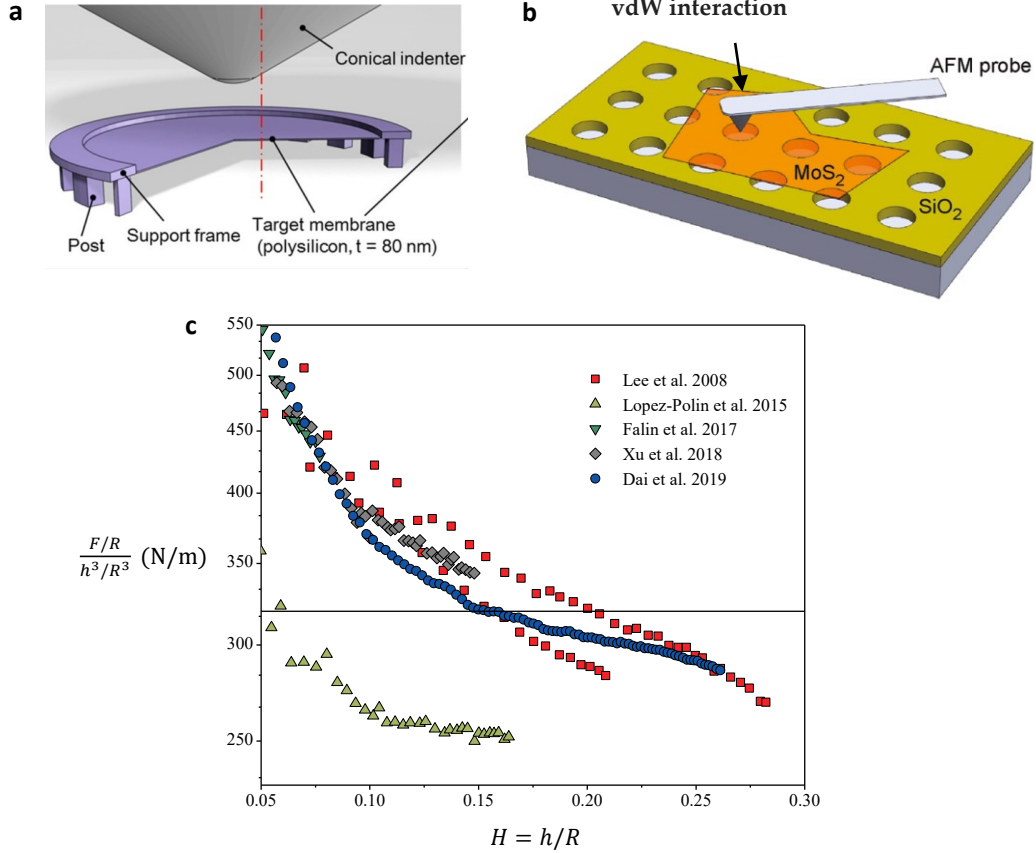


Figure 3.1: Schematic illustrations of indentation tests on freestanding thin sheets with a fixed edge (a) and a vdW-glued edge (b). (c) Rescaled indentation force-depth relation measured on monolayer graphene in the literature. (a) is adapted from (Ozaki et al., 2018)

We begin by discussing the poking/indentation experiments that seem to be the standard method for the elasticity metrology of various 2D materials. It is worth noting that tests on traditional small-scale sheets usually fix the edge of the target sheet carefully (e.g.,

using the support frame in Figure 3.1a to minimize the edge displacements) (Ozaki et al., 2018). Unfortunately, the atomic dimension of 2D materials hampers experimental efforts to constrain their edges; Instead, the spontaneous vdW interaction (Figure 3.2b) is employed to stick the sheet to its supporting substrate.

Indentation experiments on suspended 2D materials can take advantage of AFM that showed high spatial resolution and force sensitivity; Experimental data focused mainly on the indentation force-depth curves. To interpret these data, an analytical expression based on a point load as well as clamped boundary conditions has been widely adopted (Lee et al., 2008),

$$\mathcal{F} = \pi T_{\text{pre}} H + \alpha_{\mathcal{F}}(\nu) H^3, \quad (3.1)$$

where $\mathcal{F} = \frac{F}{E_{2D}R}$, $T_{\text{pre}} = \frac{t_{\text{pre}}}{E_{2D}}$, $H = h/R$, F is the applied indentation force, t_{pre} is the uniform pretension acting on the sheet, h is the indentation depth, and R is the radius of this suspended sheet or the radius of the hole pre-patterned on the substrate. The first (linear) term on the right side of (3.1) accounts for the effect of the pretension, which is significant at small indentation depths. The coefficient for the second (cubic) term was calibrated numerically for the case of a point-loaded sheet whose deflection is sufficiently large (Komaragiri et al., 2005),

$$\alpha_{\mathcal{F}}(\nu) = 1/(1.0491 - 0.1462\nu - 0.15827\nu^2)^3, \quad (3.2)$$

where ν is the Poisson's ratio of the thin sheet.

One may ask the following questions regarding these assumptions: How far is the experiment data away from the regime that could be called the small- or the large-deflection regime? Can the simple summation of the asymptotic results from these two limiting regimes provide a good approximation for the intermediate regime? What if the vertical load is applied within a finite region, instead of at a singular point? How does the edge slippage of the sheet alter (3.1) as it breaks the clamped boundary conditions?

Figure 3.1c may partially answer the first question. It is found that the \mathcal{F}/H^3 decreases throughout the experimental range of the indentation depth. It may be concluded that the linear-to-cubic transition is not complete in experiments. Recent work also showed that the finiteness of the indenter size can amplify the contribution of the linear term in (3.1) logarithmically,

$$\mathcal{F} = \frac{2\pi T_{\text{pre}}}{\log(R/R_{\text{tip}})}H + \alpha_{\mathcal{F}}(\nu, R_{\text{tip}}/R)H^3, \quad (3.3)$$

and, thus, delay the transition (Vella and Davidovitch, 2017). The first term on the right side of (3.3) was derived based on a no-slip cylinder-shaped indenter. By contrast, the correction added to the coefficient for the cubic term, i.e., $\alpha_{\mathcal{F}}(\nu, R_{\text{tip}}/R)$, approximately scales as $(R_{\text{tip}}/R)^{2/3}$.

Before further discussing the missing $\mathcal{F} \sim H^3$ relation in experiments, we note that (3.3) naively sums up the two asymptotic expressions and appears erroneous for extracting the sheet's in-plane stiffness when it is used for fitting experimental force-depth curves. The error produced by (3.3), $1 - \frac{\mathcal{F}_{(3.3)}}{\mathcal{F}_{\text{true}}}$, is $\sim \mathcal{O}(1)$. It only becomes trivial when the deflection is sufficiently large so that the cubic term in (3.3) dominates (Vella and Davidovitch, 2017). In this case, the indenter may be modeled as a point force when R_{tip} is two orders smaller than the radius of the sheet – a condition that could be satisfied in some of the experiments carried out in the literature.

Back to Figure 3.1c, the force-cubic depth relation has rarely been observed as experimental $\frac{F/R}{H^3}$ keeps decreasing and even shoots over the solid line, $\alpha_{\mathcal{F}}(\nu)E_{2D}$, where we used the data of graphene with $\nu = 0.165$ and $E_{2D} = 340 \text{ N/m}$ claimed in the literature. This suggests that the $\mathcal{F} \sim H^3$ relation may be achieved experimentally but have not been maintained under large sheet deformations due to other subtleties such as nonlinear elasticity and edge slippage. The former factor has been studied by Wei et al. (Wei et al., 2009; Wei and Kysar, 2012) but may not be able to explain the significantly

softened \mathcal{F}/H^3 ratios even at small deformations, e.g., $H \sim 0.15$ (see data regarding monolayer graphene in Figure 3.1c). We note that such softening behavior is also ubiquitous in experimental data from poking tests on multilayer graphene and other 2D materials as well as bulge tests on monolayer graphene in Figure 3.9c. Here, we suggest a new mechanism; The edge slippage may play an essential role as the edge of 2D materials is fixed by their vdW interactions with substrates.

3.3 TENTS WITHOUT INSTABILITIES

In this section, our primary interest is to clarify the effect of edge slippage on the mechanical responses of a thin sheet upon vertical poking. The detailed theory has been developed in Chapter 2, where we release the clamped boundary conditions at the blister edges by considering a finite shear stress at the sheet-substrate interface. The inward sliding might bring hoop compression to the thin sheet beyond a critical condition and thus elastic instabilities to release such compression. As a starting point, we study the base state of this problem (i.e., Case I defined in Chapter 2), in which we neglect the pretension, finite size of the indenter, and assume that instabilities are absent or in their very early stage.

3.3.1 Effect of T

We assumed a finite, constant sliding resistance/shear traction, τ , at the sheet-substrate interface though the same physical ideas apply to more complicated tangential traction-separation laws. The shear traction is normalized based on the radius and the in-plane stiffness of the thin sheet,

$$T = \frac{\tau R}{E_{2D}}. \quad (3.4)$$

As discussed in Chapter 2.4, the problem becomes to solve ODEs (2.19) and (2.20) and the size of the sliding zone ρ_o with 4 conditions in (2.21), (2.26), and (2.27). We perform the numerical calculations using Matlab routine `bvp5c`.

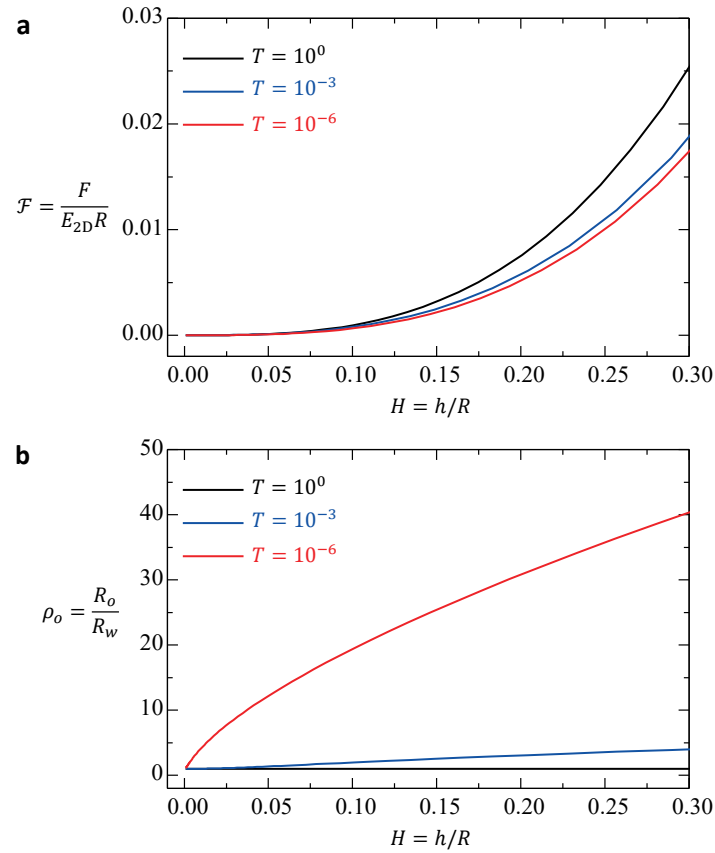


Figure 3.2: (a) Numerical indentation force-depth curves for thin sheets with various interfacial shear tractions to their substrates. (b) The dependency of the size of the sliding zone on the center deflection (i.e., indentation depth) for various interfacial shear tractions.

Figure 3.2a shows the numerical results on the indentation force-depth curves for thin sheets with various shear tractions to their substrates. As expected, with smaller resistance to the interfacial shear, thin sheets behave softer regarding the indentation stiffness. The reason is simply that more interfacial slippage is involved, which could also

be indicated by the size of the sliding zone, ρ_o , in Figure 3.2b. Besides the shear traction, the indentation depth, i.e., the center deflection of the sheet, would affect the size of the sliding zone. It is worth noting that for the case of $T = 1$, $\rho_o \approx 1$ throughout the center deflection $H \in [0, 0.3]$ and we found that $\mathcal{F} \sim H^3$, implying that the edge of the thin sheet is nearly clamped.

3.3.2 Sliding number \mathcal{S}

Since the pretension is neglected here, we expect a force-cubic deflection relation for these curves in Figure 3.1a. An effective stiffness can thus be defined

$$K(T, H) = \frac{\mathcal{F}}{H^3}. \quad (3.5)$$

to quantify how the edge slippage modifies this cubic relation. We expect this stiffness decreases as the center deflection increases and the interfacial shear traction weakens. This motivates us to define a sliding number,

$$\mathcal{S} = \frac{H^2}{T}. \quad (3.6)$$

Systems with larger sliding numbers should subject to more inward edge slippage. Since the membrane tension scales as H^2 , the sliding number may be understood as the comparison between the elastic and the interfacial shear traction. The former behaves like a driving force for interfacial sliding while the latter is a resistive force. We find that the numerical results on the effective stiffness obtained from thin sheets with various center deflections and interfacial tractions collapse onto a master curve that depends only on this sliding number.

With this sliding number, it is very convenient to quantify when the edge slippage could be considered as negligible or oppositely when the sheet-substrate interface could be considered as frictionless. We answer this question by looking into the effective poking stiffness of the thin sheet,

$$\mathcal{F} = K(\mathcal{S})H^3. \quad (3.7)$$

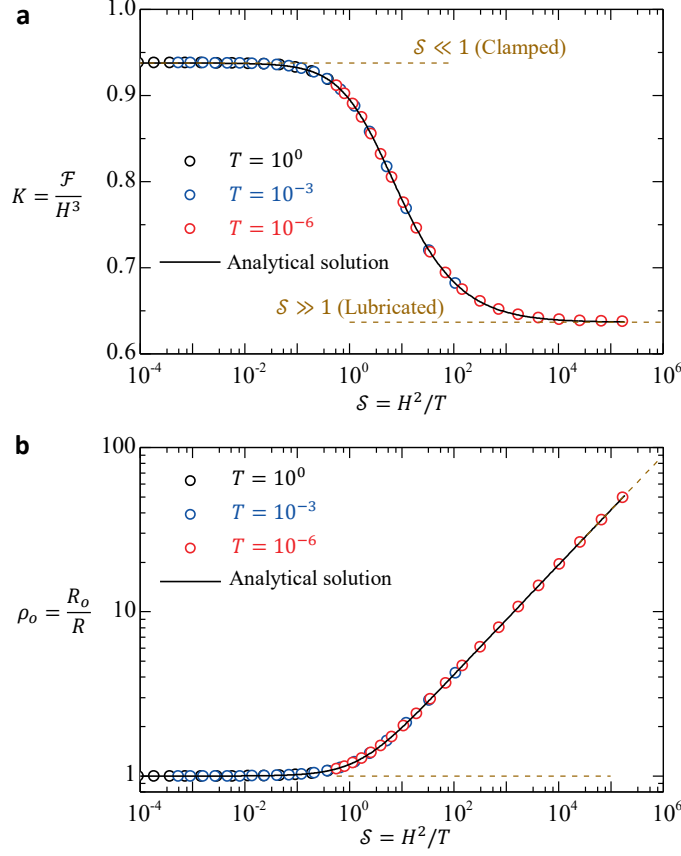


Figure 3.3: The dependency on the sliding number of the effective stiffness (a) and the size of the sliding zone (b).

In Figure 3.3a, it is found that the sheet edge is close to being clamped when $\mathcal{S} \lesssim 0.1$ while the sheet-substrate interface is close to being ultra-lubricated or frictionless when $\mathcal{S} \gtrsim 10^4$. We will show in Chapter 7 that there exists an exact analytical solution for the master $K \sim \mathcal{S}$ curve,

$$K(\mathcal{S}) = \pi \frac{\rho_o(\mathcal{S}) - 1}{\mathcal{S}} \frac{(1+\nu) \sqrt{\tilde{\psi}_1(\mathcal{S})/(1-\tilde{\psi}_1(\mathcal{S}))}}{\tan^{-1} \sqrt{\tilde{\psi}_1(\mathcal{S})/(1-\tilde{\psi}_1(\mathcal{S}))}}. \quad (3.8)$$

where $\rho_o(\mathcal{S})$ and $\tilde{\psi}_1(\mathcal{S})$ can be solved based on two algebraic equations:

$$\tilde{\psi}_1 \mathcal{S} = 4 \left(\frac{1+\nu}{2} \rho_o + \frac{1-\nu}{6} \rho_o^3 - \frac{2+\nu}{3} \right) \left(\tan^{-1} \sqrt{\frac{\tilde{\psi}_1}{1-\tilde{\psi}_1}} \right)^2 \quad (3.9)$$

and

$$\frac{3(1+\nu)(\rho_o-1)}{[3(1+\nu)\rho_o+(1-\nu)\rho_o^3-2(2+\nu)]} = 1 - \tilde{\psi}_1^{-1} + \sqrt{\frac{1-\tilde{\psi}_1}{\tilde{\psi}_1^3}} \tan^{-1} \sqrt{\frac{\tilde{\psi}_1}{(1-\tilde{\psi}_1)}}. \quad (3.10)$$

Equations (3.9) and (3.10) also give rise to the master curve for the size of the sliding zone $\rho_o(\mathcal{S})$ that can be found in Figure 3.3b.

We identify the limits for the effective stiffness and the size of the sliding zone in systems with small and large sliding numbers; we may call them strong shear limit and weak shear limit, respectively. The analytical results suggest asymptotic expressions for the two limits,

$$K \cong \begin{cases} \alpha_{\mathcal{F}}(\nu), & \mathcal{S} \lesssim 0.1 \\ \frac{2}{\pi}, & \mathcal{S} \gtrsim 10^4 \end{cases} \quad (3.11)$$

and

$$\rho_o(\mathcal{S}) \cong \begin{cases} 1, & \mathcal{S} \lesssim 0.1 \\ \left[\frac{6\mathcal{S}}{\pi^2(1-\nu)} \right]^{1/3}, & \mathcal{S} \gtrsim 10 \end{cases} \quad (3.12)$$

which are shown by brown dashed curves in Figure 3.3. Note that $\alpha_{\mathcal{F}}(\nu)$ in (3.11) is due to (3.2), and the large- \mathcal{S} limit (weak shear limit) of both K and ρ_o is independent of Poisson's ratio of the sheet.

3.4 TENTS WITH INSTABILITIES

We then move on to the cases that allow the formation of elastic instabilities and discuss when the instability initiates, how it evolves and then affects the overall poking stiffness of the thin sheet.

3.4.1 Wrinkling and no buckling delamination

In poking experiments of 2D materials, the vdW interaction between the sheet and the substrate is tangentially weak and vertically strong. This contrast may lead to the

scenario that the thin sheet wrinkles in the suspended region and remains flat in the supported region (See Figure 2.2). Due to the thinness of 2D materials, a reasonable assumption is that the wrinkling releases the compression completely, which could be described by the Tension Field theory (TFT). As discussed in Chapter 2.5, the problem (Case II defined in Chapter 2) is to solve the regular FvK equations with 4 unknown constants (due to the sliding and the wrinkling) with 7 boundary or matching conditions. Again, we perform the numerical calculations using Matlab routine `bvp5c`.

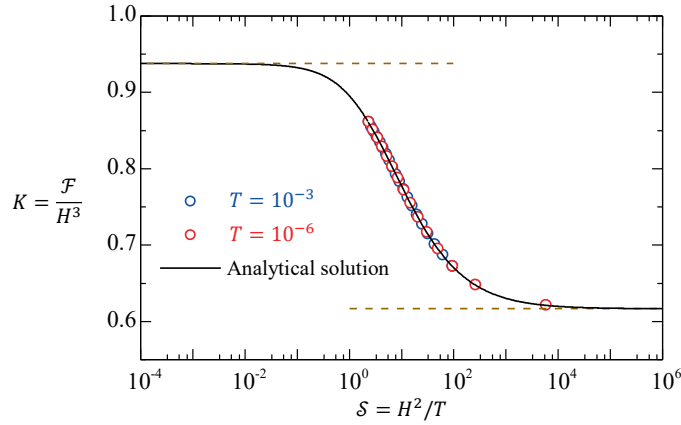


Figure 3.4: The dependency on the sliding number of the effective stiffness of poking a wrinkled sheet.

Figure 3.4 shows the numerical results on the \mathcal{S} -dependency of the effective stiffness of the sheet in response to a point force, which again falls onto a master curve. This indicates that the system involving instabilities in the suspended region still relies on the single sliding number. Particularly, for graphene, the wrinkling instability occurs when $N_{\theta\theta}(1) \leq 0$, corresponding to $\mathcal{S} \gtrsim 2.306$ (the detailed value is very sensitive to the Poisson's ratio of the material).

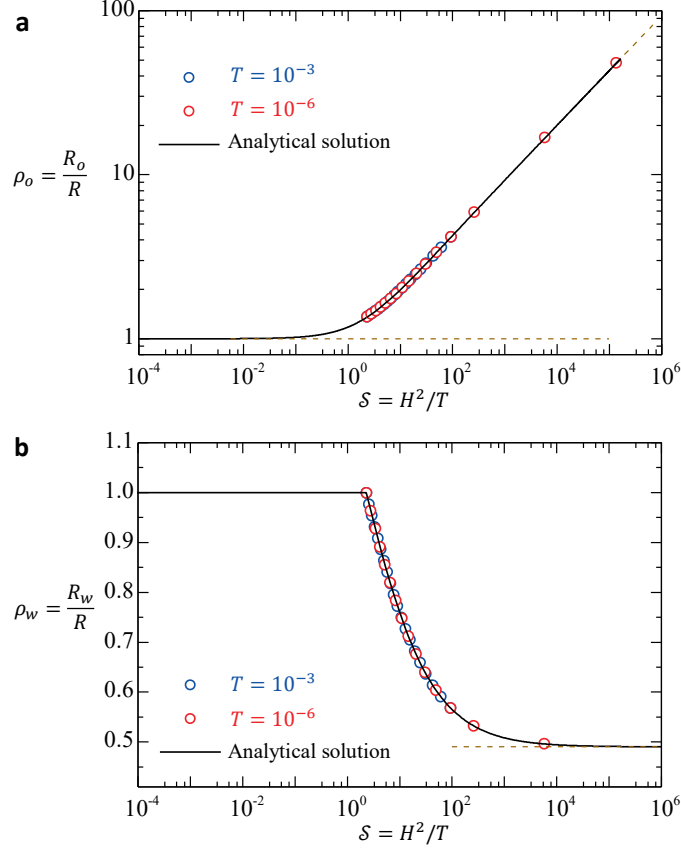


Figure 3.5: The dependency on the sliding number of the size of the sliding zone (a) and the size of the wrinkling zone (b).

Along with the same technique that will be introduced in Chapter 7, we can derive exact analytical solutions for this master curve,

$$K(\mathcal{S}) = \frac{2\pi}{\rho_w^2} \sqrt{\frac{\tilde{\psi}_w^3}{(1-\tilde{\psi}_w)}} \left(\frac{1-\rho_w}{\rho_w} \sqrt{\frac{\tilde{\psi}_w}{1-\tilde{\psi}_w}} + 2 \tan^{-1} \sqrt{\frac{\tilde{\psi}_w}{1-\tilde{\psi}_w}} \right)^{-3}, \quad (3.13)$$

where $\tilde{\psi}_w$ and ρ_w are solved based on the following three algebraic equations:

$$\sqrt{\tilde{\psi}_w^3/(1-\tilde{\psi}_w)} + 2\sqrt{\tilde{\psi}_w(1-\tilde{\psi}_w)} = 2 \tan^{-1} \sqrt{\tilde{\psi}_w/(1-\tilde{\psi}_w)}, \quad (3.14)$$

$$2\rho_w \ln \rho_w + \frac{1-\rho_w}{1-\tilde{\psi}_w} + 2\nu\rho_w - \frac{2\rho_w(1-\nu^2)(\rho_o-1)^2(\rho_o+2)}{(1-\nu)\rho_o^3 + 3(1+\nu)\rho_o - 2(2+\nu)} = 0, \quad (3.15)$$

and

$$\mathcal{S} \frac{\tilde{\psi}_w}{\rho_w} = \left[-\frac{2+\nu}{3} - \frac{\nu-1}{6} \rho_o^3 + \frac{1+\nu}{2} \rho_o \right] \left(\frac{1-\rho_w}{\rho_w} \sqrt{\frac{\tilde{\psi}_w}{1-\tilde{\psi}_w}} + 2 \tan^{-1} \sqrt{\frac{\tilde{\psi}_w}{1-\tilde{\psi}_w}} \right)^2. \quad (3.16)$$

Equations (3.14-3.16) also give rise to master curves for the size of the sliding zone $\rho_o(\mathcal{S})$ and the size of the wrinkling zone $\rho_w(\mathcal{S})$ that are shown in Figure 3.5.

We note that $\tilde{\psi}_w$ satisfies a transcendental equation with a solution of $\tilde{\psi}_w \cong 0.6965$. When the sliding number is large, we find that $\rho_w \cong 0.49048$ (independent of Poisson's ratio), defining the innermost position that the wrinkling zone can grow. Based on numerical results, we suggest several useful values for this limit,

$$K \cong \begin{cases} \alpha_{\mathcal{F}}(\nu), & \mathcal{S} \lesssim 0.1 \\ \frac{1.94}{\pi}, & \mathcal{S} \gtrsim 10^4, \end{cases} \quad (3.17)$$

$$\rho_o(\mathcal{S}) \cong \begin{cases} 1, & \mathcal{S} \lesssim 0.1 \\ \left[\frac{6.68\mathcal{S}}{\pi^2(1-\nu)} \right]^{1/3}, & \mathcal{S} \gtrsim 10, \end{cases} \quad (3.18)$$

and

$$\rho_w(\mathcal{S}) \cong \begin{cases} 1, & \mathcal{S} \lesssim 0.1 \\ 0.49048, & \mathcal{S} \gtrsim 10^4, \end{cases} \quad (3.19)$$

which lead to brown dashed lines and show excellent agreement with the numerical results in Figures 3.4 and 3.5. Note that, similar to Case I, the effective stiffness in Case II at the large- \mathcal{S} limit (weak shear limit) is independent of Poisson's ratio of the sheet.

3.4.2 Wrinkling with buckling delamination

In the last case (Case III defined in Chapter 2), elastic instabilities occur in both the suspended region (in the form of wrinkling) and the supported region (in the form of buckle delamination). This limiting case may happen when the substrate adhesion is weak or when transfer processes are involved (Chapter 7). As discussed in Chapter 2.6, the problem is to solve the regular FvK equations with 5 unknown constants (due to the sliding, wrinkling, and buckle delamination) with 9 boundary or matching conditions.

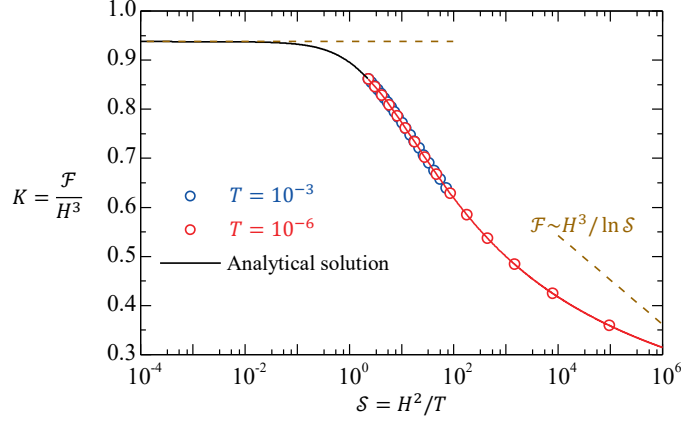


Figure 3.6: The dependency on the sliding number of the effective stiffness.

Figure 3.6 shows the numerical results on the \mathcal{S} -dependency of the effective stiffness of the sheet in response to a point force; a master curve appears again. This indicates that the system involving instabilities in both suspended and supported region relies on this sliding number. Still, for graphene, these two types of instabilities occur simultaneously when $N_{\theta\theta}(1) \leq 0$, i.e., $\mathcal{S} \gtrsim 2.306$. Along with the same technique that will be introduced in Chapter 7, we can derive exact the analytical solution for this master curve,

$$K(\mathcal{S}) = \frac{2\pi}{\rho_w^2} \sqrt{\frac{\tilde{\psi}_w^3}{(1-\tilde{\psi}_w)}} \left(\frac{1-\rho_w}{\rho_w} \sqrt{\frac{\tilde{\psi}_w}{1-\tilde{\psi}_w}} + 2 \tan^{-1} \sqrt{\frac{\tilde{\psi}_w}{1-\tilde{\psi}_w}} \right)^{-3}, \quad (3.20)$$

where $\tilde{\psi}_w$ and ρ_w are solved based on the following four algebraic equations:

$$\rho_b = \frac{1-\nu+\sqrt{9+6\nu-15\nu^2}}{4+8\nu} \rho_o, \quad (3.21)$$

$$\sqrt{\tilde{\psi}_w^3/(1-\tilde{\psi}_w)} + 2\sqrt{\tilde{\psi}_w(1-\tilde{\psi}_w)} = 2\tan^{-1} \sqrt{\tilde{\psi}_w/(1-\tilde{\psi}_w)}, \quad (3.22)$$

$$\begin{aligned} & -\frac{1}{4}(-2\rho_b^2 \ln \rho_b + \rho_b^2 - 1) + \rho_b \ln \rho_b \left[-\frac{2+\nu}{3}\rho_b - \frac{\nu-1}{6}\rho_o^3 \rho_b^{-2} + \frac{1+\nu}{2}\rho_o \right] - \\ & \frac{\nu(1+\nu)[-3(1+3\nu)+\sqrt{3}\sqrt{(1-\nu)(3+5\nu)}]}{4+8\nu} \rho_b \rho_o = \left\{ \frac{1}{2}(\rho_b^2 - 1) + \rho_b \left[-\frac{2+\nu}{3}\rho_b - \right. \right. \\ & \left. \left. \frac{\nu-1}{6}\rho_o^3 \rho_b^{-2} + \frac{1+\nu}{2}\rho_o \right] \right\} \left[\nu + \ln \rho_w + \frac{1-\rho_w}{2\rho_w} \frac{1}{1-\tilde{\psi}_w} \right], \end{aligned} \quad (3.23)$$

$$\mathcal{S} \frac{\tilde{\psi}_w}{\rho_w} = \left[-\frac{2+\nu}{3} - \frac{\nu-1}{6}\rho_o^3 + \frac{1+\nu}{2}\rho_o \right] \left(\frac{1-\rho_w}{\rho_w} \sqrt{\frac{\tilde{\psi}_w}{1-\tilde{\psi}_w}} + 2 \tan^{-1} \sqrt{\frac{\tilde{\psi}_w}{1-\tilde{\psi}_w}} \right)^2. \quad (3.24)$$

Equations (3.21-3.24) also give rise to the master curves for the size of the sliding zone $\rho_o(\mathcal{S})$, the size of the wrinkling zone $\rho_w(\mathcal{S})$, and the size of the buckling zone $\rho_b(\mathcal{S})$; the former two are shown in Figure 3.7.

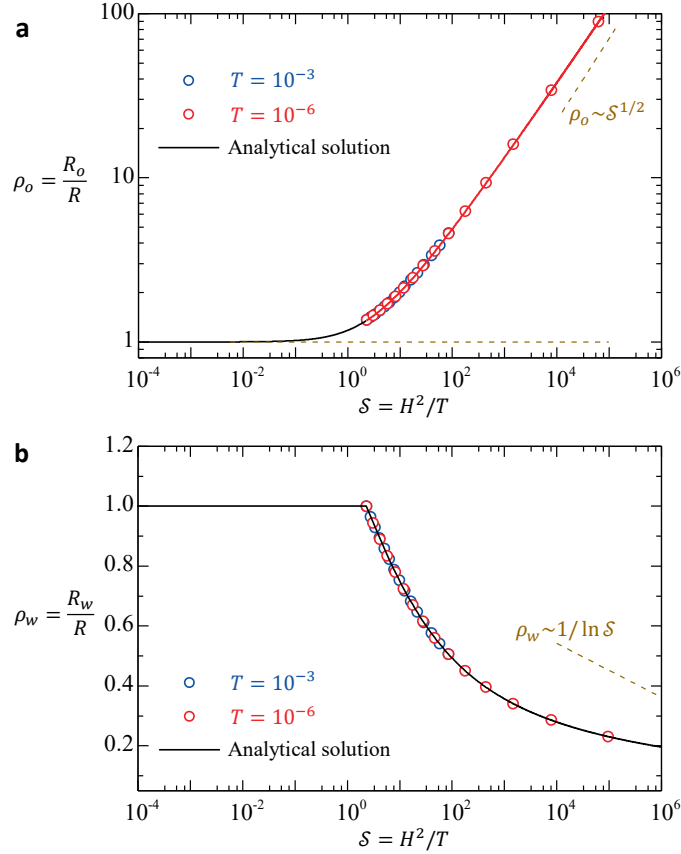


Figure 3.7: The dependency on the sliding number of the size of the sliding zone (a) and the size of the wrinkling zone (b).

Unlike in Cases I and II, the wrinkling zone keeps propagating and the effective stiffness keeps decreasing with the increasing sliding number in Case III, due to the formation of buckling delamination in the supported region. We suggest several approximated values for the weak and strong shear limits for this case,

$$K \sim \begin{cases} \alpha_{\mathcal{F}}(\nu), & \mathcal{S} \lesssim 0.1 \\ 1/\ln \mathcal{S}, & \mathcal{S} \gtrsim 10^4, \end{cases} \quad (3.25)$$

$$\rho_o(\mathcal{S}) \sim \begin{cases} 1, & \mathcal{S} \lesssim 0.1 \\ \mathcal{S}^{1/2}, & \mathcal{S} \gtrsim 10 \end{cases}, \quad (3.26)$$

and

$$\rho_w(\mathcal{S}) \sim \begin{cases} 1, & \mathcal{S} \lesssim 0.1 \\ 1/\ln \rho_b \sim 1/\ln \mathcal{S}, & \mathcal{S} \gtrsim 10^4 \end{cases}, \quad (3.27)$$

which lead to brown dashed lines in Figures 3.6 and 3.7.

3.5 IMPLICATIONS FOR INDENTATION TESTS

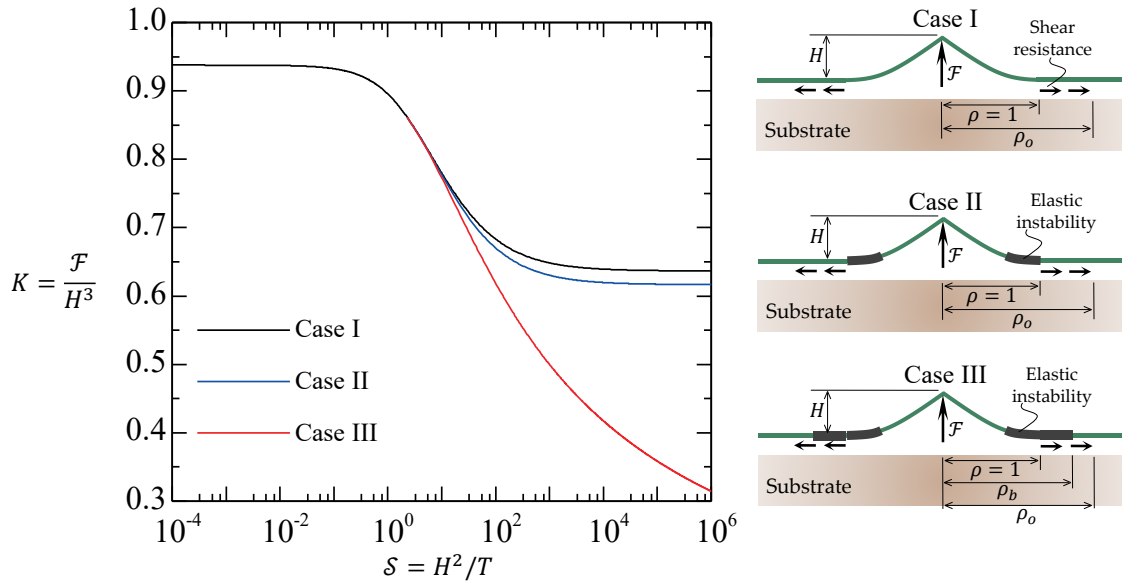


Figure 3.8: The effective stiffness of the thin sheet under poking for three possible deformed configurations, which are further illustrated in the right panel.

Now we are in a position to summarize the implications of our studies for poking/indentation tests where the edge slippage is allowed. In experiments, Cases I and II are more likely to occur. The signature of Case II happening is simply that wrinkling instabilities form in the suspended region. In both cases, we found two natural limits: the sheet edge is close to being clamped when $\mathcal{S} \lesssim 0.1$; the sheet-substrate interface is close to being ultra-lubricated or frictionless when $\mathcal{S} \gtrsim 10^4$. During loading, the experiments

belong to Case I first and then develop to be Case II when the hoop stress appears negative at the sheet edge ($\mathcal{S} \gtrsim 2.3$ for graphene with $\nu = 0.165$). However, the difference in the effective stiffness between Cases I and II is within 3% for all indentation depths (if the deflection remains moderate) and all theoretically allowable Poisson's ratios. We may use solutions to Case I for both, which is relatively simple in general, see details in Chapter 5. Unfortunately, the consideration of edge slippage, together with other factors such as pretension and indenter shaper and size, would render simple analytical formulae for poking tests such as (3.1) elusive. Given such fact, we conclude that it is still a grand challenge to measure the pretension and in-plane stiffness for an atomically thin sheet though the erroneous expression (3.1) has been widely applied and propagated in the literature.

3.6 BULGE TESTS

The second part of this chapter focuses on the bulge test. The underlying ideas when the edge slippage is considered are similar to those discussed in the poking test. For example, we will show that the bulging system is also controlled by a single sliding number, defined in the same way as the poking system. However, there are several quantitative differences between the poking and bulging problems, particularly in the size of the wrinkling zone. We did not succeed in figuring out exact solutions to the bulging problem; this part is thus numerically-based.

3.6.1 Experiments in the literature

Figure 3.9a illustrates the device of bulge tests designed for traditional aluminum alloy plates, where the edge of the plate is confined mechanically by draw beads (Chen et al., 2018; Chen et al., 2016a). Though the horizontal friction has been considerably

enhanced by such draw bead, edge slippage and instability could be observed after large pressurizations.

The experimental set-up of bulge tests typically involves the transfer of the 2D material on a substrate that is pre-patterned with micro holes and the pressurization of this sheet via the “constant gas number” technique invented by S. Bunch and coworkers (Koenig et al., 2011). For bulge tests of 2D materials whose edge is confined by the vdW-based friction, more significant edge displacement should be expected. Indeed, wrinkling can be observed even under small pressurizations, say $H < 0.1$ (Figure 3.9b). We examine how the occurrence of edge slippage weakens the effective stiffness of the thin sheet in resisting the pressure.

Analogous to the poking problem, an analytical expression based on a uniform pressure and clamped boundary conditions can be derived,

$$P = 4T_{\text{pre}}H + \alpha_P(\nu)H^3, \quad (3.28)$$

where $P = \frac{pR}{E_{2D}}$, $T_{\text{pre}} = \frac{t_{\text{pre}}}{E_{2D}}$, $H = h/R$, p is the applied pressure, t_{pre} is the uniform pretension pre-existing on the sheet, h is the center deflection, and R is the radius of this suspended sheet or the radius of the hole pre-patterned on the substrate. The first (linear) term on the right side of (3.1) accounts for the effect of the pretension, which is significant at small indentation depths. The coefficient for the second (cubic) term was calibrated numerically based on results of a pressurized, clamped and pretension-free sheet (Komaragiri et al., 2005),

$$\alpha_P(\nu) = 1/(0.7179 - 0.1706\nu - 0.1495\nu^2)^3, \quad (3.29)$$

In fact, (3.28) could offer a decent approximation for a pressurized thin sheet with a constant pretension when $T_{\text{pre}} \ll 1$.

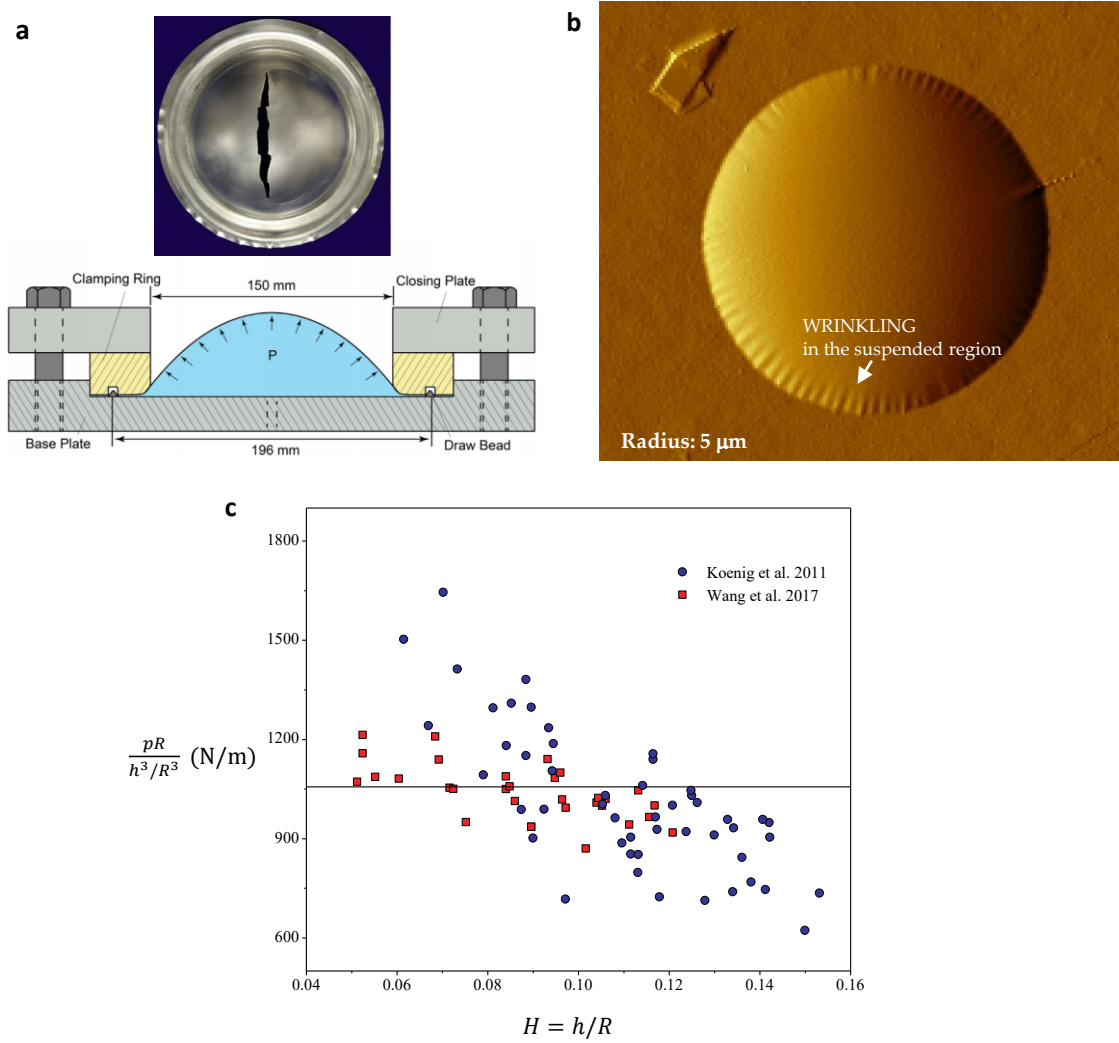


Figure 3.9: (a) Schematic illustrations of bulge tests on an aluminum alloy plate, the edge of which is constrained via the friction enhanced mechanically by draw beads. The top panel shows the photo of a plate after the test (Chen et al., 2018). (b) AFM amplitude images of a gas-pressurized bilayer graphene bubble (right, courtesy of Guorui Wang).¹ (c) Rescaled pressure-deflection relation measured on monolayer graphene in the literature.

Unlike indentation, pressurization of suspended 2D materials relies on the gas-diffusion process that makes experimental data appear “discrete” (Figure 3.19c). We still

¹ This image is also adapted for the Graphic illustration in Phys. Rev. Lett. 121, 266101 (2018) <https://journals.aps.org/prl/issues/121/26>.

find a clear trend that the pR/H^3 decreases throughout the experimental range of the pressurization and shoots over the solid line, $\alpha_P(\nu)E_{2D}$, when $H \gtrsim 0.1$, where we used the data of graphene with $\nu = 0.165$ and $E_{2D} = 340$ N/m. This again suggests the important role of edge slippage that has been hidden in clamped theory in (3.28).

3.6.3 Numerical results

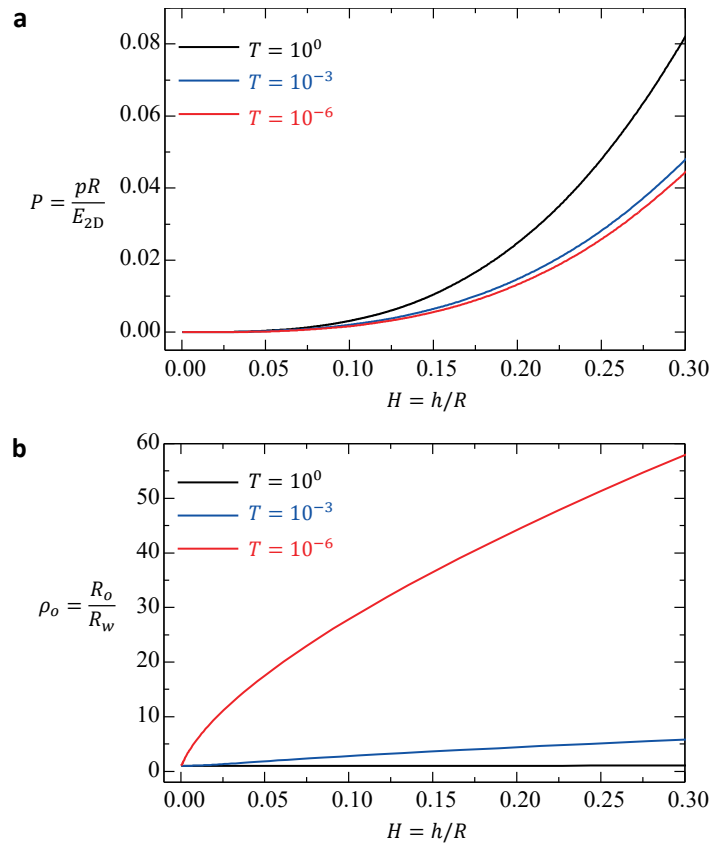


Figure 3.10: (a) The pressure-deflection curves for thin sheets with various interfacial shear tractions to their substrates. (b) The dependency of the size of the sliding zone on the center deflection for different interfacial shear tractions.

Following the same technique introduced in Chapter 2 and the first part of Chapter 3, we show numerical results on pressure-deflection curves for thin sheets with various

shear tractions to their substrates (Case I) in Figure 3.10a. As expected, with smaller resistance to the interfacial shear, thin sheets behave softer as more interfacial slippage is involved under a given pressure (also see Figure 3.10b). We define the effective stiffness of the thin sheet in resisting the pressure by,

$$K(\mathcal{S}) = \frac{P}{H^3}, \quad (3.30)$$

where \mathcal{S} is the sliding number defined by,

$$\mathcal{S} = \frac{H^2}{T}. \quad (3.6)$$

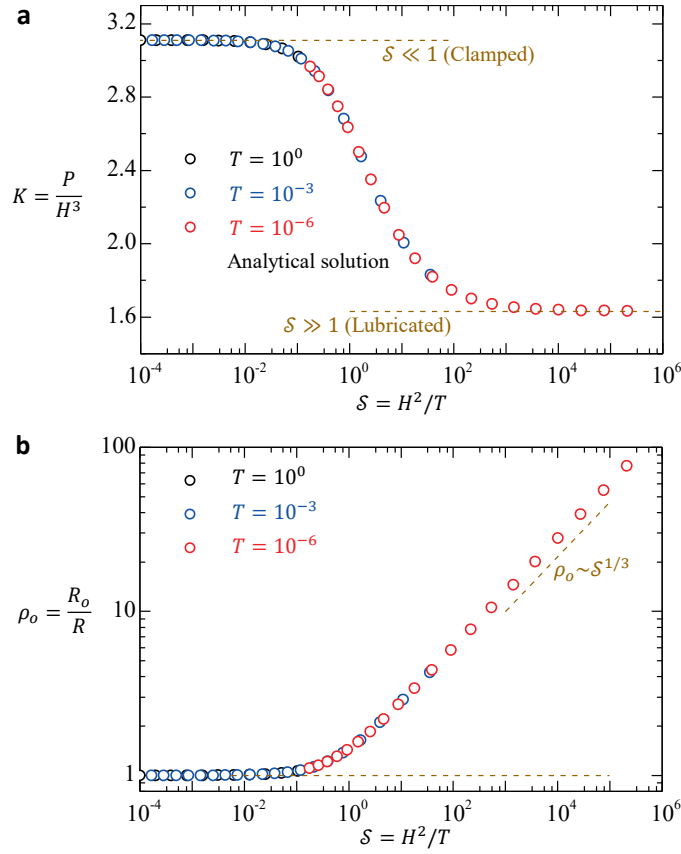


Figure 3.11: The dependency on the sliding number of the effective stiffness (a) and the size of the sliding zone (b).

Similar to the poking test, numerical results on the effective stiffness (as well as the size of the sliding zone) obtained from the pressurization of thin sheets with various center deflections and interfacial tractions collapse onto a master curve, which depends only on this sliding number (Figure 3.11). Two limits appear again: the sheet edge is close to being clamped when $\mathcal{S} \lesssim 10^{-2}$, the sheet-substrate interface is close to being ultra-lubricated or frictionless when $\mathcal{S} \gtrsim 10^3$. The scaling $\rho_o \sim \mathcal{S}^{1/3}$ derived in the poking problem also holds for the bulging problem (Figure 3.11b).

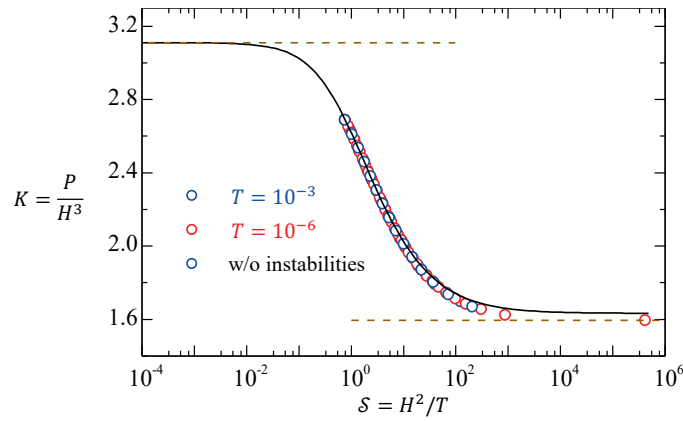


Figure 3.12: The dependency on the sliding number of the effective stiffness.

When wrinkling instabilities occur at the supported region of the bubble and buckle delamination is prohibited due to the adhesion in the supported region, we reach the Case II of the bulging problem. Following the method outlined in Chapter 2, we calculated the effective bulging stiffness of the sheet (Figure 3.12) and the associated size of sliding and wrinkling zone (Figure 3.A1) for various deflections and interfacial shear tractions. Though the analytical solutions are lacking, we identify the dependency of these results on the single sliding number. Specifically, for graphene, instabilities should be observed in the bulge tests when $\mathcal{S} \gtrsim 0.76$. The strong and weak shear limit can be observed in systems

with very small and large sliding numbers. Notably, many of the scalings derived in the poking problem still provide good predictions for quantities in the bulging problem (brown dashed lines in Figure 3.A1). It is also worth noting that the difference between Cases I and II of this bulging problem in the effective stiffness is only within 2.3%.

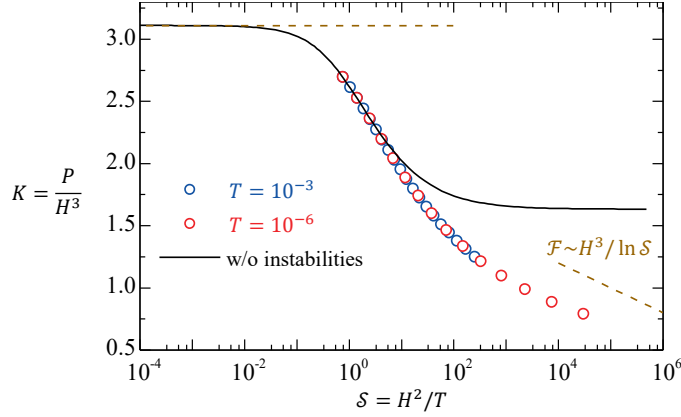


Figure 3.13: The dependency on the sliding number of the effective stiffness.

When instabilities are allowed in both supported and supported region, we reach the Case III of the bulging problem. We calculated the effective bulging stiffness of the sheet (Figure 3.13) and the associated size of the sliding and wrinkling zone (Figure 3.A2) for various deflections and interfacial shear tractions. Unsurprisingly, the sliding number governs these numerical results. In this case, the effective stiffness keeps weakening as $1/\ln S$ for thin sheets with large sliding numbers. Such scaling, again, originates from the poking problem, i.e., (3.25). In addition, the extents of the instabilities were predicted to be $\rho_o \sim S^{1/2}$ and $\rho_w \sim 1/\ln S$; the former shows good agreement with numerical results on the bulging problem while the latter cannot (Figure 3.A2).

3.7 IMPLICATIONS FOR BULGE TESTS

Now we summarize the implications of our studies on the edge slippage for bulge tests. Again, in such tests, we suggest that Cases I and II are more likely to occur; and the signature of Case II happening is that wrinkling instabilities form in the suspended region.

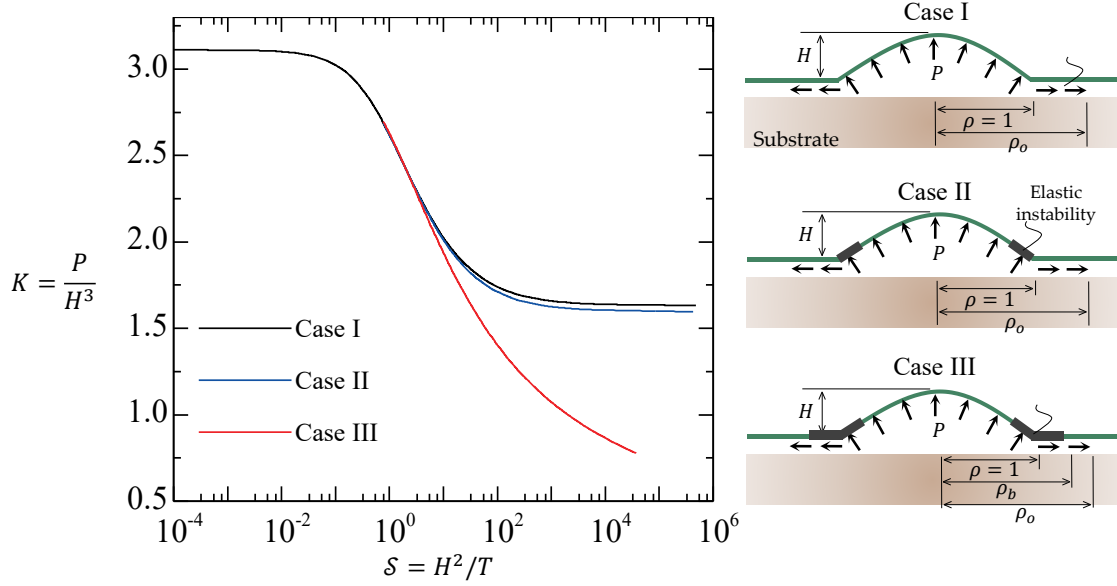


Figure 3.14: The effective stiffness of the thin sheet under poking for three possible deformed configurations, which are further illustrated in the right panel.

The strong and weak limits for the effective bulging stiffness are of interest: the sheet edge is close to being clamped when $S \lesssim 10^{-2}$; the sheet-substrate interface is close to being ultra-lubricated or frictionless when $S \gtrsim 10^4$. During loading, the experiments may first be in the state of Case I and then become Case II when the hoop stress is negative at the sheet edge ($S \gtrsim 0.76$ for graphene with $\nu = 0.165$). Due to the small difference in the effective stiffness between Cases I and II, we may also apply the Case I solutions to Case II (see details in Chapter 5). If the edge slippage and the pretension are considered simultaneously, (3.8) would lose its accuracy at large deflections – the regime where the

in-plane stiffness of the thin sheet is extracted. At small deflections where the effect of the pretension should be significant, pressurization of 2D materials is not well-controlled (very limited data lies in such regime, Figure 3.9c). Therefore, our conclusion that it remains a challenge to measure the pretension and in-plane stiffness in an atomically thin sheet still holds.

3.8 CONCLUSIONS

In this chapter, we performed the numerical calculations of the poking and bulging problem with a sliding boundary. A single controlling parameter, the sliding number \mathcal{S} , comparing the interfacial shear tractions with the membrane tension (due to out-of-plane deformations), is identified in both problems. The effective stiffness of a thin sheet in resisting a point load or a uniform pressure is found to depend on this sliding number sensitively. The numerical results suggest that the edge slippage plays an important role in deviating the force-displacement curves from a cubic relation. We also elucidated the dependency on the sliding number of the geometric features of elastic instabilities, such as the extent of the wrinkling. These results were obtained under the assumption of constant interfacial shear tractions. We expect qualitatively similar but quantitatively different outcomes when more complicated interfacial traction laws are adopted.

3.9 APPENDIX

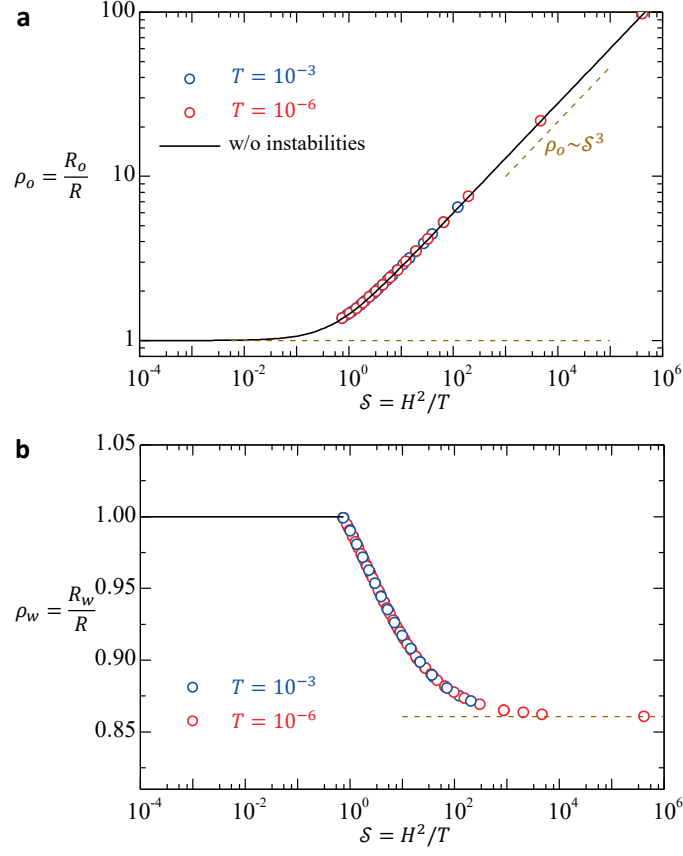


Figure 3.A1: The dependency on the sliding number of the size of the sliding zone (a) and the size of the wrinkling zone (b) in the bulge test. Markers are numerical results based on Case II of the bulging problem; black solid curves are based on Case I of the bulging problem (no instabilities); brown dashed lines are guessed according to our studies on Case II of the poking problem in section 3.4.

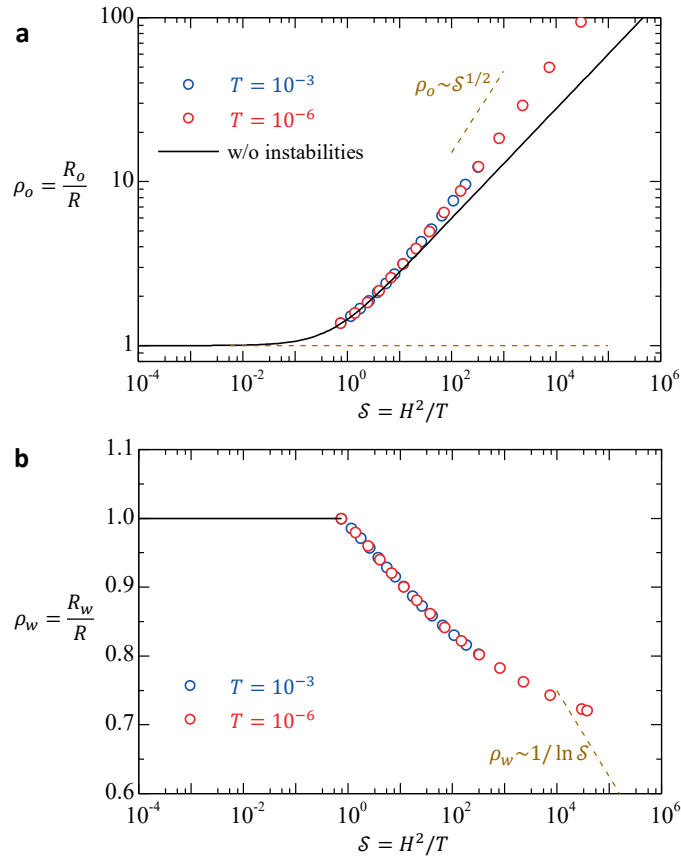


Figure 3.A2: The dependency on the sliding number of the size of the sliding zone (a) and the size of the wrinkling zone (b) in the bulge test. Markers are numerical results based on Case III of the bulging problem; black solid curves are based on Case I of the bulging problem (no instabilities); brown dashed lines are guessed according to our studies on Case III of the poking problem in section 3.4.

Chapter 4: Bending¹

In this chapter, we focus on bulge tests of multilayer 2D materials when the bending effect is nontrivial. Unlike classical linear elastic plates, multilayer 2D materials show bending rigidity that is not directly related to their Young's moduli because of the abnormal bending behavior of their building blocks (i.e., monolayers) and the atomically smooth layered structure. This has led to significant controversy on the bending rigidity of a 2D material multilayer despite extensive research for more than a decade. Here, we start with theoretical modeling of a pressurized thin sheet with Young's modulus independent bending rigidity. The results suggest the signatures of bending behavior being dominant and verify a simple analytical formula. Analysis of these results helps to design and interpret experiments towards direct measurements of bending rigidity of multilayer graphene, molybdenum disulfide (MoS_2), and hexagonal boron nitride (hBN) based on pressurized bubbles. The measured Young's moduli show good agreement with those reported in literature ($E_{\text{graphene}} > E_{\text{hBN}} > E_{\text{MoS}_2}$), but the bending rigidity follows an opposite trend: $B_{\text{graphene}} < B_{\text{hBN}} < B_{\text{MoS}_2}$ for multilayers with comparable thickness, in contrast to the classical plate theory, which is attributed to the interlayer shear effect in the multilayers.

¹A paper based on the work described in this Chapter has been published:

G. Wang[†], Z. Dai[†], J. Xiao[†], S. Feng, C. Weng, L. Liu, Z. Xu, R. Huang, Z. Zhang, *Bending of multilayer van der Waals materials*. Physical Review Letters 2019, 123, 116101. ([†] denotes equal contribution; Z.D. contributed to the design of the experiments, theoretical and results analysis, and writing of the first draft.)

4.1 INTRODUCTION

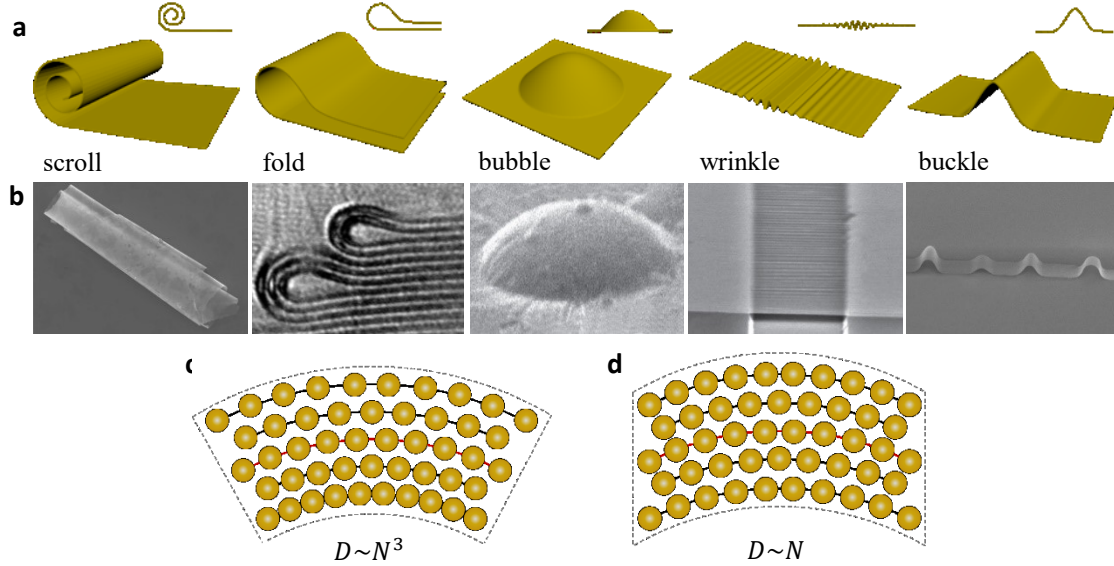


Figure 4.1: The schematics (a) and corresponding electron microscope images (b) illustrate various deformation modes. (Reproduced with permission from Ref. (Bao et al., 2009; Lee et al., 2015; Lopez-Bezanilla et al., 2012; Yang et al., 2015; Zhang et al., 2013b). Panels (c) and (d) illustrate the microstructural deformation upon bending of multilayer 2D materials with perfectly glued (c) and ultra-lubricated (d) interfaces.

2D materials possess excellent electronic, mechanical, and chemical properties that lend well to a range of applications (Geim and Grigorieva, 2013; Novoselov et al., 2016). In many instances, 2D materials come with multilayered structures (also called multilayer van der Waals (vdW) materials) and favor out-of-plane deformations such as scrolls (Cui et al., 2018; Zhang et al., 2013b), folds (Annett and Cross, 2016; Lopez-Bezanilla et al., 2012; Zhao et al., 2015), bubbles (Khestanova et al., 2016; Koenig et al., 2011; Lee et al., 2015; Levy et al., 2010; Sanchez et al., 2018; Wang et al., 2017b), wrinkles (Bao et al., 2009; Dai et al., 2019a), buckles (Castellanos-Gomez et al., 2013; Yang et al., 2015), crumples (Chen et al., 2016b; Zang et al., 2013), ripples (Tapasztó et al., 2012; Xie et al.,

2018), tents (Dai et al., 2018; Jiang et al., 2017; Reserbat-Plantey et al., 2014), and so on due to their thinness (Figures 1a and 1b). On the one hand, the out-of-plane mode of deformation is viewed as an inconvenience with research focusing on how it might be avoided (Pizzocchero et al., 2016). On the other hand, the development of 2D-material-based stretchable electronics and strained semiconductors can take advantage of these curved configurations (De Juan et al., 2011; Guinea et al., 2010). For these purposes, it is often necessary to manipulate and control the out-of-plane deformation of multilayer 2D materials, which requires the understanding of the bending mechanism of these atomically layered structures, in particular, the *bending rigidity/stiffness* as one crucial parameter.

Classical plate theory assumed that an elastic plate resists bending by tension and compression on the opposite sides of a neutral plane (Timoshenko and Woinowsky-Krieger, 1959). The bending rigidity of an elastic plate is related to its thickness (t) and the elastic moduli of the material by

$$B = \frac{Et^3}{12(1-\nu^2)}, \quad (4.1)$$

where E is Young's modulus and ν is Poisson's ratio. This relation holds well for a perfectly glued multilayer with N identical layers (Figure 1c) such that the overall bending rigidity scales as

$$B \sim N^3. \quad (4.2)$$

However, the classical relation is expected to break down for multilayer 2D materials for at least two reasons: (i) The mechanical resistance of the monolayer 2D material to bending and stretching deformation arises from different physical origins (Lu et al., 2009; Wei et al., 2013; Zelisko et al., 2017; Zhang et al., 2011). In graphene, for example, Young's modulus is related to the in-plane σ bonding, while the bending resistance is attributed to the distortion of out-of-plane π bonds (Zhang et al., 2011). (ii) The vdW interactions between the atomic layers are weak in resisting interlayer shear/sliding (Hod et al., 2018a;

Ribeiro-Palau et al., 2018), as demonstrated by recently observed self-rotation between 2D material layers (Wang et al., 2016a; Woods et al., 2016). The interlayer shear stiffness and strength of bulk 2D materials (e.g. graphite) is typically orders of magnitude lower than their in-plane Young's modulus and tensile strength (Kelly, 1981). This extreme mechanical anisotropy may subject multilayer 2D materials to the interlayer sliding. In the limiting case when the interface is ultra-lubricated (Figure 1d), each layer would bend independently such that the overall bending rigidity of the multilayer would scale linearly with the number of layers,

$$B \sim N. \quad (4.3)$$

The actual bending rigidity of various 2D materials should be within the two limits, depending on the interlayer shear/slip.

Despite extensive research into the mechanical properties of 2D materials for more than a decade, significant controversy still exists on the bending rigidity of monolayer and multilayer 2D materials (Bao et al., 2009; Tapasztó et al., 2012; Zelisko et al., 2017; Zhang et al., 2011). It remains elusive how the bending rigidity of a multilayer 2D material relates to its layer number, although the classical relation ($B \sim N^3$) has been widely applied in the literature despite the perceived breakdown. Motivated by this puzzle, in this Chapter, we focus on how the bending rigidity of multilayer 2D materials can be measured through bulge tests. We first develop a theoretical understanding of the bending behavior of a clamped, circular, thin sheet in response to pressure. With this, experiments were performed on graphene, hexagonal boron nitride (hBN), and molybdenum disulfide (MoS_2), which serve as representatives of metallic, insulating and semiconducting 2D materials, respectively. Finally, the effect of interlayer coupling on the bending rigidity of 2D materials is revealed.

4.2 CURRENT UNDERSTANDING ON 2D MATERIAL BENDING

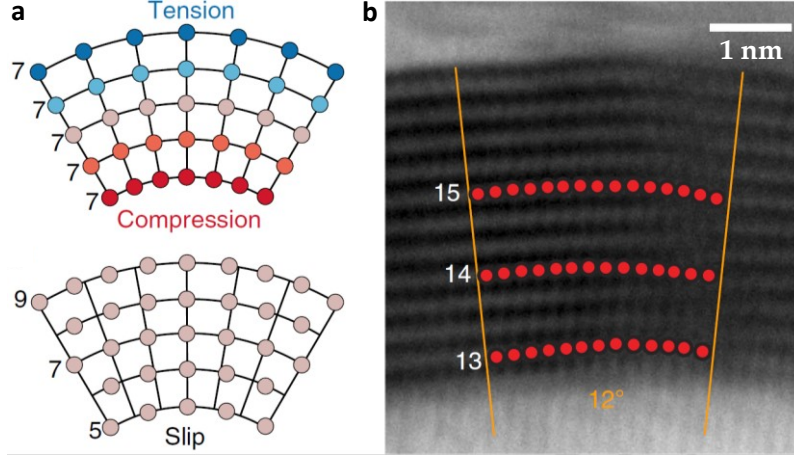


Figure 4.2: Bending of multilayer 2D materials. (a) Schematic of a bent multilayer where interlayer interfaces are glued (top panel) and lubricated (bottom panel) (Han et al., 2019). (b) Bright-field STEM image of 12-layer graphene bent to 12 °, where the number of atomic columns in the arc is provided for layers at three different locations (Han et al., 2019).

We begin by discussing recent theoretical and experimental advances in the understanding of the bending behavior of multilayer 2D materials (for the most part, graphene). Molecular dynamics (MD) simulations have shown significant deviations of bending rigidity from the classical plate theory predictions (Liu et al., 2011; Nazemnezhad et al., 2014; Pan et al., 2019). For example, Liu et al. found that the secondary resonant frequency f of N -layer graphene cantilevers with a length L follows $f \sim (1 - N^{-1})^{0.77} L^{-0.46} + f_{mono}$, instead of $f \sim NL^{-2}$ (given by the classical Euler–Bernoulli beam theory) (Liu et al., 2011). This deviation was explained well by a multibeam model that considers each layer individually and models the interlayer interactions as shear-type elastic springs (Liu et al., 2011). Recently, Pan et al. simulated the bending rigidity of multilayer graphene under relatively large curvatures using a registry-dependent interlayer

potential (Kolmogorov-Crespi potential) (Pan et al., 2019). It is found that the ratio of the simulated to the idealized bending rigidity by classical plate theory varies with the deformation levels and the layer numbers, and is always < 1 , implying the softening effect of the interlayer shear on the bending rigidity (Pan et al., 2019).

Two types of experiments have been developed recently to characterize the bending rigidity of multilayer 2D materials. As expected, the interlayer-shear-caused softening has been observed in both. The first type of experiments is indirect that measures the spontaneously deformed configuration of a multilayer and estimates its bending rigidity by making use of abovementioned “elasto-intermolecular” balances in Chapter 1.3 (Chen et al., 2015; Qu et al., 2019; Zhao et al., 2015). For example, Ke and coworkers investigated the bending rigidity of few-layer graphene and hBN through self-folding experiments and nonlinear mechanics modeling (Chen et al., 2015; Qu et al., 2019). They proposed a power function for the bending rigidity-thickness relation of these multilayers (the power index is ~ 2.35 for hBN (Qu et al., 2019) and ~ 2 for graphene (Chen et al., 2015)). This was explained by a multibeam model with relatively stiffer interlayer shear springs in hBN than graphene (Chen et al., 2015; Qu et al., 2019).

Very recently, Han et al. draped few-layer graphene over sharp steps of hBN such that the bending profiles and the interlayer slip (Figure 4) became accessible to STEM with atomic-level resolutions (Han et al., 2019). The competition between the graphene/hBN adhesion energy and the bending energy of graphene could select the geometry (e.g., bending angles) of the bending profiles. STEM measurement of such geometry then leads to the estimation of the bending rigidity of few-layer graphene, which is found to decrease dramatically with the bending angles (Han et al., 2019), agreeing with their DFT calculations.

Another type of experiments is direct that measures the bending rigidity of a multilayer through detecting its deformed deflection when a point force (typically by an AFM tip) is applied (Castellanos-Gomez et al., 2015; Poot and van der Zant, 2008; Wang et al., 2019b). At small deflections, the pretension and bending rigidity dominated the deformation, and the force/pressure-deflection curve was believed to be linear. Early AFM indentation works typically estimated both pretension and bending rigidity by the slope of the indentation force-deflection curve and further converted the bending rigidity to Young's modulus via the classical plate theory (Castellanos-Gomez et al., 2012; Castellanos-Gomez et al., 2015; Poot and van der Zant, 2008). However, such methodology, as discussed in Chapter 3.2, relies heavily on the radius of the AFM indenter, which even varies with the indentation depth. Therefore, direct experimental measurements on the bending rigidity of a 2D material multilayer based on robust methodologies remain lacking. A good deal of confusion has arisen, including the extensive yet inappropriate application of the over-simplified formula (4.1), where the bending rigidity of the multilayer is related to its Young's modulus and thickness. Such confusion motivates the theoretical and experimental studies of the bulge test of 2D material multilayers in this chapter.

4.3 THEORY OF BULGING

The theoretical setting of the bulge test of a sheet with a stretching-modulus-independent bending stiffness under moderate deflection is presented in this section.

4.3.1 FvK equations

We recall FvK equations in terms of Airy stress function and out-of-plane deflections (Mansfield, 2005) that were discussed in Chapter 2.2. The vertical equilibrium and compatibility read

$$\nabla^2(B\nabla^2 w) - [\phi, w] - q(r) = 0 \quad (4.4)$$

and

$$\nabla^4 \phi + \frac{1}{2} Et[w, w] = 0, \quad (4.5)$$

where E , B , and t are Young's modulus, bending rigidity, and the thickness of the sheet, respective; $[f, g] = r^{-1} d\left(\frac{df}{dr} \frac{dg}{dr}\right) / dr$, and $\nabla^4 = \nabla^2 \nabla^2$. We introduced the Airy stress function ϕ so that the in-plane equilibrium is satisfied automatically by setting stress resultants as $N_{rr} = \frac{1}{r} \frac{d\phi}{dr}$, $N_{\theta\theta} = \frac{d^2\phi}{dr^2}$.

It is convenient to consider the dimensionless form of FvK equations. Consistent with the convention in Chapter 2, we use the in-plane stiffness Et to normalize the force-related variables. The lengths, however, are rescaled in a different way. The radius of the bubbling device a provides a natural horizontal length scale; we consider a different vertical length scale that arises from the comparison between out-of-plane stiffness and in-plane stiffness, i.e.,

$$\ell_c = \sqrt{B/Et}. \quad (4.6)$$

The following non-dimensionalization is therefore performed,

$$R = \frac{r}{a}, \quad W = \frac{w}{\ell_c}, \quad H = \frac{h}{\ell_c}, \quad P = \frac{pa}{Et}, \quad \Phi = \frac{\phi}{Eta^2}, \quad N_{RR} = \frac{N_{rr}}{Et}, \quad N_{\theta\theta} = \frac{N_{\theta\theta}}{Et}, \quad (4.7)$$

with which FvK equations are rewritten:

$$\frac{1}{\mathcal{K}^{3/2}} \frac{1}{R} \frac{d}{dR} \left\{ R \frac{d}{dR} \left[\frac{1}{R} \frac{d}{dR} \left(R \frac{dW}{dR} \right) \right] \right\} - \frac{1}{\mathcal{K}^{1/2}} \frac{1}{R} \frac{d}{dR} \left(\frac{d\Phi}{dR} \frac{dW}{dR} \right) = P \quad (4.8)$$

and

$$\frac{1}{R} \frac{d}{dR} \left\{ R \frac{d}{dR} \left[\frac{1}{R} \frac{d}{dR} \left(R \frac{d\Phi}{dR} \right) \right] \right\} = - \frac{1}{2\mathcal{K}} \frac{1}{R} \frac{d}{dR} \left[\left(\frac{dW}{dR} \right)^2 \right]. \quad (4.9)$$

With this rescaling, we find the single controlling parameter of this system (i.e., FvK number) again,

$$\mathcal{K} = \frac{a^2}{\ell_c^2} = \frac{E_{2D}a^2}{B}. \quad (4.10)$$

\mathcal{K} can be thought of as the bendability of a thin sheet since systems with higher \mathcal{K} numbers are more comfortable to bend than to stretch. For monolayer 2D materials in experiments with radii of 100 nm, \mathcal{K} can be up to 10^7 . We will focus on multilayer 2D materials (up to 70 layers) in this chapter: the bendability of the sheet could be reduced largely with \mathcal{K} as small as 10^1 .

The following questions that are highly beneficial to the experimental design would be answered: When does the bending effect of the sheet become discernible in the bulge test? What are the signatures of bending behavior starting to dominate? Are there any analytical formulae with a good approximation for sheets with Young's modulus independent bending stiffness?

To facilitate the numerical calculations, we introduce

$$\Psi = \frac{d\Phi}{dR}, \text{ then } N_{RR} = \frac{\Psi}{R}, N_{\theta\theta} = \frac{d\Psi}{dR}, \quad (4.11)$$

and integrate (4.8) and (4.9) once to obtain

$$R \frac{d}{dR} \left[\frac{1}{R} \frac{d}{dR} \left(R \frac{dW}{dR} \right) \right] - \mathcal{K} \Psi \frac{dW}{dR} = \frac{1}{2} \mathcal{K}^{3/2} P R^2 \quad (4.12)$$

and

$$R \frac{d}{dR} \left[\frac{1}{R} \frac{d}{dR} (R\Psi) \right] = -\frac{1}{2\mathcal{K}} \left(\frac{dW}{dR} \right)^2, \quad (4.13)$$

The integration constants vanish to satisfy the normal and shear force balances. (4.12) and (4.13) could be solved with 5 boundary conditions; they are straightforward when the edge of the sheet is clamped, and the pretension is neglected. Specifically, at the center of the blister,

$$\left(\frac{dW}{dR} \right)_{R=0} = \lim_{R \rightarrow 0} \left(R \frac{d\Psi}{dR} - \nu\Psi \right) = 0 \quad (4.14)$$

and, at the edge of the sheet,

$$W(1) = \left(\frac{dW}{dR}\right)_{R=1} = \left(\frac{d\Psi}{dR}\right)_{R=1} - \nu\Psi(1) = 0, \quad (4.15)$$

where the second term in (4.14) and the third term in (4.15) leveraged Hooke's law, denoting zero in-plane displacements at the bubble center and bubble edge, respectively.

4.3.2 $h \ll \ell_c$

Before proceeding numerical computations, we start with the scaling analysis of this system. Specifically, the compatibility (4.13) indicates $\Psi \sim H^2/\mathcal{K}$. Back to (4.12), the bending term scales as H ; the stretching term scales as $\mathcal{K}\Psi H \sim H^3$. Two natural limits appear: $H \ll 1$ or $h \ll \ell_c$ (bending effect dominates) and $H \gg 1$ or $h \gg \ell_c$ (stretching effect dominates). We consider the bending limit first, where (4.12) can be simplified as

$$\frac{1}{\mathcal{K}^{3/2}} R \frac{d}{dR} \left[\frac{1}{R} \frac{d}{dR} \left(R \frac{dW}{dR} \right) \right] = \frac{1}{2} P R^2 \quad (4.16)$$

There exists an exact solution to (4.16), in which the shape of the bubble takes

$$W = H(1 - R^2)^2 \text{ or } w(r) = h \left(1 - \frac{r^2}{a^2} \right)^2, \quad (4.17)$$

and the pressure-center deflection relation is linear,

$$P = \frac{64}{\mathcal{K}^{3/2}} H \text{ or } p = \frac{64B}{a^4} h. \quad (4.18)$$

4.3.3 $h \gg \ell_c$

Moving on to the stretching limit, we may neglect the first term on the right side of (4.12) and obtain

$$\frac{1}{\mathcal{K}^{1/2}} \Psi \frac{dW}{dR} = \frac{1}{2} P R^2. \quad (4.19)$$

Unlike (4.17), (4.19) is moderately nonlinear. According to the discussion in Chapter 3.6, we may use the numerically-based analytical solution to (4.19) and (4.13), where the pressure is proportional to the cubic center deflection,

$$P = \frac{A(\nu)}{\mathcal{K}^{3/2}} H^3 \text{ or } p = A(\nu) \frac{Et}{a^4} h^3, \quad (4.20)$$

where $A(\nu) \simeq (0.7179 - 0.1706\nu - 0.1495\nu^2)^{-3}$ (Komaragiri et al., 2005). In addition, we will show soon that a spherical cap can approximately capture the shape of the deformed sheet,

$$W = H(1 - R^2) \text{ or } w(r) = h \left(1 - \frac{r^2}{a^2}\right). \quad (4.21)$$

4.3.4 An approximate solution

The simple summation of two asymptotic expressions for bending (4.18) and stretching (4.20) limits gives rise a master curve for $\mathcal{K}^{3/2}P \sim H$,

$$\mathcal{K}^{3/2} \frac{P}{H^3} = \frac{64}{H^2} + A(\nu) \quad (4.22)$$

In a similar problem, the attempt to combine expressions for pretension and out-of-plane deformation caused tension in indentation tests (in Chapter 3.2) has been proved to produce a noticeable error $1 - \mathcal{F}_{sum}/\mathcal{F} \sim \mathcal{O}(1)$ (Vella and Davidovitch, 2017). Now, the question is whether we can naively combine the bending and stretching asymptotes to describe the intermediate stage, where experiments are likely to be.

To test the accuracy of (4.22), we performed the computation outlined in section 4.3.1. Figure 4.3 shows the master curve based on (4.22) and numerical results of thin sheets with a range of bendabilities. We find excellent quantitative agreement between the analytical approximation and numerical calculations, implying that (4.22) can fully capture the bulging pressure-deflection relation from small, intermediate, all the way to large deflections. (4.22) seemingly works for 2D materials whose bendability can be up to 10^7 (the value of monolayer graphene) and be as small as 10^1 .

With these results, we are in the position to provide the following useful suggestions for bulge experiments that may measure the bending rigidity of a 2D material multilayer :

- Guides for the design of experiments. The key to achieving experimental measurement on bending rigidity of a sheet is to realize $H \sim \mathcal{O}(1)$, i.e., $h \sim \ell_c$. Due

to the softening effect of interlayer shear/slip on the bending rigidity, we expect $\ell_c < t$. This criterion precludes any experimental efforts to detect the bending behavior of monolayer 2D materials via bulge tests but is likely to be satisfied by bulging a multilayer. We suggest experiments with small horizontal radii such that the center height of the pressurized bubble is more controllable near $h \sim \ell_c$. We also suggest the analytical result in (4.22), which has been numerically verified for sheets with various bendabilities (even though their bending rigidity is Young's modulus independent).

- Signatures if a pressurized sheet being plate-like or in the bending-dominated regime. According to our numerical results, two useful signatures would help to identify whether the bending rigidity plays a role. i) When the pressure-deflection relation appears linear, the coefficient for such linearity is dominated by the bending rigidity. ii) The shape of the deformed bubble would be smooth at the bubble edge and be described by (4.17), as shown in Figure 4.4a.
- Signatures of a pressurized sheet being membrane-like or in the stretching-dominated regime. Correspondingly, when stretching effect dominates, pressure-deflection relation appears cubic, and the shape of the deformed bubble would be sharp at the bubble edge and approximated by (4.21), as shown in Figure 4.4b.

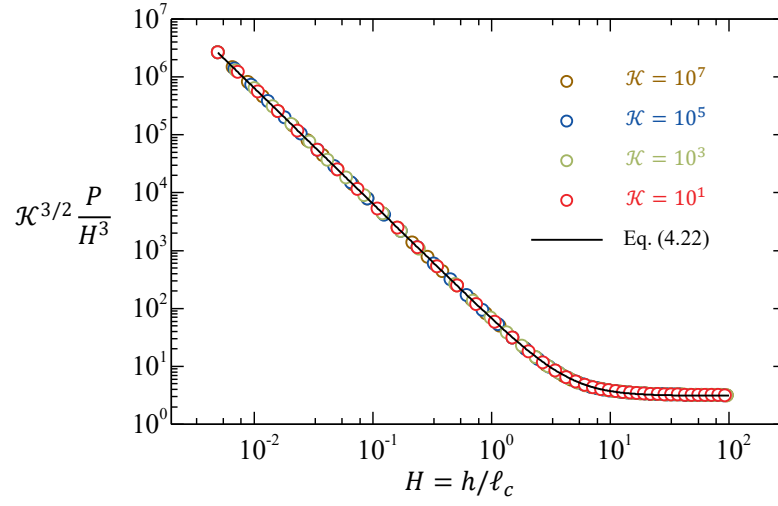


Figure 4.3: The pressure-deflection relation of a clamped, circular sheet subject to a uniform pressure. Markers denote numerical results, and the solid curve is based on (4.22)

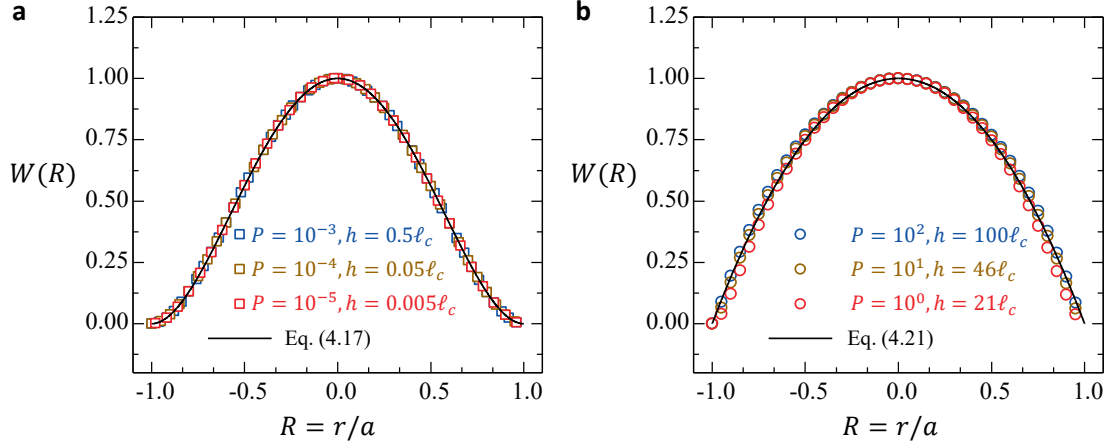


Figure 4.4: Shape of a clamped, circular sheet subject to a uniform pressure when the deflection is relatively small (a) and large (b). Markers denote numerical results based on $\mathcal{K} = 10^3$.

4.4 EXPERIMENTS OF BULGING¹

4.4.1 Set-up

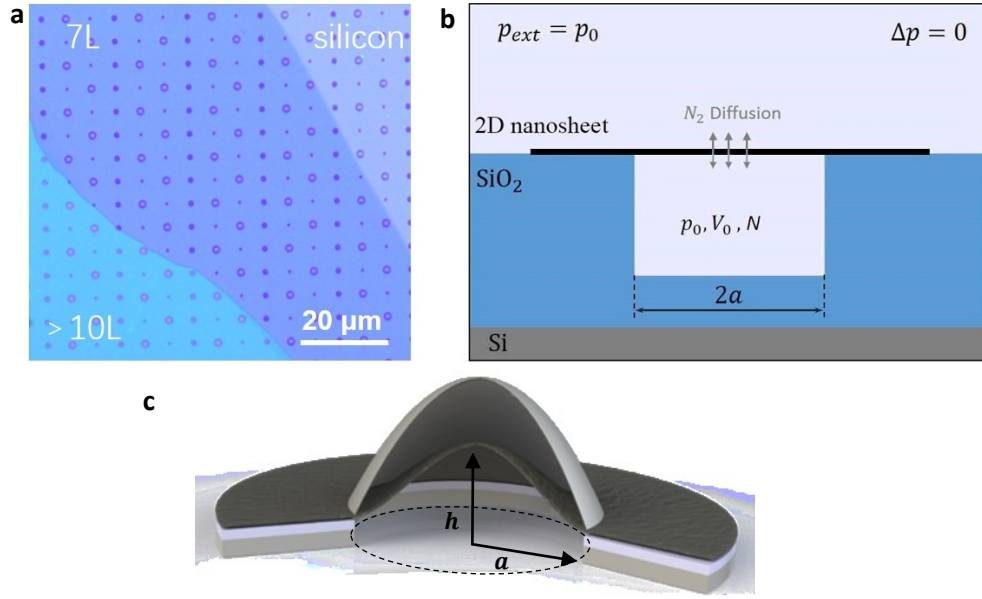


Figure 4.5: (a) An optical image of 2D materials suspended over the cavities with diameters of 0.5-1.5 μm on SiO₂/Si substrate. (b) Schematic illustration of the bubbling device with pressure difference applied across the 2D sheet. Bending of multilayer 2D materials. (c) The schematic of pressurized bubbles with two distinct shape characteristics at small and large deflections.

Figure 4.5 illustrates the pressurized bubble device that can create axisymmetric out-of-plane deformation of 2D materials. The samples are made by mechanical exfoliation of multilayer graphene, hBN, and MoS₂ over patterned holes (radius: 0.5-1.5 μm) on a SiO₂/Si substrate. The number of layers (N) in these multilayers, ranging from 7 to 70, can be identified by AFM (see details in the next section). Following a well-developed gas diffusion method (Figure 4.5b) (Koenig et al., 2011; Wang et al., 2017b), we created a

¹ The experimental set-up is based on G. Wang[†], Z. Dai[†] et al. Physical Review Letters 2017, 119, 036101. Guorui Wang and Junkai Xiao performed the bulge tests on these 2D material multilayers discussed in this Chapter.

pressure difference (p) across the suspended 2D sheets to push them upwards. The bubbling process can be well controlled through a tunable pressure, $p = \frac{p_0 V_0}{V_0 + V_b} - p_e$, according to the ideal gas law, where p_0 and p_e are the applied and external atmosphere pressures, V_0 and V_b are volumes of the hole and bubble, respectively. The height profile of each bubble is then measured by AFM.

4.4.2 Determination of the layer numbers

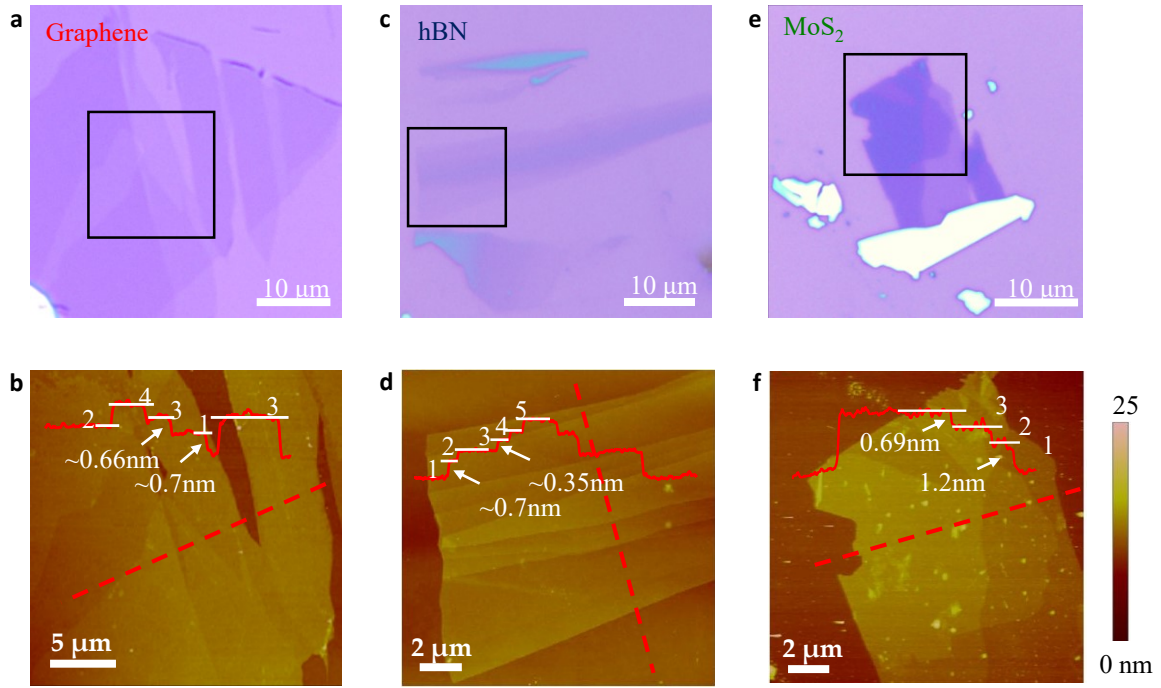


Figure 4.6: Optical images of (a) graphene, (c) hBN, and (e) MoS₂ sheets with various layer numbers. The magnified views of the rectangular regions are shown in AFM images for (b) graphene, (d) hBN, and (f) MoS₂, respectively. The insets give the height profiles along the red dashed lines, where the interlayer distance was found to be around 0.34 nm, 0.35 nm, and 0.69 nm for graphene, hBN, and MoS₂, respectively. The relatively high thickness of the bottom layer (0.7 nm for graphene and hBN, and 1.2 nm for MoS₂) was typically attributed to the instrumental scanning offset from the substrate to the 2D materials.

AFM offers a direct technique to identify the thickness of 2D materials. Take graphene as an example. Figure 4.6a shows the optical image of a graphene flake containing multiple layers on the SiO₂/Si substrate. Figure 4.6b presents the AFM image of the rectangular area highlighted in Figure 4.6a, where the tapping mode was employed to minimize possible mechanical damages. The thickness measurements were carried out by line scans, and the corresponding values are indicated in the inset of Figure 4.6b. Although the thickness of the monolayer flake may be different possibly due to the instrumental offset, the thickness difference due to different numbers of layers stacked together gave a quite consistent interlayer distance ($t_1 = 0.34$ nm). Similar phenomena were also observed for hBN and MoS₂, as shown in Figure 4.6d and 4.6f, whose interlayer distances were measured to be ~ 0.35 nm and ~ 0.69 nm, respectively. Therefore, a simple linear relationship between the number of layers (N) and total measured thickness (t_{measured}) can be obtained as

$$t_{\text{measured}} = s + Nt_1, \quad (4.23)$$

where s is the substrate-caused offset for the bottom layer (0.36 nm for graphene, 0.35 nm for hBN, and 0.51 nm for MoS₂). The layer numbers of various van der Waals materials are hence determined by the AFM measurements, with an estimated error of less than 5%.

4.4.3 Shape: plate or membrane

We first observe the shape characteristics of 2D material bubbles. Classical theory predicts the deflection of a sheet responding to a uniform pressure as follows:

$$\frac{w(r)}{h} = \left(1 - \frac{r^2}{a^2}\right)^\alpha, \quad (4.24)$$

where $w(r)$ is the out-of-plane deflection profile, h is the bubble height (deflection at the center), r is the distance from the hole center, a is the hole radius, and the exponent α is 2 for a linear elastic plate. However, such plate-like profile is rarely observed in monolayer

2D material bubbles because of the extreme thinness and flexibility of 2D materials (Khestanova et al., 2016; Koenig et al., 2011; Levy et al., 2010; Sanchez et al., 2018; Wang et al., 2017b).

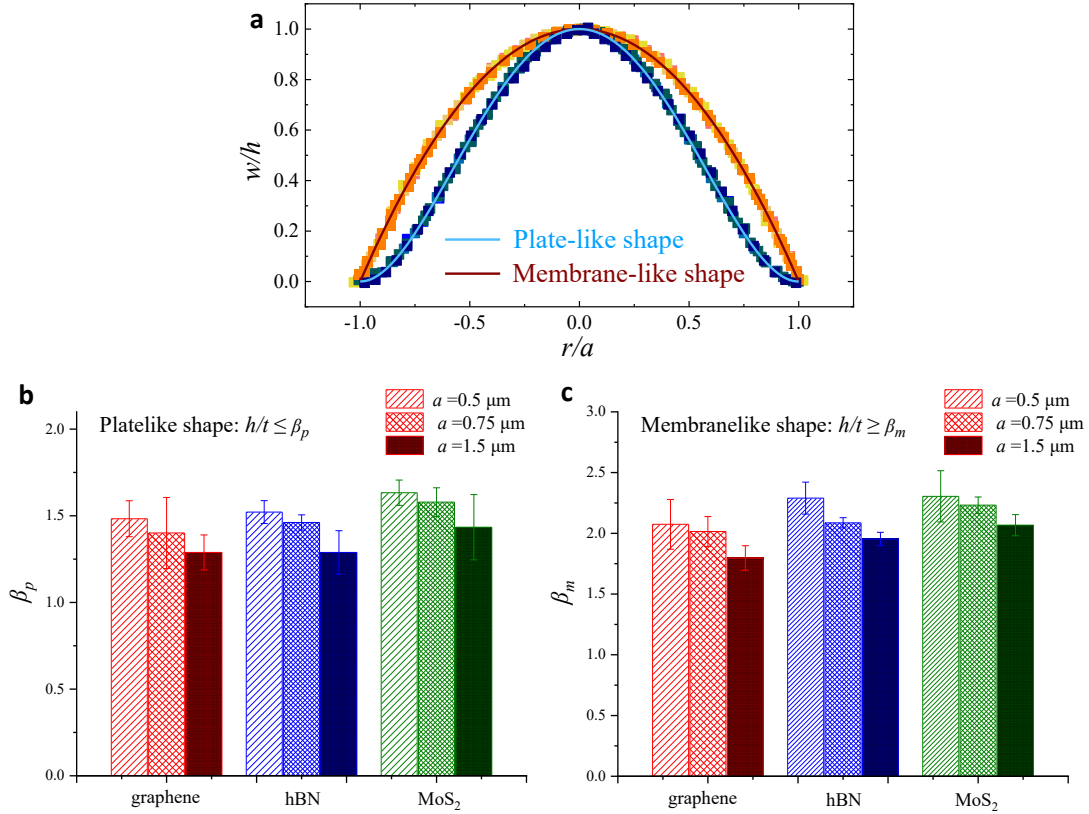


Figure 4.7: (a) Normalized deflection profiles measured from two sets of 0.5- μm -radius bubbles. We observed a membrane-like shape with a kinked edge for $h/t \gtrsim 2$ (orange markers) and a plate-like shape with a smooth edge for $h/t \lesssim 1.5$ (blue markers). (b,c) Critical ratios of bubble height to the thickness (h/t) to discriminate shapes dominated by the plate or membrane for graphene, hBN, and MoS₂.

Alternatively, the membrane limit is commonly adopted for these 2D material bubbles, where the bending rigidity is assumed to be negligible, and the deflection profile of the bubble is approximately taken as a spherical cap, i.e., $\alpha = 1$ in (4.24) (Khestanova

et al., 2016; Koenig et al., 2011; Levy et al., 2010; Sanchez et al., 2018; Wang et al., 2017b). As discussed in Chapters 1 and 3, the membrane analysis has been adopted to measure fundamental mechanical properties of 2D materials such as Young's modulus, interfacial adhesion and friction, and electromechanical coupling, but not for bending rigidity.

We show in Figure 4.7a experimentally measured profiles from graphene bubbles with a variety of thicknesses and heights. We normalized the deflection by the bubble height and the radial position by the bubble radius. For bubbles with radii of 0.5 μm , the normalized deflection profiles collapse onto one curve as predicted by the membrane analysis when the ratio between the bubble height and the thickness of the multilayer, h/t , is larger than 2 – the case of most previous works (Khestanova et al., 2016; Koenig et al., 2011; Levy et al., 2010; Sanchez et al., 2018; Wang et al., 2017b). Theoretically, the criterion is $h \gg \ell_c$. This implies that $t \gg \ell_c$ or the bending rigidity of a 2D material multilayer is much smaller than the prediction by classical plate theory in (4.1).

For bubbles with the height comparable to the thickness, i.e., $h/t \lesssim 1.5$, the bending effect becomes significant so that the deflection profiles collapse onto a different curve predicted by the plate theory. This observation implies that membrane-like behavior can transit to plate-like behavior for the bubbles of multilayer 2D materials by merely tuning the ratio h/t . The membrane-to-plate transition also makes it possible to simultaneously determine the in-plane Young's modulus and bending rigidity of the 2D multilayers. We note that the critical h/t for such transition depends on the bubble radius and also varies slightly from material to material (Figures 4.7b and 4.7c)

4.4.4 Pressure-deflection relation

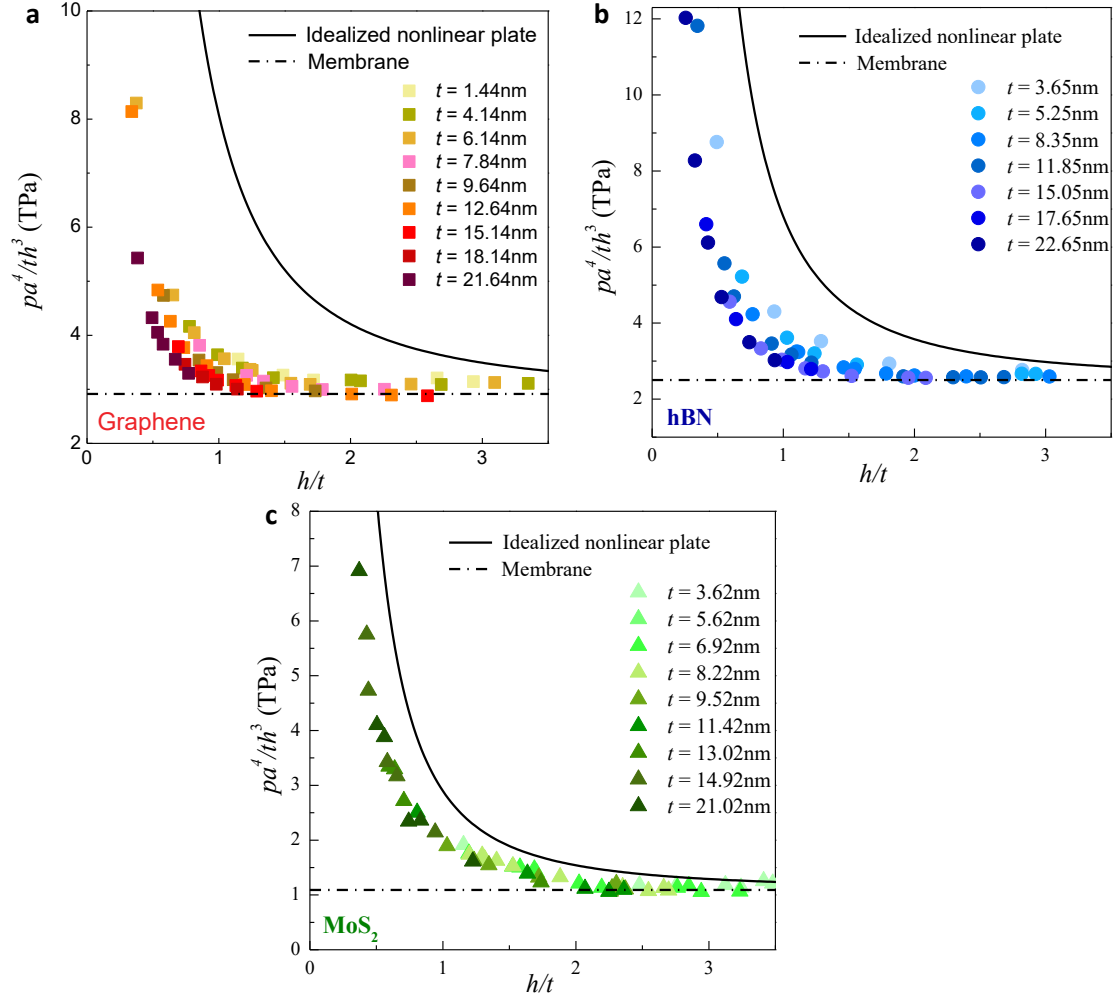


Figure 4.8: pa^4/h^3t as a function of h/t for graphene (a), hBN (b) and MoS₂ (c), respectively. The solid lines represent the idealized nonlinear plate solution, and horizontal dot-dashed lines are the membrane solution. In the color system, darker symbols denote the thicker samples.

We then consider the pressure-height relation for these multilayer 2D material bubbles. Our theoretical results in section 3 suggest a unified expression, i.e., (4.22), with excellent accuracy; its dimensional form is

$$\frac{pa^4}{h^3t} = A(\nu)E + \frac{64B}{t^3} \left(\frac{t}{h}\right)^2 \quad (4.25)$$

where $A(\nu) \simeq (0.7179 - 0.1706\nu - 0.1495\nu^2)^{-3}$, which is 3.10 for graphene with $\nu = 0.165$, 3.28 for hBN with $\nu = 0.221$, and 3.46 for MoS₂ with $\nu = 0.27$ (Bertolazzi et al., 2011). Note that (4.25) was found to be a good approximation even for monolayer graphene bubbles by using the 2D in-plane stiffness ($E_{2D} = Et$) and bending rigidity (B) that is independent on E (Wang et al., 2013b).

In Figures 4.8a-c, the dot-dashed lines represent the membrane limit of (4.25), i.e., (4.20), where the bending term is neglected. The solid lines represent the idealized nonlinear plate model assuming a bending rigidity $B = Et^3/12(1 - \nu^2)$ such that the response $\left(\frac{pa^4}{h^3t} \sim \frac{h}{t}\right)$ does not depend on the thickness. Evidently, the experimentally measured responses for all three 2D materials approach the membrane limit when the ratio h/t is greater than 2. For $h/t < 1.5$, the bubble responses exhibit a transition to the plate-like behavior but deviate considerably from the idealized nonlinear plate solution. This observation implies that the use of the classical $B - E$ relation would overestimate the bending rigidity of the multilayer 2D materials.

4.4.4 Young's modulus and Bending rigidity

Equation (4.25) allows us to determine both Young's modulus and bending rigidity of the multilayer 2D material as well as their dependency on the layer thickness. We start with Young's moduli of multilayer 2D materials by focusing on samples under relatively large pressure. In this case, h/t is relatively large and the second term on the right-hand side of (4.25) is negligible (the membrane limit) so that Young's modulus can be determined directly by measuring $\frac{pa^4}{h^3t}$. In Figures 4.8a-c, for graphene, hBN, and MoS₂ bubbles with $h/t \gtrsim 2$, the data for $\frac{pa^4}{h^3t}$ collapse onto the dot-dashed lines, as predicted by the membrane limit. The domain of h/t for the membrane-like behavior is consistent with our shape measurements in Figure 7.

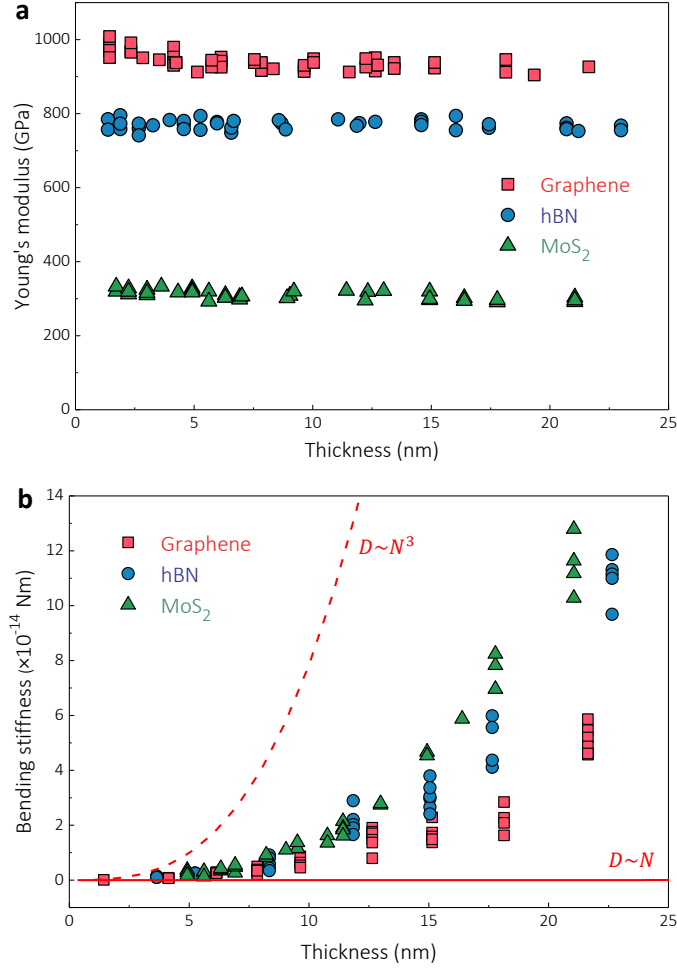


Figure 4.9: Extracted Young's modulus (a) and bending rigidity (b) as a function of thickness. At a given thickness, AFM measurements of up to 17 different bubbles produce the results plotted as symbols. The dash-dotted lines in (a) indicate the average values, while the dashed and solid lines in (b) are the theoretical predictions for the perfectly glued ($D \sim N^3$) and ultra-lubricated ($D \sim N$) cases, respectively.

We then extract Young's moduli of the multilayer 2D materials, as summarized in Figure 9a. We find that the average values are 939.5 ± 21.7 GPa, 769.9 ± 12.9 GPa, and 314.3 ± 8.4 GPa for the multilayer graphene, hBN, and MoS₂ with layer numbers ranging from ~ 10 to ~ 70 . For each 2D material, the extracted Young's modulus shows mostly no

dependency on the thickness, and the average values agree well with those measured by AFM indentation of monolayers (Bertolazzi et al., 2011; Kim et al., 2015; Lee et al., 2008).

When the height of the deformed bubble becomes comparable to the thickness of 2D multilayers, the contribution from bending substantiates, and both terms on the right-hand side of (4.25) should be accounted for. A membrane-to-plate transition is expected to occur in the mechanical response of bubbles (Figure 7). With the thickness-independent Young's modulus extracted from the membrane model, we can then calculate the bending rigidity B by comparing (4.25) with the measured response $\frac{pa^4}{h^3t}$ for bubbles with relatively small deflection ($h/t \lesssim 1.5$). Figure 9b summarizes the values of B for graphene, hBN, and MoS₂ multilayers, and the possible errors for these measurements are discussed in Table 4.1. As expected, the bending rigidity increases with the thickness of 2D materials. However, the thickness dependence does not follow either one of the two limiting cases. Specifically, the bending rigidity of multilayer graphene ($t > 5$ nm) is much lower than that expected from classical plate theory ($B \sim t^3$; dashed line in Figure 9b), but much higher than the ideally lubricated cases ($B \sim t$; solid line in Figure 9b). More interestingly, for samples with similar thickness, we find $B_{\text{MoS}_2} > B_{\text{hBN}} > B_{\text{graphene}}$, whereas the values of Young's moduli are ordered inversely, that is, $E_{\text{graphene}} > E_{\text{hBN}} > E_{\text{MoS}_2}$. This again indicates that the bending rigidity of multilayer 2D materials violates the predictions of the classical plate theory.

4.5 DISCUSSION

Our results show that the traditional relation for the bending rigidity, $B = Et^3/12(1 - \nu^2)$, in general, is not valid for multilayer 2D materials. We attribute the abnormal bending behaviors of these multilayers to the effect of interlayer shear/slippage between atomic sheets. This mechanism may be qualitatively simple to understand, but the

quantitative measurement of its impact on the bending properties of a 2D material multilayer has been challenging and has not been reported to our best knowledge.

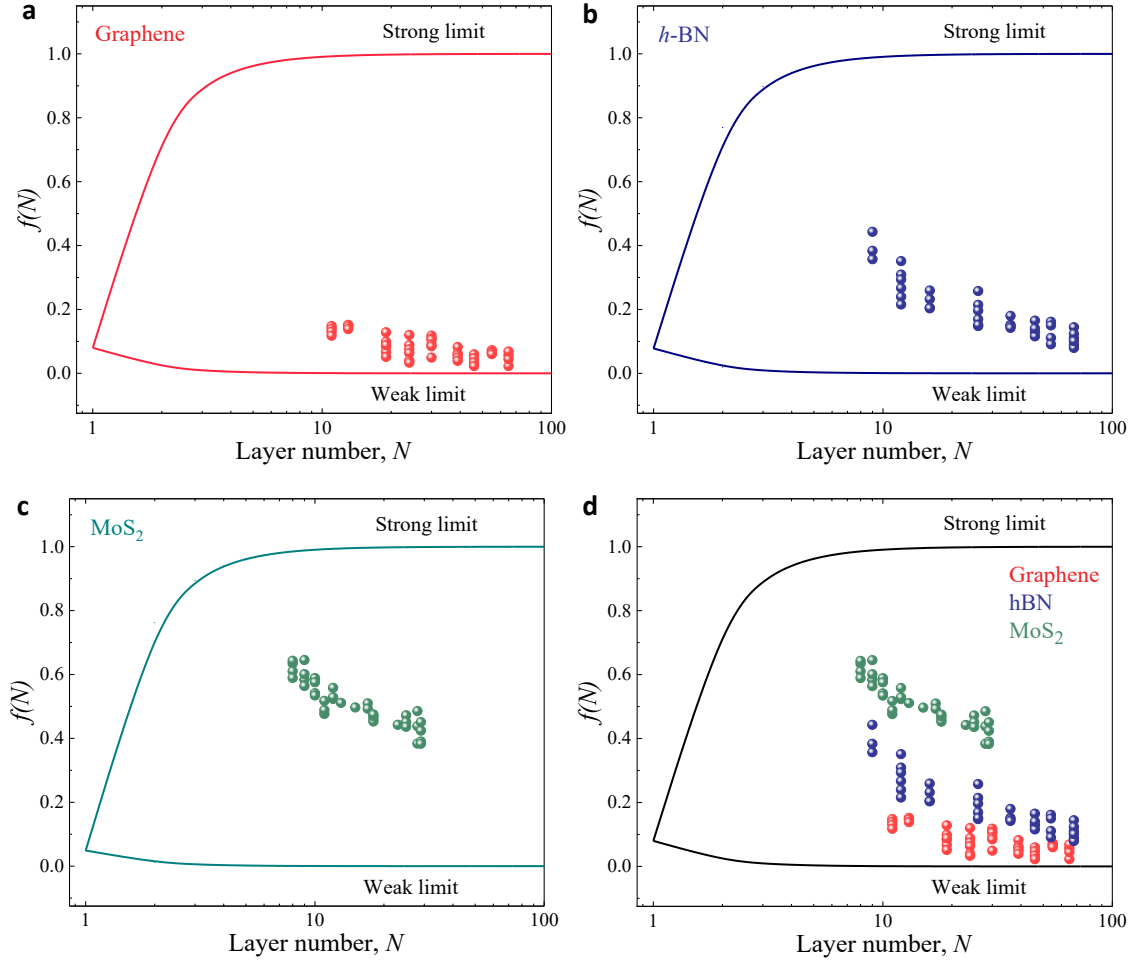


Figure 4.10: The layer-dependent function to measure the effect of interlayer coupling on the bending rigidity of multilayered graphene, hBN, and MoS₂. The black lines are theoretical predictions of the limiting cases for graphene. Our experimental results are denoted by colored markers, sitting between the two limits.

To account for such effects, we propose a modified formula for the effective bending rigidity of multilayer 2D materials as

$$B_{\text{eff}} = f(N) \cdot \frac{Et^3}{12(1-\nu^2)}, \quad (4.26)$$

where $f(N)$ is a function of the layer number. This function should depend on the strength of interlayer shear interactions, as a result of competition between the intralayer stretching/compressing and the interlayer shear/sliding.

4.5.1 Two theoretical limits

Theoretically, there are two limiting cases. The upper bound assumes perfectly bonding so that the interlayer slippage is prohibited while the lower bound corresponds to frictionless interlayer interactions or ultra-lubricated. In case that the perfect bonding between layers is assumed, the bending rigidity of multilayer 2D materials is (Gao and Huang, 2011)

$$B_{\text{eff}} = NB_1 + \frac{Et_1^3}{12(1-\nu^2)}(N^3 - N) \quad (4.27)$$

where B_1 is the bending rigidity of a monolayer, with values of 1.60 eV, 1.29 eV and 9.9 eV reported for graphene, hBN, and MoS₂, respectively (Kudin et al., 2001; Wei et al., 2013; Zhang et al., 2011; Zhao et al., 2015). Based on (4.27), we obtain

$$f(N) = \frac{12B_{\text{eff}}(1-\nu^2)}{Et_{\text{total}}^3} = 1 - \frac{1}{N^2} + \frac{12(1-\nu^2)B_1}{Et_1^3 N^2} \quad (4.28)$$

where $t_{\text{total}} = Nt_1$ and t_1 is the interlayer distance. Alternatively, for perfectly lubricated layers, the bending rigidity is simply

$$B_{\text{eff}} = NB_1, \quad (4.29)$$

and thus

$$f(N) = \frac{12(1-\nu^2)B_1}{Et_1^3 N^2} \quad (4.30)$$

The theoretical limits predicted by (4.28) and (4.30) are plotted as solid lines for graphene in Figure 10a, and for hBN in Figure 10b, and MoS₂ in Figure 10c, respectively.

4.5.2 Experimental results

In Figure 10d, we plot the two limits by solid lines using the parameters of graphene; the limits for hBN and MoS₂ are slightly different (Figure 10a-c). Experimentally, the function $f(N)$ can be determined based on (4.25):

$$f(N) = \frac{3(1-\nu^2)h^2}{16t^2} \left[\frac{pa^4}{Eth^3} - A(\nu) \right], \quad (4.31)$$

as shown in Figure 10d for multilayer graphene, hBN, and MoS₂. Evidently, the values of $f(N)$ for these multilayer 2D materials lie between the two theoretical limits. These results imply that both intralayer stretching/compressing and the interlayer shear/sliding happen when bending the multilayer 2D materials. Among the three 2D materials, the graphene multilayers have the lowest values of $f(N)$ and the MoS₂ multilayers have the highest value. Despite the highest in-plane elastic modulus of graphene, the bending rigidity of multilayer graphene is the lowest due to the interlayer slippage, close to the lower limit.

4.6 ERROR SOURCES

We conclude by discussing the possible errors in the measurement of bending rigidity of 2D material multilayers via the bulge test.

4.6.1 Edge slippage

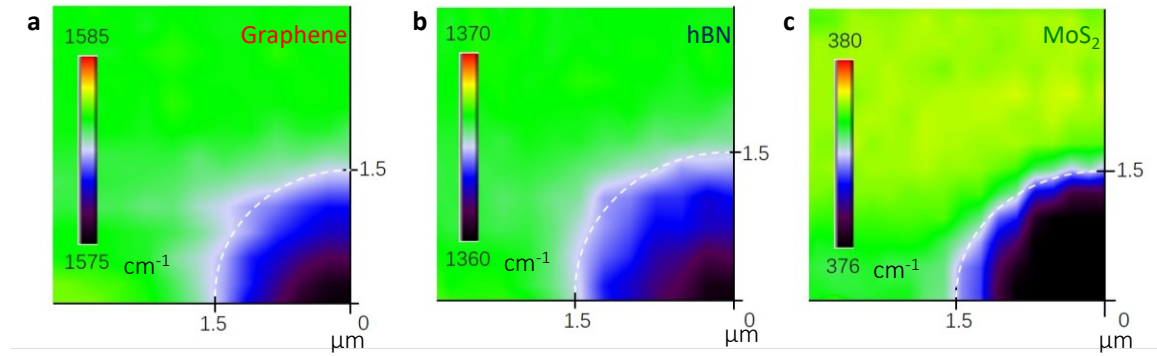


Figure 4.11: The Raman contour map of G (E_{2g}) peak positions for (a) graphene, (b) hBN, and (c) MoS₂ at $h = 33$ nm, 37 nm, 45 nm, respectively.

Recalling the sliding parameter defined in Chapters 2 and 3, the effect of edge slippage would be negligible when $\mathcal{S} = \left(\frac{h}{a}\right)^2 \frac{Et}{\tau a} \ll 1$ or $h \lesssim 100a$. This criterion can be satisfied in the bulge test attempting to characterize the bending effect since it is only robust when $h \sim t \ll a$. This is also evidenced by the uniform Raman contour of G peak position surrounding the 2D material bubble (Figure 4.11) – a significant G-peak gradient is expected in the supported region (outside the white dashed curves in Figure 4.11) when edge slippage occurs. However, such slippage may slightly soften the extracted Young's modulus, which is usually based on bubbles with relatively large center heights. Note that Raman spectra from every spot of the sample were recorded with a step size of 100 nm. All Raman characteristic bands were fitted with Lorentzian functions to obtain the peak positions. The laser intensity was kept below 0.5 mW to avoid local heating.

4.6.2 Pretension

We have neglected the pretension in these multilayer 2D materials. If considered, however, the pressure caused by pretension scales as $p \sim \frac{T_{pre}h}{a^2}$. Along with the line of non-dimensionlization in (4.25), we obtain $\frac{pa^4}{h^3t} \sim \frac{T_{pre}a^2}{t} \left(\frac{h}{t}\right)^{-2}$ that depends sensitively on the bubble radius. By contrast, in our experiments, the measured responses $\left(\frac{\Delta pa^4}{h^3t} \sim \frac{h}{t}\right)$ of our samples with different radii could almost collapse onto the radius-independent curve that is given by (4.25), as shown in Figure 4.12. We thus conclude that pretension effects in the bulge test of our relatively thick samples could be negligible.

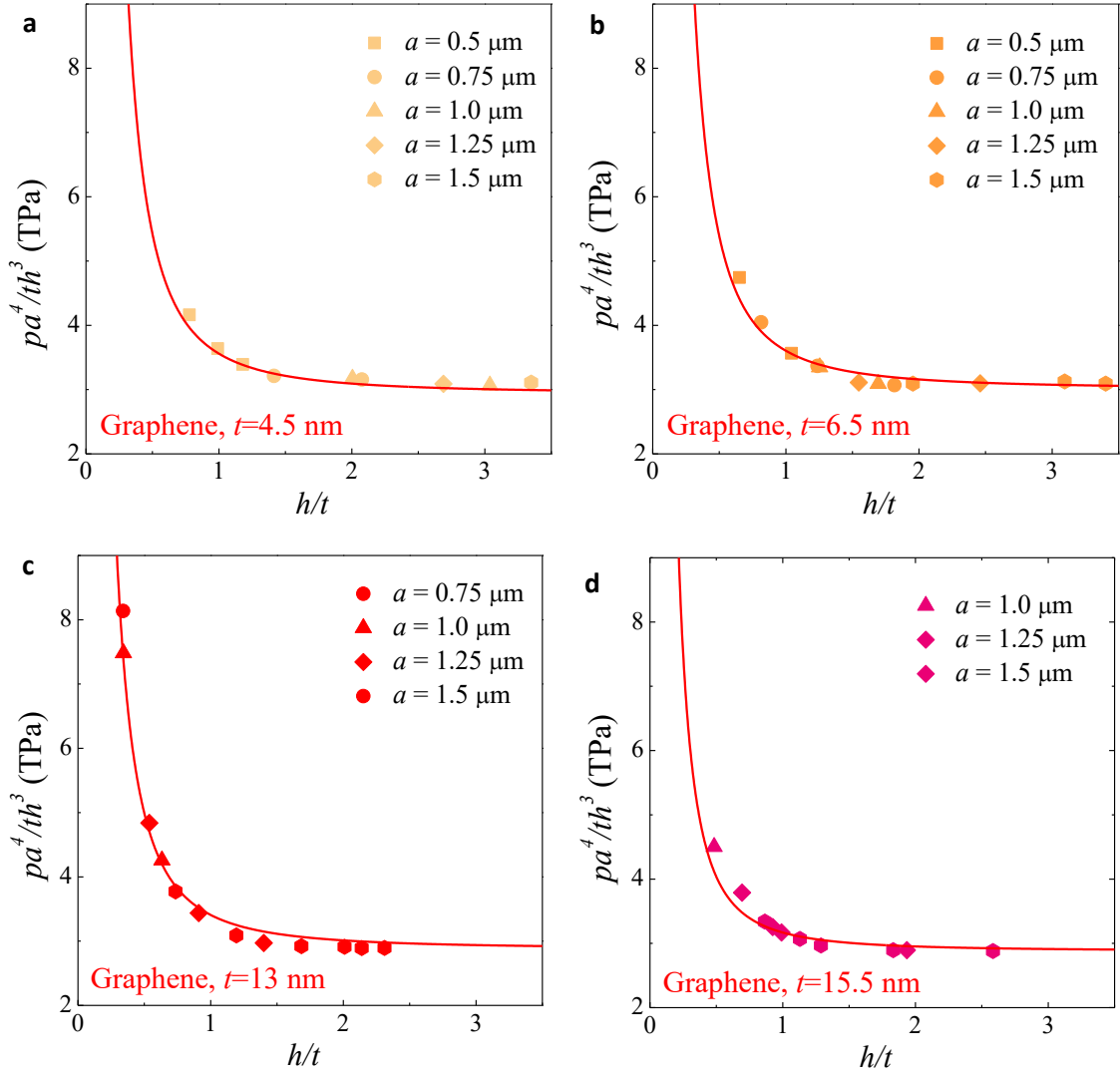


Figure 4.12: $\frac{pa^4}{h^3 t^3}$ as a function of $\frac{h}{t}$ for graphene with various thicknesses (a-d). Though these data were measured from bubbles with different radii, they can collapse to the radius-independent master curve predicted by (4.25).

4.6.3 “Sag” effect

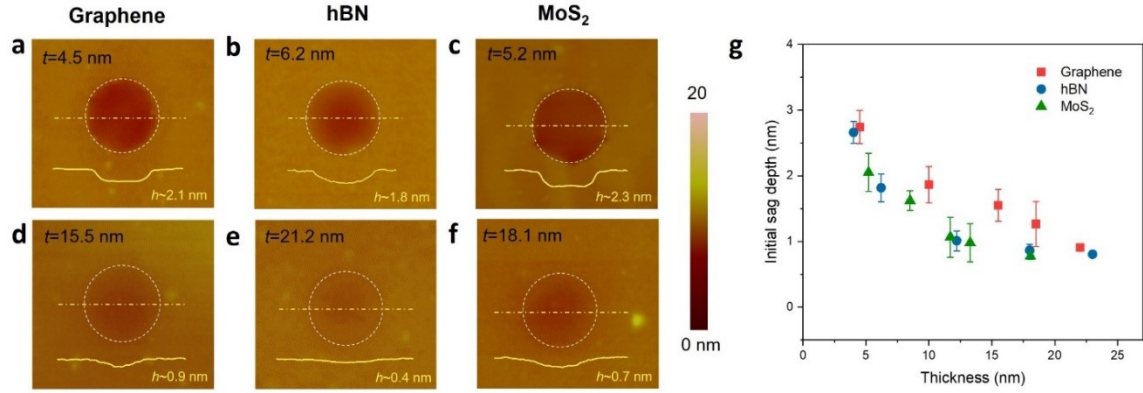


Figure 4.13: Initial surface morphology of three different 2D materials with (a-c) low and (d-f) high thickness. The white dashed circle indicates the perimeter of the hole with the diameter of 1 μm , and the height profiles of the suspended region along with the yellow dash-dotted lines are also shown in the insets. (g) Initial sag depth of three 2D materials at different thicknesses.

These multilayers typically deform downward slightly at the initial state, as shown in Figure 4.13 a-f and summarized in Figure 4.13g, which may induce experimental errors. The initial deformations were frequently observed in 2D material devices where the layer was covering a hole or a trench. They were believed to stem from the vdW interaction between the layer and the vertical sidewall of the hole/trench underneath, instead of residual strain or inelastic strain. In our experiments, it is found that the thicker samples show higher resistance to the vdW interaction and feature smaller initial deformations (solid markers in Figure 4.13g). Such interaction becomes trivial after bulging the layers upward because of the short-range nature of vdW forces (Wang et al., 2013b). In this context, the contribution of the sidewall attraction to the deformation of the layer could be reasonably neglected. For thinner samples ($t < 6$ nm), the measured heights are typically much higher than sag depths when $h/t > 1$. Our estimation of bending rigidity of these thin

samples is made by focusing on samples with h/t ranging from ~ 1 to ~ 1.5 such that the interaction between the sample and the sidewall should be negligible. Besides, their AFM morphologies match well with plate-like profiles, indicating that the bending rigidity dominates the deformation behavior and dramatically reduces the probability of tip interaction effects.

4.6.4 Summary

The error may also come from the AFM characterization systems intrinsically. However, the associated error analysis was challenging and was rarely discussed in the literature. The common way to derive an error bar for a measured quantity is to perform multiple measurements on the same set of samples and then apply the statistics. For example, the bending rigidity of the 21.64-nm-thick graphene was extracted based on measurements under six different deformation levels in our experiments. To answer the equation of what the typical error is for the measurement of bending rigidity and Young's modulus of multilayer 2D materials via the bulge test in this chapter, we make the following table based on our data in Figure 9.

graphene	t (nm)	1.44	4.14	6.24	9.64	12.64	15.14	18.64	21.64
	E (GPa)	979.1 ± 23.9	950.1 ± 21.7	937.8 ± 12.0	922.0 ± 8.4	932.2 ± 18.1	928.6 ± 8.2	929.1 ± 24.2	926.2*
	B ($\times 10^{-14}$ Nm)	0.0067 ± 0.0006	0.076 ± 0.007	0.26 ± 0.01	0.62 ± 0.18	1.50 ± 0.39	1.54 ± 0.49	2.21 ± 0.50	5.09 ± 0.51
hBN	t (nm)	3.65	5.25	8.35	11.85	15.05	17.65	22.65	
	E (GPa)	775.6 ± 10.1	775.0 ± 26.6	771.2 ± 12.8	775.3 ± 8.7	774.1 ± 7.7	766.4 ± 6.7	761.4 ± 8.8	
	B ($\times 10^{-14}$ Nm)	0.12 ± 0.02	0.23 ± 0.02	0.55 ± 0.20	2.13 ± 0.15	3.04 ± 0.49	5.01 ± 0.91	10.99 ± 1.99	
MoS ₂	t (nm)	5.62	6.92	8.22	9.52	11.42	14.92	17.78	21.02
	E (GPa)	322.8 ± 5.6	301.6 ± 4.9	301.9*	305.6 ± 3.3	320.4 ± 1.6	305.3 ± 12.5	293.9 ± 4.7	297.0 ± 6.1
	B ($\times 10^{-14}$ Nm)	0.27 ± 0.09	0.44 ± 0.12	0.87 ± 0.16	1.22 ± 0.18	1.87 ± 0.21	4.60 ± 0.09	7.67 ± 1.05	11.47 ± 1.04

Table 4.1: Summary of the thickness, Young's modulus, and bending rigidity for three 2D materials, including measurement errors. *Lack of error bar because only one measurement was achieved in this case.

4.7 CONCLUSIONS

In this chapter, combining theoretical and experimental approaches, we reported direct measurements of bending rigidity of multilayer graphene, molybdenum disulfide (MoS₂), and hexagonal boron nitride (hBN) based on pressurized bubbles. We show a transition from membrane to plate behaviors of the 2D multilayer by controlling the sample thickness and bubbling deflection and then extract both its bending rigidity and Young's modulus. We find good agreement between our measured Young's moduli with those reported in the literature: $E_{\text{graphene}} > E_{\text{hBN}} > E_{\text{MoS}_2}$. However, our bending rigidity results

seemingly break the classical plate theory down, showing a completely reversed trend: $B_{\text{MoS}_2} > B_{\text{hBN}} > B_{\text{graphene}}$ for multilayers with comparable thickness. We attribute the abnormal bending behavior of 2D multilayers to the atomic shear/friction between layers that is missing in classical plate prediction. Our findings provide the first fundamental insights into the bending of 2D material multilayers and may impact applications based on 2D materials and their homo/heterostructures that frequently exploit (or are extremely vulnerable to) out-of-plane deformations.

Chapter 5: Strain¹

In this chapter, we focus on the strain fields in nanoblisters, including bubbles and tents formed by 2D materials. Such configurations have been extensively exploited for strain engineering purposes as they can produce self-sustained, non-uniform in-plane strains through out-of-plane deformation. However, deterministic measures and control of strain fields in these systems are challenging because of the atomic thinness and unconventional interface behaviors of 2D materials. Here, we experimentally characterize a simple and unified power law for the profiles of a variety of nanobubbles and nanotents formed by 2D materials such as graphene and MoS₂ layers. Using membrane theory, we analytically unveil what sets the in-plane strains of these blisters regarding their shape and interface characteristics. Our analytical solutions are validated by Raman spectroscopy measured strain distributions in bulged graphene bubbles supported by strong and weak shear interfaces. We advocate that both the strain magnitudes and distributions can be tuned by the 2D material-substrate interface adhesion and friction properties.

¹A paper based on the work described in this Chapter has been published:
Z. Dai, Y. Hou, D. A. Sanchez, G. Wang, C. J. Brennan, Z. Zhang, L. Liu, N. Lu. *Interface-Governed Deformation of Nanobubbles and Nanotents Formed by Two-Dimensional Materials*. Physical Review Letters 2018, 121, 266101. (Z.D. contributed to conceptualization, design of the experiments, theoretical analysis, and writing of the first draft.)

5.1 INTRODUCTION

2D materials are atomically thin crystals with unique properties that lend well to next-generation ultrathin electronic and optoelectronic devices (Akinwande et al., 2014; Choi et al., 2017; Mas-Balleste et al., 2011; Novoselov et al., 2016). It has been well established that mechanical strain can strongly perturb the band structure of these materials, giving rise to the possibility of using mechanical deformation to tune their electronic and photonic performance dramatically (Branny et al., 2017; da Cunha Rodrigues et al., 2015; Li et al., 2015; Naumis et al., 2017; Yu et al., 2018). In fact, this principle, termed strain engineering, is now routinely used in manufacturing traditional semiconductor devices (Del Alamo, 2011). The strain engineering of 2D materials is particularly exciting because an individual atomic sheet is intrinsically capable of sustaining much larger mechanical strain compared to either their bulk counterparts or conventional electronic materials (Castellanos-Gomez et al., 2013; Dai et al., 2019a). Also, the atomic thickness of 2D materials allows them to be poked or pressurized from the third dimension (i.e. perpendicular to their plane of atoms) (Sanchez et al., 2018; Wang et al., 2017b; Wang et al., 2019b; Wang et al., 2017d). The resulting configurations, including nanoscale bubbles and tents, can be called by a unified name, 2D material BLISTERS. Recently, the considerable strain associated with these nanoblister have created opportunities for the study of new fundamental physics and applications such as enormous pseudo-magnetic fields, large-scale quantum emitters, and so on (Huang et al., 2018; Klimov et al., 2012; Levy et al., 2010; Los et al., 2016; Palacios-Berraquero et al., 2017; Settnes et al., 2016).

A major challenge in these systems is to find out or even control the strain in the blisters deterministically (Dai et al., 2019a). This challenge calls for a better understanding of how the blister geometry intertwines with mechanics in these atomic sheets. So far, experimental advances in the study of 2D material bubbles account for the scaling behavior

of the bubble shape (Ghorbanfekr-Kalashami et al., 2017; Khestanova et al., 2016; Sanchez et al., 2018; Zamborlini et al., 2015). However, it has been particularly challenging to perform analytical modeling that can straightforwardly relate the full-field strain distributions to the bubble and tent shape characteristics and allow accurate strain tuning through blister shape adjustments (Feng et al., 2012; Klimov et al., 2012; Levy et al., 2010). One difficulty comes from the intrinsically nonlinear coupling between in-plane strain and out-of-plane deformations predicted by the membrane theory (Mansfield, 2005). More fundamental concerns hinge upon the subtle nature of 2D material blister, where the material thickness approaches the atomic scale, and the surface is atomically smooth (Li et al., 2017b). These features challenge the applicability of continuum theories from a perspective of deformation physics (López-Polín et al., 2015; Los et al., 2016; Nicholl et al., 2017; Tapasztó et al., 2012). Consequently, existing analysis on the strain distribution and strain-coupled physics and chemistry in 2D material blisters relies heavily on numerical techniques, such as case-by-case molecular dynamics (MD) simulations (Feng et al., 2012; Klimov et al., 2012; Meng et al., 2017; Qi et al., 2014; Zhu et al., 2014). To deal with these concerns, a combination of continuum theories with microscale experiments is highly needed and yet to emerge so far.

Herein, we experimentally explore the strain field in nanoblister formed by 2D materials accounting for different natures of 2D materials interfaces. Using tapping mode atomic force microscopy (AFM), we experimentally characterized a variety of bubbles and tents formed by graphene and MoS₂ layers. Their shapes were empirically found to follow a simple power law, leading to closed-form analytical solutions to the Föppl–von Kármán equations at the membrane limit. Our results show that the strain distribution in the 2D material can be estimated by simply measuring the height and radius of the bubbles and tents and that the strain highly depends on the interfacial interaction between the 2D

material and the underlying substrate. To validate our analytical solutions, we experimentally carried out Raman mapping on pressurized graphene nanobubbles with strong (graphene-SiO₂) and weak (graphene-graphene) shear interfaces. The measured and analytically predicted Raman shifts had found good matches for both types of interfaces.

5.2 SHAPE OF BUBBLES AND TENTS

We first investigated the shape characteristics of both nanobubbles and nanotents of 2D materials, which can form spontaneously or be created in a controllable manner. For the spontaneous case, nanometer-scale bubbles and tents form when monolayer or few-layer 2D materials are exfoliated or transferred on a target substrate. The formation mechanism is typically attributed to the inevitably trapped water, hydrocarbon, and/or nanoparticles at the 2D material-substrate interface during sample preparation (Khestanova et al., 2016; Sanchez et al., 2018). The spontaneously formed nanobubbles and nanotents analyzed in this study were made by mechanically exfoliating few- and monolayer graphene and MoS₂ from their bulk crystals on a silicon substrate or transferring CVD-grown MoS₂ on gold or Al₂O₃ substrate (Huang et al., 2015). Details on the transfer process for different types of samples are provided in the Appendix in section 5.8. Figure 5.1a displays typical examples of nanobubbles formed by monolayer graphene on SiO₂. When nanoparticles were trapped, 2D materials can drape around the nanoparticle, forming micro- or nano-tents, as shown in Figures 5.1b and 5.1c. To form controllable bubbles, we transferred monolayer graphene and a 4-layer MoS₂ to cover pre-patterned micro-cavities in SiO₂ to form suspended drumheads and then followed a well-established gas diffusion procedure to bulge the drumheads (Koenig et al., 2011). In this case, the bubbles can be pressurized in a controllable manner (Figure 4.1d).

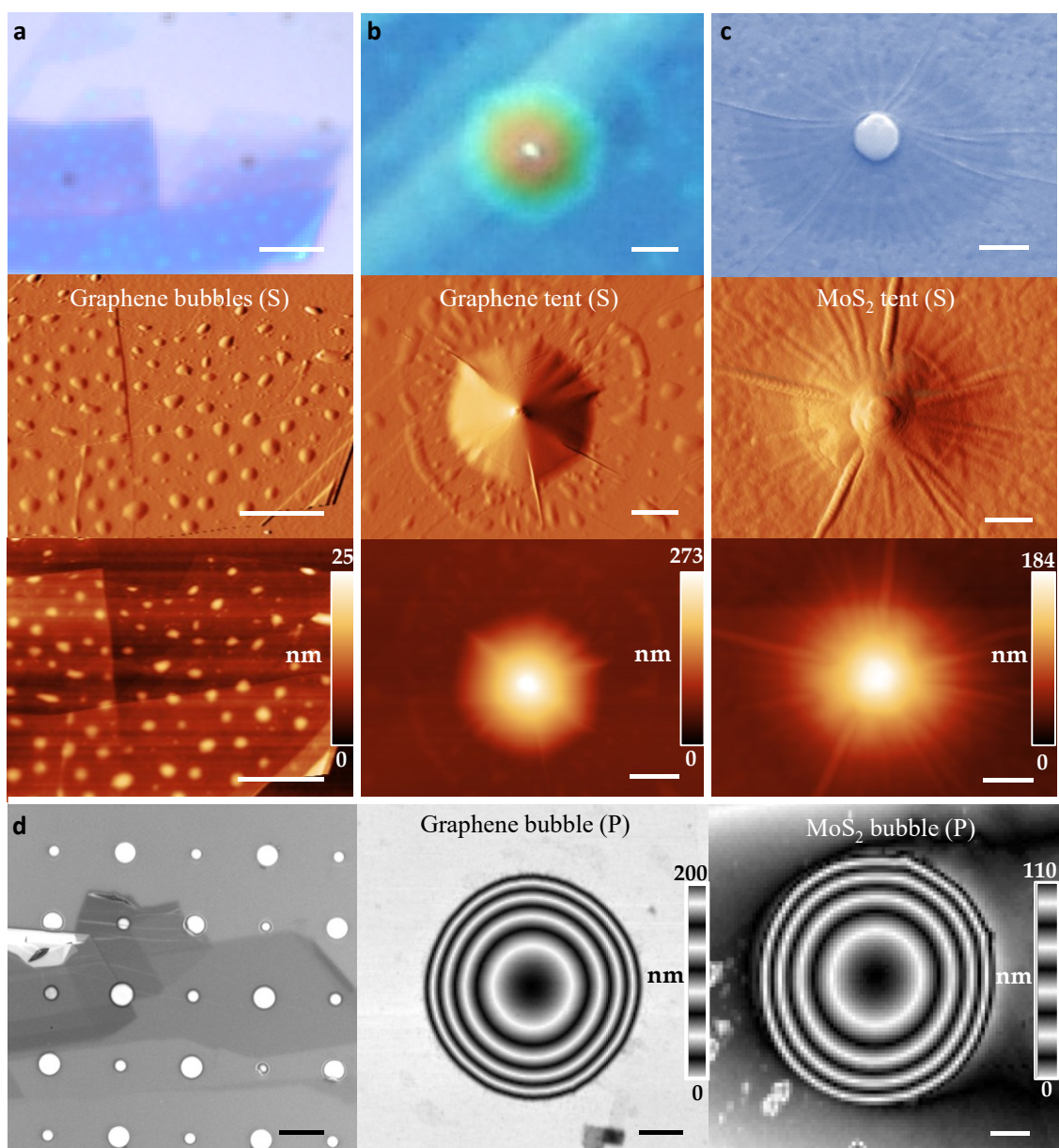


Figure 5.1: From top to bottom: Optical/SEM images, AFM amplitude and height images of spontaneously formed graphene bubbles on SiO₂ (a), a multilayer graphene tent on SiO₂ (b), and a CVD-MoS₂ tent on gold film (c). (d) From left to right: optical image of graphene flakes exfoliated on pre-patterned SiO₂ with micro-cavities, AFM height images of a monolayer graphene bubble, and a 4-layer MoS₂ bubble. Note that (S) represents bubbles or tents formed spontaneously while (P) represents those formed by controllable air pressurization. The scale bars represent 4 μm in (a), 2 μm in (b), 200 nm in (c), and 10 μm , 1 μm and 500 nm in (d) left, middle and right panels, respectively.

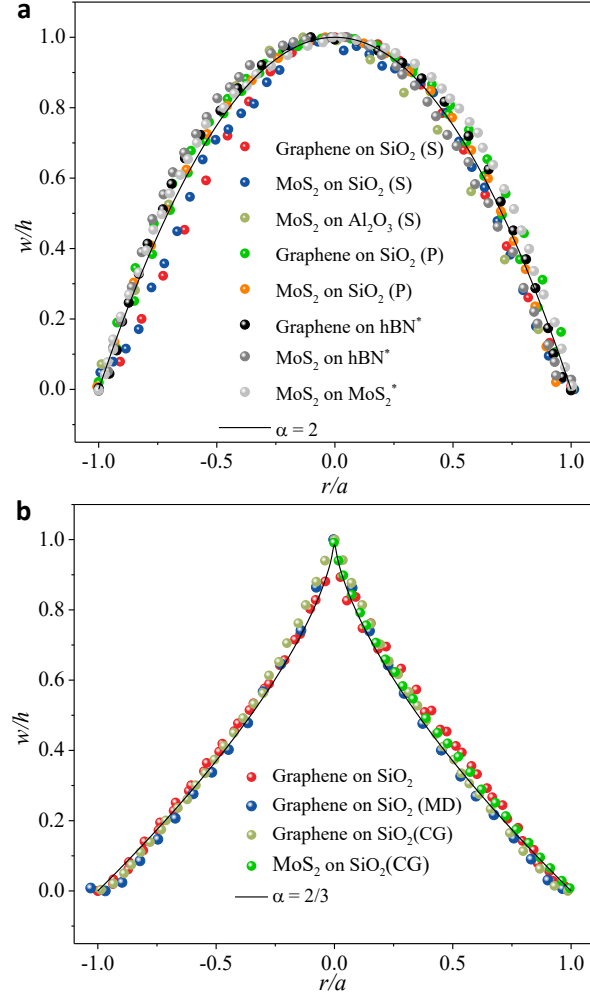


Figure 5.2: Universal shape characteristics of 2D material bubbles and tents. (a) Normalized bubble profiles measured by our experiments and collected from the literature. Note that samples from (Khestanova et al., 2016) feature atomically smooth interfaces, are labeled by *. (b) Normalized tent profiles measured by our experiments and simulation results in the literature. The simulation data about graphene and MoS_2 is from (Feng et al., 2012; Zhu et al., 2014).

The out-of-plane profiles of all the different types of bubbles and tents we prepared by ourselves or collected from literature are summarized in Figure 5.2. Although the radii of the 2D material blisters range from tens to thousands of nanometers, we realized that the height profiles of bubbles and tents collapse onto two master curves if we normalize the

out-of-plane deflection (w) of each blister by its central height (h), and the radial positions (r) by its radius (a). We discovered that the collapsed height profiles can be described by a unified power form,

$$\frac{w}{h} = 1 - \left(\frac{r}{a}\right)^\alpha, \quad (5.1),$$

where α is 2 for bubbles or 2/3 for tents. Note that Figure 5.2 summarizes graphene and MoS₂ bubbles and tents with aspect ratios ranging from 0.05 to 0.20. Remarkably, regardless of the aspect ratios, the types of 2D material, the supporting substrates (silicon, alumina, or atomically flat 2D material flakes), the content in the bubble (liquid or gas), or the fabrication methods, all bubble profiles can collapse to (5.1) with $\alpha = 2$ (Figure 5.2a).

We also found that for profiles of graphene and MoS₂ tents, data obtained from MD simulations and coarse-grained (CG) modeling [18,20,29] can also collapse to (5.1) with $\alpha = 2/3$ (Figure 5.2b). Note that for the tents obtained experimentally, (5.1) was used as a fitting function because of the finite pillar/particle size (simulation data could be thought as a point force). In fact, the empirical conclusion of $\alpha = 2$ is a widely adopted simple membrane solution for blisters (Freund and Suresh, 2004; Wang et al., 2013b) and $\alpha = 2/3$ is well-matched with the analytical solution to an indented blister in the literature (Chopin et al., 2008; Mansfield, 2005). We thus conclude that this simple power form can be a good approximation for describing the profiles of 2D material bubbles and tents.

5.3 THEORETICAL SETTING

Now that the out-of-plane displacement of 2D material blisters is readily available as given in (5.1), we can try to solve the in-plane displacement and then calculate strains out of displacements.

5.3.1 Analytical solutions

Attributing to the atomic thinness of 2D materials, it is sufficient to simply use the membrane limit of the Föppl–von Kármán equations (Freund and Suresh, 2004; Mansfield, 2005). The in-plane equilibrium equation in terms of displacements is, therefore (see details in Chapter 2.2):

$$\frac{d^2u}{dr^2} + \frac{1}{r} \frac{du}{dr} - \frac{u}{r^2} = -\frac{1-\nu}{2r} \left(\frac{dw}{dr} \right)^2 - \frac{dw}{dr} \frac{d^2w}{dr^2}, \quad (5.2),$$

where u is the in-plane displacement of the 2D material, and ν is the Poisson's ratio. Plugging (5.1) into this equation and solving the 2nd order ODE using the finite condition when $r \rightarrow 0$ can yield an analytical solution to the in-plane displacement:

$$u = \zeta(\nu) \frac{h^2}{a} \left(\frac{r}{a} - \left(\frac{r}{a} \right)^{2\alpha-1} \right) + u_s \frac{r}{a}, \quad (5.3),$$

where $\zeta(\nu) = \frac{\alpha(2\alpha-1-\nu)}{8(\alpha-1)}$ and u_s is a constant related to the slippage at the edge of the blister ($r = a$). This explicit displacement field allows for the direct solutions for both the radial and circumferential strain fields:

$$\varepsilon_r = \begin{cases} \zeta(\nu) \frac{h^2}{a^2} \left(1 - \frac{1+\nu-2\alpha\nu}{2\alpha-1-\nu} \left(\frac{r}{a} \right)^{2\alpha-2} \right) + \frac{u_s}{a}, & r \leq a \\ -\frac{au_s}{r^2}, & r > a \end{cases}, \quad (5.4a),$$

$$\varepsilon_\theta = \begin{cases} \zeta(\nu) \frac{h^2}{a^2} \left(1 - \left(\frac{r}{a} \right)^{2\alpha-2} \right) + \frac{u_s}{a}, & r \leq a \\ \frac{au_s}{r^2}, & r > a \end{cases}. \quad (5.4b).$$

Clearly, the sliding of the 2D material-substrate interface ($u_s \neq 0$) can induce non-zero strain in the supported zone ($r > a$), which is important for strain engineering applications of 2D materials (Qi et al., 2014). Typically, the edge of the 2D material blister is assumed to be fully clamped due to adhesion and strong shear interactions with the supporting substrate outside of the boundary. However, the atomically smooth surfaces of 2D materials make interfacial sliding particularly easy. Recent experiments on gas-pressurized graphene bubbles revealed that the shear interactions between graphene and its substrate could be fairly weak, leading to nonlinear, deflection-dependent interface sliding

displacements (Kitt et al., 2013; Wang et al., 2017b). It has also been discovered that well-established theories assuming clamped conditions offer good approximations only when the deflection is small ($h/a < 0.1$), while experimental measurements deviated from theories with clamped boundaries in samples with large deflection (Wang et al., 2017b). Recent advances about 2D material interface further highlighted the so-called superlubrication (near-zero friction) when a 2D material sits on atomically smooth substrates, including itself, which is very common in 2D materials devices (Hod et al., 2018b).

Our prime interest in this study is in two limits: strong-shear limit (clamped, fully bonded interface) and weak-shear limit (sliding, frictionless interface). For the former, we can apply the clamped boundary at the edge of the blister. For the latter, the stress and displacement in the outer supported region can be obtained as the classical Lamé problem in linear elasticity (Sadd, 2009). With zero shear stress at the frictionless interface between the membrane and the substrate, the stress and displacement in the annular region can be obtained as the classical Lamé problem in linear elasticity (Sadd, 2009). The radial and circumferential components of the membrane stress are:

$$N_r = \frac{C_1}{r^2} + C_2, \quad (5.5a),$$

$$N_\theta = -\frac{C_1}{r^2} + C_2, \quad (5.5b),$$

where $N_r = \sigma_r t$ and $N_\theta = \sigma_\theta t$; σ_r and σ_θ are, respectively, the radial and circumferential stresses, and t is the membrane thickness. Correspondingly, the radial displacement is

$$u = \frac{1}{E_{2D}} \left[-\frac{(1+\nu)C_1}{r} + C_2(1-\nu)r \right] \quad (5.6).$$

For an infinitely large membrane without pretension, both the stress and the displacement approach zero as $r \rightarrow \infty$, which requires $C_2 = 0$. At the edge of the blister ($r = a$), the radial stress and displacement are continuous. By letting (5.6) be u_s at $r = a$, we obtain $C_1 = -\frac{E_{2D}au_s}{1+\nu}$. For the radial stress, we have by Hooke's law

$$N_r = \frac{E_{2D}}{1-\nu^2} (\varepsilon_r + \nu \varepsilon_\theta), \quad (5.7),$$

where the strain components on the right-hand side are given by (5.4) at $r = a$, and the radial stress on the left-hand side is given by (5.5) at $r = a$. The stress continuity then leads to

$$u_s = \begin{cases} 0, & \text{strong - shear limit} \\ -\frac{\alpha(1+\nu)}{8} \frac{h^2}{a}, & \text{weak - shear limit} \end{cases} \quad (5.8).$$

Now combining (5.4) and (5.8) offers the complete analytical solutions to the strain field in 2D materials forming blisters, with either strong or weak interaction with their substrates. After appropriately choosing the α and u_s according to the specific blister shape and 2D material-substrate interface, one can easily compute the strain distribution inside and outside of a 2D blister by simply measuring its height and radius. We note that a generalized analysis may be performed by accounting for the detailed frictional resistance (e.g., the stick-slip) at the 2D material-substrate interface (Li et al., 2010).

5.3.2 Numerical verification

In Figure 5.3, we plot the strain distributions of the 2D material blister as solid curves using our equations. The strain is normalized by h^2/a^2 such that the distribution will only depend on the interface conditions and material properties, i.e., the Poisson's ratio. Comparing Figure 3a for bubbles and Figure 3b for tents, it is clear that the strain gradients are much larger in tents, with strain divergence towards the center of the tents due to the assumed point load. Note that under the same aspect ratio, interface sliding can considerably reduce the strain level in 2D material blisters in comparison with blisters with strong-shear interfaces. This highlights the importance of accounting for the ultra-lubricated interface in the case that the 2D material is supported by an atomically smooth substrate.

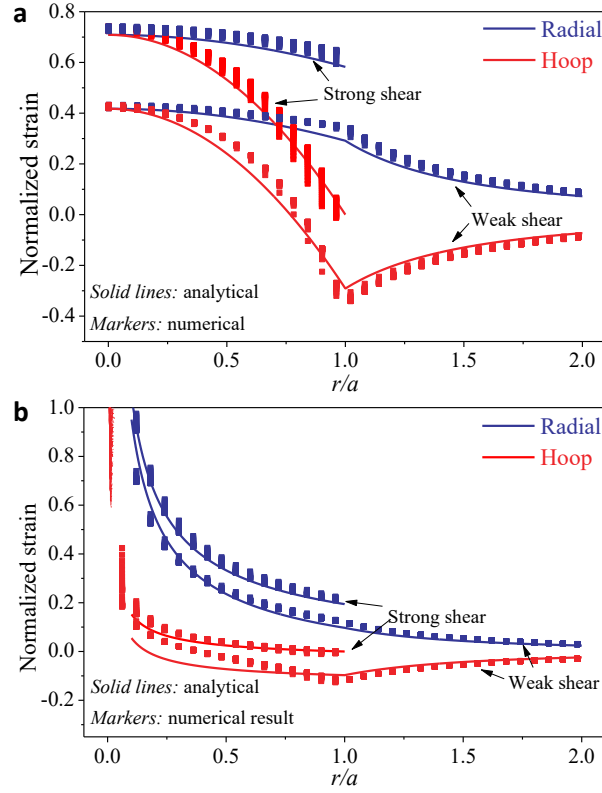


Figure 5.3: Normalized strain distribution curves predicted by our analytical solution (solid lines) and solved by numerical analysis (markers) in bubbles (a) and tents (b), subjected to both clamped (strong interface) and frictionless (sliding interfaces) boundary conditions. The strain is normalized by h^2/a^2 , giving rise to deflection-independent curves. The numerical results are solved for a monolayer graphene with aspect ratios ranging from $0.02 < h/a < 0.2$.

Next, we try to verify our analytical solutions numerically. We solved the nonlinear Föppl–von Kármán equations with clamped and slipping boundaries, where the bending behavior is also considered for generality (see Appendix in section 5.8 for details). The numerical solutions are plotted as markers in Figure 5.3 for monolayer graphene with aspect ratios ranging from 0.05 to 0.20, to compare with the analytical solutions (solid curves) directly. Since analytically solved strains are strictly proportional to h^2/a^2 , after

normalization, the solid curves are no longer dependent on the aspect ratio. However, the numerically solved strains show more complicated dependence on the aspect ratio, because the markers for different aspect ratios do not entirely collapse. Despite this small discrepancy, the overall good agreement between the two solutions indicates that for our experimentally observed blisters with aspect ratios ranging from 0.05 to 0.20, bending effects are negligible. Thus, the numerical results have verified that our analytical solution given by (5.4) is a reasonable estimation for strains in both bubbles and tents under both clamped and slipping boundary conditions.

5.4 EXPERIMENTAL VALIDATION¹

Our analytical solution, though verified numerically, is still challenged by a widespread concern on the breakdown of classical membrane theories at the atomic limit (López-Polín et al., 2015; Los et al., 2016; Nicholl et al., 2017; Tapasztó et al., 2012; Zhang et al., 2011). To examine the applicability of our analytical solutions, we performed graphene bulging experiments with intentionally designed strong- and weak-shear interfaces.

5.4.1 Pressurized bubbles

Monolayer graphene sealed micro-cavities were fabricated by micromechanical cleavage of graphene over SiO₂ substrate with pre-patterned 2.5-micron-radius holes, as illustrated in Figure 5.4a. Following a well-developed gas diffusion method (Koenig et al., 2011), we can create a pressure difference across the monolayer and bulge it in a controlled manner. The strong-shear-interface graphene bubble was generated by pressurizing a graphene monolayer on SiO₂ with the maximum deflection of less than 150 nm. Under this

¹ We acknowledge that the experiments in this section are supported by Y. Hou, G. Wang, and L. Liu.

condition, the interface sliding was found to be minimal ($\mathcal{S} \sim 0.1 \ll 1$), thus is compatible with the clamped interface assumption (Wang et al., 2017b).

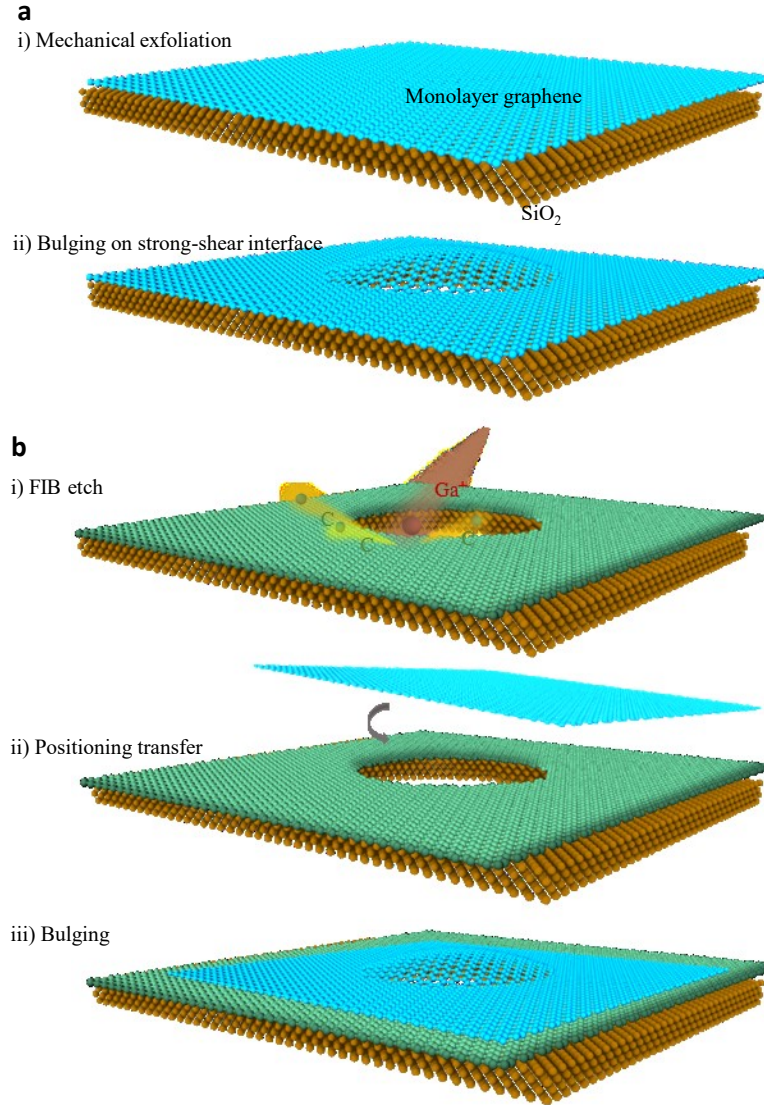


Figure 5.4: Schematics of the graphene drumheads formed on a SiO₂ substrate (a) and on a graphene-covered SiO₂ substrate (b).

To experimentally study the weak-shear case, we assembled a graphene-SiO₂ supporting substrate for the graphene bubble (Figure 5.4b). First, a few-layer graphene was

transferred over a SiO₂ micro-hole. The suspended portion of the multilayer graphene was then etched to open up the micro-hole. After creating an atomically flat region around the micro-hole, a monolayer graphene was precisely transferred to cover this micro-hole, resulting in a graphene drumhead supported by few-layer graphene. Applying a differential pressure across the suspended graphene membrane, this graphene bubble was expected to bulge under weak-shear interface as the graphene-graphene interface can be considered as ultra-lubricated ($\mathcal{S} \sim 10^3 \gg 1$).

We perform multiple AFM and Raman characterizations on the graphene bubbles with well-controlled interfaces. For an axisymmetric graphene bubble, the G band shifts in the Raman spectrum are related to the strain components through the following equation (Huang et al., 2009):

$$\frac{\Delta\omega_G}{\omega_0} = -\gamma(\varepsilon_r + \varepsilon_\theta) \pm \frac{\beta}{2}(\varepsilon_r - \varepsilon_\theta), \quad (5.9),$$

where ε_r and ε_θ are analytically expressed in (5.4), γ is the Grüneisen parameter, and β is the shear deformation potential that details the amount of splitting in the G bands, which were experimentally calibrated for monolayer graphene ($\gamma = 1.99$ and $\beta = 0.99$) (Mohiuddin et al., 2009). Therefore, analytical prediction for strain fields can be readily converted to an analytical prediction for the G band shifts using (5.9). Particularly, at the center of the bubble where $\varepsilon_r = \varepsilon_\theta$, the G band shifts are predicted by (5.4) and (5.9) to take a very simple form:

$$\Delta\omega_G = -c_\omega \gamma \omega_0 \frac{h^2}{a^2}, \quad (5.10)$$

where the constant c_ω is $\frac{3-\nu}{2}$ for bubbles supported by strong shear interfaces and is $(1 - \nu)$ by weak shear interfaces.

5.4.2 Strain at the bubble center

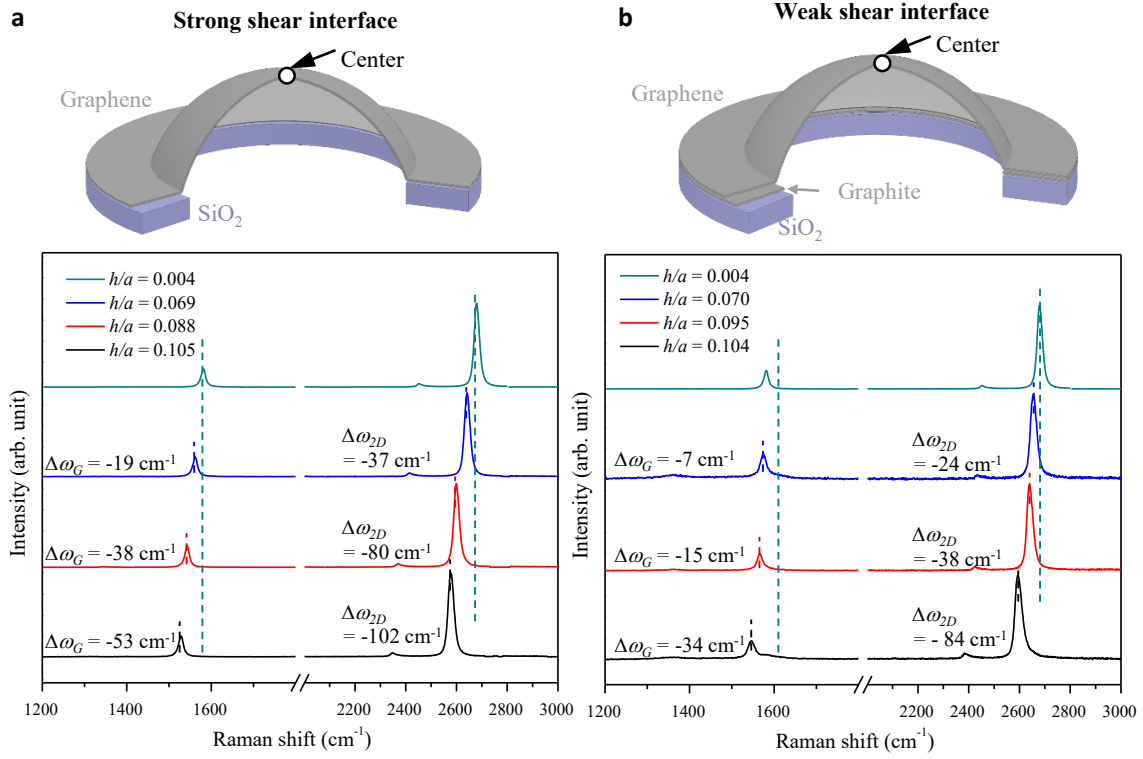


Figure 5.5: Representative Raman spectra measured at the center of the graphene bubble under different levels of deformation (h/a). (a) SiO₂-supported graphene bubbles. (b) Graphene-supported graphene bubbles. We note that when subjected to equal deformation level, SiO₂-supported graphene bubbles exhibit much more significant G and 2D band shifts than graphene-supported graphene bubbles. Specifically, when the $h/a \cong 0.1$, the G band downshifted by 53 and 34 cm⁻¹ for the SiO₂-supported and the graphene-supported graphene bubble, respectively. And the 2D band downshifted by 102 and 84 cm⁻¹ for the SiO₂-supported and the graphene-supported graphene bubble, respectively. This fact implies that the sliding behavior of the graphene-graphene interface at the edge can considerably reduce the strain magnitude in the bubble.

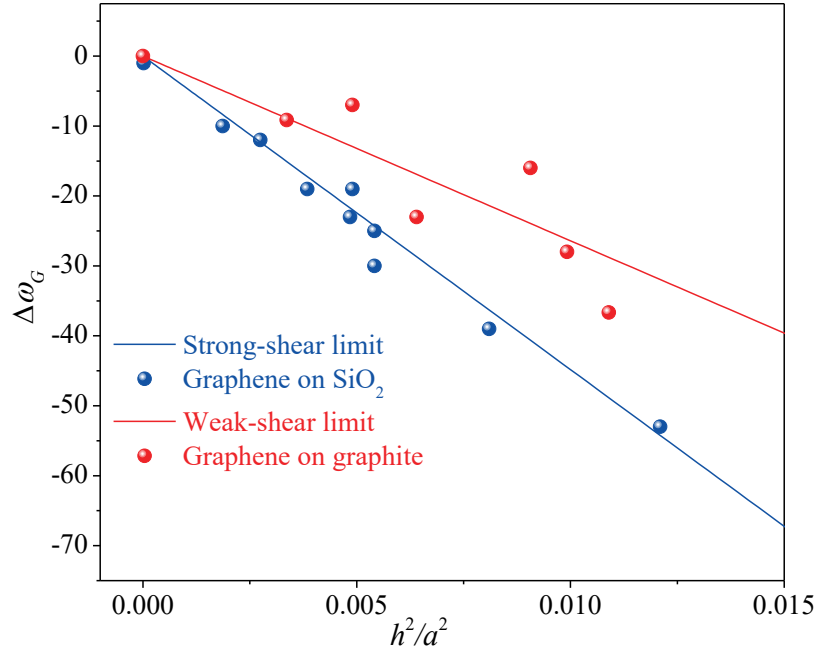


Figure 5.6: Raman shifts of the G band predicted by our analytical solution (solid curves) and measured by our experiments (markers) at the center of graphene bubbles.

Here, we first show the Raman G band shifts at the center of graphene bubbles as a function of h^2/a^2 in Figures 5.5 and 5.6, which are predicted to be linear by our analytical solution in (5.10). The markers represent experimental data for both SiO_2 - (brown) and graphene-supported (green) graphene bubbles, and the solid curves correspond to predicted G band shifts for strong- (green) and weak-shear-interfaced (brown) 2D material bubbles. By letting the Poisson's ratio of graphene be 0.165 in (5.10), we find good agreement between our theoretical predictions and experimental results. This may confirm the applicability of our simplified membrane theory in relating the out-of-plane deformations to in-plane strains for 2D material blisters.

5.4.3 Strain distributions

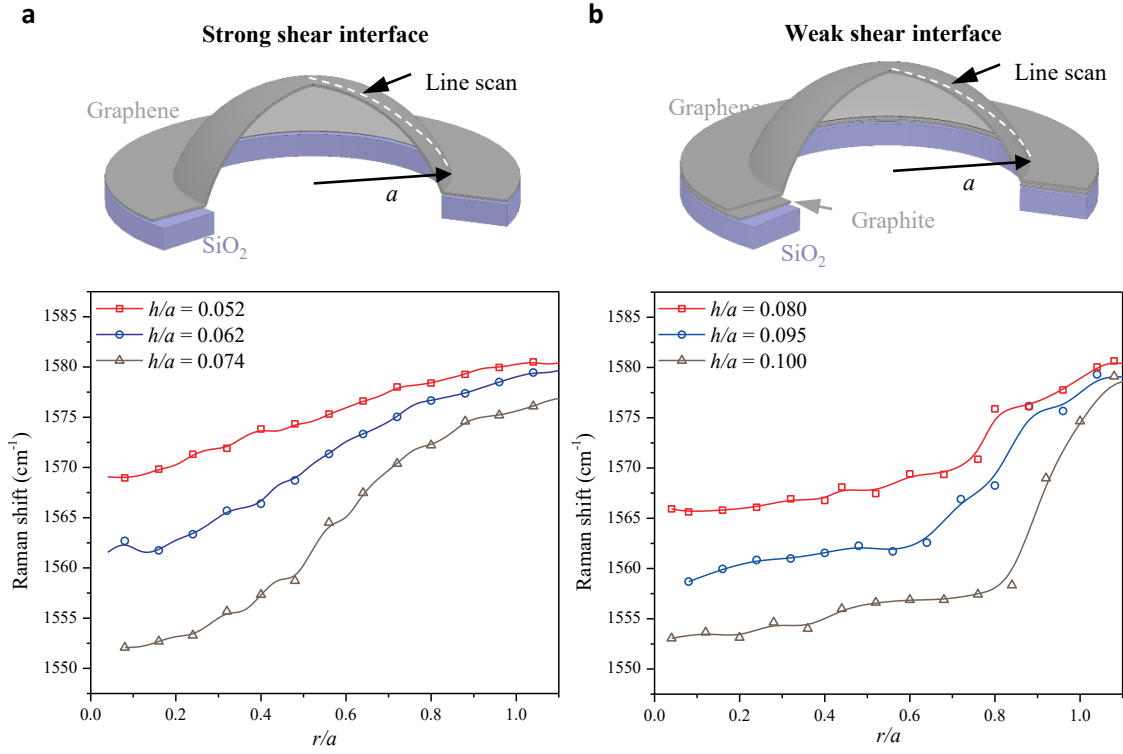


Figure 5.7: Line mapping of Raman G band frequency. (a) SiO_2 -supported graphene bubbles. (b) Graphene-supported graphene bubbles. Unsurprisingly, the Raman G band shifts increase with the applied out-of-plane deformation. Also, the shifts decrease from the center ($r/a = 0$) to the edge ($r/a = 1$) of the bubble, implying that the “strain” increases from the edge to the center. When approaching the edge, the curves of Raman G band shift (as functions of the radial position) behave differently between SiO_2 -supported and graphene-supported graphene bubbles. One possible reason likely comes from the different doping levels by the substrate, which is SiO_2 for (a) and few-layer graphene for (b). For instance, we found the upshifting of G band with 2-4 cm^{-1} by the SiO_2 doping while the downshifting of G band with 0-2 cm^{-1} by the hybrid substrate doping (few-layer graphene on SiO_2).

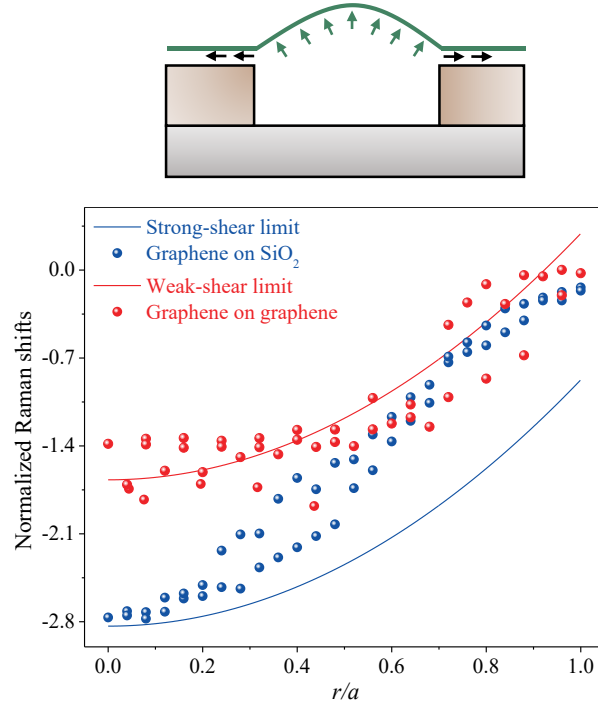


Figure 5.8: Normalized Raman shifts of the G band ($\Delta\omega_G a^2 / \omega_0 h^2$) as functions of the normalized radial position (r/a) for monolayer graphene bubbles.

In Figures 5.7 and 5.8, we turn our focus to the strain/Raman shift distribution in these bubbles. Particularly, we normalize both the measured and predicted G band shifts by h^2/a^2 and plot them as functions of the normalized radial position r/a in Figure 5.8. Our weak-shear and strong-shear model can partially capture the full-field strain distribution in graphene-on-graphene and graphene-on-SiO₂ bubbles, respectively. However, the deviation between predicted and measured G band shifts occurs and enlarges as it goes towards the edge of the bubble. We attribute such edge deviation in Figure 5.8 to the limited spatial resolution of Raman spectroscopy ($\sim 1 \mu\text{m}$) and the doping effect by the substrate. Either one may induce influenced Raman signals by the substrate or the substrate-supported graphene (see discussion in section 5.5) when the laser spot is focused within the 2.5-micron-radius graphene bubble but close to the edge (Das et al., 2008; Lee

et al., 2012). Besides, the strain fields would be altered by wrinkling instabilities at the bubble edge when the center deflection is sufficiently large ($\mathcal{S} \gtrsim 0.76$, according to Chapter 3.6).

5.5 DISCUSSION

In this section, we discuss the possible errors in experimental measurements presented in this Chapter and the defects/limits of our over-simplified analytical theory.

5.5.1 Strain distributions near the edge

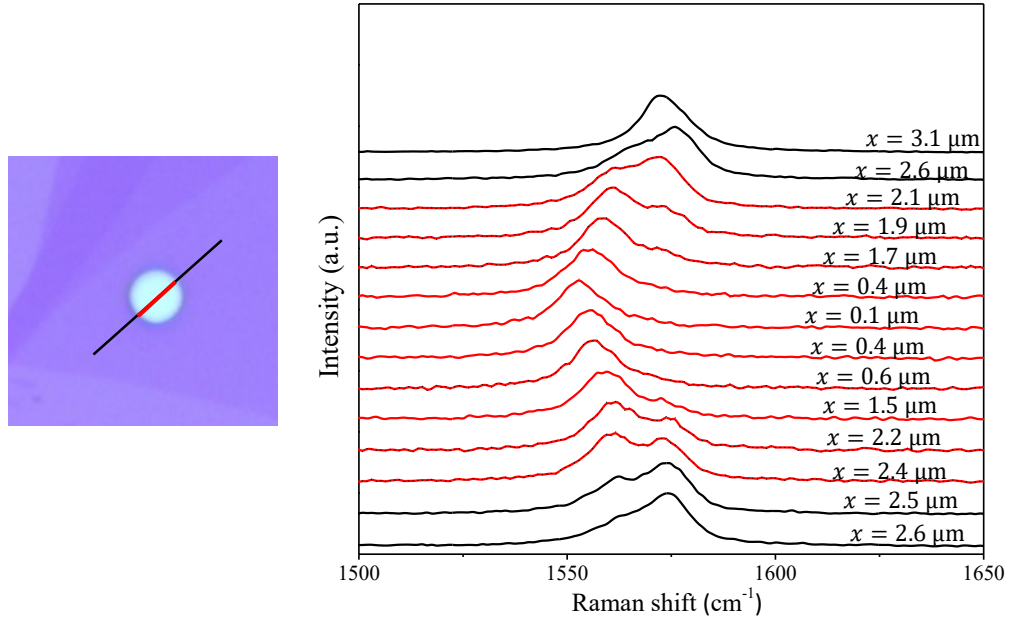


Figure 5.9: Line mapping of the width of Raman G band. For a SiO_2 -supported graphene bubble at $h/a = 0.074$, a series of Raman spectra (G band) are stacked vertically in the direction of the line scan. The x is defined by the distance to the center of the hole (the bubble). Substantial variations in both the frequency and the full width at half-maximum (FWHM) can be detected. The apparent downshift of Raman G band has been shown in Figure 5.7. The peak broadening at the edge ($x \rightarrow 2.5 \mu\text{m}$) and the sharpening at the center ($x \rightarrow 0 \mu\text{m}$) of the hole are highlighted.

Our theory cannot capture the subtle instabilities that are likely to occur due to the edge slippage of the graphene sheets. This would be one of the reasons for the deviation around the bubble edge in Figure 5.8. Besides, the inhomogeneity would cause experimental errors in Raman-based measurements that constitute an additional reason.

Raman peak width mainly relies on the lattice deformations and is regarded as a measure of strain distribution in graphene. Typically, the full width at half-maximum (FWHM) of graphene on a substrate is ranging from 11.5-14 cm^{-1} (Cançado et al., 2011; Ferrari, 2007). In Figure 5.9, we find that the formation of the suspended graphene bubble obviously enhances the FWHM of the G band, especially near the edge of the hole (up to 20 cm^{-1}). The broadening behavior of the G band FWHM is a result of so-called convoluting shifted peaks from the almost unstrained region (substrate-supported graphene) and highly strained region (suspended graphene) (Metzger et al., 2009). The FWHM starts broadening inside the hole because of the $\sim 1 \mu\text{m}$ size of the laser spot. In other words, when the laser is focused on the suspended graphene that is close to the edge, signals from both suspended graphene and supported graphene may be detected. These two signal components add up, yielding a non-Lorentzian shape with a relatively large width. Such fact may also contribute to the deviation between predicted Raman shifts by our theory and measured by experiments, especially near the edge of graphene bubbles.

5.5.2 Strain distributions at the center

Another concern comes from the case of weak shear limit, in which elastic instabilities would occur readily in the suspended region – a process that would release the compressive hoop strain (see our discussion in Chapters 2 and 3). The over-simplified analytical solutions in (5.4) are not able to capture such subtleties around the tent or bubble edge. The region where the solutions lose the accuracy is around $[0.5a, a]$ for tents and

$[0.86a, a]$ for bubbles when the supported region remains intact, i.e., delamination-free. Such an inaccurate region would be further enlarged if the interfacial buckle delamination happens that causes “damage” to the blister system.

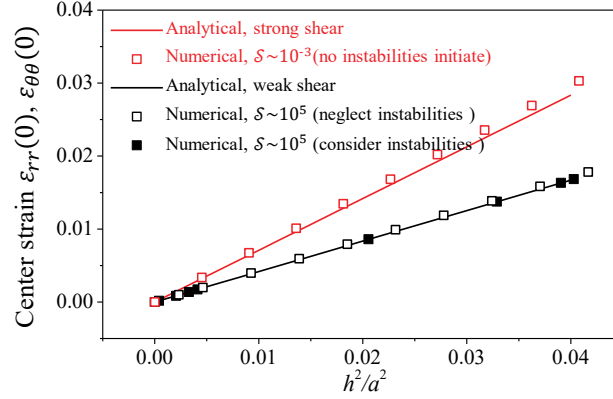


Figure 5.10: Dependency of the strain at the bubble center on the aspect ratio of the bubble.

However, the equibiaxial strain at the bubble center has been a useful quantity in recent experiments regarding strain engineering applications (Dai et al., 2019a), to which our analytical solution shows excellent predictions. According (5.4), we have

$$\varepsilon_r(0) = \varepsilon_\theta(0) = \begin{cases} \frac{3-\nu}{4} \frac{h^2}{a^2}, & \text{strong shear limit} \\ \frac{1-\nu}{2} \frac{h^2}{a^2}, & \text{weak shear limit} \end{cases}, \quad (5.11),$$

which holds good quantitative agreements with numerical results even when the wrinkling is considered (Figure 5.10). The numerical results are obtained by performing the calculations along with the technique outlined in Chapter 2.7 (Case II). We thus conclude that good approximation can be expected at the center of bubbles by (5.4) and (5.10), which may, in turn, be used to measure the Grüneisen parameter for the broadly extended 2D material family.

5.5.3 Experiments about tents in the literature

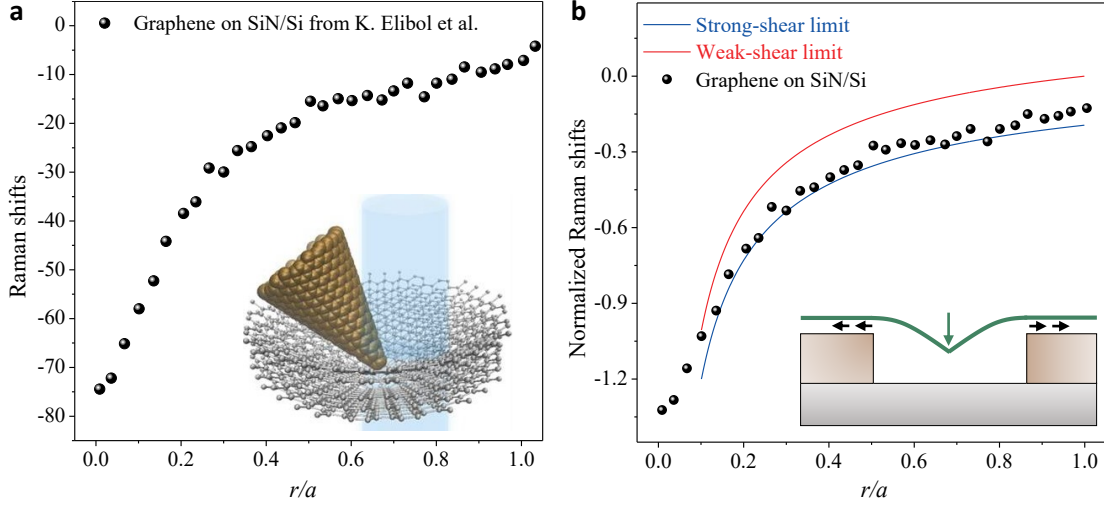


Figure 5.11: (a) Raman shifts of the 2D band of a multilayer graphene tent as a function of r/a (from (Elibol et al., 2016)). Like that in bubbles, r is defined by the distance to the center of the tent and a is the radius of the tent. (b) Normalized Raman shifts predicted by our analytical solution (solid curves) and measured by experiments (Elibol et al., 2016).

As for 2D material tents, a recent study reported the Raman 2D band shifts for a SiN/Si-supported graphene drumhead subjected to nanoindentation. Following the same strategy outlined for the bubbles, we plotted the measured and predicted 2D band shifts for strong- and weak-shear tents in Figure 5.11. Note that we adopted Grüneisen parameter $\gamma = 1$ for the 2D band shift of the multilayer graphene (Ni et al., 2008). The shear deformation potential term in (5.9) was neglected since the β is not well-characterized for multilayer graphene, and its contribution to the Raman shift is less important than the Grüneisen parameter term under biaxial stress state. The associated results are found to be captured very well by the case of a 2D material tent with the strong-shear interface (Figure 5.11).

5.6 STRAIN ENGINEERING APPLICATIONS

We conclude by highlighting the uses and implications of our work for the strain engineering of 2D materials, the technological applications that motivated our study. Recent experiments revealed that the interface-confined content or AFM tip could shape the graphene into bubble or tent configurations, which appeared as extraordinary pseudomagnetic fields (PMFs) in the graphene blister (Klimov et al., 2012; Levy et al., 2010; Qi et al., 2014; Zhu et al., 2014). Such PMFs are direct results of the non-uniform strain fields. They can spatially confine graphene charge carriers in a way similar to a lithographically defined quantum dot. While atomic simulations were utilized to interpret these intriguing experimental findings, little analytical efforts were made on predicting and controlling the strain (or pseudomagnetic) field, which is essential to the implementation of the PMFs in nanoelectronic devices.

As discussed previously, the strain in the graphene blister can be directly estimated by simply measuring its shape and can be strongly tuned by the interface adhesion and friction properties. So are the corresponding PMFs. The PMFs can be approximately calculated by

$$\mathbf{B}_{PMF} = \nabla \times \mathbf{A}_{PMF}, \quad (5.12)$$

where $\mathbf{A}_{PMF} = C(\varepsilon_{xx} - \varepsilon_{yy}, -2\varepsilon_{xy})^T$ and C is a combination of physical constants (Akinwande et al., 2017). The magnitude of PMF can also be written as

$$B_{PMF} = \frac{\beta}{\alpha} \sin 3\theta \left[\frac{2(\varepsilon_r - \varepsilon_\theta)}{r} - \frac{d(\varepsilon_r - \varepsilon_\theta)}{dr} \right]. \quad (5.13)$$

We thus can use our strain equations to analytically predict the PMFs for graphene bubbles and tents with strong and weak shear interfaces by plugging (5.4) into (5.13).

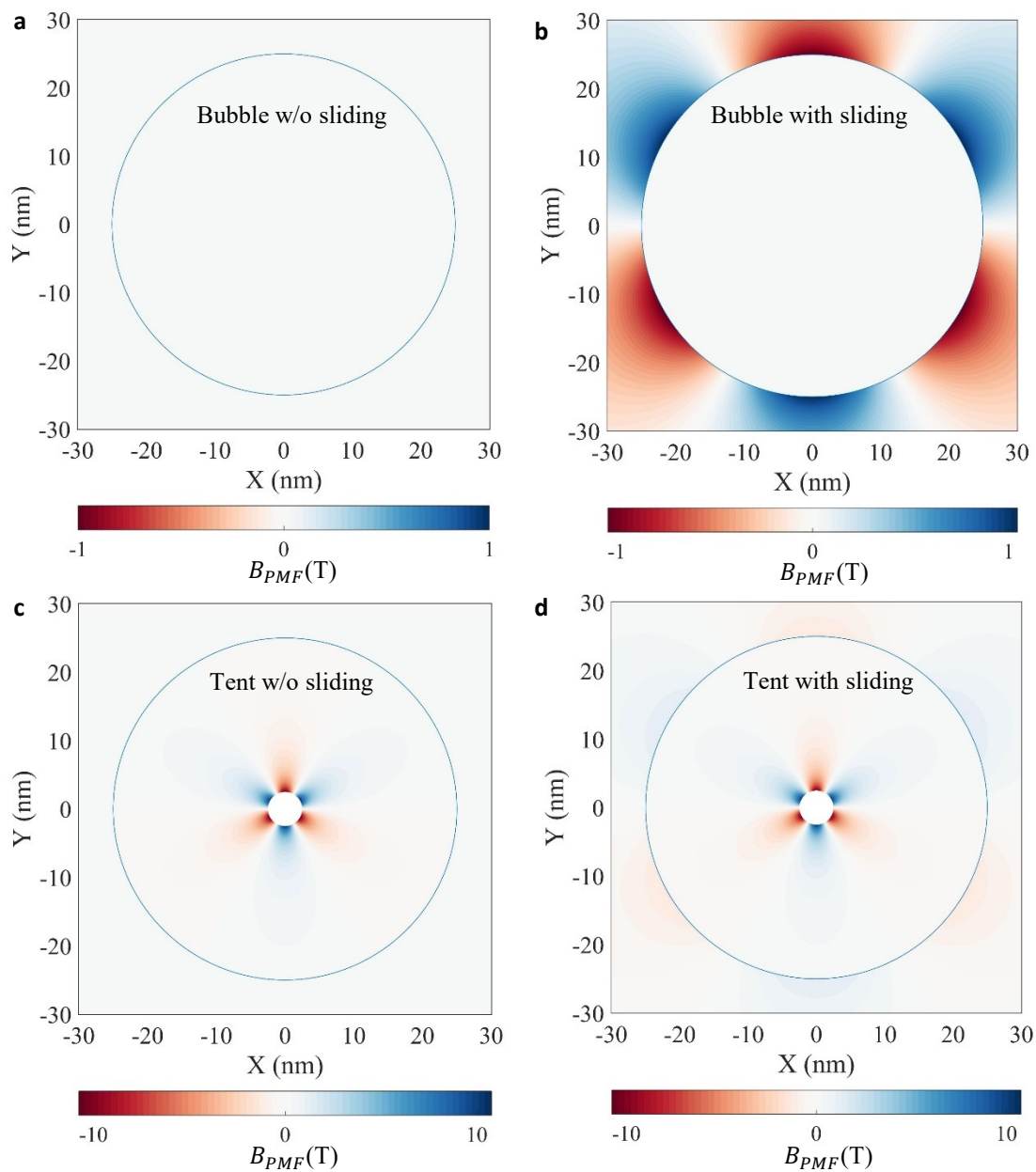


Figure 5.12: Analytically predicted pseudomagnetic fields (PMFs) in graphene bubbles and tents under strong- and weak-shear. A circular monolayer graphene drumhead of a 25-nm-radius is pressurized (a, b) or poked (c, d) with 1 nm deflection. Solid circles represent the edges of these blisters. The PMF outside the tent in (d) is magnified four times in efforts to show the sliding effects.

In Figure 5.12a, our prediction shows that the strain fields inside a graphene bubble with the strong-shear interface cannot induce pseudomagnetic fields. In comparison, nonzero PMFs appear in the sliding zone outside of the bubble in Figure 5.12b, where the weak-shear interface is considered. This implies that the PMF induced by a graphene bubble has to come from the sliding behaviors of graphene-substrate interface outside the bubble, which is consistent with previous MD simulations and tight-binding electronic structure calculations (Qi et al., 2014). Our analytical predictions for the PMFs in graphene tents with strong- and weak-shear interfaces both show three-fold symmetry and a concentrated intensity at the center. Such predictions are also consistent with previous MD and CG simulations in terms of both magnitude and distributions, further validating the good approximation of our analytical solutions to 2D material blisters (Klimov et al., 2012; Zhu et al., 2014).

5.7 CONCLUSIONS

In conclusion, we have found universal shape characteristics of nanoscale bubbles and tents formed by 2D materials, which enabled closed-form analytical solutions to the strain fields using classical membrane theories. The solutions offer a direct relation between the blister shape and the strain fields in the 2D material blisters and also unveiled the effects of the supporting interface on the strain fields. Both numerical and Raman characterizations have confirmed the validity of our analytical solutions. Through the strain equations, we have obtained analytical solutions to the PMFs associated with the non-uniform strain fields. We thus highlighted the effects of interfacial sliding on the strain, aspect ratio, and PMFs. Our results have laid a theoretical foundation for not only the strain engineering of 2D materials using tents or bubbles but also, more broadly, the potential

new physics and applications where atomic sheets on a substrate are deformed out-of-plane.

5.8 APPENDIX

5.A Experimental section¹

Fabrication of spontaneously formed graphene and MoS₂ blisters. The same exfoliation procedure is used for both HOPG and MoS₂ crystals. Blue polyethylene cleanroom tape (CRT) was used to peel large and thick flakes off the bulk crystal. The exfoliated flakes were then brought into contact with another piece of the CRT and exfoliated three more times. The flakes were then stored for a minimum of 3 hours in ambient conditions to allow ambient moisture and other contents to adsorb on the surface of the exposed flakes. The 300 nm SiO₂/Si substrate wafer was first prepared by cutting a 1 cm × 1 cm chip from the wafer. To maximize the area of monolayer regions that were transferred to SiO₂, the SiO₂ chip was exposed to O₂ plasma to remove any organic residue. Immediately after O₂ plasma exposure, the exfoliated HOPG flakes on CRT were placed onto the surface of the SiO₂ chip. Then the SiO₂ chip was placed on a hot plate and was heated at 100°C for two minutes. The sample was removed from the hot plate and cooled to room temperature, after which the CRT was removed. The MoS₂ on the Al₂O₃ sample in this work is a different location on the same sample as used in a previous work, where the fabrication and characterization details can be found (Brennan et al., 2017).

Fabrication of air-pressurized MoS₂ bubbles. MoS₂ bubbles were prepared by micromechanical cleavage of a 4-layer MoS₂ sheet on pre-patterned silicon substrates. The substrate was covered with a 300 nm thick SiO₂ layer. An array of round holes was

¹ We are grateful for these experimental results, which were due to G. Wang for pressurized bubbles with strong interfaces, Y. Hou for pressurized bubbles with weak interfaces, D. Sanchez for spontaneously formed bubbles and tents, and C. Brennan for the nice monolayer MoS₂ tent.

fabricated by photolithography and reactive ion etching, resulting in a depth of 300 nm and a diameter of 3 μm . The lateral dimension was measured by AFM. The samples were placed into a pressure chamber to establish a pressure difference across the graphene membrane, and the accuracy of the gauge was 0.01 MPa.

Fabrication of air-pressurized graphene bubbles. Few- and single-layer graphene were prepared by micromechanical cleavage on the substrates where an array of 5- μm -diameter holes was patterned. The lateral dimension of the monolayer graphene sheet was measured by the optical microscopy, and its monolayer thickness was identified by Raman spectroscopy. Monolayer graphene bubble supported by the silicon substrate (strong-shear interface) was made by following the air-pressurizing process. For the monolayer graphene bubble supported by the few-layer graphene (weak-shear interface), a FIB system (FEI 235 DualBeam) was also used to etch few-layer graphene without using masks, giving a resolution of 20 nm. The suspended part of the graphene few-layer was etched to expose the SiO_2 micro-holes, and then a graphene monolayer was transferred on the top of the perforated multilayer. In efforts to avoid the sample variation regarding the graphene-substrate interaction, we prepared multiple samples, especially for the SiO_2 -supported case. Specifically, we made four SiO_2 -supported samples to provide bubbles with nine different heights. Preparation procedures are relatively challenging and tedious for graphene-supported bubbles. We successfully made three graphene-supported samples that provided bubbles with six different heights.

Characterization of Graphene bubbles. AFM (Dimension Icon, Veeco) in the standard tapping mode was utilized to measure the shape of the graphene bubbles, including the maximum deflection and the radius. We also scanned the profiles of MoS_2 bubbles and tents and graphene tents in the main text, where are captured by (5.1). Note that for the tent case, (5.1) can be used as a fitting function. High-frequency Raman

measurements were performed using an Invo-Renishaw system with an incident wavelength of 532 nm from a diode-pumped solid-state laser. The spectral resolution was 1.0 cm^{-1} and the spatial resolution was $\sim 1 \text{ }\mu\text{m}$. The laser intensity was kept below 0.5 mW to avoid local heating induced by the laser. For the Raman scanning under various heights, Raman spectra from every spot of the sample were recorded with a step size of 100 nm. All featured bands in Raman spectra of graphene were fitted with Lorentzian functions to obtain the peak positions.

5.B Numerical section¹

We numerically solved the Föppl–von Kármán (FvK) equations for a circular membrane under uniform pressure (bubble) and a point load (tent). Unlike Chapter 3, this Chapter utilized a finite difference method. Here, we briefly introduce our modifications to a previously established finite difference method to solve the sliding boundary case for bubbles and tents (Wang et al., 2013b). We consider the bending stiffness of the membrane and write the FvK equations in terms of the displacement (see details in Chapter 2.2):

$$\frac{d^2u}{dr^2} + \frac{1}{r} \frac{du}{dr} - \frac{u}{r^2} = -\frac{1-\nu}{2r} \left(\frac{dw}{dr} \right)^2 - \frac{dw}{dr} \frac{d^2w}{dr^2} \quad (5.B1)$$

and

$$B \left(\frac{d^3w}{dr^3} + \frac{1}{r} \frac{d^2w}{dr^2} - \frac{1}{r^2} \frac{dw}{dr} \right) - \frac{E_{2D}}{1-\nu^2} \frac{dw}{dr} \left[\frac{du}{dr} + \nu \frac{u}{r} + \frac{1}{2} \left(\frac{dw}{dr} \right)^2 \right] = \frac{1}{r} \int_0^r q(r) r dr, \quad (5.B2)$$

where B is the bending rigidity of the membrane, E_{2D} is the in-plane stiffness of the membrane. The lateral loading intensity, $q(r)$, can take two forms depending on the type of load. For a bubble, $q(r)$ is a constant; for a tent, $q(r) = \frac{P\delta(r)}{2\pi r}$, where P is the magnitude of the point load and $\delta(r)$ is the Dirac delta function. We then adopt relation between the bending stiffness and in-plane stiffness such that the nominal thickness is described as $t =$

¹ I appreciate Dr. P. Wang for sharing his MATLAB codes regarding the clamped, pressurized bubbles. The related work was published in Wang, Peng, et al. "Numerical analysis of circular graphene bubbles." Journal of Applied Mechanics 80.4 (2013): 040905.

$\sqrt{12(1-\nu^2)B/E_{2D}}$. For convenience, we normalize the FvK equations using the following dimensionless quantities: $\bar{r} = r/t$, $\bar{a} = a/t$, $\bar{u} = u/t$, $\bar{w} = w/t$, $\bar{u}_s = u_s/t$, $\bar{q}(r) = q(r)t^3/B$, and $\bar{P} = Pt/B$. We replace the deflection with the angle of rotation, $\theta = dw/dr$, such that (5.B1) and (5.B2) become the following nondimensional equations:

$$g = \frac{d^2\bar{u}}{d\bar{r}^2} + \frac{1}{\bar{r}} \frac{d\bar{u}}{d\bar{r}} - \frac{\bar{u}}{\bar{r}^2} + \frac{1-\nu}{2\bar{r}} \theta^2 + \theta \frac{d\theta}{d\bar{r}} = 0 \quad (5.B3)$$

and

$$f = \frac{d^2\theta}{d\bar{r}^2} + \frac{1}{\bar{r}} \frac{d\theta}{d\bar{r}} - \frac{\theta}{\bar{r}^2} - 12\theta \left(\frac{d\bar{u}}{d\bar{r}} + \nu \frac{\bar{u}}{\bar{r}} + \frac{\theta^2}{2} \right) - \frac{1}{\bar{r}} \int_0^{\bar{r}} \bar{q}(r) \bar{r} d\bar{r} = 0. \quad (5.B4)$$

Following the finite difference method, we discretize the equations with $\Delta\bar{r} = \bar{a}/n$

and $\bar{r}_k = k\Delta\bar{r}$ for $k = 0$ to n . At each internal node ($k = 1$ to $n-1$), we have

$$g_k = \frac{n^2}{\bar{a}^2} \left(1 + \frac{1}{2k} \right) \bar{u}_{k+1} - \frac{n^2}{\bar{a}^2} \left(2 + \frac{1}{k^2} \right) \bar{u}_k + \frac{n^2}{\bar{a}^2} \left(1 - \frac{1}{2k} \right) \bar{u}_{k-1} + \frac{1-\nu}{2k\bar{a}} \theta_k^2 + \frac{n}{2\bar{a}} \theta_k (\theta_{k+1} - \theta_{k-1}) \quad (5.B5)$$

and

$$f_k = \frac{n^2}{\bar{a}^2} \left(1 + \frac{1}{2k} \right) \theta_{k+1} - \frac{n^2}{\bar{a}^2} \left(2 + \frac{1}{k^2} \right) \theta_k + \frac{n^2}{\bar{a}^2} \left(1 - \frac{1}{2k} \right) \theta_{k-1} - \frac{6n}{\bar{a}} (\bar{u}_{k+1} - \bar{u}_{k-1}) - \frac{12\nu n}{k\bar{a}} \theta_k \bar{u}_k - 6\theta_k^3 - \zeta_k = 0, \quad (5.B6)$$

where ζ_k is $\bar{q}k\bar{a}/2n$ for the bubble and is $\bar{P}n/(2\pi k\bar{a})$ for the tent. The boundary conditions are $\theta_0 = \theta_n = 0$, $\bar{u}_0 = 0$, $\bar{u}_n = \bar{u}_s$. In calculations, \bar{u}_s is a prescribed but not arbitrary quantity. For each given \bar{u}_s , the load \bar{P} needs to be solved by matching the boundary conditions at the edge: $\bar{u}_s = 0$ for a clamped interface; the displacement and radial stress component are continuous across the edge for a sliding interface. The Newton-Raphson method was used to solve (5.B5) and (5.B6). The analytical plate solution was used to provide the initial guess for the bubble, while Schwerin's classic solution was used for the tent:

$$\theta_k^{(0)}{}_{bubble} = \frac{\bar{q}k}{16n} \left(\frac{k^2}{n^2} - 1 \right), \quad (5.B7)$$

$$\theta_k^{(0)}{}_{tent} = -\frac{2}{3} \left(\frac{\bar{P}n}{4\pi(1-\nu^2)\bar{a}k} \right)^{\frac{1}{3}}, \quad (5.B8)$$

and

$$\bar{u}_k^{(0)} = 0. \quad (5.B9)$$

We successively iterate until the convergence condition is satisfied. At each iteration, the residuals are calculated by (5.B7) and (5.B8) at each internal node, and the correction vector is calculated as

$$\begin{pmatrix} \Delta \theta \\ \Delta \bar{u} \end{pmatrix} = - \begin{bmatrix} \frac{\partial f}{\partial \theta} & \frac{\partial f}{\partial \bar{u}} \\ \frac{\partial g}{\partial \theta} & \frac{\partial g}{\partial \bar{u}} \end{bmatrix}^{-1} \begin{pmatrix} f \\ g \end{pmatrix}, \quad (5.B10)$$

where $\Delta \theta$ is a vector of $n-1$ components ($\Delta \theta_k$, $k = 1$ to $n - 1$) and same for $\Delta \bar{u}$, f , and g . The Jacobian matrix on the right-hand side of (5.B10) consists of four square blocks, each with a rank of $n - 1$. This matrix can be readily constructed from (5.B5) and (5.B6). For the convergence criterion, we require that the L2-norm of the relative correction vector is smaller than 10^{-4} , i.e., 0.01% accuracy. If the convergence criterion is not satisfied, the iteration procedure then repeats with a new approximation, $\theta_k^{(i+1)} = \theta_k^{(i)} + \Delta \theta_k$ and $\bar{u}_k^{(i+1)} = \bar{u}_k^{(i)} + \Delta \bar{u}$.

Subsequently, we calculate the deflection at each node by numerical integration:

$$\bar{w}_k = -\frac{\bar{a}}{2n} \sum_{m=k}^{n-1} (\theta_m + \theta_{m+1}) \quad (5.B11)$$

for $k = 1$ to $n - 1$, and $\bar{w}_n = 0$. The strain components at each node can be calculated as

$$(\varepsilon_r)_k = \frac{n}{2\bar{a}} (\bar{u}_{k+1} - \bar{u}_{k-1}) + \frac{\theta_k^2}{2} \quad (5.B12)$$

and

$$(\varepsilon_\theta)_k = \frac{n\bar{u}_k}{k\bar{a}} \quad (5.B13)$$

for $k = 1$ to $n - 1$. At the center, $(\varepsilon_r)_0 = (\varepsilon_\theta)_0 = \frac{n\bar{u}_1}{\bar{a}}$. Note that at the edge, we can have $(\varepsilon_\theta)_n = \frac{\bar{u}_s}{\bar{a}}$ and $(\varepsilon_r)_n = -\frac{\bar{u}_s}{\bar{a}}$, due to the continuity of radial stress and displacement across the edge.

Chapter 6: Elasto-capillarity¹

In previous chapters, we have revealed the dominant role of the aspect ratio (height-to-radius ratio) of a 2D material blister (including bubble and tent) in controlling its strain fields as well as in governing the edge slippage and elastic instabilities. In this chapter, we further show that such aspect ratio often appears constant in recent experiments, which could be understood as a result of the balance of elastic and surface/interface forces in the systems. 2D material bubbles would be the focus of this chapter, and the underlying physics discussed here would also apply to 2D material tents. Usually, monolayer or few-layer 2D materials are transferred to a target substrate, including other 2D materials, and nanometer-scale bubbles form spontaneously between the 2D material and its substrate with liquids trapped inside. We develop a simple scaling law and a rigorous theoretical model for liquid-filled bubbles, which predicts that the interfacial work of adhesion is related to the fourth power of the aspect ratio of the blister and depends on the surface tension of the liquid. Our model was validated by molecular dynamics simulations, and the adhesion energy values obtained for the measured nanoblister are in good agreement with those reported in the literature. This model can be applied to estimate the work of adhesion for a variety of 2D interfaces, which provides important implications for the fabrication and deformability of 2D heterostructures and devices.

¹A paper based on the work described in this Chapter has been published:

D. Sanchez†, Z. Dai†, P. Wang, A. Cantu-Chavez, C. J. Brennan, R. Huang, N. Lu. *Mechanics of Spontaneously Formed Nanoblister Trapped by Transferred 2D Crystals*. Proceedings of the National Academy of Sciences 2018, 115, 7884. († denotes equal contribution; Z.D. contributed to the design of the experiments, theoretical analysis, and writing of the draft regarding introduction, theory, discussion on implications.)

6.1 INTRODUCTION

2D materials are atomically thin, layered materials with strong bonding in the material plane and weak bonding via van der Waals (vdW) interactions between the layers (Geim and Grigorieva, 2013; Neto et al., 2009). The discovery of 2D materials has fueled extensive fundamental and applied research due to their remarkable electronic, mechanical, optical, and magnetic properties. Rapidly emerging experimental and modeling results indicate that mechanical strains can strongly perturb the band structure of 2D materials (Akinwande et al., 2017; Klimov et al., 2012; Levy et al., 2010). In the nanoscale regime, the vdW interactions between the monolayer 2D material and its substrate can have strong influences on the mechanical behavior of 2D materials (Kitt et al., 2013; Koenig et al., 2011; Koren et al., 2015). Consequently, the performance of 2D-material-based devices relies heavily on the vdW interfaces. In reality, however, the vdW attraction between the 2D material and its substrate may cause adsorbed ambient molecules to lump together in the interface, resulting in micro- or nanoblister which often degrade device performance (Kretinin et al., 2014; Pizzocchero et al., 2016). Interfacial blisters are also frequently seen in vdW heterostructures (i.e., stacks of 2D materials), causing significant charge inhomogeneity and limiting the carrier mobilities of a device (Geim and Grigorieva, 2013; Neto et al., 2009). Alternatively, due to the strong electromechanical coupling, nanoblister have been applied for strain engineering of 2D materials (Levy et al., 2010; Lloyd et al., 2016). Moreover, interface-confined chemistry was explored within 2D material blisters leveraging the high internal pressure (Chen et al., 2017; Dai et al., 2018; Dai et al., 2019a; Ghorbanfekr-Kalashami et al., 2017; Khestanova et al., 2016; Lim et al., 2014; Lim et al., 2013; Lu et al., 2012; Vasu et al., 2016; Zamborlini et al., 2015). To either control or avoid blisters for the 2D materials, it is imperative to understand the formation mechanism for these nanoblister and reveal the key parameters.

Many studies have been carried out recently to explore various aspects of nanoblisters, including the effects of heat (Pizzocchero et al., 2016), blister content (Ghorbanfekr-Kalashami et al., 2017), humidity dependence (Bampoulis et al., 2016), and their shape characteristics (Khestanova et al., 2016). Although there is no consensus on whether the blisters are filled with air, liquid, or solid (Cao et al., 2011; Haigh et al., 2012), adhesion is one of the well-accepted governing parameters for the formation of blisters. In fact, interfacial blisters have been used as indicators of good adhesion between the constituents of vdW heterostructures (Geim and Grigorieva, 2013; Neto et al., 2009), since blisters are energetically favorable only when the adhesion between layers is relatively high. Mechanics models have been developed and widely used to relate gas-filled blister profiles to interfacial adhesion (An et al., 2017; Bampoulis et al., 2016; Falin et al., 2017; Ghorbanfekr-Kalashami et al., 2017; Yue et al., 2012). However, the subtle nature of the content inside the blisters may render the assumption of the gas content inappropriate. Direct application of this *ad hoc* model has led to unrealistically small adhesion values for graphene interfaces when compared to well-established adhesion measurements (Bampoulis et al., 2016).

The heat and humidity dependence of these blisters have suggested that it is more likely to be liquid inside; alternatively, there are increasing efforts to tune liquid chemistry in such nanoscale confinements (Ghorbanfekr-Kalashami et al., 2017). Here, we develop a scaling law and a more rigorous analytical model based on the elastic membrane theory for liquid-filled nanoblisters. Compared with gas-filled blisters assuming ideal gas law for the content, the liquid blister theory assumes that the liquid inside the blister is nearly incompressible. However, the shape characteristics of the blister may vary depending on how the liquid interacts with the membrane and the substrate. Our analytical model is then compared with molecular dynamics (MD) simulations to provide verification from the

atomistic level. Like the gas blister theory, our liquid blister theory can also be utilized to quantitatively characterize the adhesion properties for the 2D materials based on the measured blister profiles. Alternatively, the blister shape, strain, and pressure characteristics could be controlled by tuning adhesion properties and trapped contents, which provides a viable guideline for the design of 2D material blisters for various applications.

6.2 ASPECT RATIO OF BUBBLES¹

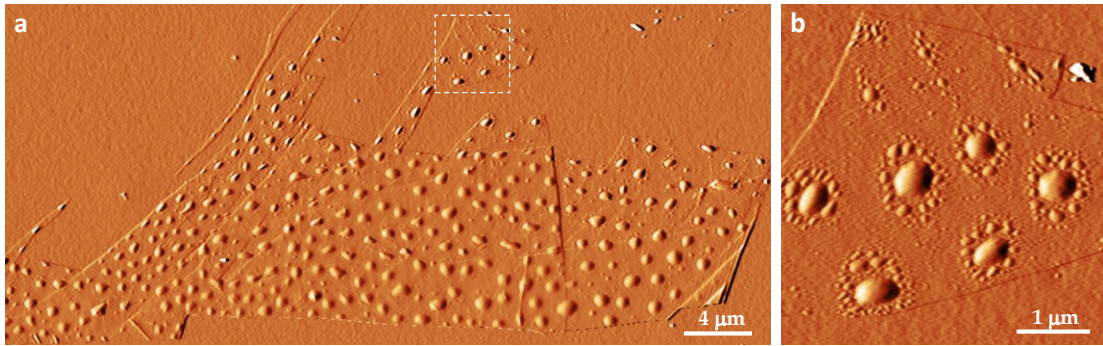


Figure 6.1: (a) Liquid-filled bubbles between graphene and a silicon substrate (AFM amplitude image, courtesy of Daniel Sanchez). (b) Satellite bubbles can be observed by zooming in on the boxed region in (a).

Our experiments focus on the characteristics of nanoblister that form at the graphene-SiO₂ and 2D MoS₂-SiO₂ interfaces, as graphene and MoS₂ are two of the most prevalent 2D materials so far. Later in this section, we will show experiments about other 2D materials that already existed in literature. Additionally, we find blisters that form when chemical vapor deposited (CVD) MoS₂ is transferred to Al₂O₃. After mechanically exfoliating highly ordered pyrolytic graphite (HOPG) onto a silicon wafer with native SiO₂

¹ Daniel Sanchez and Christopher Brennan performed experiments in which we found these spontaneously formed 2D material blisters.

(Huang et al., 2015), we identified single-layer graphene (SLG) areas that show a remarkably large number of blisters (boxed region in Figure 6.1a). The same procedure was also used to exfoliate 2D MoS₂ flakes from its bulk material onto SiO₂. For both samples, monolayer regions were identified using Raman spectroscopy (See details in Appendix in Sanchez et al. 2018).

Using tapping mode atomic force microscopy (AFM) (Figure 6.1), we can obtain the height profiles of the blisters. We denote the center height of the blister by h and its radius by a , such that the aspect ratio is given as h/a . The height and radius of the blisters are calculated by curve-fitting the assumed deflection profile for a pressurized membrane,

$$w(r) = h \left(1 - \frac{r^2}{a^2}\right) \quad (6.1),$$

to the measured data (Figure 6.2a). Further information on the experimental procedure for creating and characterizing blisters is provided in Appendix in Sanchez et al. 2018.

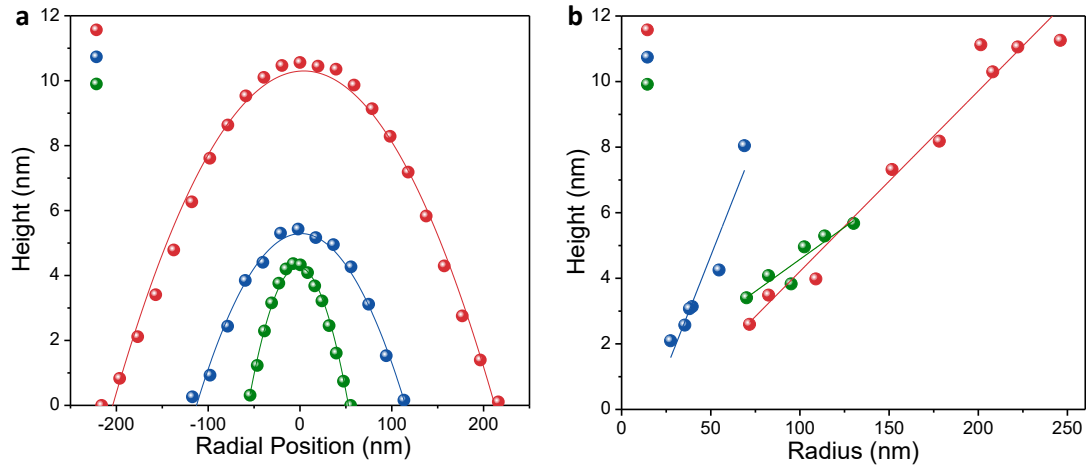


Figure 6.2: (a) By extracting the height profile of each blister, the height and radius is calculated by curve fitting a parabolic function. (b) Blisters for a specific interface show a consistent aspect ratio that is independent of volume.

To use the aspect ratio of a blister as a characterization method, the in-plane shape of the blister should be approximately circular such that the aspect ratio is reasonably consistent. The shape of the blister may become distorted due to its local environment, causing the aspect ratio to become anisotropic. For example, in Figure 6.1, blisters near the edges of graphene are elongated in the direction parallel to the edge leading to an elliptical instead of circular shape (this could be explained by the finite size effect of the 2D material in section 6.5.2. Blisters with an elliptical shape can also be found along step edges in the FLG areas.

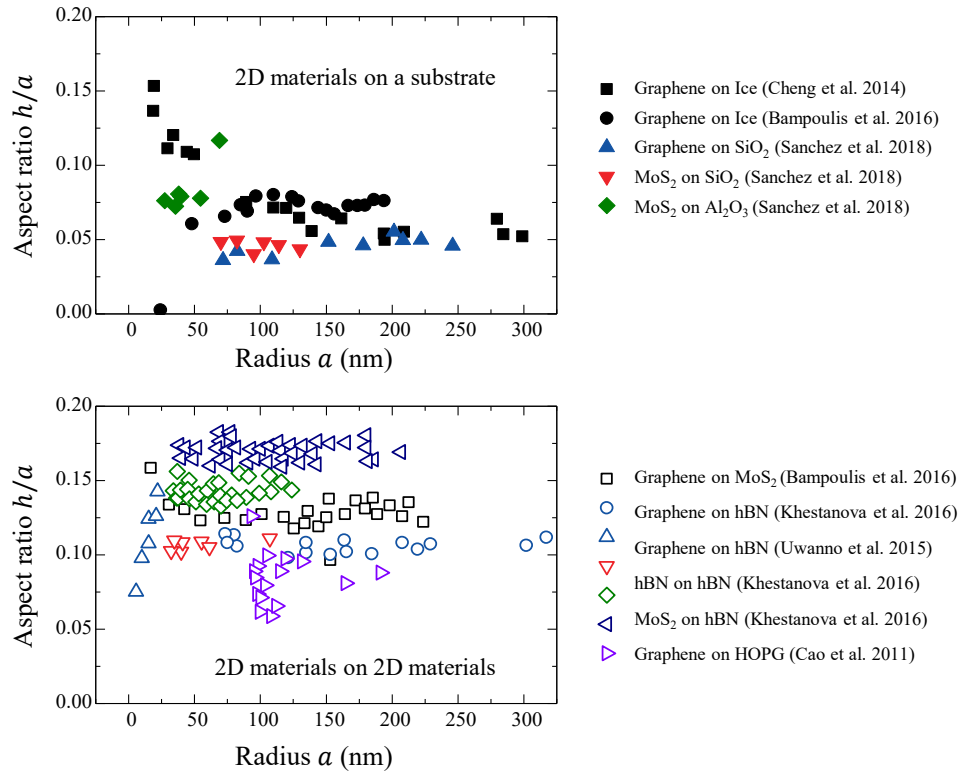


Figure 6.3: Aspect ratio of 2D material blisters in literature. The top panel shows data from the case of 2D materials on regular substrates; the bottom shows the blisters formed between 2D materials.

Focusing on approximately circular blisters, the measured height vs. radius in Figure 6.2b suggests that the aspect ratios of each type of the blisters are independent of the volume of the blister, with an average aspect ratio (h/a) of 0.049 ± 0.003 for the graphene-SiO₂ blisters, 0.046 ± 0.004 for the MoS₂-SiO₂ blisters, and 0.083 ± 0.016 for the MoS₂-Al₂O₃ blisters. A constant aspect ratio for a given 2D material-substrate pair has also been observed for other blisters reported in the literature, as summarized in Figure 6.3, indicating that the blister aspect ratio is a crucial dimensionless parameter for the material system.

The mechanical behavior of the blister is not only dictated by the 2D material-substrate interaction, but also by the interactions between the trapped content and the 2D material/substrate. However, so far, there is no consensus or direct measurement of the blister content. While several previous studies applied the gas models to analyze those blisters (Bampoulis et al., 2016; Ghorbanfekr-Kalashami et al., 2017; Temmen et al., 2014; Wang et al., 2013b; Yue et al., 2012), Geim et al. strongly advocated that the blisters are filled with hydrocarbon and liquid water (Haigh et al., 2012; Khestanova et al., 2016). Emerging observations in literature imply that the blister content is likely to be water because those blisters are found to be highly dependent on temperature (especially beyond 100°C) and humidity (Bampoulis et al., 2016; Pizzocchero et al., 2016). For example, Cao et al. noted that the number density and size of blisters at the graphene-HOPG interface were reduced when exfoliation was carried out in a low-humidity environment compared with exfoliation in ambient conditions (Cao et al., 2011). In another case, Pizzocchero et al. demonstrated that blister-free interfaces for heterostructures are possible only when the 2D material is transferred at 110 °C, and suggested adsorbed water is the most likely candidate for the contents of the interfacial blisters (Pizzocchero et al., 2016).

In Sanchez et al. 2018, we monitor the time-dependent behavior of a selected number of blisters from Figure 6.1. As noted in previous studies, graphene-SiO₂ interfacial blisters pressurized with gas typically deflate within 10 hours for H₂-filled blisters, and 7 days for N₂-filled blisters (30-32). Since graphene is impermeable to even the smallest gas molecules (Berry, 2013), it was concluded that the majority of the gas content inside the blister escaped through the graphene-SiO₂ interface. Over a period of 92 days, we performed AFM scans over the same sample using consistent scanning parameters and cantilever tips. Our data shows that the blisters in the SLG regions exhibit deflation at different rates, with some showing little overall change in their height, which is drastically different from the time-dependent behaviors of gas blisters. Hence our experiment offers evidence against the possibility of gas inside the blisters. We, therefore, suggest that the content inside the blisters is mostly liquid water, likely mixed with a certain amount of hydrocarbon contaminants. Following such hypothesis, in the following, we present a liquid-filled blister model and adopt water as the most likely representative liquid for quantitative analysis.

6.3 ANALYTICAL EXPRESSIONS

Although 2D materials are atomically thin membranes, continuum mechanics has proven to be applicable when bending is negligible (Ahmadpoor et al., 2017; Gao and Huang, 2014; Lee et al., 2008). We, therefore, employ an elastic membrane model to establish a direct relationship between the aspect ratio of the blister and the material properties of the 2D membrane and substrate. Unlike gas-filled blisters considered in previous works (Wang et al., 2013b; Yue et al., 2012), where the ideal gas law was used to relate the pressure to the blister volume, we assume that the liquid inside the blister is

nearly incompressible, but the aspect ratio (h/a) may vary depending on how the liquid interacts with the membrane and the substrate.

6.3.1 Scaling

We begin by using a simple scaling approach for determining the properties of axisymmetric blisters. The membrane over a liquid-filled blister of radius a and height h at its center is subject to a stretching strain $\varepsilon \propto h^2/a^2$ from elementary geometry. With an in-plane elastic stiffness E_{2D} , the stretching energy in the membrane scales as $U_e \propto E_{2D}\varepsilon^2 a^2 \propto E_{2D}h^4/a^2$. The bending energy of the membrane is negligible due to the thinness of the 2D membrane and relatively small aspect ratios. The adhesion energy required to form the blister is simply the energy change per unit area, $\Delta\gamma$, multiplied by the blister area, which scales as $U_i \propto \Delta\gamma a^2$. If the volume of liquid ($V \propto a^2 h$) remains a constant in the blister, the elastic energy decreases, and the interfacial energy increases with increasing a . The competition leads to an equilibrium blister radius that minimizes the total free energy ($U_e + U_i$), with $h/a \propto (\Delta\gamma/E_{2D})^{1/4}$. The scaling relation for the aspect ratio (h/a) is identical to that for gas-filled blisters (Wang et al., 2013b; Yue et al., 2012). However, the change in interfacial energy is different. For a gas-filled blister, $\Delta\gamma$ is simply taken as the adhesion energy between the membrane and the substrate ($\Delta\gamma = \Gamma$). For a liquid-filled blister, considering the interfaces between the liquid, the membrane and the substrate, the change of the interfacial energy can be written as

$$\Delta\gamma = \gamma_{ml} + \gamma_{sl} - \gamma_{ms}, \quad (6.2)$$

where γ_{ml} , γ_{sl} , and γ_{ms} are the energy densities (per unit area) for the membrane-liquid interface, substrate-liquid interface, and the membrane-substrate interface, respectively. For blisters filled with liquid water, the Young–Dupré equations (Israelachvili, 2011; Rafiee et al., 2012) further lead to:

$$\Delta\gamma = \Gamma - \gamma_w(\cos \theta_s + \cos \theta_m) \quad (6.3)$$

In (6.3), Γ is the work of adhesion (or adhesion energy) of the membrane–substrate interface, γ_w is the surface tension of water ($\sim 0.072 \text{ J/m}^2$) (Israelachvili, 2011; Rafiee et al., 2012), and θ_s and θ_m are the water contact angles of the substrate and the membrane, respectively. Thus, the scaling analysis predicts the aspect ratio for a liquid-filled blister as:

$$\frac{h}{a} = \left(\phi \frac{\Gamma - \gamma_w(\cos \theta_m + \cos \theta_s)}{E_{2D}} \right)^{\frac{1}{4}}, \quad (6.4)$$

where the dimensionless coefficient ϕ has to be determined by a detailed analysis. Clearly, by (6.4), the aspect ratio of a water-filled blister depends on the elastic property of the membrane, the adhesion of the membrane to the substrate, and the hydrophobicity of the membrane and the substrate.

Previous studies on graphene gas blisters (Yue et al., 2012) predicted a similar scaling (but with $\gamma_w = 0$) by assuming the ideal gas law for the pressure inside the blister, where the coefficient ϕ was found to be a function of Poisson’s ratio of the membrane material. The edge of the blister is often assumed to be fully clamped onto the substrate due to adhesion and strong shear interactions that prevent sliding along the interface. However, recent studies (Dai et al., 2018; Wang et al., 2017b) found that the shear interactions can be fairly weak between graphene and its substrate so that sliding may occur at the edge of the blister. As a result, the elastic deformation of the membrane depends on the shear interactions, and in turn, the coefficient ϕ depends on the shear interactions as well. Here, we first consider two limiting cases by a simple membrane analysis, one for blisters with a fully clamped edge (strong shear limit) and the other for blisters with a frictionless sliding interface (weak shear limit). This is followed by a more rigorous analysis by Hencky’s approach (Fichter, 1997; Hencky, 1915), with the shear interactions

represented by a finite interfacial shear stress between the membrane and the substrate. The effects of the finite membrane size and outer boundary conditions are discussed.

6.3.2 An energy-based membrane analysis

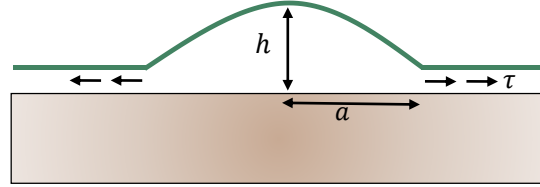


Figure 6.4: Schematic illustration of an axisymmetric bubble.

For a liquid-filled blister, the liquid within the blister is assumed to be incompressible so that the blister volume, $V = \pi a^2 h/2$, remains a constant. The area of the bulged surface $A' = \pi(a^2 + h^2) \approx \pi a^2$ for small h/a ratios. For a given liquid volume, the aspect ratio (h/a) of the blister is determined by the competition between the elastic strain energy of the membrane and the interfacial energy.

To calculate the elastic strain energy of the membrane, we assume a cubic radial displacement that is kinematically admissible:

$$u(r) = u_0 \frac{r}{a} \left(1 - \frac{r^2}{a^2}\right) + u_s \frac{r}{a}, \quad (6.5)$$

where u_0 is to be determined and u_s accounts for the in-plane sliding at the edge of the blister ($r = a$). For the strong shear limit, $u_s = 0$. For the weak shear limit, u_s is to be determined by considering elastic deformation of the membrane outside the edge of the blister. Note that previous studies have shown that the cubic radial displacement assumption can capture the deformation characteristics of a monolayer graphene sheet well (Wang et al., 2013b; Yue et al., 2012; Zhang and Arroyo, 2016). Later in this text, we will

assume a seven-term polynomial to solve the problem more accurately and compare with the results from our cubic radial displacement analysis.

With (6.1) and (6.5), the radial and circumferential strain components are obtained as:

$$\varepsilon_r = \frac{du}{dr} + \frac{1}{2} \left(\frac{dw}{dr} \right)^2 = \frac{u_s}{a} + \frac{u_0}{a} \left(1 - \frac{3r^2}{a^2} \right) + \frac{2h^2 r^2}{a^4}, \quad (6.6)$$

and

$$\varepsilon_\theta = \frac{u}{r} = \frac{u_s}{a} + \frac{u_0}{a} \left(1 - \frac{r^2}{a^2} \right). \quad (6.7)$$

Note that the circumferential strain (ε_θ) is in general not zero at the edge ($r = a$) unless the sliding displacement u_s is zero (e.g., at the strong shear limit). We can now derive the elastic strain energy, consisting of two parts, one due to stretching and the other due to bending. The elastic stretching energy per unit area of the membrane is

$$U_s(r) = \frac{E_{2D}}{2(1-\nu^2)} (\varepsilon_r^2 + 2\nu\varepsilon_r\varepsilon_\theta + \varepsilon_\theta^2), \quad (6.8)$$

where E_{2D} is 2D Young's modulus of the membrane material, and ν is Poisson's ratio. The elastic bending energy per unit area is

$$U_b(r) = \frac{B}{2} \left[\left(\frac{d^2 w}{dr^2} \right)^2 + \frac{1}{r^2} \left(\frac{dw}{dr} \right)^2 + \frac{2\nu}{r} \frac{dw}{dr} \frac{d^2 w}{dr^2} \right], \quad (6.9)$$

where B is bending stiffness of the membrane. As we discussed in Chapter 4, for graphene and other 2D membrane materials, the bending stiffness is very small, so that the bending energy is negligible for typical blisters as considered in the present study.

We first consider the strong shear limit with $u_s = 0$. In this case, the membrane outside the blister edge is not deformed. The free energy for the blister is then obtained as a function of two kinematic parameters:

$$F(a, u_0) = 2\pi \int_0^a U_s(r) r dr + \pi a^2 \Delta\gamma, \quad (6.10)$$

where $\Delta\gamma = \gamma_{ml} + \gamma_{sl} - \gamma_{ms}$ is the change of interface energy for the formation of a liquid-filled blister with γ_{ml} , γ_{sl} , and γ_{ms} being the interfacial energy densities respectively for

three interfaces involved: membrane-liquid interface, substrate-liquid interface, and membrane-substrate interface. For blisters filled with liquid water, the interfacial energies can be obtained from the water contact angles as $\Delta\gamma = \Gamma - \gamma_w(\cos \theta_s + \cos \theta_m)$, where Γ is adhesion energy of the membrane to the substrate, γ_w is surface tension of water, θ_s and θ_m are the water contact angles of the substrate and the membrane, respectively. We note that, unlike gas-pressurized blisters, the height of the blister, h ($= \frac{2V}{\pi a^2}$), is not an independent variable in (6.10) due to the assumption of incompressible liquid with a constant volume.

For a fixed radius, the mechanical equilibrium requires that

$$\left(\frac{\partial F}{\partial u_0}\right)_a = 0, \quad (6.11)$$

which leads to $u_0 = \frac{(3-\nu)h^2}{4a}$. Then, with the liquid volume fixed inside the blister, the free energy is obtained as a function of the blister radius:

$$F(a) = \frac{2(7-\nu)E_{2D}V^4}{3\pi^3(1-\nu)a^{10}} + \pi a^2 \Delta\gamma. \quad (6.12)$$

The first term on the right-hand side of (6.12) is the elastic strain energy in the membrane, which decreases with increasing blister radius a . The second term stems from the change of interface energy, which increases with increasing blister radius for $\Delta\gamma > 0$. The competition of the two leads to an equilibrium blister radius that minimizes the free energy, namely

$$\left(\frac{\partial F}{\partial a}\right)_V = 0, \quad (6.13)$$

which gives rise to (6.4) with $\phi = \frac{24(1-\nu)}{5(7-\nu)}$ for the strong shear limit. Specifically, for graphene ($\nu = 0.165$), we have $\phi = 0.6$ for the strong shear limit.

Next, consider the weak shear limit, where the membrane in the annular region outside of the blister edge ($r > a$) slides inward as the liquid pressure pushes up the membrane to form a blister. With zero shear stress at the frictionless interface between the membrane and the substrate, the stress and displacement in the annular region can be

obtained as the classical Lamé problem in linear elasticity. The radial and circumferential components of the membrane stress are (Landau et al., 1986):

$$N_r = \frac{C_1}{r^2} + C_2, \quad (6.14a)$$

$$N_\theta = -\frac{C_1}{r^2} + C_2, \quad (6.14b)$$

where $N_r = \sigma_r t$ and $N_\theta = \sigma_\theta t$; σ_r and σ_θ are, respectively, radial and circumferential stresses; t is the membrane thickness. Correspondingly, the radial displacement is

$$u = \frac{1}{E_{2D}} \left[-\frac{(1+\nu)C_1}{r} + C_2(1-\nu)r \right]. \quad (6.15)$$

For an infinitely large membrane, both the stress and the displacement approach zero as $r \rightarrow \infty$, which requires $C_2 = 0$. At the edge of the blister ($r = a$), the radial stress and displacement are continuous. By comparing (6.15) with (6.5), we obtain $C_1 = -\frac{E_{2D}au_s}{1+\nu}$ for the displacement continuity. For the radial stress, we have by Hooke's law

$$N_r = \frac{E_{2D}}{1-\nu^2} (\varepsilon_r + \nu\varepsilon_\theta), \quad (6.16)$$

where the strain components on the right-hand side are given by (6.6) and (6.7) at $r = a$, and the radial stress on the left-hand side is given by (6.14a) at $r = a$. The stress continuity then leads to $u_s = u_0 - h^2/a$, where u_0 is yet to be determined for this case.

By (6.8), we compute the elastic stretching energy per unit area of the membrane. For the region within the blister edge ($r < a$), the strain components are given by (6.6) and (6.7). For the annular region outside the blister edge ($r > a$), the strain components can be obtained as: $\varepsilon_r = \frac{du}{dr} = -\frac{au_s}{r^2}$ and $\varepsilon_\theta = \frac{u}{r} = \frac{au_s}{r^2}$. Then, the free energy for the blister at the weak shear limit is

$$F(a, u_0) = 2\pi \int_0^a U_S(r) r dr + 2\pi \int_a^\infty U_S(r) r dr + \pi a^2 \Delta\gamma. \quad (6.17)$$

Following the same process in (6.11), we obtain $u_0 = \frac{(3-\nu)h^2}{4a}$ and the free energy function

$$F(a) = \frac{8E_{2D}V^4}{3\pi^3 a^{10}} + \pi a^2 \Delta\gamma. \quad (6.18)$$

Minimization of the free energy with respect to a gives rise to (6.4) again, with $\phi = \frac{6}{5}$ for the weak shear limit. Compared to the strong shear limit, the weak shear limit predicts a larger height-to-radius ratio for the blister, about 20% higher for graphene in particular.

6.3.3 Finite sheet size in simulations

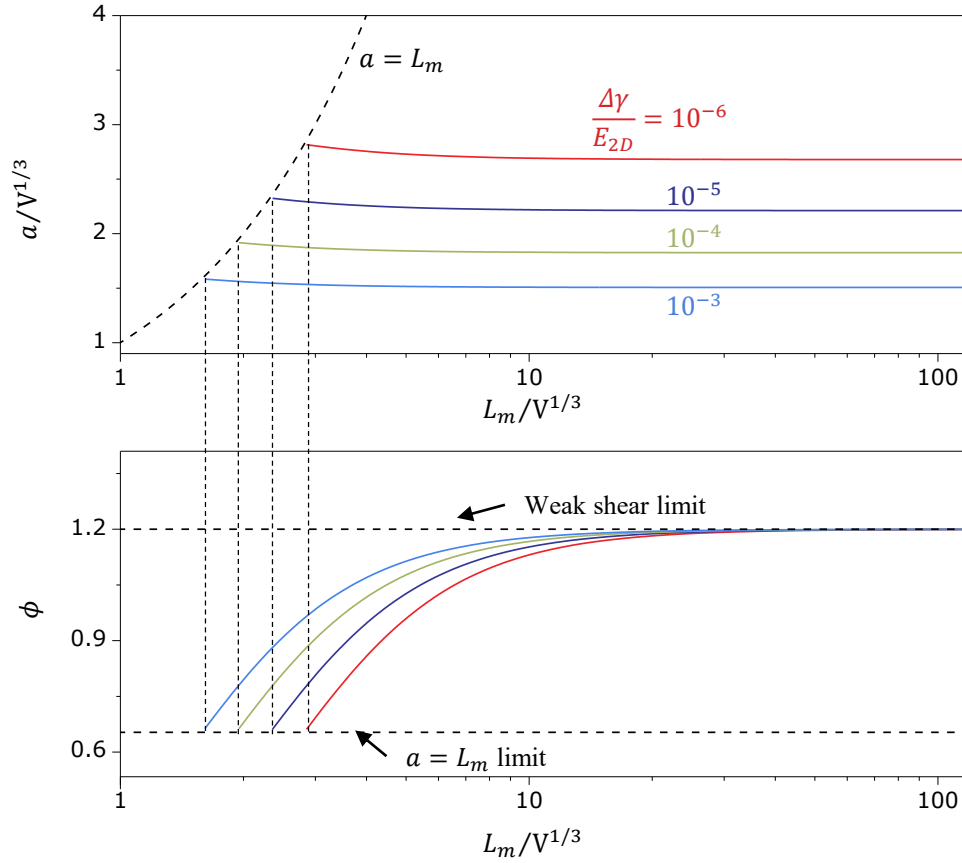


Figure 6.5: Effect of the finite membrane size in MD simulations on the blister radius a and the coefficient ϕ in the height-to-radius ratio equation (6.19).

To compare with MD simulations in section 6.6, where the graphene/substrate interface is frictionless and periodic boundary conditions are applied with a finite-sized graphene membrane, the analysis for the weak shear limit is modified so that the radial

displacement in (6.15) is zero at $r = L_m$, for the square-shaped membrane with a half side length of L_m in MD simulations. As a result, $C_2 = \frac{(1+\nu)C_1}{(1-\nu)L_m^2}$ and $u = \frac{(1+\nu)C_1}{E_{2D}L_m} \left[-\frac{L_m}{r} + \frac{r}{L_m} \right]$ for $r > a$. The displacement continuity at $r = a$ then requires that $C_1 = -\frac{E_{2D}au_s}{(1+\nu)} \left[1 - \left(\frac{a}{L_m} \right)^2 \right]^{-1}$. Following the same process in (6.16-6.18), we obtain $u_s = u_0 - h^2/a$ and $u_0 = \frac{(3-\nu)h^2}{4a}$, which then leads to (6.4) for the height-to-radius ratio with $\phi = \frac{6L_m^2(1-\nu)}{5L_m^2(1-\nu)+3a^2(1+\nu)}$.

. Note that, in this case, ϕ depends on the ratio L_m/a . For a constant liquid volume ($V = \pi a^2 h/2$), the coefficient ϕ can be determined by solving a nonlinear algebraic equation as:

$$\phi + \frac{3(1+\nu)}{5(1-\nu)} \left(\frac{2V}{\pi L_m^3} \right)^{\frac{2}{3}} \left(\frac{E_{2D}}{\Delta\gamma} \right)^{\frac{1}{6}} \phi^{\frac{5}{6}} = \frac{6}{5} \quad (6.19)$$

Apparently, in this case, the height-to-radius ratio of the blister depends on the size of the membrane through the ratio L_m^3/V . As shown in Figure 6.5, as $L_m^3/V \rightarrow \infty$, the coefficient ϕ approaches the weak shear limit ($\phi = \frac{6}{5}$). However, since the size of the membrane is limited in MD simulations, (6.19) predicts a smaller value for ϕ , and hence a smaller height-to-radius ratio for the blister by (6.4). Figure 6.5 plots the radius of the blister as a function of the membrane size, both normalized by $V^{1/3}$. Clearly, the blister radius decreases with increasing adhesion energy ($\Delta\gamma = \Gamma - \gamma_w(\cos \theta_s + \cos \theta_m)$). Meanwhile, the radius increases slightly with decreasing L_m . In any case, the radius should be no greater than the half side length of the membrane, i.e., $a \leq L_m$. In the extreme case when $a = L_m$, the edge of the blister is fixed with no sliding, and the solution reduces to the strong shear limit with $\phi \approx 0.6$ for the case of a graphene monolayer as the membrane.

6.4 ASPECT RATIOS OF VARIOUS BLISTERS

Another way to determine the coefficient in (6.4), which is much easier to implement, is to taking advantage of the analytical solutions to strain fields in Chapter 5.3.

We show that using these analytical solutions would lead to the same results as those in section 6.3. In addition, the scaling relation works for both liquid-/gas-filled bubbles and point-loaded tents. In general, the total energy of the system U_{total} consists of the following three energy terms:

$$U_{total} = U_e + U_i + U_p \quad (6.20),$$

where U_e is the elastic strain energy of the membrane, U_i is the interface adhesion energy between the membrane and the substrate, and U_p is the potential energy associated with the blister contents. We can now derive the elastic strain energy by analytical results in (5.4) in Chapter 5. Again, the bending effects can be neglected reasonably for our experimentally observed blisters. The elastic stretching energy per unit area of the membrane can still be calculated according to (6.8). This, in general, leads to the strain energy of a blister in the present study:

$$U_e = 2\pi \int_0^a U_s(r) r dr + 2\pi \int_a^\infty U_s(r) r dr, \quad (6.21)$$

where the first term represents the strain energy in the laterally loaded membrane, and the second term is a result of interface sliding (which is negligible for the strong-shear limit).

The adhesion energy required to form the blister is simply the energy change per unit area, $\Delta\gamma$, multiplied by the blister area,

$$U_i = \pi a^2 \Delta\gamma, \quad (6.22)$$

where we assume that the change in contact area due to the deformation is negligible since it scales as $a^2 \mathcal{O}(h^2/a^2)$.

The last term in the Supplementary (6.19) is the potential energy associated with contents, which is to be determined according to the interface confining conditions. For a liquid-filled bubble and a post-supported tent, $U_p = 0$. For a bubble filled with ideal gas, U_p follows the ideal gas law. Here, we derive ϕ for the six different scenarios with differing interfacial shear conditions and interfacial contents.

- i) *Liquid-filled bubbles with a strong-shear interface.* The membrane outside the bubble edge does not deform and confined liquid does not contribute to U_p due to its incompressibility. The total free energy for the bubble is then obtained as a function of two kinematic parameters

$$U_{total}(a) = \frac{2(7-\nu)E_{2D}V^4}{3\pi^3(1-\nu)a^{10}} + \pi a^2 \Delta\gamma, \quad (6.23)$$

where $V = \frac{\pi}{2}a^2h$ is the volume of the interface confined liquid. Given the incompressible V , the first term on the right-hand side of Supplementary (6.23) is the elastic strain energy in the membrane, which decreases with increasing the bubble radius a . The second term stems from the change of interface energy, which increases with increasing bubble radius. The competition between the two terms leads to an equilibrium bubble radius that minimizes the total free energy, namely

$$\left(\frac{\partial U_{total}}{\partial a}\right)_V = 0, \quad (6.24)$$

which gives rise to (6.4) with $\phi = \frac{24(1-\nu)}{5(7-\nu)}$.

- ii) *Liquid-filled bubbles with a weak-shear interface.* The elastic strain energy outside the bubble has to be considered due to the interfacial sliding. Following (6.20-6.23), the total free energy is obtained as

$$U_{total}(a) = \frac{8E_{2D}V^4}{3\pi^3a^{10}} + \pi a^2 \Delta\gamma. \quad (6.25)$$

Similarly, $\left(\frac{\partial U_{total}}{\partial a}\right)_V = 0$ gives rise to (6.4) with $\phi = \frac{6}{5}$.

- iii) *Gas-filled bubbles with a strong-shear interface.* In this case, the isothermal expansion of fixed number of interface confined gas molecules (N) contributes to the potential energy:

$$U_p = \int_{V(p)}^{V(p_0)} p dV. \quad (6.26)$$

where $V(p)$ is the volume of an ideal gas under current pressure p and $V(p_0)$ is the volume of ideal gas under atmospheric pressure. The pressure and volume of the ideal gas are assumed to follow the ideal gas law, which behaves as a constraint when minimizing the total energy of the system:

$$NkT = pV \simeq \frac{\pi(7-\nu)}{6(1-\nu)} \frac{E_2 D h^4}{a^2}, \quad (6.27)$$

where k is Boltzmann constant and T is temperature, and the right-hand side relation is readily obtained by minimizing the potential energy of the uniformly pressurized membrane. By combining (6.19-6.22) with (6.27), we write the total free energy in terms of only two kinematic parameters (N, a):

$$U_{total}(a) = \frac{NkT}{4} - NkT \ln Aa^{2/5} + \pi a^2 \Delta\gamma, \quad (6.28)$$

where A is a constant related to the reference state of gas in ambient condition. The first term on the right-hand side of (6.28) is the elastic strain energy in the membrane, which is independent of both the bubble radius and height under constant N . The second term is the potential energy of the gas, which decreases with increasing bubble radius, a . Meanwhile, the interfacial energy term increases as part of graphene is detached from the substrate. The competition of the last two terms leads to an equilibrium bubble radius when the total free energy is minimized such that

$$\left(\frac{\partial U_{total}}{\partial a} \right)_N = 0. \quad (6.29)$$

(6.29) thus gives rise to

$$\Delta\gamma = \frac{5NkT}{4\pi a^2}. \quad (6.30)$$

By plugging Supplementary (6.27), we derive $\phi = \frac{24(1-\nu)}{5(7-\nu)}$ for Supplementary (6.4), which is also the case for liquid-filled bubbles with a strong-shear interface.

- iv) *Gas-filled bubbles with a weak-shear interface.* When interface sliding occurs, (6.27) becomes

$$NkT = pV \simeq \frac{2\pi E_{2D}h^4}{3a^2}. \quad (6.31)$$

After combining (6.19-6.22) and (6.31), we find that (6.28-6.30) still work for the gas-filled bubbles with a weak-shear interface. Then combining (6.30) and (6.31) gives us $\phi = \frac{6}{5}$, which also applies to liquid-filled bubbles with a weak-shear interface.

- v) *Tents with a strong-shear interface.* The tent can be treated as a displacement-controlled delamination experiment where the height is fixed and U_p is zero. From (6.18-6.21), the total energy of a tent with clamped boundaries is

$$U_{total}(a) = \frac{\pi(5-3\nu)E_{2D}h^4}{72(1-\nu)a^2} + \pi a^2 \Delta\gamma. \quad (6.32)$$

Clearly, the competition between the elastic strain energy and the interface energy leads to

$$\left(\frac{\partial U_{total}}{\partial a}\right)_h = 0, \quad (6.33)$$

which gives rise to (6.4) with $\phi = \frac{72(1-\nu)}{5-3\nu}$.

- vi) *Tents with a weak-shear interface.* The elastic strain energy outside the tent is considered. Following (6.19-6.22), the total energy is then obtained:

$$U_{total}(a) = \frac{\pi E_{2D}h^4}{18a^2} + \pi a^2 \Delta\gamma. \quad (6.34)$$

Similarly, $\left(\frac{\partial U_{total}}{\partial a}\right)_h = 0$, which gives rise to (6.4) with $\phi = 18$.

We have determined ϕ for 2D material bubbles and tents of both strong- and weak-shear interfaces, as summarized in Table 6.1. The experimental discovery of the constant aspect ratio of 2D material bubbles for a given 2D material-substrate system may support our conclusion; experimental data for 2D material tents can also be found in the literature

(Dai et al., 2020; Zong et al., 2010) (also see references based on nanoparticle methods in Table 6.5).

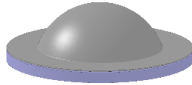
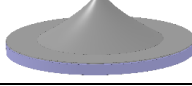
Shape		Strong shear	Weak shear
Bubble		$\frac{24(1-\nu)}{5(7-\nu)}$	$\frac{6}{5}$
Tent		$\frac{72(1-\nu)}{5-3\nu}$	18

Table 6.1: The prefactor ϕ that determines the aspect ratio by $\Delta\gamma/E_{2D}$ in (6.4).

6.5 HENCKY'S ANALYSIS

Next, we present a more rigorous analysis for the liquid-filled blisters following Hencky's approach (Fichter, 1997; Hencky, 1915).

6.5.1 Finite shear

The shear interactions between the membrane and the substrate is represented by a finite interfacial shear stress in the supported region ($a < r < \rho a$), where both the blister radius (a) and the outer radius of the shear zone (ρa) are to be determined depending on the liquid volume and the shear stress. The membrane size is assumed to be large so that the shear zone does not reach the edge of the membrane. The membrane outside the sliding zone ($r > \rho a$) is not deformed or stressed. Since h/a is typically small, the membrane is assumed to conform to the liquid ($r < a$) with a uniform pressure, similar to the gas-filled blisters. Outside the blister, the substrate-supported membrane is subject to in-plane stresses and a constant interfacial shear stress in the shear zone ($a < r < \rho a$). The two

parts are coupled at the edge of the blister ($r = a$) by the continuity conditions in terms of the stress and displacement.

According to Chapter 2.2, the mechanical equilibrium of the bulged membrane ($r < a$) over the liquid requires that:

$$\frac{d}{dr}(rN_r) - N_\theta = 0, \quad (6.35a)$$

$$\frac{d}{dr}\left(rN_r \frac{dw}{dr}\right) + qr = 0, \quad (6.35b)$$

where q is the intensity of the transverse loading (i.e., the pressure difference across the membrane). These equations assume axisymmetric deformation and ignore the bending rigidity of the membrane. With linear elasticity and nonlinear kinematics, (6.35a) and (6.35b) can be combined into one nonlinear equation:

$$N_r^2 \frac{d}{dr} \left[\frac{1}{r} \frac{d}{dr} (r^2 N_r) \right] + \frac{E_{2D} q^2}{8} r = 0. \quad (6.36)$$

Following Hencky's approach (Fichter, 1997; Hencky, 1915), the solution to (6.35-6.36) is assumed to take the polynomial form as:

$$N_r(r) = \left(\frac{E_{2D} q^2 a^2}{64} \right)^{\frac{1}{3}} \sum_{n=0}^{\infty} b_{2n} \left(\frac{r}{a} \right)^{2n}, \quad (6.37a)$$

$$N_\theta(r) = \left(\frac{E_{2D} q^2 a^2}{64} \right)^{\frac{1}{3}} \sum_{n=0}^{\infty} (2n+1) b_{2n} \left(\frac{r}{a} \right)^{2n}, \quad (6.37b)$$

$$w(r) = \left(\frac{q a^4}{E_{2D}} \right)^{\frac{1}{3}} \sum_{n=0}^{\infty} a_{2n} \left[1 - \left(\frac{r}{a} \right)^{2n+2} \right], \quad (6.37c)$$

where seven terms ($n = 0 - 6$) are typically included in each polynomial. Substituting (6.37a) into Eq. (6.36), all the coefficients b_{2n} can be determined in terms of one parameter, b_0 . That is, $b_2 = -\frac{1}{b_0^2}$; $b_4 = -\frac{2}{3b_0^5}$; $b_6 = -\frac{13}{18b_0^8}$; $b_8 = -\frac{17}{18b_0^{11}}$; $b_{10} = -\frac{37}{27b_0^{14}}$; $b_{12} = -\frac{1205}{567b_0^{17}}$. Similarly, substituting (6.37b) into Eq. (35b) yields: $a_0 = \frac{1}{b_0}$; $a_2 = \frac{1}{2b_0^4}$; $a_4 = \frac{5}{9b_0^7}$; $a_6 = \frac{55}{72b_0^{10}}$; $a_8 = \frac{7}{6b_0^{13}}$; $a_{10} = \frac{205}{108b_0^{16}}$; $a_{12} = \frac{17051}{5292b_0^{19}}$.

Given a and q , the coefficient b_0 can be determined numerically, depending on Poisson's ratio of the membrane and boundary conditions. For instance, $b_0 = 1.67$ was obtained for an elastic membrane clamped at the edge with $\nu = 0.165$ (for graphene).

Outside the blister, the supported 2D membrane is constrained to in-plane deformation with axisymmetry and a constant interfacial shear stress (frictional force per unit area), τ , which opposes sliding. For a given blister pressure or volume, there would exist an annular interfacial sliding zone ($a < r < \rho a$), beyond which there would be no sliding and thus zero shear stress. Assuming no buckling or any out-of-plane deflection (i.e., $w = 0$) for the supported membrane outside the blister, the in-plane equilibrium equation is:

$$\frac{d}{dr}(rN_r) - N_\theta + \tau r = 0. \quad (6.38)$$

With linear elasticity and in-plane kinematics, (6.38) can be re-written as:

$$\frac{d}{dr}\left[N_r + \frac{d}{dr}(rN_r)\right] = -(2 + \nu)\tau. \quad (6.39)$$

Solving (6.38) and (6.39) with the boundary condition at $r = \rho a$, where the in-plane stresses are zero ($N_r = N_\theta = 0$), we obtain:

$$N_r = \tau a \left[(2 + \nu) \left(-\frac{1}{3} \frac{r}{a} - \frac{\nu-1}{6(2+\nu)} \rho^3 \frac{a^2}{r^2} \right) + \frac{1+\nu}{2} \rho \right], \quad (6.40a)$$

$$N_\theta = \tau a \left[(2 + \nu) \left(-\frac{1+2\nu}{3(2+\nu)} \frac{r}{a} + \frac{\nu-1}{6(2+\nu)} \rho^3 \frac{a^2}{r^2} \right) + \frac{1+\nu}{2} \rho \right]. \quad (6.40b)$$

At the edge of the blister ($r = a$), the radial stress and displacement are continuous. As a result, both the strain and stress components are continuous, i.e., $N_r^{in} = N_r^{out}$ and $N_\theta^{in} = N_\theta^{out}$ at $r = a$. Based on (6.37) for the bulged membrane and (3.40) for the membrane outside the blister, the continuity conditions at the edge of the blister lead to:

$$\tau a \left[(2 + \nu) \left(-\frac{1}{3} - \frac{\nu-1}{6(2+\nu)} \rho^3 \right) + \frac{1+\nu}{2} \rho \right] = \left(\frac{E_{2D} q^2 a^2}{64} \right)^{\frac{1}{3}} \left(b_0 - \frac{1}{b_0^2} - \frac{2}{3b_0^5} - \dots \right), \quad (6.41a)$$

$$\tau a \left[(2 + \nu) \left(-\frac{1+2\nu}{3(2+\nu)} + \frac{\nu-1}{6(2+\nu)} \rho^3 \right) + \frac{1+\nu}{2} \rho \right] = \left(\frac{E_{2D} q^2 a^2}{64} \right)^{\frac{1}{3}} \left(b_0 - \frac{3}{b_0^2} - \frac{10}{3b_0^5} - \dots \right). \quad (6.41b)$$

Given τ , a and q , (6.41) can be solved to obtain the Hencky constant b_0 and the ratio ρ for the outer radius of the interfacial sliding zone.

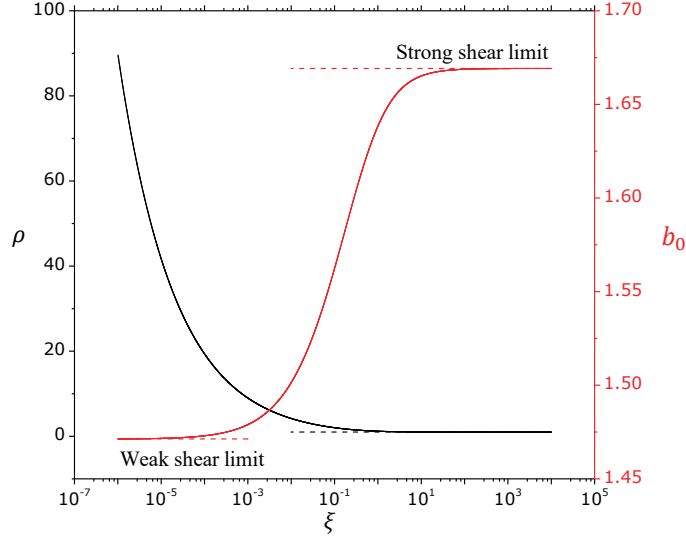


Figure 6.6: The radius ratio ρ of the interfacial sliding zone (black lines) and Hencky constant b_0 (blue lines) as a function of ξ .

For a liquid-filled blister with a constant volume (V), we define a length scale as $L_w = V^{1/3}$. By integrating the deflection in (6.37), the volume is related to the pressure difference as:

$$V = 2\pi \int_0^a w(r) r dr = \frac{2\pi a^{10/3} q^{1/3}}{E_{2D}^{1/3}} \sum_n a_{2n} \left(\frac{n+1}{2n+4} \right). \quad (6.42)$$

Thus, the normalized pressure difference is:

$$\bar{q} = \frac{q L_w}{E_{2D}} = \left(\frac{L_w}{a} \right)^{10} \left[2\pi \sum_n a_{2n} \left(\frac{n+1}{2n+4} \right) \right]^{-3}. \quad (6.43)$$

For given τ , a and V , (6.41) can be solved to obtain b_0 and ρ , both depending on three dimensionless parameters: ν , $\bar{\tau} = \frac{\tau L_w}{E_{2D}}$, and $\bar{a} = \frac{a}{L_w}$. Moreover, for a particular membrane material with a constant Poisson's ratio ν , b_0 and ρ depend on a single parameter: $\xi = \bar{\tau} \bar{a}^7$. In Figure 6.6, we plot b_0 and ρ versus ξ for graphene ($\nu = 0.165$). Clearly, when $\xi \rightarrow \infty$ (i.e., $\tau \rightarrow \infty$ or $\bar{a} \rightarrow \infty$), the results approach the strong shear limit

without any sliding (i.e., $\rho = 1$ and $b_0 = 1.67$). With a finite interfacial shear stress τ , ρ increases as ξ decreases. In the weak shear limit ($\xi \rightarrow 0$), $\rho \rightarrow \infty$ and $b_0 \rightarrow 1.47$.

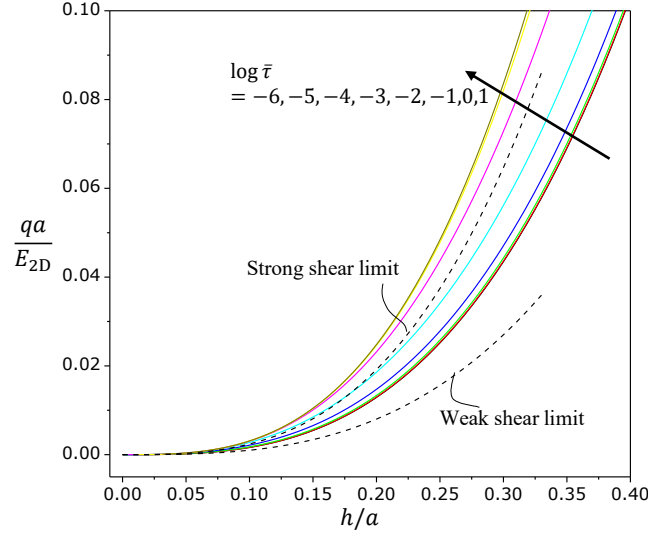


Figure 6.7: The dimensionless pressures as a function of height/radius ratio under various shear stress. Blue and red dots are from the analysis based on Section 5.3.

According to (6.37), the blister height, $h = w|_{r=0}$, and the height-to-radius ratio is:

$$\frac{h}{a} = C_1 \left(\frac{qa}{E_{2D}} \right)^{\frac{1}{3}} = C_1 \bar{a}^{-3} \left[2\pi \sum_n a_{2n} \left(\frac{n+1}{2n+4} \right) \right]^{-1}, \quad (6.44)$$

where $C_1 = \sum_n a_{2n} = \frac{1}{b_0} + \frac{1}{2b_0^4} + \frac{5}{9b_0^7} + \dots$. By (6.44), h/a depends on both \bar{a} and $\bar{\tau}$.

Similarly, by (6.43), the normalized pressure difference \bar{q} depends on \bar{a} and $\bar{\tau}$ as well. For a given $\bar{\tau}$, \bar{q} is related to \bar{a} and then to h/a . It is thus possible to determine the pressure inside the blister based on the measurement of the height and radius of the blisters.

Figure 6.7 plots $\frac{qa}{E_{2D}} (= \bar{q}\bar{a})$ as a function of h/a for blisters with various interfacial shear stresses. Note that, (6.43) can be rewritten as:

$$q = \eta(\xi, \nu) \frac{E_{2D} h^3}{a^4}, \quad (6.45)$$

where $\eta(\xi, \nu) = C_1^{-3}$. We find that the $\frac{qa}{E_{2D}} - \frac{h^3}{a^3}$ curves collapse when $\bar{\tau} \geq 1$ (strong shear)

and $\bar{\tau} \leq 10^{-4}$ (weak shear). (6.44) is similar to (6.4) by the simple analysis, but it is more

accurate. In particular, for the strong and weak shear limits, the simple analysis underestimates the pressure significantly.

For given τ and V , the blister radius is determined by minimizing the total free energy of the blister, including the elastic strain energy of the membrane and the interfacial energy. With the membrane stresses in (6.37), the strain energy for the bulged membrane can be obtained as

$$F_{e1}(a) = 2\pi \int_0^a U_S(r) r dr = E_{2D} L_w^2 \left(\frac{L_w}{a}\right)^{10} f_1(\xi, \nu). \quad (6.46)$$

Similarly, the strain energy for the supported membrane can be obtained with the in-plane stresses in (6.40) as

$$F_{e2}(a) = 2\pi \int_a^{\rho a} U_S(r) r dr = E_{2D} L_w^2 \left(\frac{L_w}{a}\right)^{10} f_2(\xi, \nu). \quad (6.47)$$

Relative to a reference state of the membrane on the substrate without liquid, the interfacial energy of the liquid-filled blister is:

$$F_i(a) = \pi a^2 (\gamma_{ws} - \gamma_{ms}) + \gamma_{wm} A', \quad (6.48)$$

where A' is the area of blister surface, i.e.,

$$A' = 2\pi \int_0^a \sqrt{1 + \left(\frac{dw}{dr}\right)^2} r dr = C_3 \pi a^2, \quad (6.49)$$

and C_3 is a constant that depends on b_0 . With $\Delta\gamma = \gamma_{mw} + \gamma_{sw} - \gamma_{ms}$, we have

$$F_i(a) = \pi a^2 \Delta\gamma \left[1 + (C_3 - 1) \frac{\gamma_{wm}}{\Delta\gamma}\right]. \quad (6.50)$$

To minimize the total free energy, we set

$$\bar{F}(\bar{a}, \bar{\tau}, \nu) = \frac{F_{e1} + F_{e2} + F_i}{E_{2D} L_w^2} = [f_1(\xi, \nu) + f_2(\xi, \nu)] \bar{a}^{-10} + \frac{\pi \Delta\gamma}{E_{2D}} \left[1 + (C_3 - 1) \frac{\gamma_{wm}}{\Delta\gamma}\right] \bar{a}^2, \quad (6.51)$$

and

$$\frac{\partial \bar{F}}{\partial \bar{a}} = 0, \quad (6.52)$$

by which $\bar{a} = a/L_w$ can be solved as a function of $\bar{\tau}$, ν , $\frac{\Delta\gamma}{E_{2D}}$ and $\frac{\gamma_{wm}}{E_{2D}}$. Then, by (6.44), the ratio h/a can be obtained as well. Since $C_3 \sim 1 + \mathcal{O}(h^2/a^2)$, here we neglect the effects of

$\frac{\gamma_{wm}}{\Delta\gamma}$ due to the small aspect ratio observed in our experiments, and only examine the effect of shear stress on h/a in Figure 6.8. Similar to the observation in Figure 6.7, $h/a - \Delta\gamma/E_{2D}$ curves collapse when $\bar{\tau} \geq 1$ (strong shear) and $\bar{\tau} \leq 10^{-4}$ (weak shear) and show agreement with the simple analysis under small h/a (< 0.15). However, slight deviations can be observed under high aspect ratios, implying the limitation of our simple analysis for large deformation.

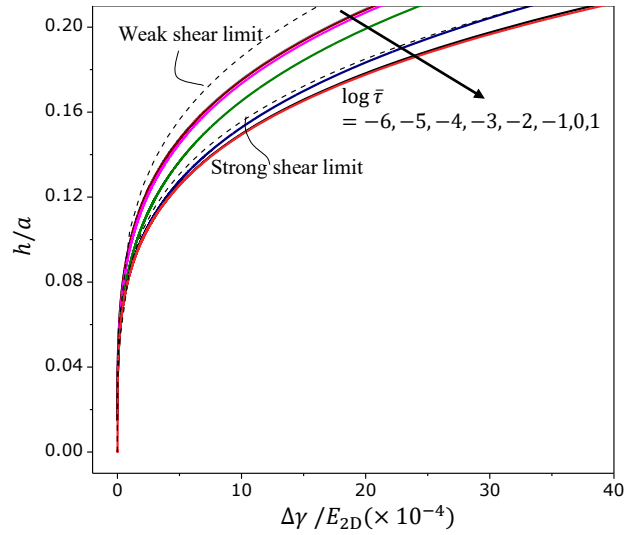


Figure 6.8: The dependency of the aspect ratio on $\Delta\gamma/E_{2D}$ for different shear stress. Blue and red dots are from a simple analysis.

6.5.2 Finite sheet size in experiments

Next, we consider the effect of finite membrane size ($\rho = \rho_0$). As the 2D membranes in experiments typically have finite lateral sizes (here, defined as $\rho_0 a$), the sliding zone around a blister could grow to the boundary of the membrane if the interface is relatively weak or if the blister is located near the edge of a membrane. In these cases, the sliding zone radius ratio ρ would become fixed once it reaches the critical value ρ_0 as shown in Fig. S9. Unlike the previous case with $N_r = N_\theta = 0$ at $r = \rho a$, the boundary

condition at $r = \rho_0 a$ is slightly different, i.e., $N_r = 0$ but $N_\theta \neq 0$. Thus, for a finite outer boundary, the (6.40) can be solved exactly to obtain:

$$N_r = \tau a \left[-\frac{(2+\nu)}{3} \frac{r}{a} + A_0 \left(\frac{a^2}{r^2} - \frac{1}{\rho_0^2} \right) + \frac{(2+\nu)}{3} \rho_0 \right], \quad (6.53a)$$

$$N_\theta = \tau a \left[-\frac{(1+2\nu)}{3} \frac{r}{a} + A_0 \left(-\frac{a^2}{r^2} - \frac{1}{\rho_0^2} \right) + \frac{(2+\nu)}{3} \rho_0 \right], \quad (6.53b)$$

where A_0 is a dimensionless constant to be determined. Then, based on (6.37) for the bulged membrane over the blister and (6.53) for the supported membrane, the continuity conditions at the edge of the blister ($r = a$) lead to:

$$\tau a \left[-\frac{(2+\nu)}{3} + A_0 \left(1 - \frac{1}{\rho_0^2} \right) + \frac{(2+\nu)}{3} \rho_0 \right] = \left(\frac{Etq^2 a^2}{64} \right)^{\frac{1}{3}} \left(b_0 - \frac{1}{b_0^2} - \frac{2}{3b_0^5} - \dots \right) \quad (6.54a)$$

$$\tau a \left[-\frac{(1+2\nu)}{3} + A_0 \left(-1 - \frac{1}{\rho_0^2} \right) + \frac{(2+\nu)}{3} \rho_0 \right] = \left(\frac{Etq^2 a^2}{64} \right)^{\frac{1}{3}} \left(b_0 - \frac{3}{b_0^2} - \frac{10}{3b_0^5} - \dots \right) \quad (6.54b)$$

Combining Eq. (6.43) and Eq. (6.54) we can solve for the constant A_0 and Hencky constant b_0 , with given ν , $\bar{\tau}$, and \bar{a} . Following the same process, we can calculate the total free energy $\bar{F}(\bar{a}, \bar{\tau}, \nu)$ and determine \bar{a} by minimizing the free energy. The ratio h/a can still be determined by (6.44), but with b_0 depending on ρ_0 . In Figure 6.9, we demonstrated the effect of ρ_0 on the ratio h/a . We find that the finite size effect is negligible when $\rho_0 > 4$, which can be readily satisfied experimentally by choosing 2D materials blisters not located too close to the edge of a membrane.

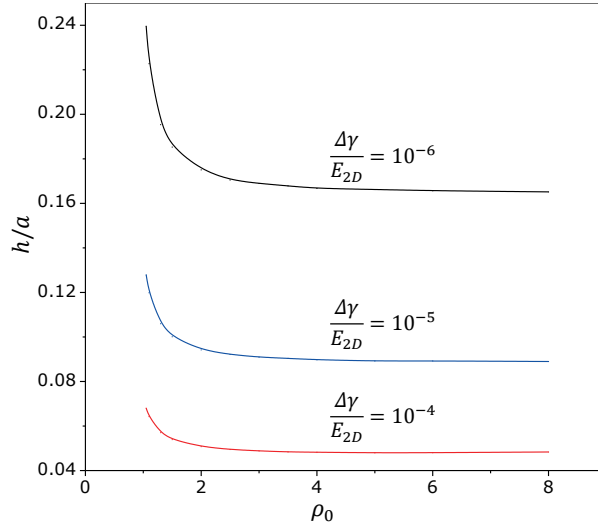


Figure 6.9: The aspect ratio as a function of ρ_0 . The shear stress used for this demonstration is $\bar{\tau} = 10^{-5}$, with which interface is more sensitive to the lateral size compared that with strong shear.

6.6 MD SIMULATIONS¹

As verification of our analytical model, MD simulations were conducted to simulate water-filled blisters trapped between a monolayer graphene membrane and a rigid substrate (See details in Appendix in Sanchez et al. 2018).

6.6.1 Comparison with analytical results

Figure 6.10 shows a snapshot of a graphene blister with 2700 water molecules shaped like a spherical cap by the top and side views. We retrieved the blister configuration by sampling 10 snapshots evenly after 1 ns relaxation. The blister height was measured as the difference between the largest z position of the carbon atoms and the average z position (~ 0) outside the blister edge (see Figure 6.10B). The blister diameter was measured as the maximum span distance for the carbon atoms with $z > 0.1$ nm. The height-radius ratio

¹ Dr. Peng Wang performed the simulations under the supervision of Prof. Rui Huang.

(h/a) was calculated by averaging over the 10 snapshots with an error bar for the standard deviation.

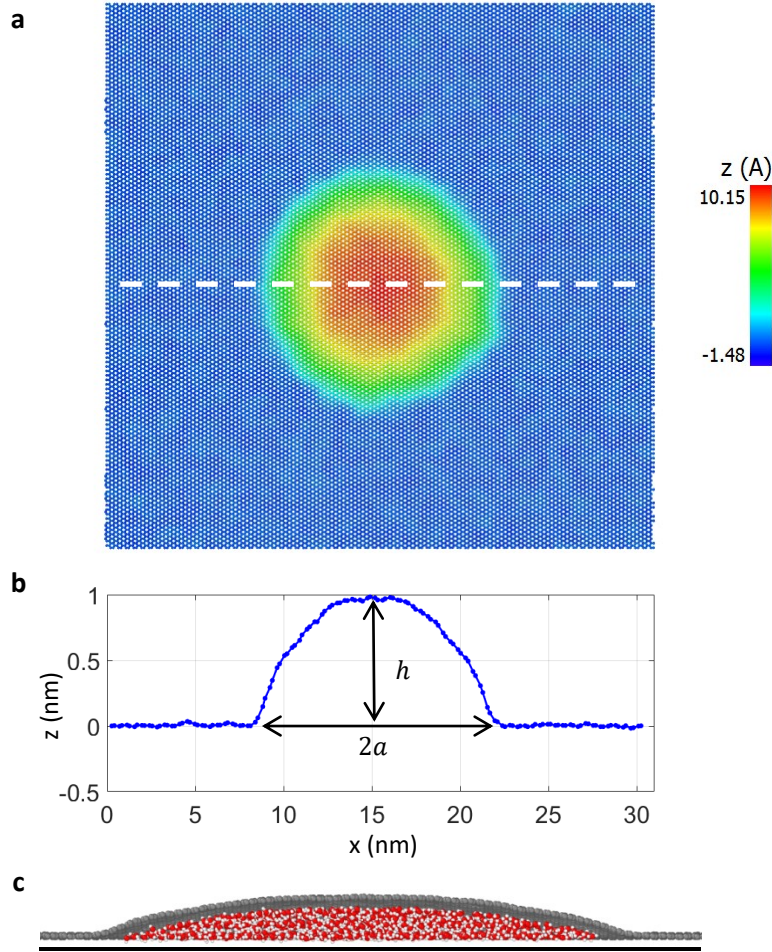


Figure 6.10: MD simulation of a graphene blister with 2700 water molecules. The adhesion energy was $\Gamma_{GS} = 0.242 \text{ J/m}^2$, while the water contact angles were 60° and 40° for graphene and the substrate, respectively. (a) A top view snapshot of the blister, with color contour for the z -position of the carbon atoms in graphene; (b) A height profile along a line scan (dashed line in a) across the blister; (c) A cross-sectional view of the blister, showing the water molecules (oxygen in red and hydrogen in white) between graphene (carbon in gray) and the substrate surface (blue line).

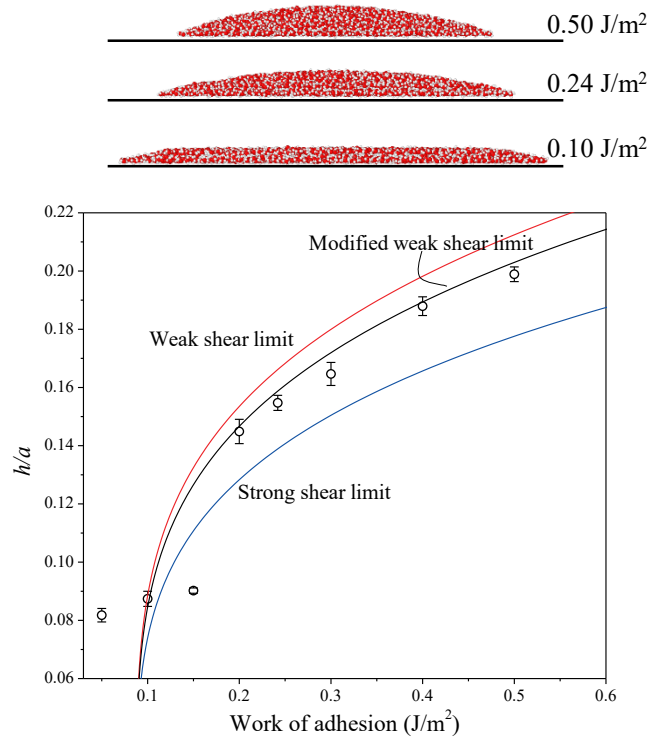


Figure 6.11: Modeling and MD simulations of water-filled blisters. MD simulation results (circular markers) best agree with our simplified model, assuming a frictionless, sliding interface (modified weak shear). The deviations, especially under small height or aspect ratio, is attributed to the size limitation of MD, which can induce discrete behaviors. The figures in the top panel demonstrate how the shape of the blister changes for different values of the work of adhesion.

As predicted by (6.4), the aspect ratio of the blister depends on the graphene-to-substrate adhesion energy (Γ) and the two water contact angles (θ_s and θ_m). For the MD simulations, we set θ_m to be 60° and θ_s to be 40° by selecting proper parameters for the interaction potentials between water and graphene and between water and the substrate. The interaction parameters between graphene and the substrate are varied to simulate graphene blisters with different aspect ratios as a result of different adhesion energy Γ . It is noted that it may not be possible to fully capture the mechanics, wetting, and surface chemistry by using the empirical force-fields in the present study.

Figure 6.11 plots the MD results in comparison with the analytical predictions, along with three snapshots for the trapped water molecules ($N = 2700$). When the adhesion energy is relatively large ($\Gamma > 0.2 \text{ J/m}^2$), the water molecules take the shape of a spherical cap as assumed in the continuum model. In this case, the aspect ratio h/a increases with increasing adhesion energy, in close agreement with the analytical prediction assuming a frictionless interface. As expected, the results are bounded by the strong shear limit $\left[\phi = \frac{24(1-\nu)}{5(7-\nu)}\right]$ and the weak shear limit $\left(\phi = \frac{6}{5}\right)$ for an infinitely large membrane. The weak shear limit overestimates the aspect ratio in MD due to the periodic boundary conditions employed in the MD simulations, and the strong shear limit underestimates the aspect ratio due to the assumption of no sliding. And the modified weak shear model described in section 6.3.3 agrees with our MD simulation results very well, except a number of data at small aspect ratios. We explain the deviation as follows.

6.6.2 Breakdown of the continuum model

By assuming the trapped water in the blister as a continuum liquid, the model predicts the shape of the blister close to a spherical cap. However, our MD simulations showed that the blister might take a different shape when the membrane/substrate adhesion energy was relatively low, and the number of water molecules was small. Instead of a spherical cap, the top of the blister was flat, indicating that the water molecules formed discrete layers. In this case, the continuum model breaks down because the trapped water cannot be treated as a continuum liquid. It is found that the breakdown occurs when the height of the blister predicted by the continuum model drops below the thickness of three water monolayers. A simple analysis is presented below to predict the breakdown condition in terms of the adhesion energy and the number of water molecules.

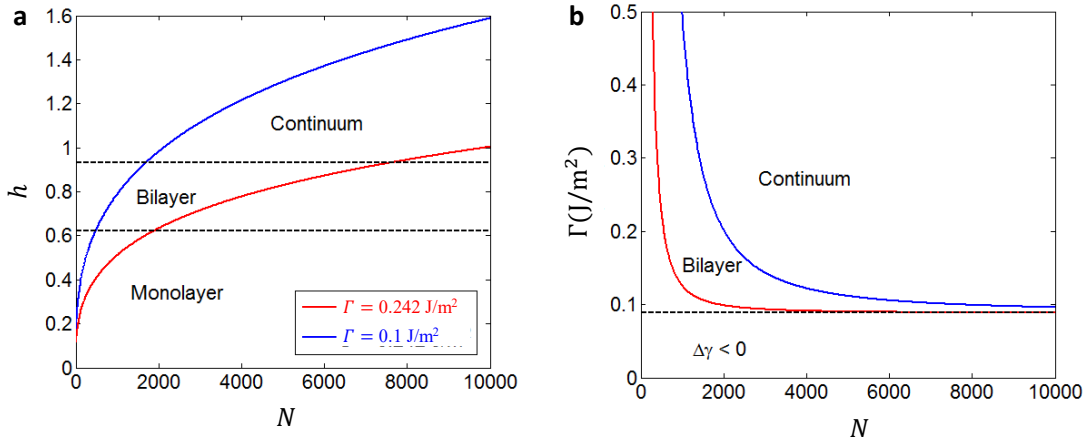


Figure 6.12: (a) The height of graphene blister as a function of the number of water molecules, predicted by the continuum model for $\Gamma_{\text{GS}} = 0.1 \text{ J/m}^2$ and 0.242 J/m^2 , where the dashed line indicates the critical height for the continuum model. (b) The breakdown limit for the continuum model, in terms of the adhesion energy Γ_{GS} and the number of water molecules N with the water contact angles being 60° and 40° for graphene and the substrate, respectively.

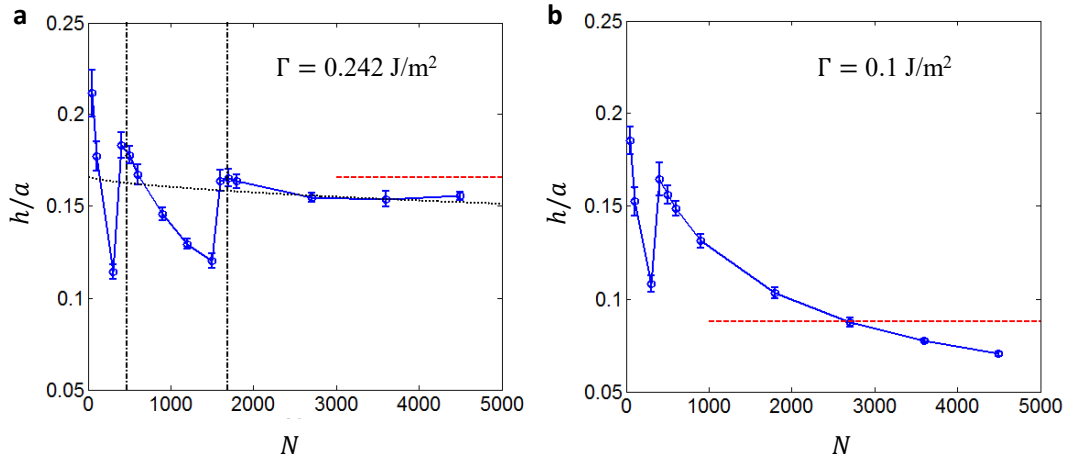


Figure 6.13: Blister aspect ratio for different numbers of water molecules, for $\Gamma_{\text{GS}} = 0.242 \text{ J/m}^2$ (a) and 0.1 J/m^2 (b) with water contact angles being 60° and 40° for graphene and the substrate, respectively. The dashed line is predicted by the continuum model. The breakdown of the continuum model is predicted at $N = 1690$ for $\Gamma_{\text{GS}} = 0.242$ (dotted vertical line in a) and $N = 7640$ for $\Gamma_{\text{GS}} = 0.1 \text{ J/m}^2$.

By the simple continuum model, the water volume in the blister is approximately

$$V = \frac{1}{2}\pi h a^2. \quad (6.55)$$

The number of water molecules can then be found as

$$N = \rho V, \quad (6.56)$$

where ρ is the number density of water, which equals 33.2 nm^{-3} at $T = 300 \text{ K}$ by the TIP4P/2005 model in MD simulations (Wang et al., 2017f). Thus, the height of the blister can be written as

$$h = \left(\frac{2N}{\pi\rho}\right)^{1/3} \left(\frac{h}{a}\right)^{2/3} = \left(\frac{2N}{\pi\rho}\right)^{1/3} \left(\phi \frac{\Gamma - \gamma_w(\cos\theta_m + \cos\theta_s)}{E_{2D}}\right)^{\frac{1}{6}}, \quad (6.57)$$

where (6.4) is used for the ratio $\frac{h}{a}$. Note that, under the condition of MD simulations, the parameter ϕ is given by (6.19) as a function of Γ and V (or N). For a given adhesion energy Γ and the water contact angles, the blister height decreases with a decreasing number of water molecules, as shown in Figure 6.12a (also 6.13a). When the height drops below a critical level, the continuum model breaks down, and the water molecules form discrete layers instead. The critical height is roughly three times the thickness of a water monolayer, which is estimated as $h_c = 3\rho^{-1/3} = 0.93 \text{ nm}$. Thus, the continuum model holds only when $h > h_c$. For $\Gamma = 0.242 \text{ J/m}^2$, the continuum model breaks down when the number of water molecules $N < 1690$, while for $\Gamma = 0.1 \text{ J/m}^2$ the breakdown occurs for $N < 7640$. By setting $h = h_c$, we obtain the critical condition in terms of Γ and N shown as the blue curve in Figure 6.12b (also 6.13b). Furthermore, when the number of water molecules drops below a second critical level ($\sim 2\rho^{-1/3} = 0.62 \text{ nm}$), we may expect the water molecules to form a single monolayer. However, since the continuum model has already broken down, it is not possible to predict exactly when the water monolayer would form.

Nevertheless, the analytical prediction based on the continuum model is confirmed by the MD simulations for the cases when the adhesion energy and the number of water

molecules combine to yield a blister in the shape of a spherical cap, such as $\Gamma > 0.2 \text{ J/m}^2$ and $N = 2700$ in Figure 6.11.

6.7 USEFUL IMPLICATIONS

Having verified our theoretical analysis with MD simulations, we now apply the model to experimentally measured aspect ratio data to extract the adhesion energy for a variety of 2D material interfaces, as well as elaborate on the implications of the data for 2D material systems.

6.7.1 Adhesion metrology

The family of 2D materials has grown appreciably in recent years (Geim and Grigorieva, 2013; Neto et al., 2009). The emergence of each new material brings demands for exploring its vdW interactions with various types of substrates and 2D materials, as many exciting applications of these materials come from stacking them into multilayers and heterostructures. Because of the significance of vdW interactions, many experimental studies have been carried out to measure the adhesion energy of 2D material interfaces, e.g. pressurized blister (Koenig et al., 2011), buckling-based metrology (Brennan et al., 2015; Dai et al., 2016b; Jiang et al., 2014), and double cantilever method (Na et al., 2014; Yoon et al., 2012), as summarized in recent review papers (Akinwande et al., 2017; Bunch and Dunn, 2012; Liechti, 2019). However, it is tedious or impossible to determine the adhesion energy for every pair of the 2D material interface. Based on the present work, we propose that the adhesion energy of a 2D material interface can be readily estimated by measuring the aspect ratio of spontaneously formed nanoblister (if present). To calculate the adhesion energy, (6.4) is rewritten as

$$\Gamma = \frac{E_{2D}h^4}{\phi a^4} + \gamma_w(\cos \theta_m + \cos \theta_s), \quad (6.58)$$

which suggests that once the relevant material properties are available, the adhesion energy can be determined by just measuring the aspect ratio of a blister.

	G-SiO ₂ (Kitt et al., 2013; Wang et al., 2017b)	G-G (Wang et al., 2017b)	HOPG-HOPG (Liu et al., 2012)	MoS ₂ -MoS ₂ (Li et al., 2017a)	G-G	G-hBN	hBN-hBN
Shear stress (MPa)	0.5-3.0	0.02-0.06	0.02-0.04	0.04-0.12	MD simulations (Li et al., 2017c) Average: ~0		
Maximum $\bar{\tau}^*$	$10^{-4}-10^{-3}^{**}$	$< 10^{-4}$	$< 10^{-4}$	$\approx 10^{-4}$			

G denotes graphene; the Blue region shows experimentally measured data; the Pink region shows simulation results, whose averages approach 0 due to their stick-slip friction with periodically changing peak shear stress.

*To estimate the maximum $\bar{\tau}$, we utilized the largest experimentally observed h/a (1.8) and the radius (~300 nm) as well as the highest shear stress in the third row and the lowest E_{2D} in Table 6.3. We conclude that for heterostructures with an atom-level smooth interface, we can safely use the model with frictionless approximations where $\phi = 6/5$.

**For a typical graphene blister on SiO₂ with h/a of ~0.8 and the radius of 200 nm, the $\bar{\tau}$ is in the range from 0.0002 to 0.001. The used ϕ will cause little influence on the adhesion energy estimation since the contact angle part contributes to the Γ greatly.

Table 6.2: Shear stress at 2D material interfaces.

	Graphene (Lee et al., 2008)	MoS ₂ (Bertolazzi et al., 2011)	hBN (Falin et al., 2017)
E (TPa)	1.00	0.27	0.87
E_{2D} (N/m)	340	180	289

Table 6.3: In-plane stiffness of 2D materials.

	G/HOPG(Kozbial et al., 2014; Li et al., 2013)	MoS ₂ (Kozbial et al., 2015)	hBN(Wu et al., 2016)	Ice(Knight, 1967)	CaF ₂ (Zhang et al., 2015)	Mica(Gong et al., 2015)
WC A (°)	64	69	47	12	20	23
	SiO ₂ (Alam et al., 2014)	SiC(Kazakova et al., 2013)	Si(Kissinger and Kissinger, 1991)	Sapphire(Zhang et al., 2013a)	Al ₂ O ₃ (Santos et al., 2003)	V ₂ O ₅ (Lim et al., 2007)
WC A (°)	40	73	60	10	36	0

Note that the exact liquid contact angle is highly challenging to measure since it can be influenced by various surface treatments, treating times, surface roughness, as well as containment types and density. In fact, even for water contact angels, there still exits inconsistency in the literature, especially for water contact angels of 2D materials. Herein, we used the most widely adopted water contact angles, which can allow further comparative studies.

Table 6.4: Water contact angle (WCA) for 2D materials and substrates used in Figure 6.14 and Table 6.5.

We take $\phi = 1.2$ by the weak interface model due to the typically weak interfacial shear resistance for most of the 2D material interfaces (i.e., $\bar{\tau} \leq 10^{-4}$ according to 6.5.1, also see Table 6.2). Note that the strong interface model gives a smaller prefactor ($\phi = 0.6$), thus overestimating the adhesion energy. Assuming water is trapped in the blisters, in Figure 6.14, we calculated the graphene-SiO₂, MoS₂-SiO₂, and MoS₂-Al₂O₃ work of adhesion by using our measurements in Figure 6.2. Our values are in reasonable agreement with values determined in similar systems via alternative methods (0.1-0.4 J/m² for graphene-SiO₂ and 0.04 J/m² for MoS₂-SiO₂, also see Table 6.5) (Boddeti et al., 2013b; Lloyd et al., 2017; Zong et al., 2010). We attribute our slightly lower adhesion values to i) previously neglected, but significant, interfacial sliding; ii) the slight amount of contaminants which can influence the surface tension and contact angle terms for water in (6.4); iii) the rough substrate surface (197 ± 19 pm in our sample) which is believed to cause scattering in adhesion measurements with SiO₂ (Koenig et al., 2011). For our Al₂O₃ substrate, the surface roughness was measured to be 251 ± 10 pm. Notably, nanoblister found in our samples often exhibit some degree of ellipticity (Figure 6.1). Therefore, only approximately circular blisters with minor-to-major axis ratios larger than 0.85 are used for the adhesion energy calculations. The resulting uncertainty in adhesion energy is calculated to be at most 1 mJ/m², 1 mJ/m², and 5 mJ/m² for graphene-SiO₂, MoS₂-SiO₂, and MoS₂-Al₂O₃ interfaces, respectively.

We further provide a survey of the relevant parameters from several studies of water-filled blisters in the literature (Bampoulis et al., 2016; Khestanova et al., 2016; Uwanno et al., 2015). The material properties used in adhesion energy calculations are summarized in Table 6.3 and 6.4. By substituting these values into (6.58), we are able to estimate the interfacial adhesion energies for a variety of interfaces (Figure 6.14, also summarized in Table 6.5).

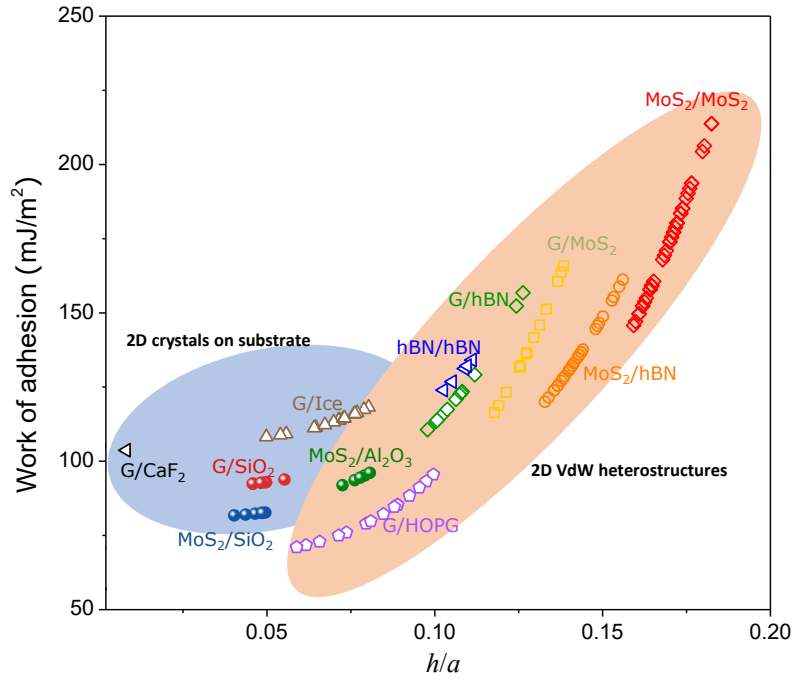


Figure 6.14: Work of adhesion values for various 2D material interfaces estimated according to blister profiles, including many interfaces found in 2D heterostructures. Solid markers indicate our own experiments, while open markers are for blisters reported in the literature.

If the affinity between the 2D material and its substrate is smaller than the affinity of the 2D material to the entrapped liquid, then the energetically favorable configuration should be the one that maximizes the contact between the 2D material and the liquid. To achieve this configuration, the liquid would spread out and form a layered, ice-like structure with almost zero h/a . Our model can hence predict an upper limit for the adhesion energy of these 2D material interfaces as $\Gamma \leq \gamma_w(\cos \theta_m + \cos \theta_s)$ (Table 6.5). This simple relation may also quantitatively offer a criterion for the interesting observation of room-temperature ice formation in a 2D nanochannel (Gowthami et al., 2015; He et al., 2012; Kazakova et al., 2013; Ochedowski et al., 2014; Shim et al., 2012; Xu et al., 2010). This formula can also help explain the so-called self-cleaning mechanism (formation of blisters).

2D-3D interfaces			
Materials	Adhesion/Separation Energy (mJ/m ²)	Method	Ref
G-SiO ₂	93 ± 1 (A)	Spontaneous bubbles	(Sanchez et al., 2018)
	567.14 (A)	Nanoparticle	(Torres et al., 2018)
	276 - 453 (A)	Double nanoparticle	(Gao et al., 2017)
	310 - 450 (S)	Pressurized blisters	(Koenig et al., 2011)
	460 ± 23 (S)	Nanoindentation	(Jiang and Zhu, 2015)
	580 ± 20 (S)	Nanoindentation	(Li et al., 2019)
G-Si	151 ± 28 (A)	Nanoparticle	(Zong et al., 2010)
	357 ± 16 (S)	DCB	(Na et al., 2014)
G-Cu	210-510 (S)	Pressurized blisters	(Cao et al., 2015, 2016; Cao et al., 2014)
	720 ± 70 (S)	DCB	(Yoon et al., 2012)
	750 ± 38 (S)	Nanoindentation	(Jiang and Zhu, 2015)
G-Pt	4021(A)	Nanoparticle	(Torres et al., 2018)
G-Au	7687(A)		
G-CaF ₂	104 (A)	Spontaneous bubbles	(Sanchez et al., 2018)
G-Ice	124 ± 30 (A)		
G-PMMA	2.8-84.4 (S)	Buckle delamination	(Dai et al., 2016b)
MoS ₂ -PDMS	18 ± 2 (S)	Buckle delamination	(Brennan et al., 2015)
MoS ₂ -Al ₂ O ₃	101 ± 15 (A)	Spontaneous bubbles	(Sanchez et al., 2018)
MoS ₂ -SiO ₂	82 ± 1 (A)	Spontaneous bubbles	(Sanchez et al., 2018)
	482.48 (A)	Nanoparticle	(Torres et al., 2018)
	170 ± 33 (S)	Buckle delamination	(Deng et al., 2017)
MoS ₂ -SiO _x	42 ± 20 (A)	Pressurized blisters	(Lloyd et al., 2017)
	220 ± 35 (S)		
MoS ₂ -Si ₃ N ₄	429 (A)	Nanoparticle	(Torres et al., 2018)
	252 ± 41 (S)	Buckle delamination	(Deng et al., 2017)
MoS ₂ -Pt	690 (A)	Nanoparticle	(Torres et al., 2018)
MoS ₂ -Au	1207 (A)		
Ti ₂ CT _x -SiO ₂	400 ± 20 (S)	Nanoindentation	(Li et al., 2019)
Ti ₃ C ₂ T _x -SiO ₂	900 ± 30 (S)		
2D-2D interfaces			
G-G	86 ± 16 (A)	Spontaneous bubbles	(Sanchez et al., 2018)
	221 ± 11 (S)	Atomic intercalation	(Wang et al., 2016c)
G-hBN	126 ± 20 (A)	Spontaneous bubbles	(Sanchez et al., 2018)
hBN-hBN	129 ± 4 (A)		
MoS ₂ -hBN	136 ± 11 (A)		
G-MoS ₂	140 ± 26 (A)		
MoS ₂ -MoS ₂	174 ± 18 (A)		
Graphite-Graphite	227 ± 5 (S)	Shearing	(Koren et al., 2015)
	370 ± 10 (S)		(Wang et al., 2015c)

Table 6.5: Adhesion energies of 2D material interfaces obtained in this work and in literature.

Knowing the adhesion values of various vdW interfaces of 2D materials is very beneficial to the fabrication of 2D material-based devices. The fabrication typically involves either exfoliation of 2D layers from bulk material or transfer of synthesized 2D materials from a donor substrate to a target substrate. Such processes rely on the competing adhesion energies between the 2D material and its “stamp”, and the various surfaces that it contacts. For example, Brennan et al. reported the adhesion of MoS₂ to polydimethylsiloxane (PDMS) is 18 ± 2 mJ/m² (Brennan et al., 2015), which is relatively weak compared with the adhesion between MoS₂ and SiO₂, or MoS₂ and graphene, as estimated in Fig. 4. As a result, delivering 2D MoS₂ to those substrates from an elastomeric stamp is mechanically viable (Brennan et al., 2017; Wang et al., 2016b; Wang et al., 2015a; Wang et al., 2017e). Therefore, the adhesion energy values obtained by our blister metrology (Figure 6.14 and Table 6.5) can help guide and optimize the transfer of 2D materials.

6.7.2 Applications of 2D material blisters

We conclude by highlighting some of the implications of our work for the applications of 2D material blisters. In addition to adhesion energy, our liquid-filled blister model can also predict the confinement pressure, Δp , inside the blisters, and the strain distribution in the 2D membrane. The confinement pressure was previously estimated by capturing pressure-sensitive molecules trapped inside the blister, studying molecular structural and conformational changes, and observing the specific chemistry inside the blister (Lim et al., 2014; Lim et al., 2013; Vasu et al., 2016). Our model offers a direct relation between the confinement pressure and the geometry of the blisters (see section 6.5.1), namely

$$\Delta p = \frac{1}{a} \left(\eta E_{2D} \frac{h^3}{a^3} \right), \quad (6.59)$$

where $\eta \simeq 3.1$ for a graphene blister with a strong shear interface and $\eta \simeq 1.6$ for a weak shear interface (this relation is also discussed for thin sheets with various Poisson's ratios in Chapter 3.6). Note that unlike the adhesion energy, which only depends on the aspect ratio of the blister, the confinement pressure given in (6.59) depends on the size of the blister and has to be estimated with both the height and radius known. For a particular 2D material and interface, the aspect ratio (h/a) is a constant, and the confining pressure is inversely proportional to the blister radius. For the water-filled nanoblister confined between MoS₂ and Al₂O₃ in our experiment (e.g., $h = 4$ nm, $a = 50$ nm), we estimate the confinement pressure to be around 7 MPa.

Furthermore, in applications of 2D material blisters, it is vital that the blister shape and confinement conditions can be controlled. (6.4) provides direct guidance to the aspect ratio of the blisters. For a given interface with fixed adhesion, trapping different types of liquids with different surface energies and contact angles can tune the blister shape and membrane strain. In fact, a recent study by Neek-Amal et al. demonstrated the dependence of the shape of graphene nanoblister on trapped substance (Ghorbanfekr-Kalashami et al., 2017). Our proposed strategies are also consistent with our MD simulations in Figure 6.11.

6.8 CONCLUSIONS

In summary, spontaneously formed nanoblister are almost inevitable when transferring 2D materials to a substrate. We hypothesized that those nanoblister are filled with liquid according to our time-lapse atomic force microscopy scans and reasonable estimation of adhesion energy. We showed that the liquid-filled nanoblister form as a result of competition between the elastic energy of the deformed 2D material, the interfacial energy associated with van der Waals interactions and surface tension of the liquid contents. Besides pointing to solutions for controlling their shape and internal

pressure, our analysis provides a method to estimate the work of adhesion of 2D material interfaces by simply measuring the aspect ratios of the blisters, which is essential for the design and fabrication of 2D material-based applications.

Chapter 7: Buckles¹

In previous chapters, we have mainly studied the blisters where buckle delamination in the supported region is fully suppressed by the interface adhesion (Case I and II). In this chapter, we present comprehensive discussions on microscale tents formed when transferring 2D materials over nanoparticles or nanopillars, in the periphery of which radial buckle delamination has been often observed (Case III). Unlike previous chapters that are numerically-based, we characterize the shape of the buckles by AFM experiments and obtain theoretical predictions for the extent of those buckles by exact closed-form solutions to Föppl–von Kármán (FvK) equations in this chapter. Analytical solutions to both near-threshold (Case I) and far-from-threshold (Case III) conditions are given. These results would provide a direct means to estimate the interfacial shear and adhesive properties of the 2D material-substrate system based on simple topological characterizations of buckles. In addition, the theoretical understandings establish a fundamental base for the rational design of 2D material tents.

¹A paper based on the work described in this Chapter has been accepted:

Z. Dai, D. Sanchez, C. J. Brennan, N. Lu. *Radial Buckle Delamination around 2D Material Tents*. Journal of the Mechanics and Physics of Solids 2020, 137, 103843. (Z.D. contributed to conceptualization, analysis of experiments, theory, and writing.)

7.1 INTRODUCTION

Two-dimensional (2D) materials are a relatively new class of atomically thin materials with emerging mechanical and electronic properties that lend well to next-generation electronics and photonics (Geim and Grigorieva, 2013; Neto et al., 2009). Applications in this context typically involve transferring 2D materials to a supporting substrate. When 2D materials are transferred over nanoparticles on the substrate, nanotents are formed. Initially, these tents were viewed as disruptions for device applications (Akinwande et al., 2017; Pizzocchero et al., 2016). However, recent works discovered considerable mechanical strain within the tent, which is useful for many exciting electromechanical applications of 2D materials (Chaste et al., 2018; Dai et al., 2018; Dai et al., 2019a; Feng et al., 2012; Klimov et al., 2012; Tomori et al., 2011). As a result, microscale tents were designedly created by transferring 2D materials to substrates pre-patterned with nanopillars (Figure 7.1a) (Branny et al., 2017; Jiang et al., 2017). For example, 2D semiconductors draping over an array of nanopillars were demonstrated with the possibility to become large-scale quantum emitters, except that sometimes the pillars pierce through the 2D materials without mechanically guided design (Branny et al., 2017; Palacios-Berraquero et al., 2017). Moreover, the nanoindentation of 2D material drumheads also represents a common type of inverse 2D material tents (Cao and Gao, 2019; Lee et al., 2008). Both types of tents have been approximately modeled as circular membranes subjected to a point load at the center and clamped at the edge (Dai et al., 2019b; Vella and Davidovitch, 2017). Such modeling, together with experiments on these 2D materials tents of different origins, has facilitated many vital metrologies for 2D materials, such as Young's moduli, mechanical strength, and adhesion energies to the substrate as we discussed in Chapters 2-6.

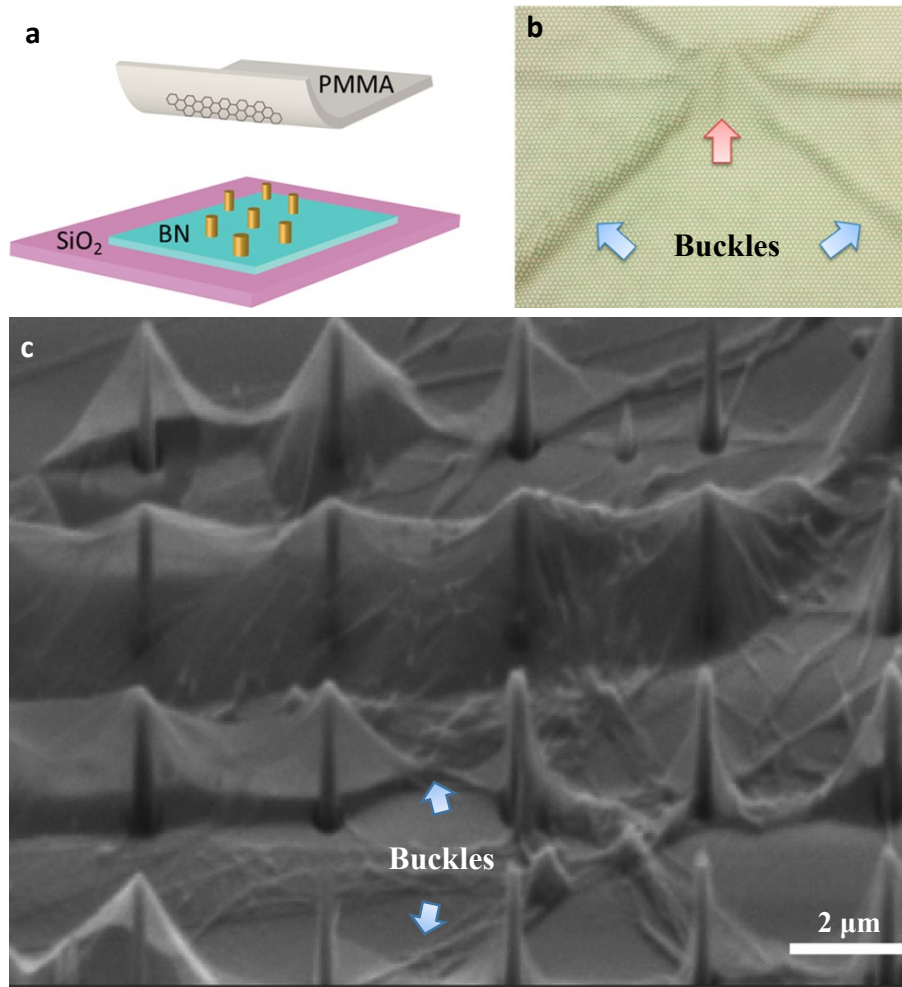


Figure 7.1: (a) A schematic of transferring graphene over a pillared substrate. (b) A schematic of radial buckles (blue arrows) surrounding a graphene tent formed over an Au pillar (red arrow). (c) Scanning electron microscope (SEM) image of monolayer graphene covering a periodic array of nanopillars. Each nanopillar has a height of about 260 nm and an apex radius of 20 nm – 50 nm. The pillar pitch is 1.4 μm. Source: Figures adapted from (Xu et al., 2016) (a and b) and (Reserbat-Plantey et al., 2014) (c).

Both experimental and theoretical studies of 2D material tents assume that the 2D material perfectly conforms to the substrate outside the tent. However, radial buckle delamination has been widely observable in the substrate-supported zone (Figure 7.1) (Jiang et al., 2017; Reserbat-Plantey et al., 2014), which is prohibited under such

assumption. Since the buckles can reflect 2D material-substrate interfacial interactions and affect device design, it is crucial to achieve a comprehensive mechanistic understanding for them (Dai et al., 2020).

In this Chapter, we characterize radial buckles that form at the periphery of multilayer graphene and monolayer MoS₂ tents. Using atomic force microscopy (AFM), we find that the buckle profiles along the hoop direction follow a simple cosine function, and the wavelength and height of the buckles are proportional to a characteristic length. We attribute the radial buckles to the interface sliding between the 2D material and its substrate. A simplified 1D analysis, along with the Lamé problem, can quantitatively explain the decay of the wavelength and the height of the buckling profile with the increasing radial position. Finally, we present theory built upon the membrane limit of Föppl–von Kármán (FvK) equations and account for the interfacial sliding in the periphery of the 2D material tents. These results show important implications for the adhesion and friction metrology of 2D materials as well as for the rational design of 2D material tents.

7.2 EXPERIMENTS

7.2.1 Sample preparation¹

To obtain accurate profiles of the radial buckles, we experimentally produced graphene and MoS₂ tents as graphene and MoS₂ are two of the most prevalent 2D materials studied in recent years. We prepared graphene samples by exfoliating SPI-1 grade highly ordered pyrolytic graphite (HOPG) on SiO₂. Blue polyethylene cleanroom tape (CRT) was used to peel large and thick flakes off the bulk crystal. The exfoliated flakes were brought into contact with another piece of the CRT and exfoliated three more times. The flakes were then stored for a minimum of three hours in ambient conditions to allow ambient

¹ Daniel Sanchez and Christopher Brennan prepared the tent samples discussed in this Chapter.

moisture and other contents to adsorb on the surface of the exposed flakes. The SiO₂ chip was exposed to O₂ plasma using a Nordson MARCH Plasma CS170IF Etching System for two minutes at 150 W to remove any organic residue. Immediately after O₂ plasma exposure, the exfoliated HOPG flakes on CRT were placed onto the surface of the SiO₂ chip. Then the SiO₂ chip was placed on a hot plate and was heated at 100 °C for two minutes. The sample was removed from the hot plate and cooled to room temperature, after which the CRT was removed. AFM step height measurement suggested that the multilayer graphene sample contained 10-20 layers, as this method is known to be inaccurate for determining 2D material thickness (Brennan et al., 2015).

We prepared monolayer MoS₂ by chemical vapor deposition (CVD) on SiO₂ from solid precursors (Brennan et al., 2017). A polydimethylsiloxane (PDMS) stamp and a water bath were used to separate the MoS₂ from the growth substrate. The PDMS/MoS₂ was then placed on the receiving substrate, Al₂O₃/Si, and heated with a hot plate to 50 °C. Slowly peeling away, the PDMS transferred the MoS₂ to the substrate. We found that tents spontaneously formed when HOPG was mechanically exfoliated onto SiO₂ (left panel in Figure 7.2a), and when CVD-grown monolayer MoS₂ was transferred to Al₂O₃ (right panel in Figure 7.2a). Similar tents were also observed in many 2D material devices in the literature (Budrikis et al., 2015; Jiang et al., 2017; Reserbat-Plantey et al., 2014). The formation of tents is typically attributed to nanostructures or nanoparticles confined at the interface. In this work, we focus on the radial buckles that commonly formed at the periphery of the 2D material tents (Figure 7.2a), which have been overlooked in previous experimental characterizations and theoretical analysis. We note that the substrates used here are relatively stiff as Young's moduli of silicon dioxide (supporting the multilayer graphene) and aluminum oxide (supporting the monolayer MoS₂) are around 70 GPa and 300 GPa, respectively.

7.2.2 Shapes

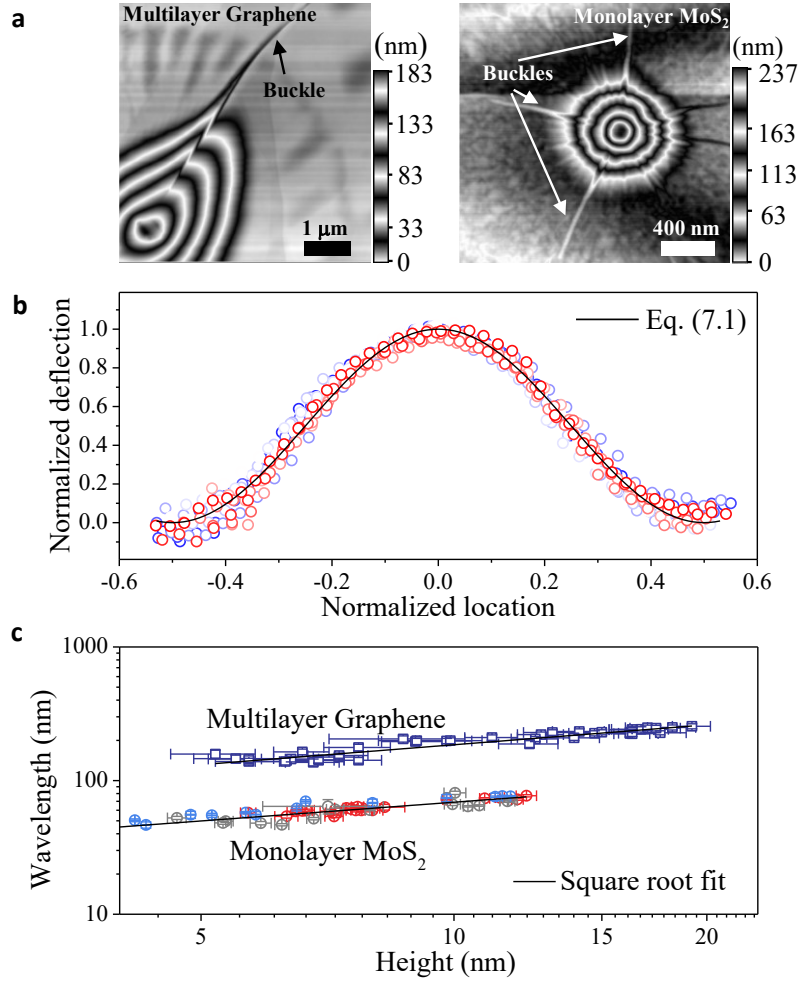


Figure 7.2: (a) AFM images of a multilayer graphene tent and a monolayer MoS₂ tent. The vertical scales indicate the height of the tents. Radial buckles can be found at the substrate-supported regime outside the tent, and their profiles can be obtained by taking scans transverse to the buckles in the AFM height image. (b) Normalizing these AFM scans gives the characteristic buckle profile, which is well fitted by the cosine function given by (7.1) (black curve). This fit can yield the buckle wavelength λ and height δ . Different colors of the markers represent scans at different radial locations in the MoS₂ tent while these profiles are normalized by their fitted wavelength and height. (c) The wavelength (λ) of the multilayer graphene and monolayer MoS₂ buckles as a function of their height (δ) in a log-log plot. Colored markers are used to differentiate different buckles surrounding the same tent. The black lines correspond to a power-law fit with an exponent of $\frac{1}{2}$.

Using tapping mode AFM, we obtained the height images of a multilayer graphene tent and a monolayer MoS₂ tent as well as the radial buckles surrounding them (Figure 7.2a).¹ From these images, we extracted the height profile of a buckle by scanning transversely to the buckle (i.e., along the circumferential direction). Though depending on the radial position, i.e., the distance to the center of the tent r , all buckle profiles in the hoop direction could be well approximated by a cosine function (Figure 7.2b),

$$y(x) = \frac{\delta}{2} \left(1 + \cos \frac{2\pi x}{\lambda} \right), \quad (7.1)$$

where λ and δ are the wavelength and height of the buckle, respectively. In fact, a column undergoing Euler buckling would deflect into a shape also characterized by (7.1) (Timoshenko and Gere, 2009). It has been well studied that the profile of a buckle could be modified by the deformation of a soft substrate at the edge of the buckle (Audoly and Pomeau, 2000; Boijoux et al., 2018; Parry et al., 2005). The substrates (silicon dioxide and aluminum oxide) used here, however, are relatively stiff in comparison with the bending stiffness of the 2D material flakes, and hence render the good approximation of (7.1).

Using (7.1) to fit the measured buckle profiles can readily yield λ and δ (Vella et al., 2009). We find that both λ and δ decay over r , and finally disappear at a finite distance from the center of the tent, reminiscent of the finite wrinkling zone of a water-supported elastic membrane (Huang et al., 2007; Vella et al., 2010). Figure 7.2c plots experimentally measured buckle wavelength as a function of the buckle height. The power-law fitting reveals that λ is proportional to $\sqrt{\delta}$, with a different prefactor for the multilayer graphene and the monolayer MoS₂. Physically, λ^2/δ represents the radius of the curvature of the buckle's crest in the hoop direction (Aoyanagi et al., 2010; Zhang and Yin, 2018). Constant λ^2/δ implies that the profiles of buckles measured at different locations are self-similar as

¹ Daniel Sanchez and Christopher Brennan performed the AFM measurements on these 2D material tents.

long as they are associated with the same tent. This observation suggests that each transverse scan of the buckles may be considered as an isolated one-dimensional (1D) buckle.

7.2.3 1D analysis

We recall the case of 1D buckling, where an elastic membrane buckles when subject to a uniaxial, end-to-end compressive displacement Δ (Figure 7.3a). We limit ourselves to the inextensional analysis and neglect any compression of the relatively stiff thin membrane (Vella et al., 2009). The elastic energy of the system, therefore, comes from the bending of the 2D material

$$U = \frac{1}{2} B \int_{-\lambda/2}^{\lambda/2} y''(x)^2 dx = \frac{\pi^4 B \delta^2}{\lambda^3}, \quad (7.2)$$

where B is the bending stiffness of the membrane and $y''(x)$ is the second derivative with respect to x of the tent profile given in (7.1), i.e., the curvature. The inextension of the membrane dictates the following geometrical relationship

$$\Delta = \int_{-\lambda/2}^{\lambda/2} \sqrt{1 + y'(x)^2} dx - \lambda = \frac{\pi^4 \delta^2}{4\lambda}, \quad (7.3)$$

which may be used to eliminate δ from (7.2) in favor of Δ . Through $-\partial U / \partial \lambda = \Delta \gamma$, we obtain the following energy release rate

$$\Delta \gamma = 2\pi^4 \frac{B \delta^2}{\lambda^4}. \quad (7.4)$$

This result is identical to the previously reported macro/microscopic 1D buckles (Deng et al., 2017). However, we should be careful with the change of interfacial energy. When the delaminated interface is filled with gas, $\Delta \gamma$ is simply the adhesion energy between the membrane and the substrate

$$\Delta \gamma_{\text{gas}} = \Gamma. \quad (7.5)$$

However, recent works showed strong evidence that the 2D material-substrate interface can spontaneously confine hydrocarbons and liquid water (Haigh et al., 2012; Khestanova

et al., 2016; Sanchez et al., 2018). When the delaminated interface is filled with liquid content, the formation of a buckle involves the interfaces between the liquid, the membrane, and the substrate. In this case, the change of the interfacial energy should be written as $\Delta\gamma = \gamma_{ml} + \gamma_{sl} - \gamma_{ms}$, where γ_{ml} , γ_{sl} , and γ_{ms} are the energy densities (per unit area) for the membrane-liquid interface, substrate-liquid interface, and membrane-substrate interface, respectively. We can further use Young–Dupré equations to derive

$$\Delta\gamma_{\text{liquid}} = \Gamma - \gamma_l(\cos \theta_s + \cos \theta_m), \quad (7.6)$$

where γ_l is the surface tension of the liquid, and θ_s and θ_m are the liquid contact angles of the substrate and the membrane, respectively (Israelachvili, 2011). If given the surface tension of the confined liquid and its contact angle to the 2D material and the substrate, with $\Delta\gamma$ estimated by (7.4), one may extract the interface adhesion for the 2D material-substrate interface, a key interface parameter for 2D material-based devices (Koenig et al., 2011). It is worth mentioning that special attention should be given to the bending stiffness of 2D materials since the classical bending stiffness-Young’s modulus relation for a plate breaks down when bending monolayer or multilayer 2D materials (Lu et al., 2009; Wang et al., 2019b; Zhang et al., 2011).

The 1D analysis gives a characteristic length scale $\lambda^2/\delta \sim \sqrt{B/\Delta\gamma}$, which compares surface tension and/or adhesion with bending stiffness and has been referred to as the elasto-capillary length (Schroll et al., 2013; Vella et al., 2009). Such scaling can explain our experimental observation of constant λ^2/δ in Figure 7.2c, although these radial buckles, unlike the 1D buckles, involve bending energy from two principal curvatures, i.e., both radial and circumferential. However, if the curvature of the crest line (κ_r) is much smaller than the hoop curvature of the buckle (κ_θ) as illustrated in Figure 7.3b, the bending energy of the radial buckle can reasonably reduce to the 1D estimate. Experimentally, we found that κ_r decays over r and the maximum κ_r is found near the edge of the tent (~ 0.1

μm^{-1} for monolayer MoS_2 tent) while the maximum κ_θ is at the buckle crest appearing to be a r -independent constant ($\sim 2 \mu\text{m}^{-1}$). Indeed, $\kappa_r \ll \kappa_\theta$.

7.2.4 Formation mechanism of radial buckles

Having analyzed the hoop-direction profile characteristics of the 2D material radial buckles, we move on with the investigation of how these characteristic parameters vary with the radial position r . In Figure 7.3c, we plot the measured $\lambda, \delta, \lambda^2/\delta, \delta^2/\lambda$ of the MoS_2 buckles shown in Figure 7.2a vs. r . Here, our primary interest is in the size of the buckled region, which might be equivalent to the region in which there is a hoop compression (Vella et al., 2010). If we assume that the 2D material-substrate interface is frictionless, the 2D material inside the tent pulls the 2D material outside the tent inward, and hence the hoop stress is negative, leading to the buckle delamination of the atomically thin membrane, i.e., the 2D material. If we estimate the size of the buckled zone by the size of the compression zone, the analysis of $\Delta \sim r$ relation then becomes a classical problem of linear elasticity – the Lamé problem (Davidovitch et al., 2011; Sadd, 2009). We can, therefore, obtain the stress and displacement field of the planar, axisymmetric state and reach the conclusion that both stress and strain $\sim r^{-2}$ and $\Delta \sim r^{-1}$ if we apply a traction-free boundary condition at infinity (Davidovitch et al., 2011; Sadd, 2009). Combining with the characteristic length scale yields the following scaling predictions:

$$\Delta = \frac{\pi^4 \delta^2}{4\lambda} \sim r^{-1}, \quad \frac{\lambda^2}{\delta} \sim \sqrt{\frac{B}{\Delta \gamma}} \sim r^0, \quad \delta \sim r^{-2/3}, \quad \lambda \sim r^{-1/3}. \quad (7.7)$$

We plot these scaling relations in Figure 7.3c and find reasonable agreement with experimental results. We thus suggest that the formation of the 2D material buckles around a tent is a result of interface sliding and their profiles are governed by the competition between the bending energy and the interface energies.

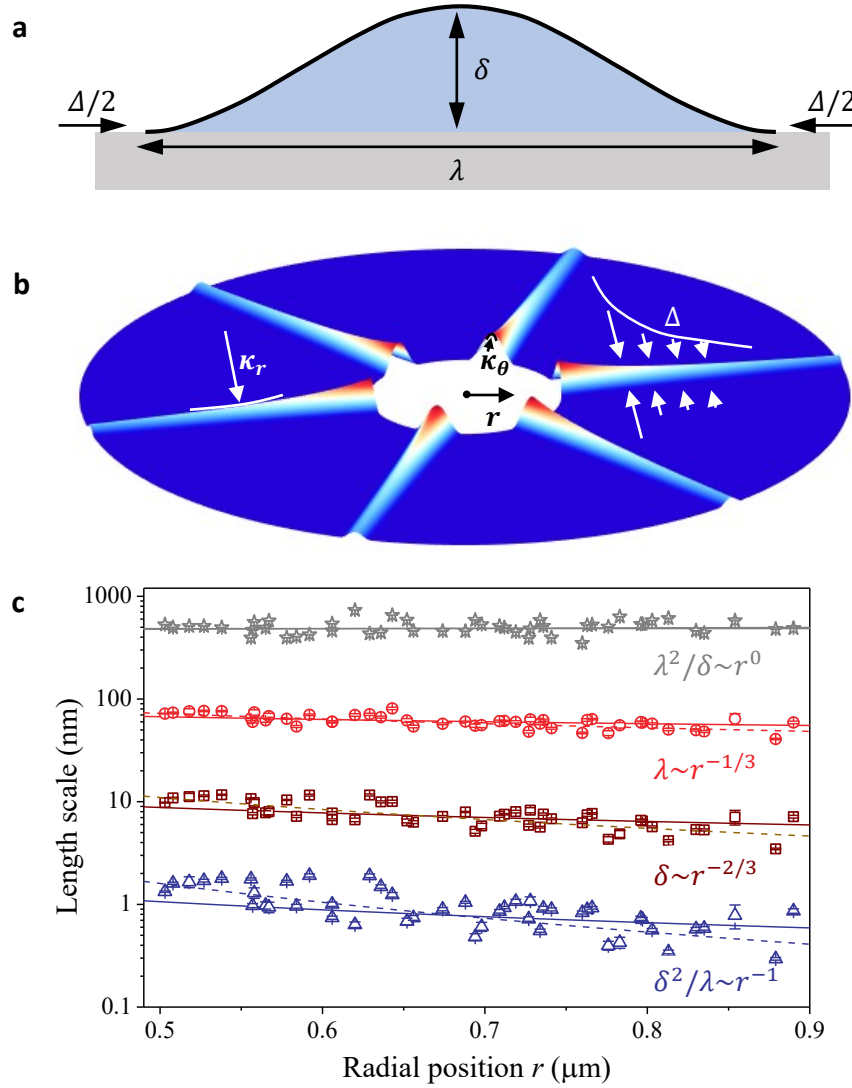


Figure 7.3: (a) A schematic of a 1D buckle where Δ represents the compressive displacement. (b) Schematic illustration of radial buckles at the periphery of a tent. r represents the radial position. κ_θ and κ_r denote the buckle crest curvature in the hoop and radial direction, respectively. Δ represents the compressive displacement in the hoop direction which varies with r . (c) Experimentally measured δ^2/λ , λ^2/δ , λ , δ of the buckles formed by the monolayer MoS₂ tent as a function of the radial position. Solid lines are based on the scaling law given in (7.7), and the dashed lines represent the best fitting.

However, the frictionless assumption indicates that the entire substrate-supported part of the membrane undergoes the hoop compression and thus over-predicts the extent of the buckled region compared with that observed experimentally. Specifically, the best fittings in Figure 7.3c (dashed lines) yield a much faster decay of Δ than r^{-1} ($r^{-2.3 \pm 0.2}$ in fact), of δ than $r^{-2/3}$ ($r^{-1.5 \pm 0.1}$), as well as a slightly faster decay of λ than $r^{-1/3}$ ($r^{-0.7 \pm 0.1}$). This motivates the following analysis accounting for above-overlooked factors such as interfacial shear traction, pretension, and the finite size of the nanopillar and the membrane, all of which may affect the size/extent of the zone subjected to hoop compression (we then call it the compression zone). Since these factors are possible to be controlled in experiments, knowing their effects may guide the rational design of 2D material tents with or without peripheral instabilities.

Another important reason for the deviation between Lamé predictions and the observation in Figure 7.3 is that a highly bendable sheet cannot sustain compressive stresses and instabilities occur and release the hoop compression (Box et al., 2019). It is thus necessary to perform an analysis to consider that the negative stresses are relaxed in the membrane (frequently referred to as tension field theory or far-from threshold analysis) (Davidovitch et al., 2011; King et al., 2012; Vella, 2019). Note that such relaxation may not be complete for relatively thick 2D material membranes because of the stiff, adhesive substrate. We will demonstrate an example of this case in Section 7.8.

Therefore, in the following sections, we first consider a limiting case in Section 7.4 assuming that the hoop compressive stress is maintained (instabilities are suppressed) such that we can adopt near-threshold (NT) modeling with the consideration of interfacial shear traction, pretension, and the finite size of pillar and membrane. Parametric studies based on NT modeling are performed in Section 7.5. For thin sheets, a more representative case arises from that the hoop compressive stress is fully relaxed. We describe this case through

far-from-threshold (FFT) modeling in Section 7.6. The analysis of FFT modeling and its comparison with NT modeling are discussed in Section 7.7. The NT and FFT modeling would provide upper/lower limits for the tent system in general, and we will leverage them to interpret our experimental observations in Section 7.8.

7.4 NEAR-THRESHOLD MODELING

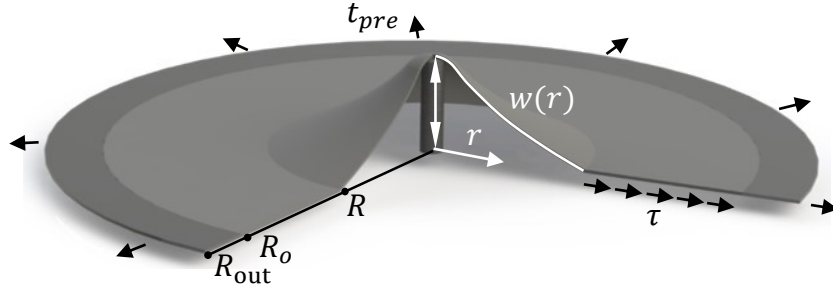


Figure 7.4: Notations for the analysis of an axisymmetric tent, where a finite zone in the substrate-supported regime ($R < r < R_o$) undergoes hoop compression caused by interface sliding. R is the edge of the tent, R_o is the edge of the compression zone, and R_{out} is the outer radius of consideration. τ is the membrane-substrate interface shear traction and t_{pre} is the pretension in the membrane.

7.4.1 General theory

We first present a theoretical framework for considering the finite interfacial shear traction between the 2D material and its substrate. We will show that other factors (i.e., pretension, and the finite size of the nanopillar and the membrane) come into play through boundary conditions. A theoretical idealization of an axisymmetric tent formed by 2D materials is shown in Figure 7.4. Inside the tent ($r < R$), the vertical displacement $w(r)$ caused by a point load F is related to the Airy stress function $\phi(r)$ by Föppl–von Kármán (FvK) equations (Mansfield, 2005; Vella and Davidovitch, 2017),

$$\nabla^2(B\nabla^2 w) - [\phi, w] - \frac{F}{2\pi} \frac{\delta(r)}{r} = 0 \quad (7.8)$$

and

$$\nabla^4 \phi + \frac{1}{2} E_{2D} [w, w] = 0, \quad (7.9)$$

where E_{2D} is the in-plane stiffness of the membrane, $\delta(r)$ is the Dirac delta function, the operators $[f, g] = (f_{,rr}g_{,r} + f_{,r}g_{,rr})/r$, $\nabla^2 f = f_{,rr} + f_{,r}/r$, $\nabla^4 = \nabla^2 \nabla^2$, and $(\quad)_{,r}$ denotes differentiation with respect to r . The radial and circumferential stress resultants can take the form

$$N_{rr} = \phi_{,r}/r \text{ and } N_{\theta\theta} = \phi_{,rr}. \quad (7.10)$$

For the membrane outside the tent ($R < r < R_o$), we assume $w = 0$, i.e., no buckling and hence compressive stress not relaxed. R_o is the outer radius of the compression zone. Considering the thinness of 2D materials, we can treat the interface shear traction, τ , as a body force and assume that it is derivable from an in-plane potential function v such that (Sadd, 2009)

$$v_{,r} + \tau = 0. \quad (7.11)$$

This assumption is not very restrictive because many models about interfacial interactions between the 2D material and its substrate followed this approach (Zhang and Arroyo, 2013; Zhang and Arroyo, 2014, 2016; Zhang and Tadmor, 2018). The equilibrium can be automatically satisfied by taking stress resultants as

$$N_{rr} = \phi_{,r}/r + v \text{ and } N_{\theta\theta} = \phi_{,rr} + v. \quad (7.12)$$

In the NT analysis, the strain compatibility holds and provides the governing equation

$$\nabla^4 \phi + (1 - \nu) \nabla^2 v = 0. \quad (7.13)$$

7.4.2 Non-dimensionalization

Equations (7.8-7.13) complete the governing equations for the tent problem accounting for finite interface shear and are to be solved along with boundary conditions. Before proceeding, we note that the first term in (7.8), representing bending, can be

neglected due to the thinness of 2D materials. The tent radius R and the membrane stiffness E_{2D} are experimentally accessible, and sometimes (e.g. in nanoindentation tests) the radius is prescribed by a hole patterned on the substrate. We then use these two quantities to non-dimensionalize the variables as follows

$$\rho = \frac{r}{R}, \rho_o = \frac{R_o}{R}, W = \frac{w}{R}, H = \frac{w(0)}{R}, \bar{F} = \frac{F}{E_{2D}R}, \Phi = \frac{\phi}{E_{2D}R^2}, T = \frac{\tau R}{E_{2D}}, V = \frac{v}{E_{2D}}. \quad (7.14)$$

Now, inside the tent ($\rho \leq 1$), we integrate (7.8) and (7.9) once and find that (Chopin et al., 2008)

$$\Phi'W' + \frac{\bar{F}}{2\pi} = 0 \quad (7.15)$$

and

$$\rho \frac{d}{d\rho} \left[\frac{1}{\rho} \frac{d}{d\rho} (\rho \Phi') \right] + \frac{1}{2} W'^2 = 0, \quad (7.16)$$

where $(\)'$ denotes differentiation with respect to ρ . Outside the tent ($1 \leq \rho \leq \rho_o$), (7.11) and (7.13) become

$$V' + T = 0 \quad (7.17)$$

and

$$\frac{d}{d\rho} \left[\frac{1}{\rho} \frac{d}{d\rho} (\rho \Phi') \right] + (1 - \nu)V' = 0. \quad (7.18)$$

The four boundary value problems, i.e. $\Phi'(\rho)$ and $W(\rho)$ when $\rho \leq 1$, and $\Phi'(\rho)$ and $V(\rho)$ when $\rho \geq 1$, can be solved according to boundary conditions. In this work, we present closed-form analytical solutions to them, by which several useful composite parameters emerge naturally and relate to experiments directly.

7.4.3 Analytical results: outside the tent

There has been a surge of interest in the sliding between 2D materials and their substrates in recent years (Xu and Zheng, 2018). Micro-scale Raman characterizations indicated nonlinear shear responses of the 2D material-substrate interface (Dai et al., 2016b; Guo and Zhu, 2015; Jiang et al., 2014; Wang et al., 2016b; Wang et al., 2017b).

Moreover, many subtle features of the interface shear/friction appeared when measurement resolutions downsized to the atomic level (Kitt et al., 2013; Wang et al., 2017b). For example, the frictional resistance is found to be particularly sensitive to chemical bonding, substrate roughness, and the local lattice state of the interface. So-call superlubricity (a nearly frictionless state) can be achieved between incommensurately stacked 2D materials (Liu et al., 2012). Here, we take the first-order approximation and assume a constant interface shear traction within the sliding zone (i.e., the compression zone), like the perfect plasticity behaviors (Gong et al., 2010; Kitt et al., 2013; Wang et al., 2017b). With this simplification, (7.17) can be integrated once such that

$$V = -T\rho + A. \quad (7.19)$$

Equation (7.18) can then be solved directly

$$\Phi'(\rho) = B\rho + \frac{C}{\rho} + \frac{1-\nu}{3}T\rho^2. \quad (7.20)$$

At the outer edge of the circumferentially compressed zone ($\rho = \rho_o$), both radial and circumferential stress resultants decay to zero, i.e. $\Phi'(\rho_o)/\rho_o + V = \Phi''(\rho_o) + V = 0$, leading to

$$A + B = \frac{1+\nu}{2}T\rho_o \text{ and } C = \frac{1-\nu}{6}T\rho_o^3. \quad (7.21)$$

7.4.4 Analytical results: inside the tent

Nonlinear FvK equations for thin membranes are difficult to solve, but analytical progress has been recently made for axisymmetric cases (Jin et al., 2017; Vella and Davidovitch, 2017; Vella and Davidovitch, 2018). Here, we adopted the strategy proposed by Vella *et al.* (Chopin et al., 2008; Vella and Davidovitch, 2017). Using (7.15) can eliminate W' in (7.16),

$$\rho \frac{d}{d\rho} \left[\frac{1}{\rho} \frac{d}{d\rho} (\rho \Phi') \right] + \frac{1}{2} \left(\frac{\bar{F}}{2\pi \Phi'} \right)^2 = 0. \quad (7.22)$$

It is convenient to introduce (Bhatia and Nachbar, 1968)

$$\psi(\eta) = \rho\Phi'(\rho), \eta = \rho^2, \quad (7.23)$$

such that (7.22) can be simplified as

$$\frac{d^2\psi}{d\eta^2} = -\frac{\bar{F}^2}{32\pi^2\psi^2}. \quad (7.24)$$

We integrate once to obtain

$$\frac{d\psi}{d\eta} = \frac{\bar{F}}{4\pi} \sqrt{(\alpha\psi + 1)/\psi}, \quad (7.25)$$

where α is a negative constant to be determined based on boundary conditions. Using $\tilde{\psi} = -\alpha\psi$, (7.25) becomes

$$\frac{d\tilde{\psi}}{d\eta} = \frac{\bar{F}\sqrt{(-\alpha)^3}}{4\pi} \sqrt{(1 - \tilde{\psi})/\tilde{\psi}}. \quad (7.26)$$

Further integrating analytically (Chopin et al., 2008), we have

$$\frac{\bar{F}\sqrt{(-\alpha)^3}}{4\pi} \eta = -\sqrt{\tilde{\psi}(1 - \tilde{\psi})} + \tan^{-1} \sqrt{\tilde{\psi}/(1 - \tilde{\psi})}, \quad (7.27)$$

where we used the zero radial displacement condition at the center of the tent, i.e. $\lim_{\rho \rightarrow 0} \rho[\phi''(\rho) - \nu\phi'(\rho)] = 0$ or essentially

$$\tilde{\psi}(0) = 0. \quad (7.28)$$

At the edge of the tent ($\eta = 1$), a useful parameter $\tilde{\psi}_1 = \tilde{\psi}(1)$ can be defined that satisfies

$$\frac{\bar{F}\sqrt{(-\alpha)^3}}{4\pi} = -\sqrt{\tilde{\psi}_1(1 - \tilde{\psi}_1)} + \tan^{-1} \sqrt{\tilde{\psi}_1/(1 - \tilde{\psi}_1)}. \quad (7.29)$$

Invoking the continuity condition of radial stress and displacement, we have

$$\Phi'(1^-) = \Phi'(1^+) + V(1^+) \quad \text{and} \quad \Phi''(1^-) - \nu\Phi'(1^-) = \Phi''(1^+) - \nu\Phi'(1^+) + (1 - \nu)V(1^+), \quad (7.30)$$

which further lead to

$$\tilde{\psi}_1 = -\alpha T \left(\frac{1+\nu}{2} \rho_o + \frac{1-\nu}{6} \rho_o^3 - \frac{2+\nu}{3} \right) \quad (7.31)$$

and

$$\frac{d\tilde{\psi}}{d\eta} \big|_{\eta=1} = -\alpha T \frac{1+\nu}{2} (\rho_o - 1). \quad (32)$$

Ostensibly, the boundary value problem in (7.24) is a 2nd order system with three boundary conditions, i.e., (7.28), (7.31), and (7.32). However, the size of the compression

zone, ρ_o , is unknown. In fact, (7.32) can be used to give an equation for the integration constant α in (7.26)

$$-\alpha T \frac{1+\nu}{2} (\rho_o - 1) = \frac{\bar{F}(-\alpha)^{3/2}}{4\pi} \sqrt{\frac{1-\tilde{\psi}_1}{\tilde{\psi}_1}}. \quad (7.33)$$

Further, combining (7.29) and (7.33) can eliminate \bar{F} and relate the α to $\tilde{\psi}_1$, T , and ρ_o by

$$\alpha = \frac{2 \left[1 - \tilde{\psi}_1 - \sqrt{(1-\tilde{\psi}_1)/\tilde{\psi}_1} \tan^{-1} \sqrt{\tilde{\psi}_1/(1-\tilde{\psi}_1)} \right]}{(1+\nu)T(\rho_o-1)}. \quad (7.34)$$

We then use (7.34) to eliminate the constant α in (7.31), and finally, find $\tilde{\psi}_1$ as a function of ρ_o

$$\frac{3(1+\nu)(\rho_o-1)}{[3(1+\nu)\rho_o + (1-\nu)\rho_o^3 - 2(2+\nu)]} = 1 - \tilde{\psi}_1^{-1} + \sqrt{(1-\tilde{\psi}_1)/\tilde{\psi}_1^3} \tan^{-1} \sqrt{\tilde{\psi}_1/(1-\tilde{\psi}_1)}. \quad (7.35)$$

It is found that $\tilde{\psi}_1 \rightarrow 1$ represents the lubricated membrane-substrate interface as the size of the compression zone $\rho_o \rightarrow \infty$. In general, for a given size of the compression zone ρ_o , we can figure out the required parameters $\tilde{\psi}_1$ by (7.35), α by (7.34), and then the point force \bar{F} by (7.33) in terms of the interfacial shear traction T .

7.4.5 A composite parameter

We aim to relate to the size of the compression zone ρ_o to the center height of the tent $H = W(0)$ because the latter one is experimentally accessible. Note that from (7.15),

$$H = \int_0^1 \frac{\bar{F} d\rho}{2\pi\Phi'} = \frac{-\bar{F}\alpha}{4\pi} \int_0^{\tilde{\psi}_1} \frac{d\tilde{\psi}}{\tilde{\psi}\tilde{\psi}'}. \quad (7.36)$$

Combining (7.36) with (7.26) can analytically obtain

$$H = \frac{2}{\sqrt{-\alpha}} \tan^{-1} \sqrt{\tilde{\psi}_1/(1-\tilde{\psi}_1)}. \quad (7.37)$$

Equations (7.34), (7.35), and (7.37) complete the analytical solutions to the problem where a circular membrane is poked with a height of H and is supported by an interface with a constant shear traction T . Particularly, (7.34) and (7.37) can cancel the constant α out and hence the size of the compressive/buckling zone ρ_o depends on a single composite

parameter $\mathcal{S} = H^2/T$. This suggests that reducing the interfacial shear resistance and increasing the tent height can extend the compression zone outside the tent.

7.5 PARAMETRIC STUDIES BASED ON NEAR-THRESHOLD MODELING

Based on NT modeling, we now present how the size of the compression zone changes with the height of the tent and other parameters of the system, including the shear traction of the 2D material-substrate interface, pretension in the 2D material, size of the 2D material, and the pillar radius.

7.5.1 Effect of \mathcal{S}

We start with the distribution of the hoop compressive displacement in the substrate-supported region ($\rho \geq 1$) by considering the shortened perimeter of a material circle. Hooke's law can relate the hoop strain to stress resultants by

$$\epsilon_{\theta\theta} = \frac{N_{\theta\theta} - \nu N_{rr}}{E_{2D}}. \quad (7.38)$$

The stress resultants can be readily calculated through (7.12) and (7.19-7.21). We normalize the hoop compression by the tent radius such that

$$\bar{\Delta} = -\frac{2\pi r \epsilon_{\theta\theta}}{R} = \frac{\pi(1-\nu^2)}{3} T \rho \left(-3\rho_o + \frac{\rho_o^3}{\rho^2} + 2\rho \right). \quad (7.39)$$

In Figure 7.5a, we plot $\bar{\Delta}$ as a function of ρ for tents subject to different center heights and various interfacial tractions. Evidently, when $T \rightarrow 0$, the limit of $\bar{\Delta}(\rho) \sim \rho^{-1}$ can be observed, which is consistent with what was predicted under the assumption of the frictionless interface in Section 7.3.3. The maximum compressive displacement is thus located at the edge of the tent, i.e. $\bar{\Delta}_1 = \bar{\Delta}(1)$. However, with finite interfacial shear traction, the compression zone outside the tent is confined within a finite region ($1 \leq \rho \leq \rho_o$). As a result, the hoop compressive displacement decays faster than ρ^{-1} when approaching ρ_o , especially for tents with small center heights.

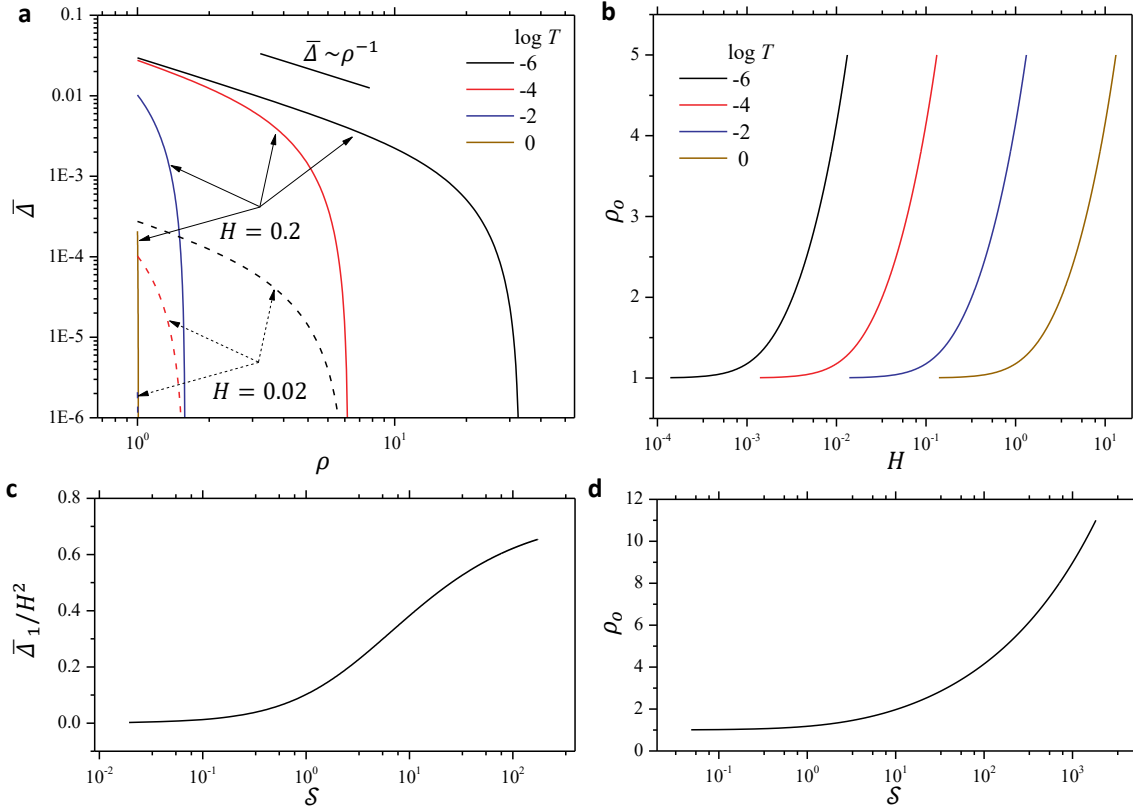


Figure 7.5: (a) Hoop compressive displacement along the radial direction for various interfacial shear tractions. Solid curves denote tents with a center height $H = 0.2$ while dashed curves denote $H = 0.02$. (b) The size of the compression zone versus the center height of the tent for various interfacial shear tractions. (c) The dependency on \mathcal{S} of the hoop compressive displacement at the edge of the tent. (d) The dependency on \mathcal{S} of the size of the compression zone. All quantities are normalized quantities in this figure.

The detailed size of the compression zone versus center height for various interfacial tractions is further plotted in Figure 7.5b. As expected, large center deflection and weak shear traction at the membrane-substrate interface can facilitate the propagation of the compression zone in the supported region. Notably, both $\bar{\Delta}_1/H^2$ and ρ_o depend on the single sliding parameter \mathcal{S} monotonically, and the corresponding master curves are shown in Figures 5c and d. We may point out that this composite parameter compares the

shear traction at the interface with the stretching forces in the membrane since the latter one scales as H^2 inside the tent.

7.5.2 Effect of \mathcal{J}

We consider the pretension ($T_{pre} = t_{pre}/E_{2D}$, Figure 7.4) in 2D materials that may be introduced when transferring them to target substrates (Brennan et al., 2015). For simplicity, we focus on a limiting case – frictionless interface – such that the general solution for the Airy stress function outside the tent (also known to Lamé) takes a simple form

$$\Phi' = a\rho + b/\rho. \quad (7.40)$$

In addition, we expect $a = T_{pre}$ since the stress resultants approach the applied pretension as $\rho \rightarrow \infty$. The constant b can be determined analytically in terms of the applied pretension T_{pre} and the center height of the tent H based on the continuity conditions at the edge of the tent (Appendix 7.B). With (7.38-7.40), we can derive circumferential compressive displacement

$$\bar{\Delta} = 2\pi(1 + \nu)b/\rho - 2\pi(1 - \nu)T_{pre}\rho. \quad (7.41)$$

Figure 7.6a shows the $\bar{\Delta}$ as a function of ρ for tents subject to different center heights and various values of pretension. Analogous to the effect of T in Figure 7.5a, the distribution of compressive displacement approaches $\bar{\Delta} \sim \rho^{-1}$ as $T_{pre} \rightarrow 0$. Also, the finite pretension makes the decay of $\bar{\Delta}$ faster than ρ^{-1} , especially for tents with small center deflections since the size of the compression zone outside the tent becomes finite. These results are similar to the finite wrinkling zone of a thin polymeric film floating on the water surface while undergoing a point force at the center and surface tension at the edge of the film (Vella et al., 2015).

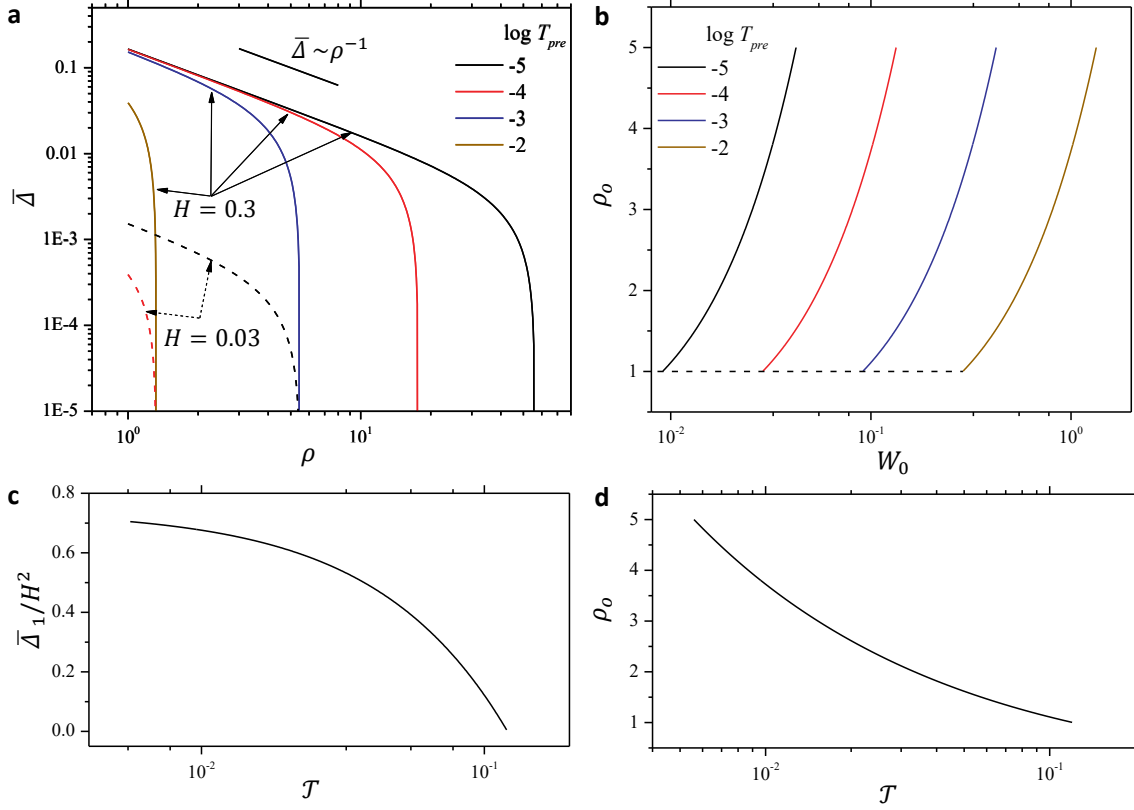


Figure 7.6: (a) Hoop compressive displacement along the radial direction for different values of pretension. Solid curves denote tents with a center height $H = 0.3$ while dashed curves denote $H = 0.03$. Note that for the cases of $T_{pre} = 10^{-3}$ and 10^{-2} , the tent of $H = 0.03$ shows hoop tension across the entire membrane indeed. (b) The size of the compression zone versus the center height of the tent for different values of pretension. The dashed line shows that a critical center deflection is required for the onset of a compression zone outside the tent due to the existence of pretension. (c) The dependency on $\mathcal{T} = T_{pre}/H^2$ of the compressive displacement at the edge of the tent. (d) The dependency on \mathcal{T} of the size of the compression zone. All quantities are normalized quantities in this figure.

We find that when pretension exists, a critical center deflection is required for the onset of the compression zone outside the tent. For example, in the cases of $T_{pre} \geq 10^{-3}$ and $H = 0.03$ in Figure 7.6a, the thin sheet is subject to tension everywhere across its

entire area and hence, circumferential compression is prohibited. This phenomenon can be further elucidated by $\rho_o \sim H$ curves in Figure 7.6b where the outer radius of the compression zone is identified by

$$\bar{\Delta}(\rho_o) = 0. \quad (7.42)$$

Clearly, the critical center deflection ensuring $\rho_o > 1$ increases with increasing pretension in the membrane. Interestingly, the normalized maximum compressive displacement ($\bar{\Delta}_1/H^2$) and the size of the compression zone (ρ_o) depend on a composite parameter $\mathcal{T} = T_{pre}/H^2$ as shown in Figures 7.6c and 7.6d (Appendix 7.B). As the center deflection of the tent causes a strain scaling as $(w(0)/R)^2$ or H^2 , and associated stress scaling as $E_{2D}H^2$, the composite parameter, \mathcal{T} , thus compares the pre-stress with the stress associated with the out-of-plane deformation of the tent. Notably, buckling instabilities are likely to occur only when $\mathcal{T} \lesssim 0.12$. When the interfacial shear traction is considered, we expect two governing parameters: \mathcal{T} and \mathcal{S} .

7.5.3 Effect of ρ_{out}

We now turn to the case that the compression zone engulfs the entire membrane since the size of the 2D materials ($\rho_{out} = R_{out}/R$, Figure 7.4) is typically limited in experiments. Before the outer edge of the compression zone approaches the edge of the 2D material flake ($\rho_o \leq \rho_{out}$), our analysis in Section 7.5.1. should still hold. However, when $\rho_o \equiv \rho_{out}$, we neglect the pretension for simplicity such that the edge of the membrane becomes traction-free, i.e., $N_{rr}(\rho_{out}) = 0$, or

$$\frac{\Phi'(\rho_{out})}{\rho_{out}} + V = 0. \quad (7.43)$$

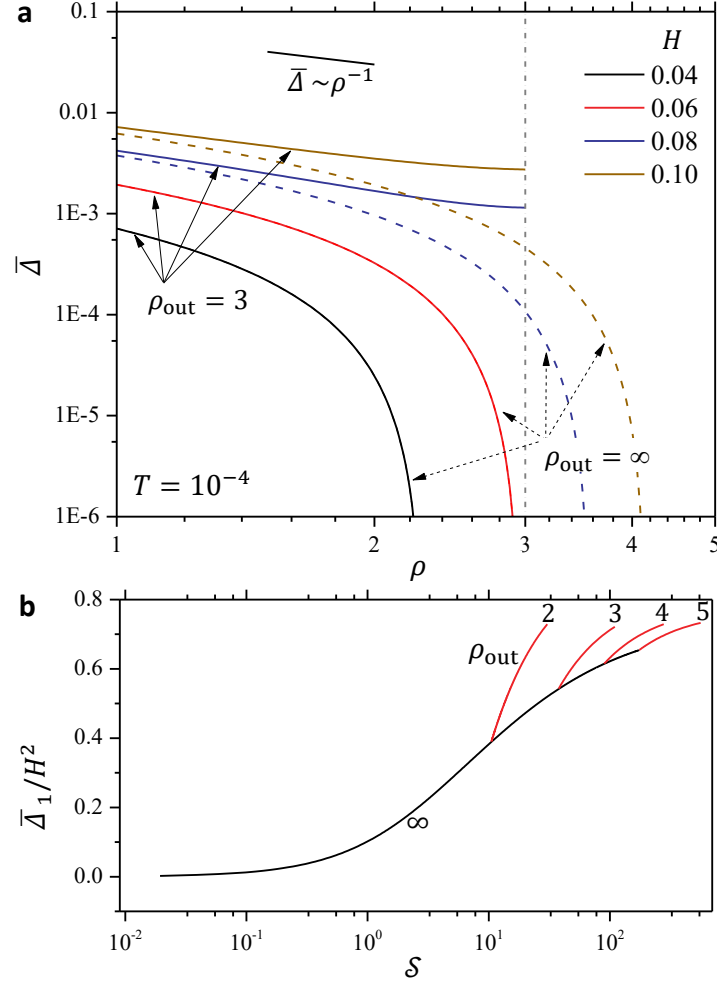


Figure 7.7: (a) Hoop compressive displacement along the radial direction for tents with various center heights. Solid curves denote tents with an outer radius $\rho_{\text{out}} = 3$ while dashed curves denote the case where the membrane size is sufficiently large. Note that when the center height is small (i.e. $H = 0.04$ and 0.06), the solid and dashed curves overlap because $\rho_o \leq \rho_{\text{out}}$. (b) The dependency on T/H^2 of the normalized compressive displacement at the edge of the tent.

We then write circumferential compressive displacement regarding the interfacial shear traction and the size of the 2D material

$$\bar{\Delta} = 2\pi T \rho \left[\frac{c_1}{T} \left(\frac{1-\nu}{\rho_{\text{out}}^2} + \frac{1+\nu}{\rho^2} \right) - \frac{1-\nu^2}{3} \left(\frac{2+\nu}{1+\nu} \rho_{\text{out}} - \rho \right) \right], \quad (7.44)$$

where the constant C_1 can be determined by the abundant continuity conditions at the edge of the tent (Appendix 7.B).

Figure 7.7a shows the evolution of $\bar{\Delta}$ with increasing tent height where solid curves represent membranes with ρ_{out} of 3 and dashed curves represent sufficiently large membranes ($\rho_{\text{out}} > \rho_o$). After $\rho_o \rightarrow 3$, differences between the two types of tents appear regarding the displacement fields. Specifically, further increasing the center height of the tent, dashed curves approach $\bar{\Delta} \sim \rho^{-1}$ from below (the same as the observations in Figure 7.5), while solid curves show larger compressive displacement and even overshoot the $\bar{\Delta} \sim \rho^{-1}$ limit near the outer edge of the thin membrane. In addition, we found that C_1/T is a function of the parameters \mathcal{S} and ρ_{out} (Appendix 7.B), as is the normalized compressive displacement at the edge of the tent $\bar{\Delta}_1/H^2$ as shown in Figure 7.7. When the pretension is considered, we expect three governing parameters in this system: \mathcal{T} , \mathcal{S} and ρ_{out} .

7.5.4 Effect of ρ_{in}

Up to now, we have assumed a point force acting at the tent center. However, in many experimental setups, the radius of the pillar ($\rho_{\text{in}} = R_{\text{in}}/R$) is finite, which may have a nontrivial effect on the size of the compression zone. When accounting for the finite radius of the circular plateau at the tip of the pillar, the differential equations inside the tent, i.e., (7.15) and (7.16), are still applicable, while the integrating domain to derive them becomes $[\rho_{\text{in}}, 1]$. We may consider the following “boundary” values at the edge of the pillar and tent,

$$W(\rho_{\text{in}}) = H, \tilde{\psi}(\rho_{\text{in}}^2) = \tilde{\psi}_{\text{in}}, \tilde{\psi}(1) = \tilde{\psi}_1. \quad (7.45)$$

$\tilde{\psi}_1$ is constrained by the continuity conditions and then relates to the size of the compression zone by (7.30). In addition, we assume that the radial displacement is fixed at the edge of the pillar for simplicity that requires

$$\left. \frac{d\tilde{\psi}}{d\eta} \right|_{\eta=\rho_{\text{in}}^2} = \frac{1+\nu}{2} \frac{\tilde{\psi}_{\text{in}}}{\rho_{\text{in}}^2}. \quad (7.46)$$

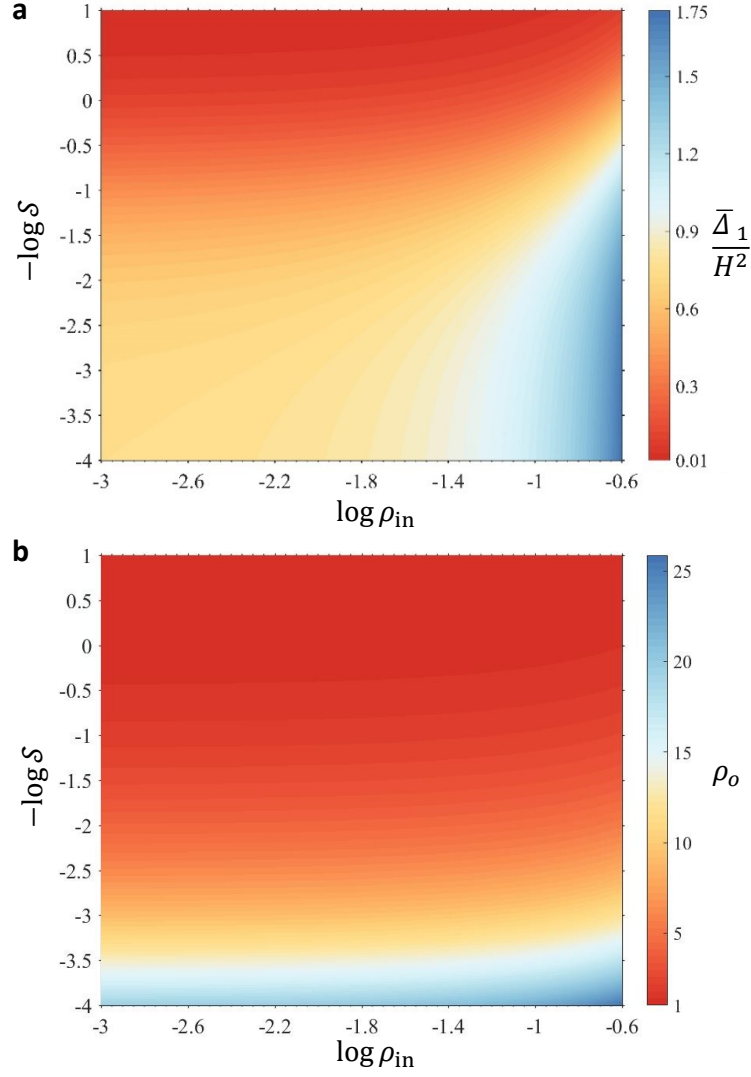


Figure 7.8: Contour plots for the normalized compressive displacement at the edge of the tent $\bar{\Delta}_1/H^2$ (a) and the size of the compression zone ρ_o (b) as a function of two governing parameters: ρ_{in} and \mathcal{S} .

We still pursue exact analytical solutions using the same technique as outlined in Section 7.4 (effects of the finite size of the 2D material and pretension are neglected, see details in Appendix 7.C). This allows us to eliminate intermediate parameters and find out

governing ones: the radius of the pillar and the combined parameter \mathcal{S} . In Figure 7.8, we show the dependency of the normalized compressive displacement at the edge of the tent $\bar{\Delta}_1/H^2$ and the size of the compression zone ρ_o on ρ_{in} and \mathcal{S} . As $\rho_{in} \rightarrow 0$, we verify that these results recover those obtained by assuming a point force in Figure 7.5. Furthermore, we find that the hoop compression at the edge of the tent increases significantly as the pillar radius increases from 0.001 to 0.25, (Figure 7.8a) while the size of the compression zone increases slightly (Figure 7.8b). When the finite size of the 2D material and pretension are considered, we expect four governing parameters: \mathcal{T} , \mathcal{S} , ρ_{in} , and ρ_{out} .

7.6 FAR-FROM-THRESHOLD MODELING

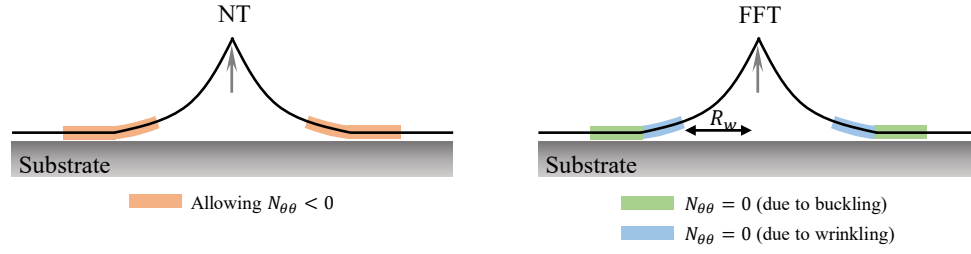


Figure 7.9: Schematic illustration of the difference between near-threshold (NT) and far-from-threshold (FFT) modeling of a thin sheet tent.

Based on the NT analysis, we have derived four controlling parameters exactly: \mathcal{S} , \mathcal{T} , ρ_{out} , and ρ_{in} . However, such analysis may approximate well only when the sheet is very thick and the substrate can largely constrain the formation of the buckling (the ~ 15 -layer graphene sample shown in Figure 7.15 would be an example). FFT analysis comes naturally from that buckle instabilities occur and relax the hoop compressive stress such that $N_{\theta\theta} \approx 0$ or $|N_{\theta\theta}| \ll N_{rr}$ (Davidovitch et al., 2011; Vella and Davidovitch, 2018). This scenario would be particularly true for a highly bendable sheet that is wrinkled in the suspended region and buckled in the substrate-supported region, for example, the

monolayer MoS₂ sample shown in Figure 7.2a right panel and Figure 7.14. As a result, a number of regions should be considered in general, including a central suspended and unwrinkled region $[0, \rho_w]$, a suspended and wrinkled region $[\rho_w, 1]$, a supported and buckled region outside the tent $[1, \rho_b]$, and then an outmost unbuckled region $[\rho_b, \rho_o]$. In this case, the size of the buckled zone can be estimated by the size of the zero- $N_{\theta\theta}$ region (denoted by ρ_b). Note that the last region needs more thoughts when the pretension applies or when the buckled zone propagates and engulfs the finite membrane. For simplicity, we neglect the finite size effect of the sheet and the pretension (due to a number of uncertainties as discussed later in Section 7.8.2.) for this FFT analysis and focus on the main physics associated with the interfacial shear traction.

We define $\rho = \rho_w$ (i.e. $r = \rho_w R$) as the boundary between the unwrinkled and wrinkled region in the suspended region of a tent (Figure 7.9). When $0 \leq \rho \leq \rho_w$, the regular FvK equations, i.e. (7.15) and (7.16), and their analytical solutions, still apply. Particularly, at $\rho = \rho_w$, we can define a useful parameter $\tilde{\psi}_w = \tilde{\psi}(\rho_w^2)$ that satisfies

$$\frac{\bar{F}\sqrt{(-\alpha)^3}}{4\pi}\rho_w^2 = -\sqrt{\tilde{\psi}_w(1-\tilde{\psi}_w)} + \tan^{-1}\sqrt{\tilde{\psi}_w/(1-\tilde{\psi}_w)}. \quad (7.47)$$

At this boundary, we also let the hoop stress be zero (Vella and Davidovitch, 2018) and, according to (7.26), obtain

$$\frac{\bar{F}\sqrt{(-\alpha)^3}}{2\pi}\rho_w^2 = \sqrt{\frac{\tilde{\psi}_w^3}{(1-\tilde{\psi}_w)}} \quad (7.48)$$

Interestingly, combining (7.47) and (7.48) can eliminate \bar{F} , α , and ρ_w simultaneously, such that $\tilde{\psi}_w$ must satisfy the transcendental equation

$$\sqrt{\tilde{\psi}_w^3/(1-\tilde{\psi}_w)} + 2\sqrt{\tilde{\psi}_w(1-\tilde{\psi}_w)} = 2\tan^{-1}\sqrt{\tilde{\psi}_w/(1-\tilde{\psi}_w)}, \quad (7.49)$$

whose nontrivial solution is $\tilde{\psi}_w \cong 0.6965$. However, ρ_w is not known *a priori*, which prevents the solution to $\bar{F}\sqrt{(-\alpha)^3}$.

To deal with this unknown, we move on to the wrinkled region, $\rho_w \leq \rho \leq 1$, within which the second FvK equation concerning the compatibility is replaced by $N_{\theta\theta} = 0$. This leads to a constant Φ' , and a linear out-of-plane profile of the tent according to the first FvK equation (within which $\bar{F} = 0$),

$$\Phi' = -\frac{\tilde{\psi}_w}{\alpha\rho_w} \text{ and } W = C_w(1 - \rho), \quad (7.50)$$

where we used the continuity of radial stress at $\rho = \rho_w$ and the boundary condition $W(1) = 0$. To ensure the continuity of in-plane displacement ($u = R\tilde{u}$), we recall the kinematics within the wrinkled region to show that

$$\epsilon_{\rho\rho} = \frac{d\tilde{u}}{d\rho} + \frac{1}{2}\left(\frac{dW}{d\rho}\right)^2 \text{ or } -\frac{\tilde{\psi}_w}{\alpha\rho_w\rho} = \frac{d\tilde{u}}{d\rho} + \frac{1}{2}C_w^2. \quad (7.51)$$

Integrating (7.51) once, we have

$$\tilde{u}(\rho_w) - \tilde{u}(1) = -\frac{\tilde{\psi}_w}{\alpha\rho_w} \ln \rho_w + \frac{1}{2}C_w^2(1 - \rho_w). \quad (7.52)$$

This means the in-plane displacement difference across the wrinkled region is enlarged by the in-plane stretch of the sheet (since $\rho_w \leq 1$ and $\alpha < 0$) while reduced by the out-of-plane rotation of the sheet. We can detail $\tilde{u}(\rho_w)$ by Hooke's law and stress states in the unwrinkled region at $\rho = \rho_w$,

$$\tilde{u}(\rho_w) = \frac{\rho_w(N_{\theta\theta} - \nu N_{rr})}{E_{2D}} = \nu \frac{\tilde{\psi}_w}{\alpha\rho_w}. \quad (7.53)$$

To detail $\tilde{u}(1)$, we consider the stress field in the compression-free, supported region ($1 \leq \rho \leq \rho_b$), where (7.18) is modified by the release of the hoop stress due to buckling. We rewrite the in-plane force balance equation that reads

$$\frac{d}{dr}(rN_{rr}) + \tau r = 0. \quad (7.54)$$

We can find the exact solution to (7.54) when the pretension is absent (see Appendix 7.D),

$$\frac{N_{rr}}{E_{2D}} = \frac{T}{2}(\rho_b^2\rho^{-1} - \rho) + C_N T\rho^{-1}, \quad (7.55)$$

where $C_N = -\frac{2+\nu}{3}\rho_b^2 - \frac{\nu-1}{6}\rho_o^3\rho_b^{-1} + \frac{1+\nu}{2}\rho_o\rho_b$ and $\rho_b = \frac{1-\nu+\sqrt{9+6\nu-15\nu^2}}{4+8\nu}\rho_o$. The

associated displacement at the edge of the tent,

$$\tilde{u}(1) = \int_{\rho_c}^1 \frac{N_{rr}}{E_{2D}} d\rho = \frac{T}{4}(-2\rho_b^2 \ln \rho_b + \rho_b^2 - 1) - C_N T \ln \rho_b + C_v T \rho_b \rho_c, \quad (7.56)$$

where $C_v = \nu(1+\nu) \left[-3(1+3\nu) + \sqrt{3(1-\nu)(3+5\nu)} \right] / (4+8\nu)$. The continuity of radial stress at $\rho = 1$ can then give rise to

$$\alpha\rho_w T(\rho_b^2 - 1) + 2\tilde{\psi}_w + 2\alpha C_N T \rho_w = 0 \quad (7.57)$$

and the continuity of the in-plane displacement, together with (7.52) and (7.53), leads to

$$\frac{\tilde{\psi}_w}{\rho_w} \ln \rho_w - \frac{\alpha C_w^2}{2}(1 - \rho_w) + \frac{\nu \tilde{\psi}_w}{\rho_w} - \frac{\alpha T}{4}(-2\rho_b^2 \ln \rho_b + \rho_b^2 - 1) + \alpha C_N T \ln \rho_b - \alpha C_v T \rho_b \rho_o = 0. \quad (7.58)$$

Along the line of NT modeling in Section 7.4, we relate the parameter of interest (i.e. ρ_o and ρ_w) to the center height of the tent,

$$H = W(\rho_w) + \int_{\rho_w}^0 \frac{-\bar{F} d\rho}{2\pi\Phi'} = C_w(1 - \rho_w) + \frac{2}{\sqrt{-\alpha}} \tan^{-1} \sqrt{\tilde{\psi}_w/(1 - \tilde{\psi}_w)}. \quad (7.59)$$

Finally, the continuity of the tent's slope at $\rho = \rho_w$ should be satisfied, giving an equation for C_w according to (7.15) and (7.48)

$$C_w = \frac{1}{\rho_w \sqrt{-\alpha}} \sqrt{\frac{\tilde{\psi}_w}{1 - \tilde{\psi}_w}}. \quad (7.60)$$

The problem containing multiple regions is then largely simplified (see Appendix 7.D), which is to solve analytical (7.57-7.60) for ρ_b and ρ_w with the prescribed center height of the tent W_0 and interfacial shear traction T . We find $\sqrt{-\alpha}H \sim f(\rho_w)$ from (7.59) and (7.60) and $\alpha T \sim g(\rho_b, \rho_w)$ from (7.57), which again enable the composite parameter \mathcal{S} to select ρ_b and ρ_w .

7.7 PARAMETRIC STUDIES BASED ON FAR-FROM-THRESHOLD MODELING

With the analytical FFT modeling, we are able to elucidate how the size of the buckled and wrinkled region evolves with the controlling composite parameter. It is worth noting that in FFT modeling, buckling instabilities take place and ρ_b characterizes the

extent of the buckled region by the size of the zero- $N_{\theta\theta}$ region; in NT modeling, instabilities are suppressed and ρ_o represents the supported region where sliding radially inward occurs (i.e. $u < 0$). The extent of the buckled region (i.e. ρ_b in FFT modeling) is directly accessible to AFM-based topographical characterizations; the sheet sliding around a tent accompanies radial tension and hoop compression – both of them vary radially, making ρ_o in NT modeling accessible to Raman spectroscopy (Kitt et al., 2013; Wang et al., 2017b).

7.7.1 Extent of the buckled and wrinkled region

The $\rho_b - T/W_0^2$ and $\rho_w - T/W_0^2$ relations are plotted in Figure 7.10a and b, respectively. As expected, like the size of the compression zone in the NT modeling, the extent of both buckled (ρ_b) and wrinkled ($1 - \rho_w$) region increases in the FFT modeling as the sliding parameter \mathcal{S} increases. A key difference is that the formation of wrinkling and buckling requires a critical \mathcal{S} (≈ 0.43), beyond which the buckled region appears and grows. The critical \mathcal{S} for the onset of instabilities results from Poisson's effect: a material circle (e.g. at the edge of the tent) is likely to wrinkle/buckle only when its inward shrinkage caused by the sliding overwhelms the lateral shrinkage caused by the radial tension. This critical value thus vanishes as the Poisson's ratio goes to zero.

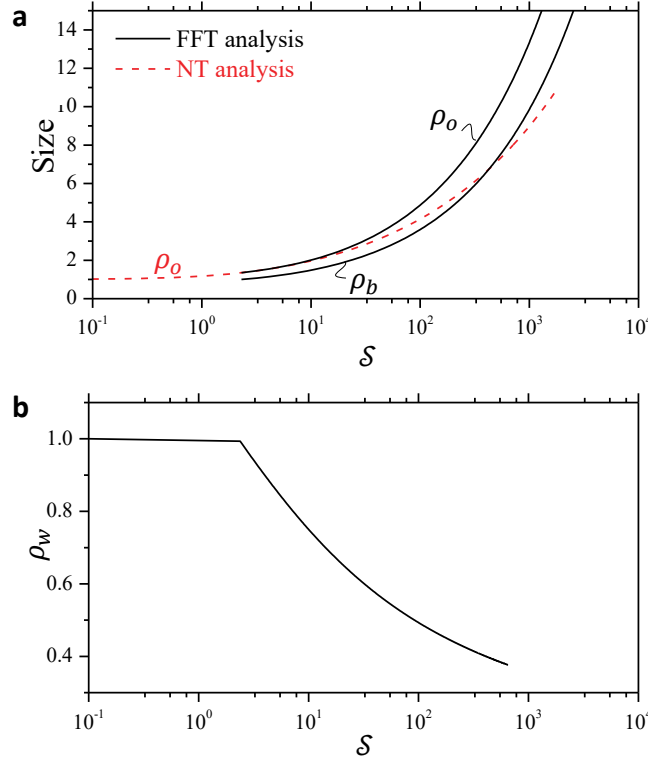


Figure 7.10: (a) The dependency on T/H^2 of the extent of the buckled region ρ_b (black solid curve, predicted by FFT analysis) and the size of the compression zone ρ_o (black solid curve predicted by FFT analysis and red dashed curve predicted by NT analysis). (b) The dependency on T/H^2 of the extent of the wrinkled region ρ_w in the suspended region of the tent (predicted by FFT analysis).

7.7.2 NT and FFT modeling

It is natural to compare FFT with NT modeling regarding how ρ_o evolves (Figure 7.10a) as both types of modeling characterize $\rho = \rho_o$ by the position where the stresses decay to zero (neglecting the pretension and finite size of the sheet). We find that these two types of modeling give close $\rho_o - T/H^2$ prediction when $\rho_o < 3$ (the difference is within 20%), implying that the formation of buckling and wrinkling causes only a small perturbation to the stress state of a tent under such condition. However, the difference

becomes increasingly significant as ρ_o grows (in particular, it grows faster in the FFT modeling).

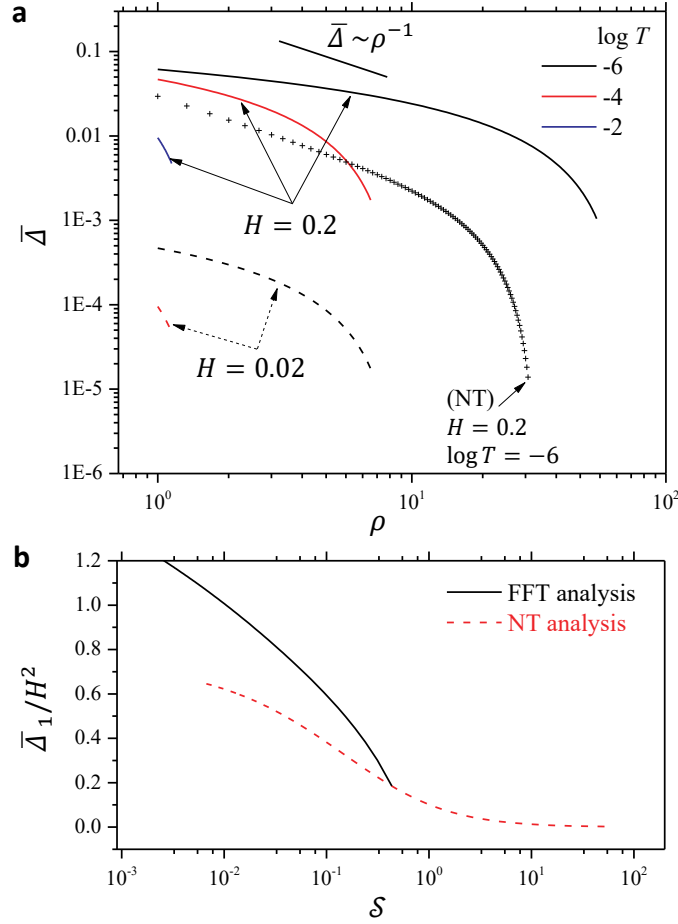


Figure 7.11: (a) Hoop compressive displacement along the radial direction for various interfacial shear tractions. Solid curves denote tents with a center height $H = 0.2$ while dashed curves denote $H = 0.02$. The markers are from NT modeling in Figure 7.5a. (b) The dependency on S of the compressive displacement at the edge of the tent. The red dashed curve is from NT modeling in Figure 7.5c.

Besides, the spatial distribution of the hoop compression, $\bar{\Delta}$, (i.e. the shortened perimeter of a material circle) is intrinsically different between NT and FFT modeling. We have shown the scaling $\bar{\Delta} \sim \rho^{-1}$ in the analysis of NT modeling (Section 7.5) when the deformation is large, or the interfacial shear traction is small. In FFT modeling, the hoop compression is calculated from (7.55) that allows the hoop compressive stress to be relaxed by buckling,

$$\bar{\Delta} = -2\pi\tilde{u} = \pi T \left[\rho_b^2 \ln \frac{\rho_b}{\rho} + \frac{1}{2}\rho^2 - \frac{1}{2}\rho_b^2 + 2C_N \ln \frac{\rho_b}{\rho} + \frac{(1-\nu)(\rho_o - \rho_b)^2(\rho_o + 2\rho_b)}{3\rho_b} \right]. \quad (7.61)$$

We plot $\bar{\Delta}$ as a function of ρ in Figure 7.11a for tents subject to different center heights and interfacial shear tractions. Clearly, the $\bar{\Delta} \sim \rho^{-1}$ relation breaks down (see solid and dashed curves). Besides, we find that the buckling instability brings more slip and hence, a larger hoop compression compared with the results in the NT modeling under the same loading condition. The physical interpretation is that the formation of the buckle delamination in the supported region makes the sheet (and its interface) less resistive to the inward sliding. We may also draw this conclusion by considering the shortened perimeter of the material circle at the edge of the tent, $\bar{\Delta}_1$ in Figure 7.11b, where $\bar{\Delta}_1/H^2$ depends on a single parameter, \mathcal{S} . Based on the analysis of NT modeling in Section 7.5, we also expect three additional governing parameters: \mathcal{T} , ρ_{out} , and ρ_{in} in this FFT modeling when the pretension, the sheet's finite size, and the pillar's finite radius are taken into account. Here, we focus on the effect of the pillar's radius because of its particular uses in the mechanical metrology of interfacial shear traction and the design of pillar-poked tents that will be discussed in Section 7.8.

7.7.3 Finite pillar radius

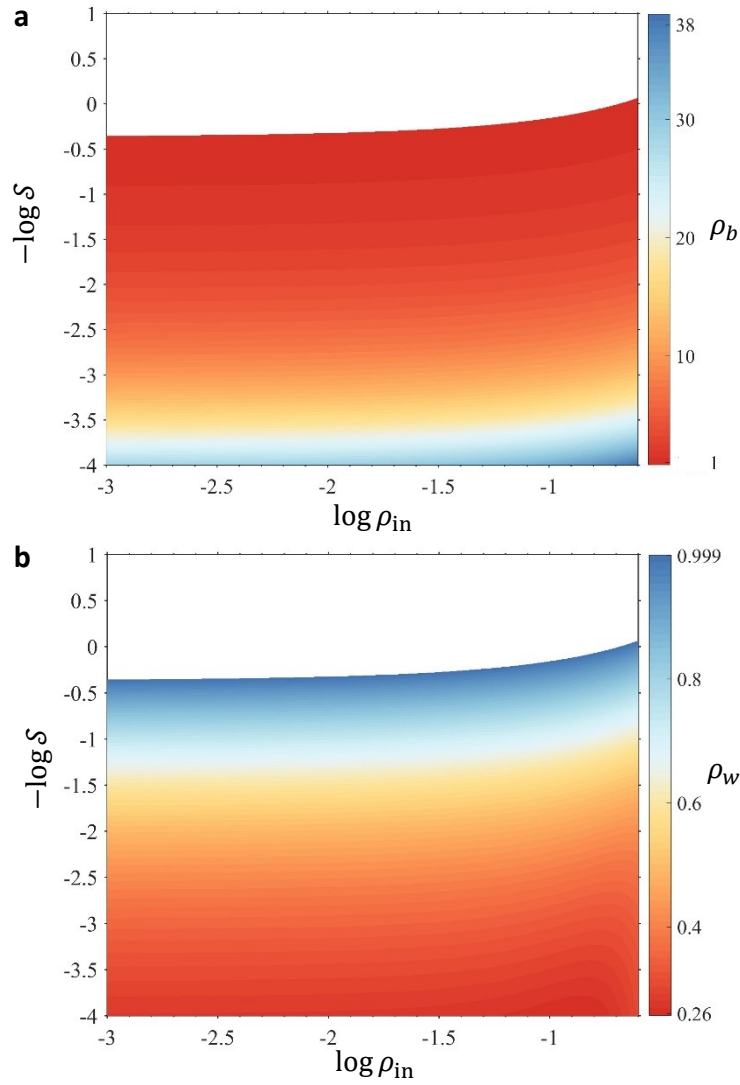


Figure 7.12: Contour plots for the extent of the buckled region ρ_b outside the tent (a) and the extent of the wrinkled region ρ_w inside the tent (b) as a function of two governing parameters: ρ_{in} and \mathcal{S} .

We still consider the exemplary case where the radial displacement is fixed at the edge of the pillar. Using the same technique as outlined in Section 7.5.4, we show exact analytical solutions based on the FFT modeling in Appendix 7.E. Similarly, two governing parameters appear in the FFT modeling: the radius of the pillar ρ_{in} and the combined

parameter $\mathcal{S} = T/H^2$. We then show the dependency of the extent of the buckled region and wrinkled region on these two governing parameters in Figure 7.12. To be consistent with Figure 7.8, we focus on the domain $0.001 \leq \rho_{\text{in}} \leq 0.25$. The results as $\rho_{\text{in}} \rightarrow 0$ can recover those obtained by assuming a point force in Figure 7.10 and the upper limit of ρ_{in} also avoids $\rho_w < \rho_{\text{in}}$ (Figure 7.12). Note that the blank regime in Figure 7.12 covers the conditions under which instabilities are prohibited, and hence the nonzero radius of a pillar essentially facilitates the onset of instabilities. In general, tents poked by sharper pillars feature a shorter extent of the buckled and wrinkled region. However, non-monotonic behavior arises for ρ_w in the bottom right corner of the contour plot in Figure 7.12b. It would be interesting to clarify how the growth of the wrinkled region benefits from the pillar at its early stage, yet becomes suppressed by the pillar when the wrinkle gets close to the pillar edge as well as how the system behaves after the wrinkle comes into contact with the pillar in a future study.

7.8 IMPLICATIONS FOR 2D MATERIAL APPLICATIONS

Having characterized buckles around the 2D material tent and modeled the tent with a sliding boundary analytically, we conclude by highlighting the implications of our results for 2D-material-based applications.

7.8.1 Estimation of interface adhesion

In the nanoscale regime, the interactions between the 2D material and its substrate become relatively significant such that the performance of 2D-material-based devices relies heavily on the mechanical behaviors of interfaces (Geim and Grigorieva, 2013; Neto et al., 2009). This fact has motivated extensive efforts to understand the mechanics of 2D

material interfaces, especially adhesion and friction (Akinwande et al., 2017; Lloyd et al., 2017; Zong et al., 2010).

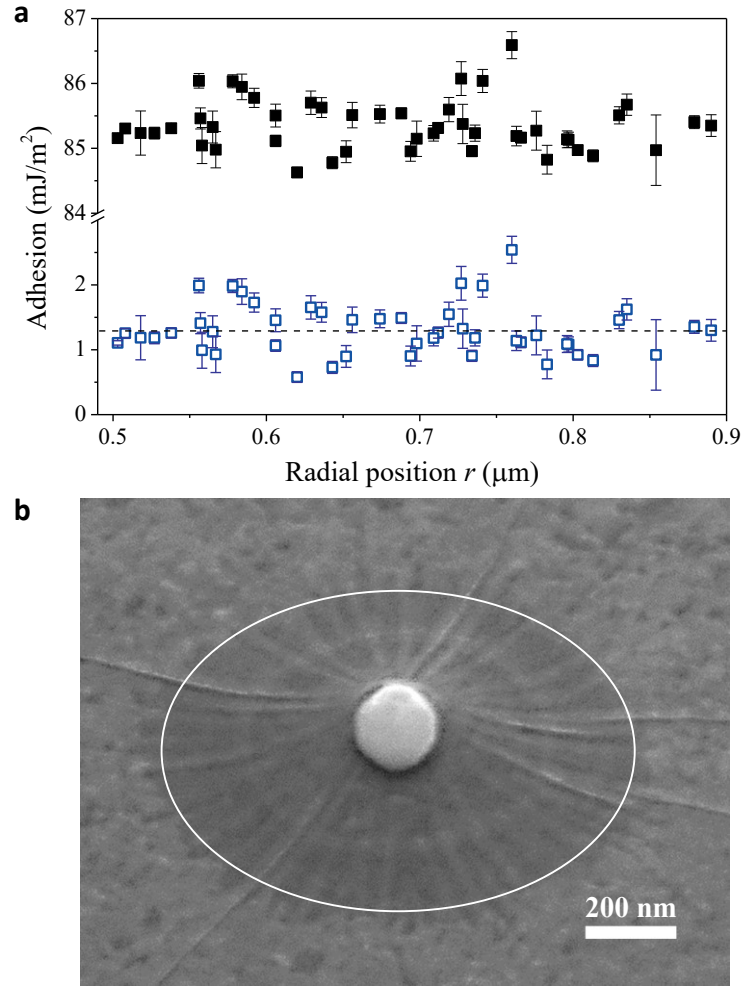


Figure 7.13: (a) The estimated adhesion energy between CVD-grown monolayer MoS_2 and the Al_2O_3 substrate. This estimation is enabled by measuring the buckle profiles at different radial locations, which are offered in Figure 7.3c. Blue markers are based on gas-filled buckles and solid markers are based on water-filled buckles. (b) The SEM image of the monolayer MoS_2 tent in Figure 7.2a. The solid white circle highlights the edge of the tent.

In Section 7.3.1, we pointed out that the crest curvature of the buckles can be used to estimate the interface adhesion between the 2D material and its substrate after identifying the content (i.e., gas or liquid) trapped inside the buckle. Plugging our measurements in Figure 7.2c into (7.4) and (7.5), the extracted adhesion energy between the monolayer CVD-grown MoS₂ and Al₂O₃ is $\sim 1.3 \text{ mJ/m}^2$ by taking the content as gas and the bending stiffness as 10 eV (Figure 7.13a) (Androulidakis et al., 2018). If we assume that the buckles are filled with water such that $\gamma_l = 72 \text{ mJ/m}^2$, $\theta_s = 36^\circ$, and $\theta_m = 69^\circ$ (Kozbial et al., 2015; Rafiee et al., 2012; Santos et al., 2003), (7.6) offers a more reasonable adhesion value of $\sim 85.3 \text{ mJ/m}^2$, which is comparable with many adhesion values reported in the literature (Deng et al., 2017; Lloyd et al., 2017; Sanchez et al., 2018).

We have claimed that the water-filled buckle model could give a more reasonable adhesion value (comparable previous reports) than the gas model. The reason is that the former considers essentially three interfaces (water-membrane, water-substrate, and membrane-substrate) such that the wetting properties of the system will contribute to the extracted value of the membrane-substrate adhesion. However, so far there is no solid evidence for the presence of water trapped inside the buckle through the SEM image in Figure 13b shows likely liquid fringes near the edge of the tent (the darkish region near the white circle). The authors are working on characterizations of the trapped chemical components. It is expected that the detailed trapped substance contains both water and hydrocarbon that are readily absorbed in the 2D material-substrate interface (Khestanova et al., 2016), thus affecting the surface tension of the liquid, contact angle, and the extracted adhesion energy in (7.6). Besides, the mixed-mode adhesive interactions between the membrane and the substrate are not considered in this work. The above-mentioned adhesion is more rigorously called adherence (Boijoux et al., 2018; Faou et al., 2015; Hutchinson and Suo, 1991). However, the difference between adhesion and adherence in

our system may be small due to the facts that (i) the bending may dominate the deformation, and (ii) the interfacial shear traction is typically much weaker than normal traction as the interface is adhered by pure van der Waals (vdW) forces and 2D materials are atomically smooth. It would be interesting to examine the exact phase angle of mode-mix in this buckled configuration (Boijoux et al., 2018; Faou et al., 2015; Hutchinson and Suo, 1991), particularly with the consideration of the frictional features of the vdW interface (Ruffini et al., 2012a; Ruffini et al., 2012b).

7.8.2 Estimation of interface friction (FFT)

Our present analysis relates the size of the compression zone (in NT) and the extent of the buckled and wrinkled region (in FFT) to four governing parameters: \mathcal{S} , \mathcal{T} , ρ_{out} and ρ_{in} . Experimentally, the effect of a sheet's finite size can be neglected, the tent height and the pillar radius can be accessible through AFM-based characterizations, while the force terms, i.e., interfacial shear traction and pretension, are relatively elusive. The pretension was extensively used as a fitting parameter in indentation tests and found to be less than $\sim 0.4 \text{ N/m}$, i.e., $T_{\text{pre}} \sim 10^{-3}$ for graphene (Lee et al., 2008). However, the exact pretension varies heavily with materials, substrate, and transfer processes, and even appears to be negative (residual compression). Herein, we neglect the pretension effect such that we are able to estimate the interfacial shear traction via experimentally accessible parameters, including ρ_b , ρ_{in} , and H . It is worth noting that the pretension may be caused by surface tension at the outer edge of the membrane, epitaxial growth, thermal expansion and so on, which would modify such estimation (Dai et al., 2019a; Davidovitch et al., 2019). Experimentally, mapping of Raman bands may shed light on the level of the pretension but uncertainties are nontrivial due to the so-called doping effect from the substrate (Dai et al., 2019a).

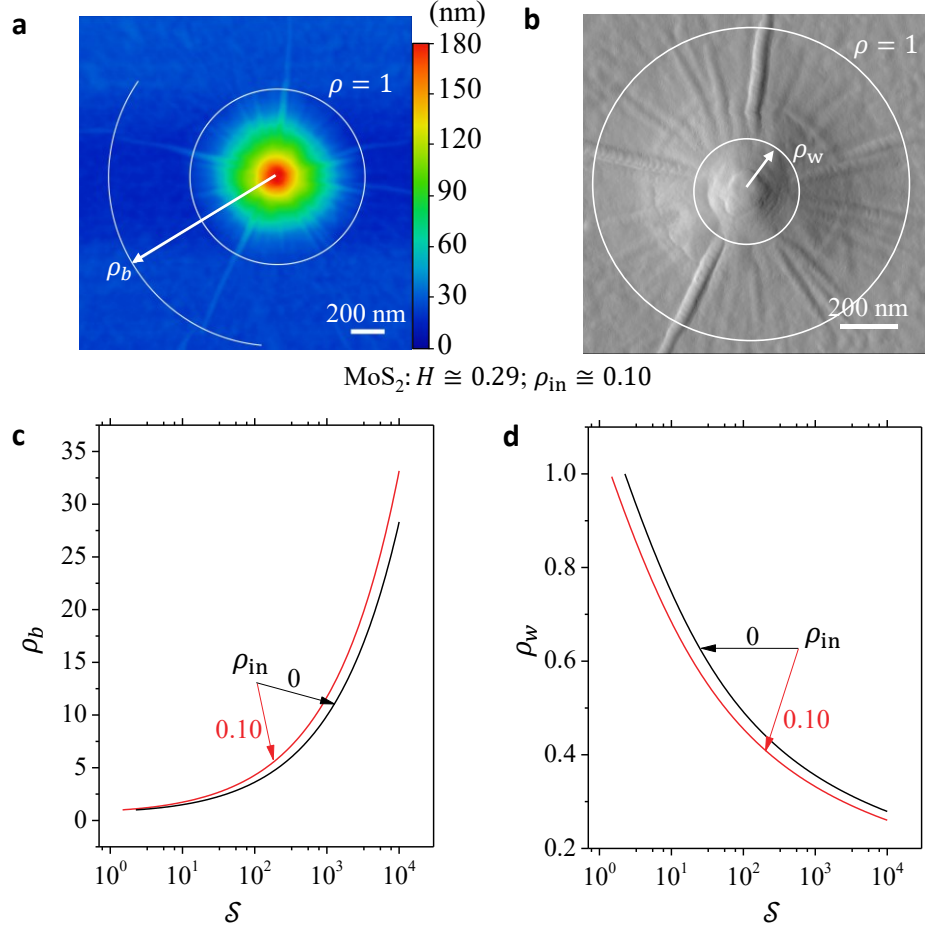


Figure 7.14: AFM height (a) and amplitude (b) images of a monolayer MoS_2 tent, based on which ρ_{in} , H , ρ_b and ρ_w are extracted (These two are the same with the Figure 1c in (Dai et al., 2018)). The extent of the buckled region (c) and wrinkled region (d) depends on the interface shear traction T , the height of the tent H , and the radius of the pillar ρ_{in} .

We first focus on a CVD-grown monolayer MoS_2 tent. From its AFM height and amplitude image in Figure 7.14a and b, we see both suspended, wrinkled region and supported, buckled region. We then assume that such instabilities can relax the hoop compressive stress in this atomically thin sheet such that our analytical FFT results in Section 7.7.3 can be leveraged directly. We measure the H of this monolayer MoS_2 tent from its AFM height image and determine the tent radius by line-scans across the tent

center as well as the ratio of pillar radius to tent radius ($\rho_{in} \sim 0.10$). The tent's ρ_b is simply estimated to be 1.89 ± 0.17 through the location beyond which the buckles disappear (Figure 7.14a) and, similarly, the tent's ρ_w is found to be 0.35 ± 0.04 (Figure 7.14b).

We plot the master $\rho_b \sim \mathcal{S}$ curve for the specific ρ_{in} in Figure 7.14c. Plugging the geometrical parameters obtained above into the master curve leads to shear traction ranging from 1.7 to 2.9 MPa for the CVD-grown monolayer MoS₂ on Al₂O₃. However, our criterion that buckle delamination occurs in the supported region whenever the sheet is under compressive stress may cause errors in predicting the extent of the buckled region. The errors mainly come from the fact that the onset of buckle delamination of a sheet typically needs a nontrivial compressive strain (Vella et al., 2009) because of adhesion. Therefore, our criterion may underestimate the extent of the buckled region and hence overestimate the traction. We also plot the master curve for the extent of the wrinkled region in Figure 7.14d, plug the measured ρ_w into it, and find a much weaker interfacial shear traction (~ 0.04 MPa). The huge inconsistency between ρ_w -based and ρ_o -based estimations may be a result of the complexity in real experimental fabrications: the sheet is transferred with a pre-existing nanoparticle on the substrate, and the complicated contact occurs spontaneously. Our model is idealized for the situation that the center height of the tent is loaded quasi-statically, which calls for further controlled indentation experiments (possibly at larger scales) for validations.

7.8.3 Estimation of interface friction (NT)

We then move on to a relatively thick 2D flake, i.e. the ~ 15 -layer graphene tent in Figure 7.15. For this multilayer sample, the hoop compressive stress in the supported region may not be completely relaxed, and we then prefer to apply the NT analysis developed in Section 7.5.4 though the difference between FFT and NT analysis here could

be minor since $\rho_o < 2$. More appropriate modeling might be achieved by considering the wrinkling instability in the suspended region of the tent but neglecting the buckle or the buckle-caused stress relaxation in the supported region (we expect that the results should lie in between FFT and NT limits and the difference could be negligible for small ρ_o).

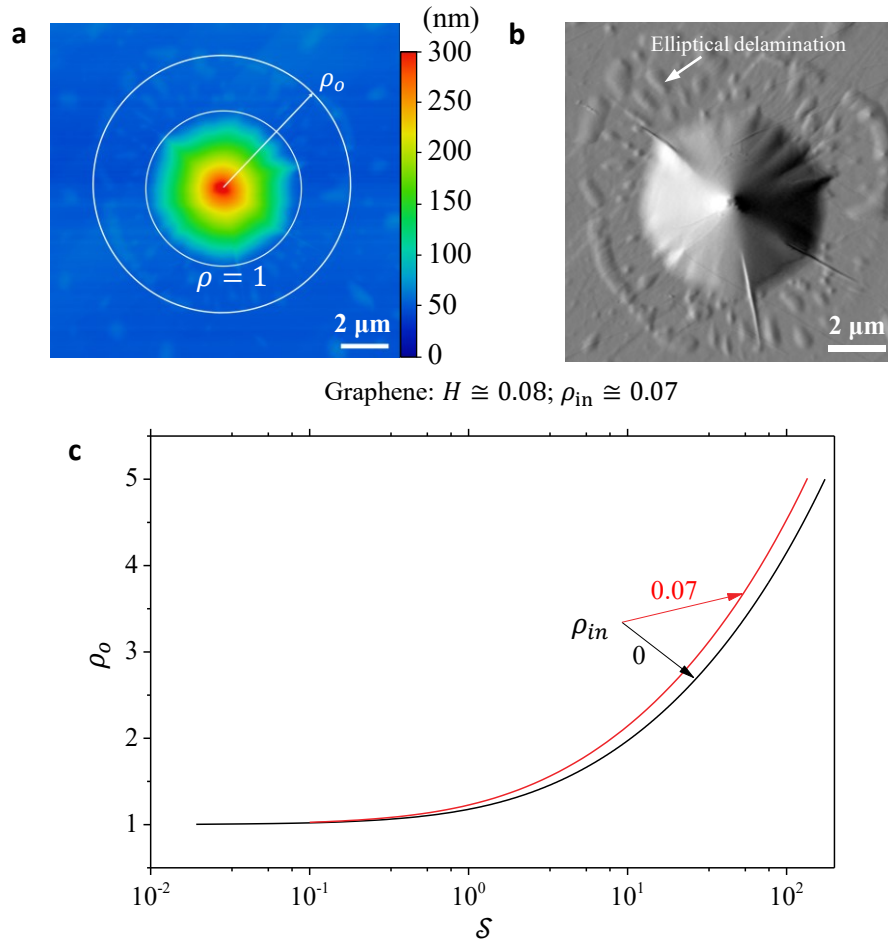


Figure 7.15: AFM height (a) and amplitude (b) images of a ~ 15 -layer graphene tent, based on which ρ_{in} , H , and ρ_o are extracted (These two are the same with the Figure 7.1b in (Dai et al., 2018)). (c) The radius of the compression zone outside the tent depends on the interface shear traction T , the height of the tent H , and the radius of the pillar ρ_{in} .

We find an obvious coffee-ring-like domain in the supported region (see the AFM amplitude image in Figure 7.15b). Inside this domain, the local delamination (labeled by the arrow) takes elliptical shapes with the long axis along the radial direction of the tent. Similar features have been observed recently in thin-film-capped droplets when an anisotropic stretch is applied to the thin film (Schulman and Dalnoki-Veress, 2018). In our case, the anisotropy within this coffee-ring-like domain should arise from the local hoop compression and radial tension, i.e. $N_{rr} > N_{\theta\theta}$, which are indeed caused by the inward sliding of the sheet ($u < 0$). We therefore approximately extract the corresponding $\rho_o = 1.72 \pm 0.26$ by the outer radius of this domain.

From the AFM height image of the multilayer graphene tent, we extract H (~ 0.08) and ρ_{in} (~ 0.07). The master $\rho_c \sim \mathcal{S}$ curves for this specific ρ_{in} is plotted in Figure 7.15c based on NT modeling. Plugging these geometrical parameters into the master curve leads to shear traction ranging from 0.9 to 5.6 MPa for the exfoliated multilayer graphene on SiO₂. This result shows quantitative agreement with the shear traction, also called interfacial shear stress, which was measured to be 1-3 MPa for monolayer graphene on SiO₂ via bulge tests of drumhead specimens (Kitt et al., 2013; Wang et al., 2017b). The relatively large uncertainty for the multilayer graphene sample comes from the uncertainty in both ρ_o and the number of layers (see Section 7.2).

7.8.4 Guidelines for fabricating arrays of 2D material tents

Recently, arrays of micro-tents became a popular strategy for the periodic strain engineering of 2D materials due to their self-sustainability and designability. A typical puzzle when designing arrays of 2D material tents comes from the dimensions of the supporting micro/nanopillars. Though the sharpness of pillar tips is limited by the fabrication resolution, the pillar height h and the pillar-pillar distance d are relatively easy

to control (Figure 7.11a). However, improper design, such as $d \leq 2R$, may exclude the formation of tents (Figure 7.11b); insufficient pillar-pillar distance, such as $2R \leq d \leq 2R_b$, may cause a network of buckles between tents (Figure 7.11c); isolated tents require $d \geq 2R_b$ (Figure 7.11d), which have been used as strain-engineered arrays of quantum emitters in applications (Branny et al., 2017).

Chopin *et al.* and Dai *et al.* have shown a linear relation between R and h , i.e. $h/R \sim (\Delta\gamma/E_{2D})^{1/4}$, in thin membrane tent and the prefactors at two limits (i.e. $T \rightarrow \infty$ and $T \rightarrow 0$) were derived (Chopin et al., 2008; Dai et al., 2018). Our results in Section 7.5 and 7.7 further provide exact solutions to the nonlinear relation between R_b/R (i.e. ρ_b) and \mathcal{S} as well as how such relation is affected by the radius of pillars. In other words, by knowing the elastic properties of the 2D material as well as the adhesion and friction properties of the 2D material-substrate interface, the configurations in Figures 7.11b-d can be designedly avoided or achieved by tuning the pillar-pillar distance, the pillar radius, and the pillar height. Furthermore, we suggest the formation of buckles may be suppressed by introducing pretension in this system (and *vice versa*). We hope that these quantitative understandings would lead to the deterministic design of arrays of 2D material tents in the future.

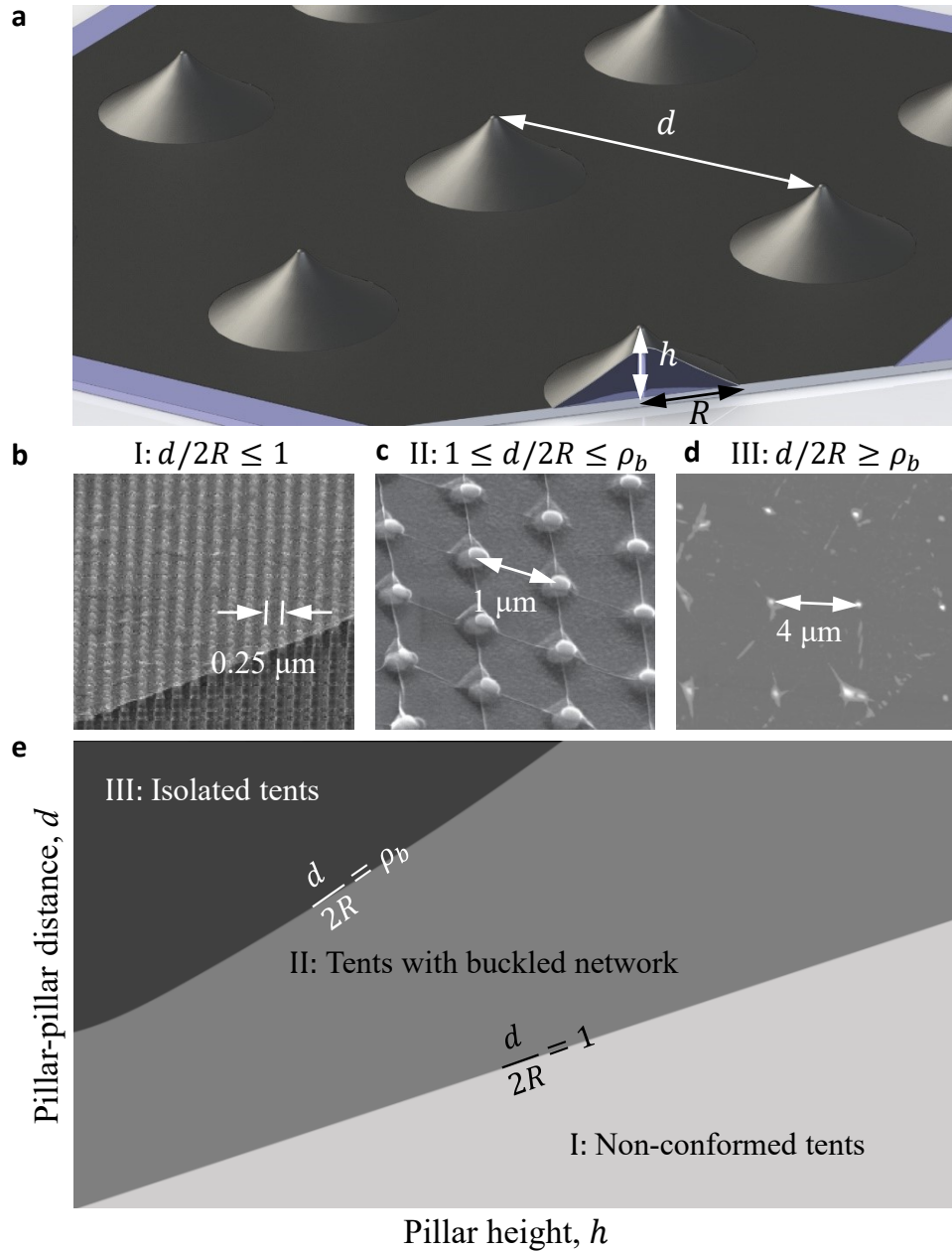


Figure 7.16: (a) Schematic of an array of 2D material tents. (b) SEM image of CVD-grown monolayer graphene on silicon pillars (Reserbat-Plantey et al., 2014). (c) SEM image of CVD-grown monolayer graphene on lift-off resist nanopillars (Tomori et al., 2011). (d) AFM image of the topography of an exfoliated monolayer WSe₂ flake on top of negative resist nanopillars (Branny et al., 2017). (e) A Phase diagram of three configurations of 2D material tent arrays.

7.9 CONCLUSIONS

We presented experimental observations on the radial buckles formed around 2D material tents and found an interesting characteristic length for the hoop-direction curvature of the buckle crests. A simple 1D model is adopted to show how the buckle shape relates to the material properties and the interface adhesion properties. The dependence of the buckle profile on the radial position further suggests that the interface sliding outside the tent may be the origin of hoop compression and buckle delamination. We establish analytical models for cases as simple as tents subjected to a point load at the center, zero shear traction at the interface, and zero pretension on the periphery all the way to tents with finite pillar size, finite pretension as well as finite flake size. Two types of modeling (i.e. NT and FFT modeling) accounting for none and complete compression relaxation are presented and may provide the upper and lower limits for this instability problem, respectively. Several governing composite parameters have been found for each case analytically by which the design of arrays of 2D material tents could be guided in a deterministic way. Furthermore, our theoretical analysis shows that the simple geometrical characterization of these buckles might be utilized for the adhesion and friction metrology of the 2D material-substrate interface.

7.10 APPENDIX

7.A Pretension (NT)

We enforce the continuity of radial stress and displacement at $\rho = 1$,

$$\Phi'(1^-) = \Phi'(1^+) \text{ and } \Phi''(1^-) - \nu\Phi'(1^-) = \Phi''(1^+) - \nu\Phi'(1^+), \quad (7.A1)$$

which lead to

$$\tilde{\psi}_1 = -\alpha(T_{pre} + b), \quad (7.A2)$$

and

$$\frac{d\tilde{\psi}}{d\eta} \big|_{\eta=1} = -\alpha T_{pre}. \quad (7.A3)$$

The continuity of displacement in (7.A3), together with (7.26), can give an equation for the constant α

$$-\alpha T_{pre} = \frac{\bar{F}(-\alpha)^{3/2}}{4\pi} \sqrt{\frac{1-\tilde{\psi}_1}{\tilde{\psi}_1}}. \quad (7.A4)$$

We can eliminate the point force in (7.A4) by (7.29),

$$\alpha(T_{pre}, \tilde{\psi}_1) = \frac{1}{T_{pre}} \left[1 - \tilde{\psi}_1 - \sqrt{\frac{1-\tilde{\psi}_1}{\tilde{\psi}_1}} \tan^{-1} \sqrt{\frac{\tilde{\psi}_1}{(1-\tilde{\psi}_1)}} \right]. \quad (7.A5)$$

If we relate α to the center height of the tent H by (7.37), it is readily found that the constant $\tilde{\psi}_1$ only rely on a combined parameter, $\mathcal{T} = T_{pre}/H^2$. Also, the continuity of radial stress in (7.A2) indicates that b/T_{pre} is a function of $\tilde{\psi}_1$ or \mathcal{T} by

$$\frac{T_{pre}}{b+T_{pre}} = 1 - \frac{1}{\tilde{\psi}_1} + \sqrt{\frac{1-\tilde{\psi}_1}{\tilde{\psi}_1^3}} \tan^{-1} \sqrt{\frac{\tilde{\psi}_1}{1-\tilde{\psi}_1}}. \quad (7.A6)$$

Finally, the size of the compression zone can be determined by (7.42)

$$\rho_o^2 = \frac{1+\nu}{1-\nu} \frac{b}{T_{pre}}, \quad (7.A7)$$

which implies $\rho_o \sim \rho_o(\mathcal{T})$.

7.B Finite sheet size (NT)

The zero radial stress in (7.43) gives that

$$A + B = -\frac{C_1}{\rho_{out}^2} + \frac{2+\nu}{3} T \rho_{out}. \quad (7.B1)$$

The continuity conditions of radius stress and displacement in (7.30) hold and can lead to

$$\tilde{\psi}_1 = -\alpha \left[\left(1 - \frac{1}{\rho_{\text{out}}^2}\right) C_1 + \frac{2+\nu}{3} T(\rho_{\text{out}} - 1) \right], \quad (7.B2)$$

and

$$\frac{d\tilde{\psi}}{d\eta} \big|_{\eta=1} = -\alpha \left(-\frac{1}{\rho_{\text{out}}^2} C_1 + \frac{2+\nu}{3} T \rho_{\text{out}} - \frac{1+\nu}{2} T \right). \quad (7.B3)$$

Still utilizing the intermediate parameter $\tilde{\psi}_1$ in (7.26) and (7.29), equation (7.B3) can give an equation for α

$$-\alpha \left(-\frac{1}{\rho_{\text{out}}^2} C_1 + \frac{2+\nu}{3} T \rho_{\text{out}} - \frac{1+\nu}{2} T \right) = -1 + \tilde{\psi}_1 + \sqrt{\frac{1-\tilde{\psi}_1}{\tilde{\psi}_1}} \tan^{-1} \sqrt{\frac{\tilde{\psi}_1}{1-\tilde{\psi}_1}}. \quad (7.B4)$$

We can further eliminate α by (7.B2) that provides an expression for the $C_1/T \sim \tilde{\psi}_1$ relation

$$\frac{-6C_1/T + 2(2+\nu)\rho_{\text{out}}^3 - 3(1+\nu)\rho_{\text{out}}^2}{6(\rho_{\text{out}}^2 - 1)C/T + 2(2+\nu)(\rho_{\text{out}} - 1)\rho_{\text{out}}^2} = 1 - \frac{1}{\tilde{\psi}_1} + \sqrt{\frac{1-\tilde{\psi}_1}{\tilde{\psi}_1^3}} \tan^{-1} \sqrt{\frac{\tilde{\psi}_1}{1-\tilde{\psi}_1}}. \quad (7.B5)$$

We may also eliminate α in a different way, that is combining (7.B2) and (7.37)

$$\tilde{\psi}_1 = \frac{4T}{H^2} \left[\left(1 - \frac{1}{\rho_{\text{out}}^2}\right) \frac{C_1}{T} + \frac{2+\nu}{3} (\rho_{\text{out}} - 1) \right] \left[\tan^{-1} \sqrt{\frac{\tilde{\psi}_1}{1-\tilde{\psi}_1}} \right]^2. \quad (7.B6)$$

Equations (7.B5) and (7.B6) indicates that C_1/T is a function of the combined parameter $\mathcal{S} = T/W_0^2$ and the geometrical parameter $\rho_{\text{out}} (> 1)$.

7.C Finite pillar radius (NT)

When the pillar radius is finite, we lose the condition of $\tilde{\psi}(0) = 0$ in (7.28). Instead, the integration of (7.26) in this case brings a constant term

$$\frac{\bar{F}\sqrt{(-\alpha)^3}}{4\pi} \eta = -\sqrt{\tilde{\psi}(1-\tilde{\psi})} + \tan^{-1} \sqrt{\frac{\tilde{\psi}}{1-\tilde{\psi}}} + C_{\text{pillar}}. \quad (7.C1)$$

However, this constant can be eliminated by considering the values of $\tilde{\psi}$ at $\rho = \rho_{\text{in}}$ and $\rho = 1$,

$$\begin{aligned} \frac{\bar{F}\sqrt{(-\alpha)^3}}{4\pi} (1 - \rho_{\text{in}}^2) &= -\sqrt{\tilde{\psi}_1(1-\tilde{\psi}_1)} + \sqrt{\tilde{\psi}_{\text{in}}(1-\tilde{\psi}_{\text{in}})} + \tan^{-1} \sqrt{\frac{\tilde{\psi}_1}{1-\tilde{\psi}_1}} - \\ \tan^{-1} \sqrt{\frac{\tilde{\psi}_{\text{in}}}{1-\tilde{\psi}_{\text{in}}}}. \end{aligned} \quad (7.C2)$$

The $\bar{F}\sqrt{(-\alpha)^3}$ can be related to the intermediate parameter $\tilde{\psi}_{\text{in}}$ by (7.26) and the condition of fixed displacement at the edge of the tip in (7.46),

$$\frac{\bar{F}\sqrt{(-\alpha)^3}}{4\pi} = \frac{1+\nu}{2} \rho_{\text{in}}^{-2} \sqrt{\frac{\tilde{\psi}_{\text{in}}^3}{1-\tilde{\psi}_{\text{in}}}}. \quad (7.C3)$$

Then (7.C2) can be written as

$$\begin{aligned} \frac{1+\nu}{2} \sqrt{\frac{\tilde{\psi}_{\text{in}}^3}{1-\tilde{\psi}_{\text{in}}}} \left(\frac{1}{\rho_{\text{in}}^2} - 1 \right) = & -\sqrt{\tilde{\psi}_1(1-\tilde{\psi}_1)} + \sqrt{\tilde{\psi}_{\text{in}}(1-\tilde{\psi}_{\text{in}})} + \tan^{-1} \sqrt{\frac{\tilde{\psi}_1}{1-\tilde{\psi}_1}} - \\ & \tan^{-1} \sqrt{\frac{\tilde{\psi}_{\text{in}}}{1-\tilde{\psi}_{\text{in}}}}. \end{aligned} \quad (C4)$$

The continuity of displacement at the edge of the tent, i.e. (7.33), still requires

$$-\alpha T \frac{1+\nu}{2} (\rho_o - 1) = \frac{\bar{F}(-\alpha)^{3/2}}{4\pi} \sqrt{\frac{1-\tilde{\psi}_1}{\tilde{\psi}_1}}. \quad (7.C5)$$

By combining (7.C4), (7.C5), and (7.31) for the continuity of radial stress, we eliminate \bar{F} and α :

$$\frac{6\rho_{\text{in}}^2(\rho_o-1)}{3(1+\nu)\rho_o+(1-\nu)\rho_o^3-2(2+\nu)} = \sqrt{\frac{\tilde{\psi}_{\text{in}}^3(1-\tilde{\psi}_1)}{\tilde{\psi}_1^3(1-\tilde{\psi}_{\text{in}})}} \quad (7.C6)$$

As we aim to relate to the size of the compression zone ρ_o to the height of the tent H , the integration domain is from ρ_{in} to 1 in (7.36) such that

$$W_0 = \frac{-\bar{F}\alpha}{4\pi} \int_{\tilde{\psi}_{\text{in}}}^{\tilde{\psi}_1} \frac{d\tilde{\psi}}{\tilde{\psi}\tilde{\psi}'} = \frac{2}{\sqrt{-\alpha}} \left[\tan^{-1} \sqrt{\frac{\tilde{\psi}_1}{1-\tilde{\psi}_1}} - \tan^{-1} \sqrt{\frac{\tilde{\psi}_{\text{in}}}{1-\tilde{\psi}_{\text{in}}}} \right], \quad (7.C7)$$

where (7.26) was used for the analytical solution. Again, using (7.C7) and (7.31) can cancel out α and lead to

$$\tilde{\psi}_1 \left[\tan^{-1} \sqrt{\frac{\tilde{\psi}_1}{1-\tilde{\psi}_1}} - \tan^{-1} \sqrt{\frac{\tilde{\psi}_{\text{in}}}{1-\tilde{\psi}_{\text{in}}}} \right]^{-2} = \frac{4T}{H^2} \left(\frac{1+\nu}{2} \rho_o + \frac{1-\nu}{6} \rho_o^3 - \frac{2+\nu}{3} \right). \quad (7.C8)$$

Now, $\tilde{\psi}_{\text{in}}$, $\tilde{\psi}_1$, and ρ_o can be analytically solved by (7.C4), (7.C6), and (7.C8) that only depend on two parameters – they are the size of the tip, ρ_{in} , and the combined parameter, $\mathcal{S} = T/H^2$.

7.D The composite parameter (FFT)

Equation (7.54) is solved based on the continuity of the hoop and radial stresses. Particularly, in the unbuckled, supported domain $[\rho_b, \rho_o]$, (7.19-7.21) hold; and at the inner boundary of this domain, the hoop stress is released to be zero, which leads to

$$\rho_b = \frac{1-\nu+\sqrt{9+6\nu-15\nu^2}}{4+8\nu} \rho_o, \quad (7.D1)$$

and

$$\frac{N_{rr}(\rho_b)}{E_{2D}} = T \left(-\frac{2+\nu}{3} \rho_b - \frac{\nu-1}{6} \rho_o^3 \rho_b^{-2} + \frac{1+\nu}{2} \rho_o \right). \quad (7.D2)$$

We highlight the fast and easy implementation of our analytical solutions in calculating how the extent of wrinkles in the suspended region and buckles in the supported region evolves. Essentially, $\tilde{\psi}_w = 0.6965$ is an independent constant and the intermediate parameters C_w and α can be eliminated by combining (7.57), (7.58), and (7.60)

$$2 \ln \rho_w + 2\nu + \frac{1}{\rho_w} \frac{1-\rho_w}{1-\tilde{\psi}_w} = \frac{2\rho_b^2 \ln \rho_b - \rho_b^2 + 1 + 4C_N \ln \rho_b - 4C_N \rho_b \rho_o}{\rho_b^2 - 1 + 2C_N}, \quad (7.D3)$$

or (7.57), (7.59), and (7.60)

$$\frac{H^2}{T} \frac{2\tilde{\psi}_w}{\rho_w(\rho_b^2-1)+2C_N\rho_w} = \left(\frac{1-\rho_w}{\rho_w} \sqrt{\frac{\tilde{\psi}_w}{1-\tilde{\psi}_w}} + 2 \tan^{-1} \sqrt{\frac{\tilde{\psi}_w}{1-\tilde{\psi}_w}} \right)^2, \quad (7.D4)$$

where the governing parameter $\mathcal{S} = T/H^2$ appears.

7.E Finite pillar radius (FFT)

In this case, the unwrinkled domain becomes $\rho_{in} \leq \rho \leq \rho_w$ where $\rho_{in} < \rho_w$. The integration of (7.26) over this domain gives

$$\frac{\bar{F}\sqrt{(-\alpha)^3}}{4\pi} \eta = -\sqrt{\tilde{\psi}(1-\tilde{\psi})} + \tan^{-1} \sqrt{\frac{\tilde{\psi}}{(1-\tilde{\psi})}} + C_{pillar}. \quad (7.E1)$$

We eliminate the integration constant by considering boundary values of $\tilde{\psi}$ at $\rho = \rho_{in}$ and

$\rho = \rho_w$,

$$\frac{\bar{F}\sqrt{(-\alpha)^3}}{4\pi} (\rho_w^2 - \rho_{in}^2) = -\sqrt{\tilde{\psi}_w(1-\tilde{\psi}_w)} + \sqrt{\tilde{\psi}_{in}(1-\tilde{\psi}_{in})} + \tan^{-1} \sqrt{\frac{\tilde{\psi}_w}{1-\tilde{\psi}_w}} - \tan^{-1} \sqrt{\frac{\tilde{\psi}_{in}}{1-\tilde{\psi}_{in}}}. \quad (7.E2)$$

The condition of fixed displacement at the edge of the tip in (7.C3) holds. Plugging it into

(7.E2) can give

$$\begin{aligned} \frac{1+\nu}{2} \sqrt{\frac{\tilde{\psi}_{\text{in}}^3}{1-\tilde{\psi}_{\text{in}}}} \left(\frac{\rho_w^2}{\rho_{\text{in}}^2} - 1 \right) &= -\sqrt{\tilde{\psi}_w(1-\tilde{\psi}_w)} + \sqrt{\tilde{\psi}_{\text{in}}(1-\tilde{\psi}_{\text{in}})} + \tan^{-1} \sqrt{\frac{\tilde{\psi}_w}{1-\tilde{\psi}_w}} - \\ \tan^{-1} \sqrt{\frac{\tilde{\psi}_{\text{in}}}{1-\tilde{\psi}_{\text{in}}}}, \end{aligned} \quad (7.E3)$$

and into the condition of zero hoop stress at $\rho = \rho_w$, i.e. (7.48), leads to

$$(1+\nu)\rho_{\text{in}}^{-2} \sqrt{\frac{\tilde{\psi}_{\text{in}}^3}{1-\tilde{\psi}_{\text{in}}}} = \rho_w^{-2} \sqrt{\frac{\tilde{\psi}_w^3}{1-\tilde{\psi}_w}}. \quad (7.E4)$$

We note that (7.57), (7.58), and (7.60) still apply because they are based on the continuity conditions at $\rho = \rho_w$ and $\rho = 1$. However, to obtain the center height of the tent, (7.59) needs to change its integration domain,

$$\begin{aligned} H &= W(\rho_w) + \int_{\rho_w}^{\rho_{\text{in}}} \frac{-\bar{F}d\rho}{2\pi\Phi'} = C_w(1-\rho_w) + \frac{2}{\sqrt{-\alpha}} \left[\tan^{-1} \sqrt{\frac{\tilde{\psi}_w}{1-\tilde{\psi}_w}} - \right. \\ \tan^{-1} \sqrt{\frac{\tilde{\psi}_{\text{in}}}{1-\tilde{\psi}_{\text{in}}}} \Big]. \end{aligned} \quad (7.E5)$$

As a result, the controlling equations discussed in Appendix 7.D are modified,

$$2 \ln \rho_w + 2\nu + \frac{1}{\rho_w} \frac{1-\rho_w}{1-\tilde{\psi}_w} = \frac{2\rho_b^2 \ln \rho_b - \rho_b^2 + 1 + 4C_N \ln \rho_b - 4C_v \rho_b \rho_o}{\rho_b^2 - 1 + 2C_N}, \quad (7.E6)$$

$$\frac{H^2}{T} \frac{2\tilde{\psi}_w}{\rho_w(\rho_b^2-1)+2C_N\rho_w} = \left(\frac{1-\rho_w}{\rho_w} \sqrt{\frac{\tilde{\psi}_w}{1-\tilde{\psi}_w}} + 2 \tan^{-1} \sqrt{\frac{\tilde{\psi}_w}{1-\tilde{\psi}_w}} - 2 \tan^{-1} \sqrt{\frac{\tilde{\psi}_{\text{in}}}{1-\tilde{\psi}_{\text{in}}}} \right)^2. \quad (7.E7)$$

With the prescribed ρ_{in} and a given composite parameter \mathcal{S} , equations (7.E3), (7.E4), (7.E6), and (7.E7) complete the conditions to determine $\tilde{\psi}_{\text{in}}$, $\tilde{\psi}_w$, ρ_w , and ρ_o . When the pillar has a finite radius, $\tilde{\psi}_w$ is not necessary to be a constant.

Chapter 8: Epilogue

In this dissertation, we have studied a series of problems associated with the mechanics of 2D material bubbles and tents. A particular feature of these problems arises from the lubricated 2D material interface that allows the sheet to slide on its supporting substrate when the load (a point force for the tent; a uniform pressure for the bubble) acts on the sheet. In this chapter, we summarize our findings and outlook future work.

8.1 CONCLUSIONS

Chapter 1 introduced that 2D materials often occupy the 3rd dimension via the out-of-plane deformation, particularly in research areas of functionalities and metrologies. 2D material bubbles and tents stand out as two commonly deformed configurations; they can be called by a unified name, 2D material blisters. We also reviewed experimental and theoretical understandings on the vdW interaction between the 2D material and its substrate; In brief, they are relatively strong in the normal direction but extremely weak in the tangential direction.

In Chapter 2, we studied the governing equations and the boundary and matching conditions for a thin sheet with a sliding boundary under a transverse point load or pressure. The theoretical framework considered elastic instabilities of the thin sheet in tents and bubbles that have been observed in recent experiments yet remain poorly understood. Such instabilities take the form of wrinkling in regions where the sheet is suspended and the form of buckle delamination in regions where the sheet is in adhesive contact with a substrate. Such observations motivated us to consider three possible cases: the instability-free base state, the state with wrinkling but without buckle delamination, and the state with both wrinkling and buckle delamination. This theoretical setting is built for 2D materials sticking to a substrate via vdW interactions and the physical concept may also apply for a range of ultrathin sheets if their edge cannot be constrained completely. For example, some larger-scale systems such as pulling of polymeric sheets from a liquid-lubricated solid surface follow the same physical idea.

Numerical calculations on these problems have been the focus of Chapter 3. An interesting parameter, *sliding number*, is identified in both bubble and tent problems. The physical quantities, such as the effective stiffness and the extent of the stabilities, are found to depend on this composite number. We understand this number by how the membrane

tension competes for the edge constraint (i.e., interfacial shear traction) in each system. Particularly, when the constraint dominates (we call strong shear limit), a small sliding number is obtained – the system approaches the so-called clamped boundary conditions. When the membrane tension (scaling as the quadratic center deflection) is sufficiently large (we obtain weak shear limit naturally), the sheet-substrate interface would then behave like ultra-lubricated. For intermediated situations, we elucidated the dependency on the sliding number of the effective poking/bulging stiffness as well as the geometrical features of elastic instabilities (if happened).

Chapter 4 presented a special case of bubbles when the center deflection is comparable to the sheet thickness that allows for direct measurements of the bending rigidity of the sheet. We studied multilayer graphene, molybdenum disulfide (MoS_2), and hexagonal boron nitride (hBN). The transition from membrane to plate behaviors of the 2D multilayer was achieved by controlling the sample thickness and bubbling deflection. We extracted both bending rigidity and Young's modulus of the sheet according to experimental results at bending- and stretching-dominated asymptotic regimes. Interestingly, the measured Young's moduli agree with those reported in the literature: $E_{\text{graphene}} > E_{\text{hBN}} > E_{\text{MoS}}$ but bending rigidity results show a completely reversed trend: $B_{\text{MoS}_2} > B_{\text{hBN}} > B_{\text{graphene}}$ for multilayers with comparable thickness. We attributed the abnormal bending behavior of 2D multilayers to the atomic shear/friction between layers that is missing in classical plate prediction.

In Chapter 5, we move on to the shape characteristics of nanoscale bubbles and tents formed by 2D materials in experiments (the bending effect is negligible), which led to a simple power-law approximation. The approximation further enabled closed-form analytical solutions to the strain fields using classical membrane theories. The solutions were given under the strong and weak shear limits. A useful feature of the solutions for the

emerging strain engineering applications of 2D materials was that they drew a direct relation between the aspect ratio and the strain fields in the 2D material bubbles and tents. Both numerical and Raman characterizations have confirmed the decent accuracy of our analytical solutions. Though these analytical results failed to capture the wrinkling instabilities at the tent or bubble edges, we suggest that they may provide good approximations for the radial strains as well as hoop strains in areas far away from the wrinkling region. This could be explained by the fact that the release of the compression by wrinkling would not cause significant perturbation to the system. Caution, however, must be exercised when buckling delamination occurs in the supported region as it could ruin the analytical solutions obtained in this chapter.

The aspect ratio of bubbles has been extensively reported to be constant if the bubbles were formed spontaneously during the transfer process and filled with liquids. Chapter 6 explained these observations through the concept of elasto-capillarity. We showed that the liquid-filled bubbles form as a result of competition between the elastic energy of the deformed 2D material, the interfacial energy associated with van der Waals interactions and surface tension of the liquid contents. Taking advantage of analytical approximations derived in Chapter 5, we reported an analytical relation between the bubble aspect ratio and the mechanical and surface properties of the system; similar results were also derived for tents. The analytical relation was verified by more rigorous solutions to the governing equations and by molecular dynamics simulations on water-filled graphene systems. We then applied this relation to estimate the adhesion energy for more than ten 2D materials interfaces, many of which have never been obtained before.

The last chapter focused on buckle delamination around 2D material tents. We showed how the buckle shape relates to the material properties and the interface adhesion properties as well as how the buckle profile varies with the radial position. An important

finding in this chapter came from the exact analytical solutions to the tent problems with the consideration of edge slippage. Parametrical studies were performed for cases as simple as tents subjected to a point load at the center, zero shear traction at the interface, and zero pretension on the periphery all the way to tents with finite pillar size, finite pretension as well as finite flake size. In addition, two types of modeling accounting for none and complete compression relaxation were presented. We identified several governing parameters that may also lead to future works discussed as follows: the sliding number, the indenter/tip size, the pretension number.

8.2 FUTURE WORK

Measuring the mechanical behavior of 2D materials. In Chapter 3, we concluded that it remains a grand challenge to measure the pretension and in-plane stiffness for an atomically thin sheet so far. The reason comes from: in poking tests, the consideration of edge slippage, pretension, and indenter shape and size would render simple analytical formulae such as (3.1) elusive and the interpretation of experimental data highly challenging. However, the erroneous expression (3.1) has been widely applied and propagated in the literature; In the bulge test, the pressure cannot be fine controlled at small deflections – the regimes where pretension in the thin sheet is more likely to be detected. Recent work by (Vella and Davidovitch, 2017) proposed a methodology through poking bulged thin sheets. The advantage of this method is that the pretension effect would be tuned by the applied pressure, and the contact stiffness of a shallow poking can give rise to the more accurate extraction of the pretension and in-plane stiffness. The realization of such methodology needs verifications. We suggest three controlling parameters that need to be verified along with the technique outlined in Chapter 2: the sliding number $\mathcal{S} = H^2/T$, the pretension number $\mathcal{T} = T_{\text{pre}}/H^2$, and the size effect of the indenter $\rho_{\text{in}} =$

R_{in}/R . In particular, it is possible to test whether the regime of $\mathcal{S} \ll 1, \mathcal{T} \gg 1, \rho_{\text{in}} \ll 1$ exists in experiments so that the pretension in the thin sheet could be extracted without the influence of the pressure-induced tension; Similarly, the existence of the regime of $\mathcal{S} \ll 1, \mathcal{T} \ll 1, \rho_{\text{in}} \ll 1$ can allow the in-plane stiffness of the thin sheet to be extracted without fitting deep indentation force-depth curves that span two asymptotic regimes.

2D material wrinkling instabilities. In Chapter 3, we have shown the maximum radial size of the wrinkling zone for tents ($\sim 0.5R$) and bubbles ($\sim 0.15R$), as shown in Figure 8.1. The detailed evolution of the extent of the wrinkling zone brings an additional means for the mechanics metrology of thin sheets. For example, the onset of the wrinkling is extremely sensitive to the Poisson's ratio of the thin sheet, which might be beneficial to future measurement on thin-film Poisson's ratio. Besides, the dependency of the instability extent on the sliding number may lead to quantitative information regarding the interfacial shear tractions of the 2D material-substrate interfaces. Finally, we have neglected bending rigidity of the thin sheet and adopted the tension field theory to describe the stress state in the wrinkling zone; However, the local features such as the wavelength and the number of wrinkles would need the considerations of the sub-dominant bending effect. It would be interesting to answer the question of what sets the local geometrical feature of wrinkles in the poking and bulging problem in a future study.

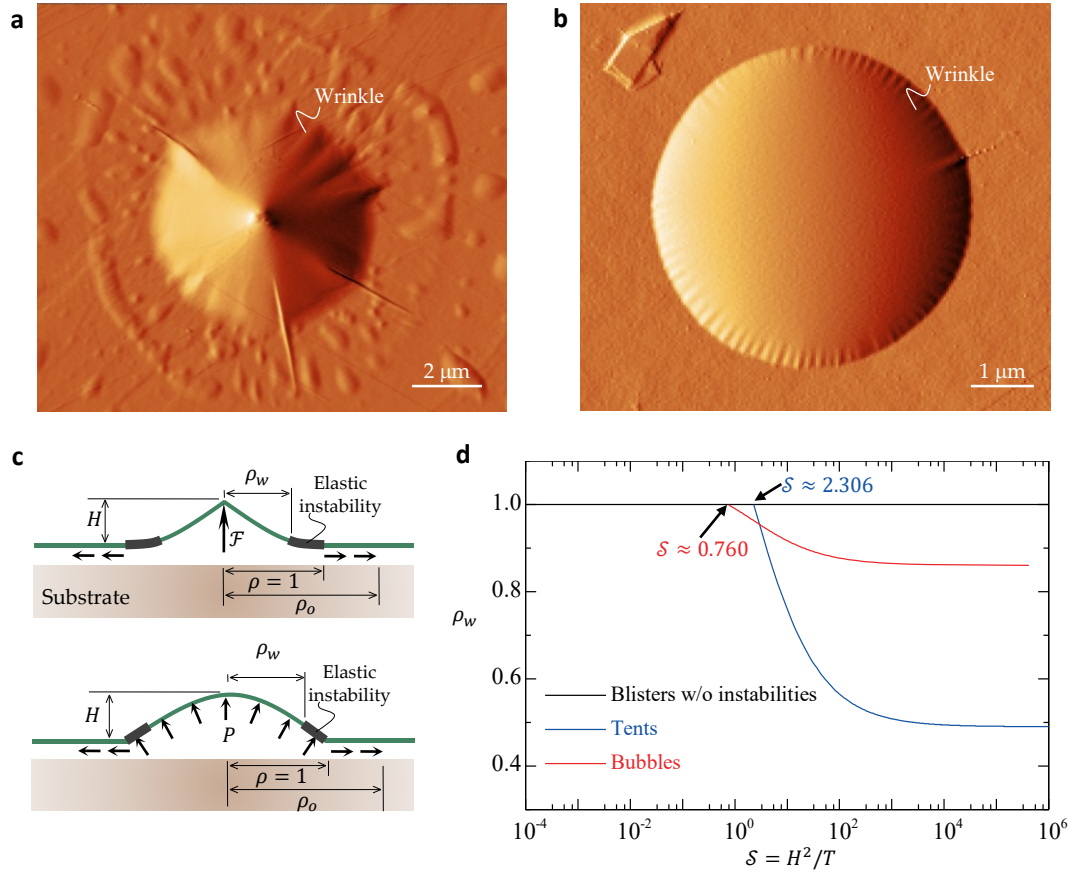


Figure 8.1: AFM amplitude images of a spontaneous multilayer graphene tent (a, courtesy of Daniel Sanchez) and a gas-pressurized bilayer graphene bubble (b, courtesy of Guorui Wang).¹ (c) Schematics for case II of the tent problem (top panel) and the bubble problem (bottom panel) when the sheet is allowed to slide over its supporting substrate and wrinkling forms. (d) The dependency of the extent of the wrinkling zone on the sliding number from bubbles and tents.

¹ These two images are also adapted for the Graphic illustration in Phys. Rev. Lett. 121, 266101 (2018) <https://journals.aps.org/prl/issues/121/26>.

8.3 DISCUSSION

The relatively simple framework of the theory for substrate-supported 2D materials has allowed the exploration of some of the key mechanical behaviors of 2D material blister systems. However, our analysis neglects some important aspects of interface mechanics.

The plane-stress state. We assumed that the unbuckled sheet in the supported region remains flat so that the plane stress analysis with a body force was adopted. This assumption may approximate well when the blister is formed between a 2D material sheet and a 2D materials substrate where the resulted interface is atomically flat. However, when the 2D material is supported by a regular substrate (e.g., SiO_2), the effect of the substrate roughness needs to be considered. Such effect on the effective poking or bulging stiffness of the sheet may be negligible since the sliding number in these systems is relatively small (the systems are close to being clamped); the size of the sliding zone may be influenced by the substrate roughness in a nontrivial manner. This also brings an interesting question of how the substrate roughness tunes the tangential properties and behavior of 2D material-substrate interfaces.

Tension field theory (TFT). We adopted TFT to describe the buckled sheet in the supported region, such as vanishing hoop stress and negligible bending energy. However, these conclusions are derived based on ultrathin freestanding wrinkled sheets according to an energetically-based analysis. It is unclear whether the compressive stress is allowed (or not completely released) in the supported buckled sheet, particularly under the circumstances that the radial buckled delamination is asymmetric and an additional length scale appears about the spacing of these buckles. Recently, Davidovitch et al., reported a relevant problem where a circular sheet with an outer traction-free edge conforms onto a rigid sphere through a linear Winkler foundation (so-called inverted TFT) (Davidovitch et al., 2011). The task of extending this concept to our problems is challenging due to the

asymmetric nature of these buckles and the consideration of interfacial friction. In addition, we assumed the hoop stress continuity at the outer buckling tip for simplicity while the sheet-substrate adhesion may allow a jump of the hoop stress. The detailed value may be evaluated by considering the energy release rate of the system; a 1D case has been studied in the literature (Vella et al. 2009).

Traction-separation (TS) laws. We have used the simplest tangential traction-separation law where the traction remains a constant. Apparently, our conclusions will be modified if a different TS law is adopted. A number of interesting subtleties may be introduced and further discussed, such as the rate-dependency and the small-scale characteristics at 2D-2D interfaces. Notably, we still expect the existence of a strong- and a weak-shear limit. Besides, blisters are inherently mixed mode with both normal and shear tractions at the interface (Cao, 2015; Cao et al., 2015, 2016; Cao et al., 2014; Liechti, 2019). For example, by varying the thickness of the backing layer in their bulge tests, Cao et al. showed that the interfacial toughness between graphene and substrates had a strong dependence on the fracture mode-mix (Cao, 2015; Cao et al., 2015, 2016; Cao et al., 2014). However, this important feature has been neglected in this dissertation. In bubbles and tents formed by ultrathin 2D materials, from the point of view of intermolecular interactions, the normal interfacial separation should further weaken the tangential shear resistance, leading to a larger sliding number or more significant interfacial sliding when the coupling is considered. However, it is unclear how the shear sliding modifies the normal interfacial traction and further affect the interfacial adherence. In-depth studies are needed to improve our understanding of the mode-mix of the atomic-level interfaces between 2D materials and their substrates.

Bibliography

- Ahmadpoor, F., Wang, P., Huang, R., Sharma, P., 2017. Thermal fluctuations and effective bending stiffness of elastic thin sheets and graphene: A nonlinear analysis. *J. Mech. Phys. Solids* 107, 294-319.
- Ahn, G.H., Amani, M., Rasool, H., Lien, D.H., Mastandrea, J.P., Ager Iii, J.W., Dubey, M., Chrzan, D.C., Minor, A.M., Javey, A., 2017. Strain-engineered growth of two-dimensional materials. *Nat. Commun.* 8, 608.
- Akinwande, D., Brennan, C.J., Bunch, J.S., Egberts, P., Felts, J.R., Gao, H., Huang, R., Kim, J.-S., Li, T., Li, Y., 2017. A review on mechanics and mechanical properties of 2D materials—Graphene and beyond. *Extreme Mech. Lett.* 13, 42-77.
- Akinwande, D., Petrone, N., Hone, J., 2014. Two-dimensional flexible nanoelectronics. *Nat. Commun.* 5, 5678.
- Akies, K., van Ruitenbeek, J., 2018. Graphene nano-origami using Scanning Tunneling Microscopy. arXiv preprint arXiv:1812.09501.
- Alam, A., Howlader, M., Deen, M., 2014. The effects of oxygen plasma and humidity on surface roughness, water contact angle and hardness of silicon, silicon dioxide and glass. *J. Micromech. Microeng.* 24, 035010.
- Alden, J.S., Tsen, A.W., Huang, P.Y., Hovden, R., Brown, L., Park, J., Muller, D.A., McEuen, P.L., 2013. Strain solitons and topological defects in bilayer graphene. *Proc. Natl. Acad. Sci. U. S. A.* 110, 11256-11260.
- Amani, M., Chin, M.L., Mazzoni, A.L., Burke, R.A., Najmaei, S., Ajayan, P.M., Lou, J., Dubey, M., 2014. Growth-substrate induced performance degradation in chemically synthesized monolayer MoS₂ field effect transistors. *Appl. Phys. Lett.* 104, 203506.
- An, H., Tan, B.H., Moo, J.G.S., Liu, S., Pumera, M., Ohl, C.-D., 2017. Graphene nanobubbles produced by water splitting. *Nano Lett.* 17, 2833-2838.
- Andreotti, B., Snoeijer, J.H., 2019. Statics and Dynamics of Soft Wetting. *Annu. Rev. Fluid Mech.* 52, 285-308.
- Androulidakis, C., Sourlantzis, D., Koukaras, E., Manikas, A.C., Galiotis, C., 2019. Stress-transfer from polymer substrates to monolayer and few-layer graphenes. *Nanoscale Adv.* 1, 4972.
- Androulidakis, C., Zhang, K., Robertson, M., Tawfick, S.H., 2018. Tailoring the mechanical properties of 2D materials and heterostructures. *2D Mater.* 5, 032005.
- Annett, J., Cross, G.L., 2016. Self-assembly of graphene ribbons by spontaneous self-tearing and peeling from a substrate. *Nature* 535, 271-275.
- Aoyanagi, Y., Hure, J., Bico, J., Roman, B., 2010. Random blisters on stickers: metrology through defects. *Soft Matter* 6, 5720-5728.
- Audoly, B., Pomeau, Y., 2000. Elasticity and geometry, Peyresq Lectures On Nonlinear Phenomena. World Scientific, pp. 1-35.
- Bampoulis, P., Teernstra, V.J., Lohse, D., Zandvliet, H.J., Poelsema, B., 2016. Hydrophobic Ice Confined between Graphene and MoS₂. *J. Phys. Chem. C* 120, 27079-27084.
- Bao, W., Miao, F., Chen, Z., Zhang, H., Jang, W., Dames, C., Lau, C.N., 2009. Controlled ripple texturing of suspended graphene and ultrathin graphite membranes. *Nat. Nanotechnol.* 4, 562-566.

- Begley, M.R., Mackin, T.J., 2004. Spherical indentation of freestanding circular thin films in the membrane regime. *J. Mech. Phys. Solids* 52, 2005-2023.
- Berry, V., 2013. Impermeability of graphene and its applications. *Carbon* 62, 1-10.
- Bertolazzi, S., Brivio, J., Kis, A., 2011. Stretching and breaking of ultrathin MoS₂. *ACS nano* 5, 9703-9709.
- Bhatia, N.M., Nachbar, W., 1968. Finite indentation of an elastic membrane by a spherical indenter. *Int. J. Non-Linear Mech.* 3, 307-324.
- Bico, J., Reyssat, E., Roman, B., 2018. Elastocapillarity: When Surface Tension Deforms Elastic Solids. *Annu. Rev. Fluid. Mech.* 50, 629-659.
- Blees, M.K., Barnard, A.W., Rose, P.A., Roberts, S.P., McGill, K.L., Huang, P.Y., Ruyack, A.R., Kevek, J.W., Kobrin, B., Muller, D.A., 2015. Graphene kirigami. *Nature* 524, 204.
- Boddeti, N.G., Koenig, S.P., Long, R., Xiao, J., Bunch, J.S., Dunn, M.L., 2013a. Mechanics of adhered, pressurized graphene blisters. *J. Appl. Mech.* 80, 040909.
- Boddeti, N.G., Liu, X., Long, R., Xiao, J., Bunch, J.S., Dunn, M.L., 2013b. Graphene blisters with switchable shapes controlled by pressure and adhesion. *Nano Lett.* 13, 6216-6221.
- Boijoux, R., Parry, G., Coupeau, C., 2018. Buckle depression as a signature of Young's modulus mismatch between a film and its substrate. *Thin Solid Films* 645, 379-382.
- Box, F., O'Kiely, D., Kodio, O., Inizan, M., Castrejon-Pita, A.A., Vella, D., 2019. Dynamics of wrinkling in ultrathin elastic sheets. *Proc. Natl. Acad. Sci. U. S. A.* 116, 20875-20880.
- Box, F., Vella, D., Style, R.W., Neufeld, J.A., 2017. Indentation of a floating elastic sheet: geometry versus applied tension. *Proc. R. Soc. A* 473, 20170335.
- Branny, A., Kumar, S., Proux, R., Gerardot, B.D., 2017. Deterministic strain-induced arrays of quantum emitters in a two-dimensional semiconductor. *Nat. Commun.* 8, 15053.
- Braun, O.M., Kivshar, Y.S., 2013. *The Frenkel-Kontorova model: concepts, methods, and applications*. Springer Science & Business Media.
- Brennan, C.J., Ghosh, R., Koul, K., Banerjee, S.K., Lu, N., Yu, E.T., 2017. Out-of-Plane Electromechanical Response of Monolayer Molybdenum Disulfide Measured by Piezoresponse Force Microscopy. *Nano Lett.* 17, 5464-5471.
- Brennan, C.J., Nguyen, J., Yu, E.T., Lu, N., 2015. Interface Adhesion between 2D Materials and Elastomers Measured by Buckle Delaminations. *Adv. Mater. Interfaces* 2, 1500176.
- Budrikis, Z., Sellerio, A.L., Bertalan, Z., Zapperi, S., 2015. Wrinkle motifs in thin films. *Sci. Rep.* 5, 8938.
- Buehler, M.J., Kong, Y., Gao, H.J., Huang, Y.G., 2006. Self-Folding and Unfolding of Carbon Nanotubes. *J. Eng. Mater-T. ASME* 128, 3-10.
- Bunch, J.S., Dunn, M.L., 2012. Adhesion mechanics of graphene membranes. *Solid State Commun.* 152, 1359-1364.
- Burch, K.S., Mandrus, D., Park, J.-G., 2018. Magnetism in two-dimensional van der Waals materials. *Nature* 563, 47.
- Butz, B., Dolle, C., Niekief, F., Weber, K., Waldmann, D., Weber, H.B., Meyer, B., Spiecker, E., 2014. Dislocations in bilayer graphene. *Nature* 505, 533-537.
- Cançado, L.G., Jorio, A., Ferreira, E.M., Stavale, F., Achete, C.A., Capaz, R.B., Moutinho, M.V.d.O., Lombardo, A., Kulmala, T., Ferrari, A.C., 2011. Quantifying defects in

- graphene via Raman spectroscopy at different excitation energies. *Nano Lett.* 11, 3190-3196.
- Cao, G., Gao, H., 2019. Mechanical properties characterization of two-dimensional materials via nanoindentation experiments. *Prog. Mater. Sci.* 103, 558-595.
- Cao, P., Xu, K., Varghese, J.O., Heath, J.R., 2011. The microscopic structure of adsorbed water on hydrophobic surfaces under ambient conditions. *Nano Lett.* 11, 5581-5586.
- Cao, Y., Fatemi, V., Demir, A., Fang, S., Tomarken, S.L., Luo, J.Y., Sanchez-Yamagishi, J.D., Watanabe, K., Taniguchi, T., Kaxiras, E., 2018a. Correlated insulator behaviour at half-filling in magic-angle graphene superlattices. *Nature* 556, 80.
- Cao, Y., Fatemi, V., Fang, S., Watanabe, K., Taniguchi, T., Kaxiras, E., Jarillo-Herrero, P., 2018b. Unconventional superconductivity in magic-angle graphene superlattices. *Nature* 556, 43.
- Cao, Z., 2015. The adhesive interactions between graphene and substrates by blister tests. UT Austin PhD Dissertation.
- Cao, Z., Tao, L., Akinwande, D., Huang, R., Liechti, K.M., 2015. Mixed-Mode Interactions between Graphene and Substrates by Blister Tests. *J. Appl. Mech.* 82, 081008.
- Cao, Z., Tao, L., Akinwande, D., Huang, R., Liechti, K.M., 2016. Mixed-mode traction-separation relations between graphene and copper by blister tests. *Int. J. Solids Struct.* 84, 147-159.
- Cao, Z., Wang, P., Gao, W., Tao, L., Suk, J., Ruoff, R., Akinwande, D., Huang, R., Liechti, K., 2014. A blister test for interfacial adhesion of large-scale transferred graphene. *Carbon* 69, 390-400.
- Carbone, M.G.P., Manikas, A.C., Souli, I., Pavlou, C., Galiotis, C., 2019. Mosaic pattern formation in exfoliated graphene by mechanical deformation. *Nat. Commun.* 10, 1572.
- Castellanos-Gomez, A., Poot, M., Steele, G.A., Van der Zant, H.S., Agraït, N., Rubio-Bollinger, G., 2012. Mechanical properties of freely suspended semiconducting graphene-like layers based on MoS₂. *Nanoscale Res. Lett.* 7, 233.
- Castellanos-Gomez, A., Roldán, R., Cappelluti, E., Buscema, M., Guinea, F., van der Zant, H.S., Steele, G.A., 2013. Local strain engineering in atomically thin MoS₂. *Nano Lett.* 13, 5361-5366.
- Castellanos-Gomez, A., Poot, M., Steele, G.A., van der Zant, H.S., Agraït, N., Rubio-Bollinger, G., 2012. Elastic properties of freely suspended MoS₂ nanosheets. *Adv. Mater.* 24, 772-775.
- Castellanos-Gomez, A., Singh, V., van der Zant, H.S., Steele, G.A., 2015. Mechanics of freely-suspended ultrathin layered materials. *Annalen der Physik* 527, 27-44.
- Chang, J.S., Kim, S., Sung, H.J., Yeon, J., Chang, K.J., Li, X., Kim, S., 2018. Graphene Nanoribbons with Atomically Sharp Edges Produced by AFM Induced Self-Folding. *Small* 14, 1803386.
- Chaste, J., Missaoui, A., Huang, S., Henck, H., Ben Aziza, Z., Ferlazzo, L., Balan, A., Johnson, A.T.C., Braive, R., Ouerghi, A., 2018. Intrinsic Properties of Suspended MoS₂ on SiO₂/Si Pillar Arrays for Nanomechanics and Optics. *ACS Nano* 12, 3235-3242.

- Chen, H., Zhang, X.-L., Zhang, Y.-Y., Wang, D., Bao, D.-L., Que, Y., Xiao, W., Du, S., Ouyang, M., Pantelides, S.T., 2019. Atomically precise, custom-design origami graphene nanostructures. *Science* 365, 1036-1040.
- Chen, K., Scales, M., Kyriakides, S., 2018. Material hardening of a high ductility aluminum alloy from a bulge test. *Int. J. Mech. Sci.* 138, 476-488.
- Chen, K., Scales, M., Kyriakides, S., Corona, E., 2016a. Effects of anisotropy on material hardening and burst in the bulge test. *Int. J. Solids Struct.* 82, 70-84.
- Chen, P.Y., Sodhi, J., Qiu, Y., Valentin, T.M., Steinberg, R.S., Wang, Z., Hurt, R.H., Wong, I.Y., 2016b. Multiscale Graphene Topographies Programmed by Sequential Mechanical Deformation. *Adv. Mater.* 28, 3564-3571.
- Chen, X.M., Yi, C.L., Ke, C.H., 2015. Bending stiffness and interlayer shear modulus of few-layer graphene. *Appl. Phys. Lett.* 106, 101907.
- Chen, Z., Leng, K., Zhao, X., Malkhandi, S., Tang, W., Tian, B., Dong, L., Zheng, L., Lin, M., Yeo, B.S., Loh, K.P., 2017. Interface confined hydrogen evolution reaction in zero valent metal nanoparticles-intercalated molybdenum disulfide. *Nat. Commun.* 8, 14548.
- Choi, C., Choi, M.K., Liu, S., Kim, M.S., Park, O.K., Im, C., Kim, J., Qin, X., Lee, G.J., Cho, K.W., 2017. Human eye-inspired soft optoelectronic device using high-density MoS₂-graphene curved image sensor array. *Nat. Commun.* 8, 1664.
- Choi, J., Kim, H.J., Wang, M.C., Leem, J., King, W.P., Nam, S., 2015. Three-dimensional integration of graphene via swelling, shrinking, and adaptation. *Nano Lett.* 15, 4525-4531.
- Chopin, J., Vella, D., Boudaoud, A., 2008. The liquid blister test. *Proc. R. Soc. A.* 464, 2887-2906.
- Cui, X., Kong, Z., Gao, E., Huang, D., Hao, Y., Shen, H., Di, C.-a., Xu, Z., Zheng, J., Zhu, D., 2018. Rolling up transition metal dichalcogenide nanoscrolls via one drop of ethanol. *Nat. Commun.* 9, 1301.
- da Cunha Rodrigues, G., Zelenovskiy, P., Romanyuk, K., Luchkin, S., Kopelevich, Y., Kholkin, A., 2015. Strong piezoelectricity in single-layer graphene deposited on SiO₂ grating substrates. *Nat. Commun.* 6, 7572.
- Dai, Z., Hou, Y., Sanchez, D.A., Wang, G., Brennan, C.J., Zhang, Z., Liu, L., Lu, N., 2018. Interface-Governed Deformation of Nanobubbles and Nanotents Formed by Two-Dimensional Materials. *Phys. Rev. Lett.* 121, 266101.
- Dai, Z., Liu, L., Zhang, Z., 2019a. Strain Engineering of 2D Materials: Issues and Opportunities at the Interface. *Adv. Mater.* 31, 1805417.
- Dai, Z., Sanchez, D.A., Brennan, C.J., Lu, N., 2020. Radial buckle delamination around 2D material tents. *J. Mech. Phys. Solids* 137, 103843.
- Dai, Z., Wang, G., Zheng, Z., Wang, Y., Zhang, S., Qi, X., Tan, P., Liu, L., Xu, Z., Li, Q., Cheng, Z., Zhang, Z., 2019b. Mechanical responses of boron-doped monolayer graphene. *Carbon* 147, 594-601.
- Dai, Z., Weng, C., Liu, L., Hou, Y., Zhao, X., Kuang, J., Shi, J., Wei, Y., Lou, J., Zhang, Z., 2016a. Multifunctional Polymer-Based Graphene Foams with Buckled Structure and Negative Poisson's Ratio. *Sci. Rep.* 6, 32989.

- Dai, Z., Wang, G.R., Liu, L.Q., Hou, Y., Wei, Y.G., Zhang, Z., 2016b. Mechanical behavior and properties of hydrogen bonded graphene/polymer nano-interfaces. *Compos. Sci. Technol.* 136, 1-9.
- Dai, Z., Wang, Y.L., Liu, L.Q., Liu, X.L., Tan, P.H., Xu, Z.P., Kuang, J., Liu, Q., Lou, J., Zhang, Z., 2016c. Hierarchical Graphene-Based Films with Dynamic Self-Stiffening for Biomimetic Artificial Muscle. *Adv. Funct. Mater.* 26, 7003-7010.
- Das, A., Pisana, S., Chakraborty, B., Piscanec, S., Saha, S.K., Waghmare, U.V., Novoselov, K.S., Krishnamurthy, H.R., Geim, A.K., Ferrari, A.C., Sood, A.K., 2008. Monitoring dopants by Raman scattering in an electrochemically top-gated graphene transistor. *Nat. Nanotechnol.* 3, 210-215.
- Davidovitch, B., Schroll, R.D., Vella, D., Adda-Bedia, M., Cerda, E.A., 2011. Prototypical model for tensional wrinkling in thin sheets. *Proc. Natl. Acad. Sci. U. S. A.* 108, 18227-18232.
- Davidovitch, B., Sun, Y., Grason, G.M., 2019. Geometrically incompatible confinement of solids. *Proc. Natl. Acad. Sci. U. S. A.* 116, 1483-1488.
- De Juan, F., Cortijo, A., Vozmediano, M.A., Cano, A., 2011. Aharonov–Bohm interferences from local deformations in graphene. *Nat. Phys.* 7, 810.
- Del Alamo, J.A., 2011. Nanometre-scale electronics with III–V compound semiconductors. *Nature* 479, 317.
- Deng, S., Gao, E., Xu, Z., Berry, V., 2017. Adhesion Energy of MoS₂ Thin Films on Silicon-Based Substrates Determined via the Attributes of a Single MoS₂ Wrinkle. *ACS Appl. Mater. Interfaces* 9, 7812-7818.
- Deng, S., Sumant, A.V., Berry, V., 2018. Strain engineering in two-dimensional nanomaterials beyond graphene. *Nano Today* 22, 14-35.
- Deng, S., Berry, V., 2016. Wrinkled, rippled and crumpled graphene: an overview of formation mechanism, electronic properties, and applications. *Mater. Today* 19, 197-212.
- Dou, W., Xu, C., Guo, J.-G., Du, H., Qiu, W., Xue, T., Kang, Y., Zhang, Q., 2018. Interfacial mechanical properties of double-layer graphene with consideration of the effect of stacking mode. *ACS Appl. Mater. Interfaces* 10, 44941-44949.
- Elibol, K., Bayer, B.C., Hummel, S., Kotakoski, J., Argentero, G., Meyer, J.C., 2016. Visualising the strain distribution in suspended two-dimensional materials under local deformation. *Sci. Rep.* 6, 28485.
- Falin, A., Cai, Q., Santos, E.J., Scullion, D., Qian, D., Zhang, R., Yang, Z., Huang, S., Watanabe, K., Taniguchi, T., 2017. Mechanical properties of atomically thin boron nitride and the role of interlayer interactions. *Nat. Commun.* 8, 15815.
- Faou, J.-Y., Parry, G., Grachev, S., Barthel, E., 2015. Telephone cord buckles—a relation between wavelength and adhesion. *J. Mech. Phys. Solids* 75, 93-103.
- Feng, J., Qian, X., Huang, C.-W., Li, J., 2012. Strain-engineered artificial atom as a broad-spectrum solar energy funnel. *Nat. Photonics* 6, 866-872.
- Ferrari, A.C., 2007. Raman spectroscopy of graphene and graphite: disorder, electron–phonon coupling, doping and nonadiabatic effects. *Solid State Commun.* 143, 47-57.
- Fichter, W., 1997. Some solutions for the large deflections of uniformly loaded circular membranes. National Aeronautics and Space Administration, Langley Research Center.

- Fonseca, A.F., Galvão, D.S., 2019. Self-tearing and self-peeling of folded graphene nanoribbons. *Carbon* 143, 230-239.
- Freund, L.B., Suresh, S., 2004. Thin film materials: stress, defect formation and surface evolution. Cambridge University Press.
- Frisenda, R., Navarro-Moratalla, E., Gant, P., De Lara, D.P., Jarillo-Herrero, P., Gorbachev, R.V., Castellanos-Gomez, A., 2018. Recent progress in the assembly of nanodevices and van der Waals heterostructures by deterministic placement of 2D materials. *Chem. Soc. Rev.* 47, 53-68.
- Gao, E., Lin, S.-Z., Qin, Z., Buehler, M.J., Feng, X.-Q., Xu, Z., 2018. Mechanical exfoliation of two-dimensional materials. *J. Mech. Phys. Solids* 115, 248-262.
- Gao, W., Huang, R., 2011. Effect of surface roughness on adhesion of graphene membranes. *J. Phys. D: Appl. Phys.* 44, 452001.
- Gao, W., Huang, R., 2014. Thermomechanics of monolayer graphene: Rippling, thermal expansion and elasticity. *J. Mech. Phys. Solids* 66, 42-58.
- Gao, X., Yu, X., Li, B., Fan, S., Li, C., 2017. Measuring Graphene Adhesion on Silicon Substrate by Single and Dual Nanoparticle-Loaded Blister. *Adv. Mater. Interfaces* 4, 1601023.
- Geim, A.K., Grigorieva, I.V., 2013. Van der Waals heterostructures. *Nature* 499, 419-425.
- Ghorbanfekr-Kalashami, H., Vasu, K.S., Nair, R.R., Peeters, F.M., Neek-Amal, M., 2017. Dependence of the shape of graphene nanobubbles on trapped substance. *Nat. Commun.* 8, 15844.
- Gong, L., Kinloch, I.A., Young, R.J., Riaz, I., Jalil, R., Novoselov, K.S., 2010. Interfacial stress transfer in a graphene monolayer nanocomposite. *Adv. Mater.* 22, 2694-2697.
- Gong, X., Kozbial, A., Li, L., 2015. What causes extended layering of ionic liquids on the mica surface? *Chem. Sci.* 6, 3478-3482.
- Gowthami, T., Tamilselvi, G., Jacob, G., Raina, G., 2015. The role of ambient ice-like water adlayers formed at the interfaces of graphene on hydrophobic and hydrophilic substrates probed using scanning probe microscopy. *Phys. Chem. Chem. Phys.* 17, 13964-13972.
- Guinea, F., Katsnelson, M.I., Geim, A.K., 2010. Energy gaps and a zero-field quantum Hall effect in graphene by strain engineering. *Nat. Phys.* 6, 30-33.
- Guo, G., Zhu, Y., 2015. Cohesive-shear-lag modeling of interfacial stress transfer between a monolayer graphene and a polymer substrate. *J. Appl. Mech.* 82, 031005.
- Haigh, S.J., Gholinia, A., Jalil, R., Romani, S., Britnell, L., Elias, D.C., Novoselov, K.S., Ponomarenko, L.A., Geim, A.K., Gorbachev, R., 2012. Cross-sectional imaging of individual layers and buried interfaces of graphene-based heterostructures and superlattices. *Nat. Mater.* 11, 764-767.
- Hallam, T., Berner, N.C., Yim, C., Duesberg, G.S., 2014. Strain, Bubbles, Dirt, and Folds: A Study of Graphene Polymer-Assisted Transfer. *Adv. Mater. Interfaces* 1, 1400115.
- Han, E., Yu, J., Annevelink, E., Son, J., Kang, D.A., Watanabe, K., Taniguchi, T., Ertekin, E., Huang, P.Y., van der Zande, A.M., 2019. Ultrasoft slip-mediated bending in few-layer graphene. *Nat. Mater.* DOI: 10.1038/s41563-019-0529-7
- Han, Y., Nguyen, K.X., Cao, M., Cueva, P.D., Xie, S., Tate, M.W., Purohit, P., Gruner, S.M., Park, J., Muller, D.A., 2018. Strain Mapping of Two-Dimensional Heterostructures with Sub-Picometer Precision. *Nano Lett.* 18, 3746-3751.

- Hattab, H., N'Diaye, A.T., Wall, D., Klein, C., Jnawali, G., Coraux, J., Busse, C., van Gastel, R., Poelsema, B., Michely, T., 2012. Interplay of wrinkles, strain, and lattice parameter in graphene on iridium. *Nano Lett.* 12, 678-682.
- He, K., Poole, C., Mak, K.F., Shan, J., 2013. Experimental demonstration of continuous electronic structure tuning via strain in atomically thin MoS₂. *Nano Lett.* 13, 2931-2936.
- He, K.T., Wood, J.D., Doidge, G.P., Pop, E., Lyding, J.W., 2012. Scanning tunneling microscopy study and nanomanipulation of graphene-coated water on mica. *Nano Lett.* 12, 2665-2672.
- He, Z.-Z., Zhu, Y.-B., Wu, H.-A., 2018. Self-folding mechanics of graphene tearing and peeling from a substrate. *Front. Phys.* 13, 138111.
- Hencky, H., 1915. On the stress state in circular plates with vanishing bending stiffness. *Z. Math. Phys.* 63, 311-317.
- Hod, O., Meyer, E., Zheng, Q., Urbakh, M., 2018a. Structural superlubricity and ultralow friction across the length scales. *Nature* 563, 485.
- Hod, O., Urbakh, M., Naveh, D., Bar-Sadan, M., Ismach, A., 2018b. Flatlands in the Holy Land: The Evolution of Layered Materials Research in Israel. *Adva. Mater.* 30, 1706581.
- Holmes, D.P., 2019. Elasticity and stability of shape-shifting structures. *Curr. Opin. Colloid Interface Sci.* 40, 118-137.
- Huang, J., Juszkievicz, M., De Jeu, W.H., Cerda, E., Emrick, T., Menon, N., Russell, T.P., 2007. Capillary wrinkling of floating thin polymer films. *Science* 317, 650-653.
- Huang, M., Yan, H., Chen, C., Song, D., Heinz, T.F., Hone, J., 2009. Phonon softening and crystallographic orientation of strained graphene studied by Raman spectroscopy. *Proc. Natl. Acad. Sci. U. S. A.* 106, 7304-7308.
- Huang, X., Zhang, S., 2011. Morphologies of monolayer graphene under indentation. *Modell. Simul. Mater. Sci. Eng.* 19, 054004.
- Huang, Y., Sutter, E., Shi, N.N., Zheng, J., Yang, T., Englund, D., Gao, H.J., Sutter, P., 2015. Reliable Exfoliation of Large-Area High-Quality Flakes of Graphene and Other Two-Dimensional Materials. *ACS Nano* 9, 10612-10620.
- Huang, Y., Wang, X., Zhang, X., Chen, X., Li, B., Wang, B., Huang, M., Zhu, C., Zhang, X., Bacsá, W.S., 2018. Raman Spectral Band Oscillations in Large Graphene Bubbles. *Phys. Rev. Lett.* 120, 186104.
- Hutchinson, J.W., Suo, Z., 1991. Mixed mode cracking in layered materials, *Adv. Appl. Mech.* 29, 63-191.
- Iguñiz, N., Frisenda, R., Bratschitsch, R., Castellanos-Gomez, A., 2019. Revisiting the Buckling Metrology Method to Determine the Young's Modulus of 2D Materials. *Adv. Mater.* 31, 1807150.
- Israelachvili, J.N., 2011. Intermolecular and surface forces. Academic press.
- Jang, H., Dai, Z., Ha, K.-H., Ameri, S.K., Lu, N., 2020. Stretchability of PMMA-Supported CVD Graphene and of Its Electrical Contacts. *2D Mater.* 7, 014003.
- Jia, P., Chen, W., Qiao, J., Zhang, M., Zheng, X., Xue, Z., Liang, R., Tian, C., He, L., Di, Z., Wang, X., 2019. Programmable graphene nanobubbles with three-fold symmetric pseudo-magnetic fields. *Nat. Commun.* 10, 3127.

- Jiang, L., Shi, Z., Zeng, B., Wang, S., Kang, J.-H., Joshi, T., Jin, C., Ju, L., Kim, J., Lyu, T., 2016. Soliton-dependent plasmon reflection at bilayer graphene domain walls. *Nat. Mater.* 15, 840.
- Jiang, L., Wang, S., Shi, Z., Jin, C., Utama, M.I.B., Zhao, S., Shen, Y.-R., Gao, H.-J., Zhang, G., Wang, F., 2018. Manipulation of domain-wall solitons in bi-and trilayer graphene. *Nat. Nanotechnol.* 13, 204.
- Jiang, T., Huang, R., Zhu, Y., 2014. Interfacial Sliding and Buckling of Monolayer Graphene on a Stretchable Substrate. *Adv. Funct. Mater.* 24, 396-402.
- Jiang, T., Zhu, Y., 2015. Measuring graphene adhesion using atomic force microscopy with a microsphere tip. *Nanoscale* 7, 10760-10766.
- Jiang, Y., Mao, J., Duan, J., Lai, X., Watanabe, K., Taniguchi, T., Andrei, E.Y., 2017. Visualizing strain-induced pseudomagnetic fields in graphene through an hBN magnifying glass. *Nano Lett.* 17, 2839-2843.
- Jin, C., Davoodabadi, A., Li, J., Wang, Y., Singler, T., 2017. Spherical indentation of a freestanding circular membrane revisited: Analytical solutions and experiments. *J. Mech. Phys. Solids* 100, 85-102.
- Jin, C., Regan, E.C., Yan, A., Iqbal Bakti Utama, M., Wang, D., Zhao, S., Qin, Y., Yang, S., Zheng, Z., Shi, S., Watanabe, K., Taniguchi, T., Tongay, S., Zettl, A., Wang, F., 2019. Observation of moiré excitons in WSe₂/WS₂ heterostructure superlattices. *Nature* 567, 76-80.
- Ju, L., Shi, Z., Nair, N., Lv, Y., Jin, C., Velasco Jr, J., Ojeda-Aristizabal, C., Bechtel, H.A., Martin, M.C., Zettl, A., 2015. Topological valley transport at bilayer graphene domain walls. *Nature* 520, 650.
- Kazakova, O., Panchal, V., Burnett, T.L., 2013. Epitaxial graphene and graphene-based devices studied by electrical scanning probe microscopy. *Crystals* 3, 191-233.
- Kelly, B.T., 1981. Physics of graphite.
- Khestanova, E., Guinea, F., Fumagalli, L., Geim, A.K., Grigorieva, I.V., 2016. Universal shape and pressure inside bubbles appearing in van der Waals heterostructures. *Nat. Commun.* 7, 12587.
- Kim, S.M., Hsu, A., Park, M.H., Chae, S.H., Yun, S.J., Lee, J.S., Cho, D.-H., Fang, W., Lee, C., Palacios, T., 2015. Synthesis of large-area multilayer hexagonal boron nitride for high material performance. *Nature communications* 6, 8662.
- King, H., Schroll, R.D., Davidovitch, B., Menon, N., 2012. Elastic sheet on a liquid drop reveals wrinkling and crumpling as distinct symmetry-breaking instabilities. *Proc. Natl. Acad. Sci. U. S. A.* 109, 9716-9720.
- Kissinger, G., Kissinger, W., 1991. Hydrophilicity of silicon wafers for direct bonding. *physica status solidi (a)* 123, 185-192.
- Kitt, A.L., Qi, Z., Rémi, S., Park, H.S., Swan, A.K., Goldberg, B.B., 2013. How graphene slides: Measurement and theory of strain-dependent frictional forces between graphene and SiO₂. *Nano Lett.* 13, 2605-2610.
- Klimov, N.N., Jung, S., Zhu, S., Li, T., Wright, C.A., Solares, S.D., Newell, D.B., Zhitenev, N.B., Strosio, J.A., 2012. Electromechanical properties of graphene drumheads. *Science* 336, 1557-1561.

- Knight, C.A., 1967. The contact angle of water on ice. *J. Colloid Interface Sci.* 25, 280-284.
- Koenig, S.P., Boddeti, N.G., Dunn, M.L., Bunch, J.S., 2011. Ultrastrong adhesion of graphene membranes. *Nat. Nanotechnol.* 6, 543-546.
- Komaragiri, U., Begley, M., Simmonds, J., 2005. The mechanical response of freestanding circular elastic films under point and pressure loads. *J. Appl. Mechan.* 72, 203-212.
- Koren, E., Lörtscher, E., Rawlings, C., Knoll, A.W., Duerig, U., 2015. Adhesion and friction in mesoscopic graphite contacts. *Science* 348, 679-683.
- Kozbial, A., Gong, X., Liu, H., Li, L., 2015. Understanding the intrinsic water wettability of molybdenum disulfide (MoS₂). *Langmuir* 31, 8429-8435.
- Kozbial, A., Li, Z., Sun, J., Gong, X., Zhou, F., Wang, Y., Xu, H., Liu, H., Li, L., 2014. Understanding the intrinsic water wettability of graphite. *Carbon* 74, 218-225.
- Kretinin, A., Cao, Y., Tu, J., Yu, G., Jalil, R., Novoselov, K., Haigh, S., Gholinia, A., Mishchenko, A., Lozada, M., 2014. Electronic properties of graphene encapsulated with different two-dimensional atomic crystals. *Nano Lett.* 14, 3270-3276.
- Kudin, K.N., Scuseria, G.E., Yakobson, B.I., 2001. C 2 F, BN, and C nanoshell elasticity from ab initio computations. *Phys. Rev. B* 64, 235406.
- Kumar, H., Dong, L., Shenoy, V.B., 2016. Limits of Coherency and Strain Transfer in Flexible 2D van der Waals Heterostructures: Formation of Strain Solitons and Interlayer Debonding. *Sci. Rep.* 6, 21516.
- Kushima, A., Qian, X., Zhao, P., Zhang, S., Li, J., 2015. Ripplations in van der Waals Layers. *Nano Lett.* 15, 1302-1308.
- Landau, L.D., Kosevich, A., Pitaevskii, L.P., Lifshitz, E.M., 1986. *Theory of elasticity*.
- Lee, C., Wei, X., Kysar, J.W., Hone, J., 2008. Measurement of the elastic properties and intrinsic strength of monolayer graphene. *Science* 321, 385-388.
- Lee, J., Zheng, X., Roberts, R.C., Feng, P.X.-L., 2015. Scanning electron microscopy characterization of structural features in suspended and non-suspended graphene by customized CVD growth. *Diamond Relat. Mater.* 54, 64-73.
- Lee, J.E., Ahn, G., Shim, J., Lee, Y.S., Ryu, S., 2012. Optical separation of mechanical strain from charge doping in graphene. *Nat. Commun.* 3, 1024.
- Levy, N., Burke, S., Meaker, K., Panlasigui, M., Zettl, A., Guinea, F., Neto, A.C., Crommie, M., 2010. Strain-induced pseudo-magnetic fields greater than 300 tesla in graphene nanobubbles. *Science* 329, 544-547.
- Li, H., Contryman, A.W., Qian, X., Ardakani, S.M., Gong, Y., Wang, X., Weisse, J.M., Lee, C.H., Zhao, J., Ajayan, P.M., 2015. Optoelectronic crystal of artificial atoms in strain-textured molybdenum disulphide. *Nat. Commun.* 6, 7381.
- Li, H., Du, M., Mleczko, M.J., Koh, A.L., Nishi, Y., Pop, E., Bard, A.J., Zheng, X., 2016a. Kinetic study of hydrogen evolution reaction over strained MoS₂ with sulfur vacancies using scanning electrochemical microscopy. *J. Am. Chem. Soc.* 138, 5123-5129.
- Li, H., Li, M., Kang, Z., 2018. Mechanics of the scrolling and folding of graphene. *Nanotechnology* 29, 245604.
- Li, H., Tsai, C., Koh, A.L., Cai, L., Contryman, A.W., Fragapane, A.H., Zhao, J., Han, H.S., Manoharan, H.C., Abild-Pedersen, F., 2016b. Activating and optimizing MoS₂ basal

- planes for hydrogen evolution through the formation of strained sulphur vacancies. *Nat. Mater.* 15, 48-53.
- Li, H., Wang, J., Gao, S., Chen, Q., Peng, L., Liu, K., Wei, X., 2017a. Superlubricity between MoS₂ Monolayers. *Adv. Mater.* 29, 1701474.
- Li, Q., Lee, C., Carpick, R.W., Hone, J., 2010. Substrate effect on thickness-dependent friction on graphene. *physica status solidi (b)* 247, 2909-2914.
- Li, X., Tao, L., Chen, Z., Fang, H., Li, X., Wang, X., Xu, J.-B., Zhu, H., 2017b. Graphene and related two-dimensional materials: Structure-property relationships for electronics and optoelectronics. *Appl. Phys. Rev.* 4, 021306.
- Li, Y., Huang, S., Wei, C., Wu, C., Mochalin, V.N., 2019. Adhesion of two-dimensional titanium carbides (MXenes) and graphene to silicon. *Nat. Commun.* 10, 3014.
- Li, Y., Zhang, W., Guo, B., Datta, D., 2017c. Interlayer Shear of Nanomaterials: Graphene-Graphene, Boron Nitride-Boron Nitride and Graphene-Boron Nitride. *Acta Mech. Solida Sin.* 30, 234-240.
- Li, Z., Wang, Y., Kozbial, A., Shenoy, G., Zhou, F., McGinley, R., Ireland, P., Morganstein, B., Kunkel, A., Surwade, S.P., 2013. Effect of airborne contaminants on the wettability of supported graphene and graphite. *Nat. Mater.* 12, 925-931.
- Liang, J., Zhang, J., Li, Z., Hong, H., Wang, J., Zhang, Z., Zhou, X., Qiao, R., Xu, J., Gao, P., 2017. Monitoring Local Strain Vector in Atomic-Layered MoSe₂ by Second-Harmonic Generation. *Nano Lett.* 17, 7539-7543.
- Liechti, K.M., 2019. Characterizing the Interfacial Behavior of 2D Materials: a Review. *Exp. Mech.* 59, 395-412.
- Lim, C.H.Y.X., Nesladek, M., Loh, K.P., 2014. Observing High-Pressure Chemistry in Graphene Bubbles. *Angew. Chem., Int. Ed.* 53, 215-219.
- Lim, C.H.Y.X., Sorkin, A., Bao, Q., Li, A., Zhang, K., Nesladek, M., Loh, K.P., 2013. A hydrothermal anvil made of graphene nanobubbles on diamond. *Nat. Commun.* 4, 1556.
- Lim, H.S., Kwak, D., Lee, D.Y., Lee, S.G., Cho, K., 2007. UV-driven reversible switching of a rose-like vanadium oxide film between superhydrophobicity and superhydrophilicity. *J. Am. Chem. Soc.* 129, 4128-4129.
- Lipatov, A., Lu, H., Alhabeab, M., Anasori, B., Gruverman, A., Gogotsi, Y., Sinitskii, A., 2018. Elastic properties of 2D Ti₃C₂T_x MXene monolayers and bilayers. *Sci. Adv.* 4, eaat0491.
- Liu, X., Boddeti, N.G., Szpunar, M.R., Wang, L., Rodriguez, M.A., Long, R., Xiao, J., Dunn, M.L., Bunch, J.S., 2013. Observation of pull-in instability in graphene membranes under interfacial forces. *Nano Lett.* 13, 2309-2313.
- Liu, Y., Weiss, N.O., Duan, X.D., Cheng, H.C., Huang, Y., Duan, X.F., 2016. Van der Waals heterostructures and devices. *Nat. Rev. Mater.* 1, 16042.
- Liu, Y.L., Xu, Z.P., Zheng, Q.S., 2011. The interlayer shear effect on graphene multilayer resonators. *J. Mech. Phys. Solids* 59, 1613-1622.
- Liu, Z., Amani, M., Najmaei, S., Xu, Q., Zou, X., Zhou, W., Yu, T., Qiu, C., Birdwell, A.G., Crowne, F.J., 2014. Strain and structure heterogeneity in MoS₂ 2 atomic layers grown by chemical vapour deposition. *Nat. Commun.* 5, 5246.

- Liu, Z., Yang, J., Grey, F., Liu, J.Z., Liu, Y., Wang, Y., Yang, Y., Cheng, Y., Zheng, Q., 2012b. Observation of microscale superlubricity in graphite. *Phys. Rev. Lett.* 108, 205503.
- Lloyd, D., Liu, X., Boddeti, N., Cantley, L., Long, R., Dunn, M.L., Bunch, J.S., 2017. Adhesion, Stiffness, and Instability in Atomically Thin MoS₂ Bubbles. *Nano Letters*.
- Lloyd, D., Liu, X., Christopher, J.W., Cantley, L., Wadehra, A., Kim, B.L., Goldberg, B.B., Swan, A.K., Bunch, J.S., 2016. Band Gap Engineering with Ultra-Large Biaxial Strains in Suspended Monolayer MoS₂. *Nano Lett.* 17, 5329-5334.
- Lopez-Bezanilla, A., Campos-Delgado, J., Sumpter, B.G., Baptista, D.L., Hayashi, T., Kim, Y.A., Muramatsu, H., Endo, M., Achete, C.A., Terrones, M., 2012. Geometric and electronic structure of closed graphene edges. *J. Phys. Chem. Lett.* 3, 2097-2102.
- López-Polín, G., Gómez-Navarro, C., Parente, V., Guinea, F., Katsnelson, M.I., Pérez-Murano, F., Gómez-Herrero, J., 2015. Increasing the elastic modulus of graphene by controlled defect creation. *Nat. Phys.* 11, 26-31.
- Los, J., Fasolino, A., Katsnelson, M., 2016. Scaling behavior and strain dependence of in-plane elastic properties of graphene. *Phys. Rev. Lett.* 116, 015901.
- Lou, S., Liu, Y., Yang, F., Lin, S., Zhang, R., Deng, Y., Wang, M., Tom, K.B., Zhou, F., Ding, H., Bustillo, K.C., Wang, X., Yan, S., Scott, M., Minor, A., Yao, J., 2018. Three-dimensional Architecture Enabled by Strained Two-dimensional Material Heterojunction. *Nano Lett.* 18, 1819-1825.
- Lu, J., Neto, A.C., Loh, K.P., 2012. Transforming moiré blisters into geometric graphene nanobubbles. *Nat. Commun.* 3, 823.
- Lu, Q., Arroyo, M., Huang, R., 2009. Elastic bending modulus of monolayer graphene. *J. Phys. D Appl. Phys.* 42, 102002.
- Lu, X., Stepanov, P., Yang, W., Xie, M., Aamir, M.A., Das, I., Urgell, C., Watanabe, K., Taniguchi, T., Zhang, G., Bachtold, A., MacDonald, A.H., Efetov, D.K., 2019. Superconductors, orbital magnets and correlated states in magic-angle bilayer graphene. *Nature* 574, 653-657.
- Ly, T.H., Yun, S.J., Thi, Q.H., Zhao, J., 2017. Edge Delamination of Monolayer Transition Metal Dichalcogenides. *ACS Nano* 11, 7534-7541.
- Lyublinskaya, A., Babkin, S., Burmistrov, I., 2019. The effect of anomalous elasticity on the bubbles in van der Waals heterostructures. *arXiv preprint arXiv:1909.12650*.
- Mansfield, E.H., 2005. The bending and stretching of plates. Cambridge University Press.
- Mas-Balleste, R., Gomez-Navarro, C., Gomez-Herrero, J., Zamora, F., 2011. 2D materials: to graphene and beyond. *Nanoscale* 3, 20-30.
- Meng, L., Su, Y., Geng, D., Yu, G., Liu, Y., Dou, R.-F., Nie, J.-C., He, L., 2013a. Hierarchy of graphene wrinkles induced by thermal strain engineering. *Appl. Phys. Lett.* 103, 251610.
- Meng, X., Li, M., Kang, Z., Zhang, X., Xiao, J., 2013b. Mechanics of self-folding of single-layer graphene. *J. Phys. D Appl. Phys.* 46, 055308.
- Meng, Z., Soler-Crespo, R.A., Xia, W., Gao, W., Ruiz, L., Espinosa, H.D., Keten, S., 2017. A coarse-grained model for the mechanical behavior of graphene oxide. *Carbon* 117, 476-487.

- Metzger, C., Rémi, S., Liu, M., Kusminskiy, S.V., Castro Neto, A.H., Swan, A.K., Goldberg, B.B., 2009. Biaxial strain in graphene adhered to shallow depressions. *Nano Lett.* 10, 6-10.
- Mikata, Y., 2010. Approximate Solutions for a Self-Folding Problem of Carbon Nanotubes. *J. Eng. Mater-T. ASME* 132, 011013.
- Mohiuddin, T., Lombardo, A., Nair, R., Bonetti, A., Savini, G., Jalil, R., Bonini, N., Basko, D., Galiotis, C., Marzari, N., 2009. Uniaxial strain in graphene by Raman spectroscopy: G peak splitting, Grüneisen parameters, and sample orientation. *Phys. Rev. B* 79, 205433.
- Na, S.R., Suk, J.W., Ruoff, R.S., Huang, R., Liechti, K.M., 2014. Ultra Long-Range Interactions between Large Area Graphene and Silicon. *ACS Nano* 8, 11234-11242.
- Na, S.R., Wang, X., Piner, R.D., Huang, R., Willson, C.G., Liechti, K.M., 2016. Cracking of Polycrystalline Graphene on Copper under Tension. *ACS Nano* 10, 9616-9625.
- Naumis, G.G., Barraza-Lopez, S., Oliva-Leyva, M., Terrones, H., 2017. Electronic and optical properties of strained graphene and other strained 2D materials: a review. *Rep. Prog. Phys.* 80, 096501.
- Nazemnezhad, R., Shokrollahi, H., Hosseini-Hashemi, S., 2014. Sandwich beam model for free vibration analysis of bilayer graphene nanoribbons with interlayer shear effect. *J. Appl. Phys.* 115, 174303.
- Nemes-Incze, P., Kukucska, G., Koltai, J., Kürti, J., Hwang, C., Tapasztó, L., Biró, L.P., 2017. Preparing local strain patterns in graphene by atomic force microscope based indentation. *Sci. Rep.* 7, 3035.
- Neto, A.C., Guinea, F., Peres, N.M., Novoselov, K.S., Geim, A.K., 2009. The electronic properties of graphene. *Rev. Mod. Phys.* 81, 109.
- Ni, G.X., Wang, H., Jiang, B.Y., Chen, L.X., Du, Y., Sun, Z.Y., Goldflam, M.D., Frenzel, A.J., Xie, X.M., Fogler, M.M., Basov, D.N., 2019. Soliton superlattices in twisted hexagonal boron nitride. *Nat. Commun.* 10, 4360.
- Ni, Z.H., Yu, T., Lu, Y.H., Wang, Y.Y., Feng, Y.P., Shen, Z.X., 2008. Uniaxial strain on graphene: Raman spectroscopy study and band-gap opening. *ACS nano* 2, 2301-2305.
- Nicholl, R.J., Lavrik, N.V., Vlassiounk, I., Srijanto, B.R., Bolotin, K.I., 2017. Hidden area and mechanical nonlinearities in freestanding graphene. *Phys. Rev. Lett.* 118, 266101.
- Novoselov, K.S., Geim, A.K., Morozov, S.V., Jiang, D., Zhang, Y., Dubonos, S.V., Grigorieva, I.V., Firsov, A.A., 2004. Electric field effect in atomically thin carbon films. *science* 306, 666-669.
- Novoselov, K.S., Mishchenko, A., Carvalho, A., Castro Neto, A.H., 2016. 2D materials and van der Waals heterostructures. *Science* 353.
- Ochedowski, O., Bussmann, B.K., Schleberger, M., 2014. Graphene on mica-intercalated water trapped for life. *Sci. Rep.* 4, 6003.
- Ortolani, L., Cadelano, E., Veronese, G.P., Boschi, C.D., Snoeck, E., Colombo, L., Morandi, V., 2012. Folded Graphene Membranes: Mapping Curvature at the Nanoscale. *Nano Lett.* 12, 5207-5212.
- Ozaki, T., Koga, T., Fujitsuka, N., Makino, H., Hohjo, H., Kadoura, H., 2018. Biaxial flexure testing of free-standing thin film membrane with nanoindentation system. *Sens. Actuators A* 278, 48-59.

- Palacios-Berraquero, C., Kara, D.M., Montblanch, A.R.-P., Barbone, M., Latawiec, P., Yoon, D., Ott, A.K., Loncar, M., Ferrari, A.C., Atatüre, M., 2017. Large-scale quantum-emitter arrays in atomically thin semiconductors. *Nat. Commun.* 8, 15093.
- Pan, F., Wang, G.R., Liu, L.Q., Chen, Y.L., Zhang, Z., Shi, X.H., 2019. Bending induced interlayer shearing, rippling and kink buckling of multilayered graphene sheets. *Int. J. Solids Struct.* 122, 340-363.
- Pan, K., Ni, Y., He, L., Huang, R., 2014. Nonlinear analysis of compressed elastic thin films on elastic substrates: From wrinkling to buckle-delamination. *Int. J. Solids Struct.* 51, 3715-3726.
- Papageorgiou, D.G., Kinloch, I.A., Young, R.J., 2017. Mechanical properties of graphene and graphene-based nanocomposites. *Prog. Mater. Sci.* 90, 75-127.
- Parry, G., Colin, J., Coupeau, C., Foucher, F., Cimetière, A., Grilhé, J., 2005. Effect of substrate compliance on the global unilateral post-buckling of coatings: AFM observations and finite element calculations. *Acta Mater.* 53, 441-447.
- Pizzocchero, F., Gammelgaard, L., Jessen, B.S., Caridad, J.M., Wang, L., Hone, J., Boggild, P., Booth, T.J., 2016. The hot pick-up technique for batch assembly of van der Waals heterostructures. *Nat. Commun.* 7, 11894.
- Plechinger, G., Castellanos-Gomez, A., Buscema, M., van der Zant, H.S., Steele, G.A., Kuc, A., Heine, T., Schüller, C., Korn, T., 2015. Control of biaxial strain in single-layer molybdenite using local thermal expansion of the substrate. *2D Mater.* 2, 015006.
- Pochet, P., McGuigan, B.C., Coraux, J., Johnson, H.T., 2017. Toward Moiré engineering in 2D materials via dislocation theory. *Appl. Mater. Today* 9, 240-250.
- Poot, M., van der Zant, H.S., 2008. Nanomechanical properties of few-layer graphene membranes. *Appl. Phys. Lett.* 92, 063111.
- Qi, Z., Kitt, A.L., Park, H.S., Pereira, V.M., Campbell, D.K., Neto, A.C., 2014. Pseudomagnetic fields in graphene nanobubbles of constrained geometry: A molecular dynamics study. *Phys. Rev. B* 90, 125419.
- Qu, W.Y., Bagchi, S., Chen, X.M., Chew, H.B., Ke, C.H., 2019. Bending and interlayer shear moduli of ultrathin boron nitride nanosheet. *J. Phys. D Appl. Phys.* 52, 465301.
- Quereda, J., San-Jose, P., Parente, V., Vaquero-Garzon, L., Molina-Mendoza, A.J., Agraït, N., Rubio-Bollinger, G., Guinea, F., Roldán, R., Castellanos-Gomez, A., 2016. Strong modulation of optical properties in black phosphorus through strain-engineered rippling. *Nano Lett.* 16, 2931-2937.
- Rafiee, J., Mi, X., Gullapalli, H., Thomas, A.V., Yavari, F., Shi, Y., Ajayan, P.M., Koratkar, N.A., 2012. Wetting transparency of graphene. *Nat. Mater.* 11, 217-222.
- Raju, A.P.A., Lewis, A., Derby, B., Young, R.J., Kinloch, I.A., Zan, R., Novoselov, K.S., 2014. Wide-Area Strain Sensors based upon Graphene-Polymer Composite Coatings Probed by Raman Spectroscopy. *Adv. Funct. Mater.* 24, 2865-2874.
- Reserbat-Plantey, A., Kalita, D., Han, Z., Ferlazzo, L., Autier-Laurent, S., Komatsu, K., Li, C., Weil, R.I., Ralko, A., Marty, L.t., 2014. Strain superlattices and macroscale suspension of graphene induced by corrugated substrates. *Nano Lett.* 14, 5044-5051.

- Ribeiro-Palau, R., Zhang, C.J., Watanabe, K., Taniguchi, T., Hone, J., Dean, C.R., 2018. Twistable electronics with dynamically rotatable heterostructures. *Science* 361, 690-693.
- Rode, J.C., Zhai, D., Belke, C., Hong, S.J., Schmidt, H., Sandler, N., Haug, R.J., 2018. Linking interlayer twist angle to geometrical parameters of self-assembled folded graphene structures. *2D Mater.* 6, 015021.
- Roldán, R., Castellanos-Gomez, A., Cappelluti, E., Guinea, F., 2015. Strain engineering in semiconducting two-dimensional crystals. *J. Phys. Condens. Matter* 27, 313201.
- Ruffini, A., Durinck, J., Colin, J., Coupeau, C., Grilhé, J., 2012a. Effects of sliding on interface delamination during thin film buckling. *Scr. Mater.* 67, 157-160.
- Ruffini, A., Durinck, J., Colin, J., Coupeau, C., Grilhé, J., 2012b. Gliding at interface during thin film buckling: A coupled atomistic/elastic approach. *Acta Mater.* 60, 1259-1267.
- Ruiz, L., Xia, W., Meng, Z., Keten, S., 2015. A coarse-grained model for the mechanical behavior of multi-layer graphene. *Carbon* 82, 103-115.
- Sadd, M.H., 2009. *Elasticity: theory, applications, and numerics*. Academic Press.
- Sampathkumar, K., Androulidakis, C., Koukaras, E.N., Rahova, J., Drogowska, K., Kalbac, M., Vetushka, A., Fejfar, A., Galiotis, C., Frank, O., 2019. Sculpturing graphene wrinkle patterns into compliant substrates. *Carbon* 146, 772-778.
- Sanchez, D.A., Dai, Z., Wang, P., Cantu-Chavez, A., Brennan, C.J., Huang, R., Lu, N., 2018. Mechanics of spontaneously formed nanoblister trapped by transferred 2D crystals. *Proc. Natl. Acad. Sci. U. S. A.* 115, 7884-7889.
- Santos, F.d.P., Campos, E.d., Costa, M., Melo, F.C.L., Honda, R.Y., Mota, R.P., 2003. Superficial modifications in TiO₂ and Al₂O₃ ceramics. *Mater. Res.* 6, 353-357.
- Sarwat, S.G., Tweedie, M., Porter, B.F., Zhou, Y., Sheng, Y., Mol, J.A., Warner, J.H., Bhaskaran, H., 2018. Revealing Strain Induced Effects in Ultrathin Heterostructures at the Nanoscale. *Nano Lett.* 18, 2467-2474.
- Schmidt, H., Rode, J.C., Smirnov, D., Haug, R.J., 2014. Superlattice structures in twisted bilayers of folded graphene. *Nat. Commun.* 5, 5742.
- Schniepp, H.C., Kudin, K.N., Li, J.L., Prud'homme, R.K., Car, R., Saville, D.A., Aksay, I.A., 2008. Bending properties of single functionalized graphene sheets probed by atomic force microscopy. *ACS Nano* 2, 2577-2584.
- Schroll, R.D., Adda-Bedia, M., Cerda, E., Huang, J., Menon, N., Russell, T.P., Toga, K.B., Vella, D., Davidovitch, B., 2013. Capillary deformations of bendable films. *Phys. Rev. Lett.* 111, 014301.
- Schulman, R.D., Dalnoki-Veress, K., 2018. Droplets Capped with an Elastic Film Can Be Round, Elliptical, or Nearly Square. *Phys. Rev. Lett.* 121, 248004.
- Schwerin, E., 1929. Über Spannungen und Formänderungen kreisringförmiger Membranen. *ZAMM-Journal of Applied Mathematics and Mechanics/Zeitschrift für Angewandte Mathematik und Mechanik* 9, 482-483.
- Settnes, M., Power, S.R., Brandbyge, M., Jauho, A.P., 2016b. Graphene Nanobubbles as Valley Filters and Beam Splitters. *Phys. Rev. Lett.* 117, 276801.

- Seyler, K.L., Rivera, P., Yu, H., Wilson, N.P., Ray, E.L., Mandrus, D.G., Yan, J., Yao, W., Xu, X., 2019. Signatures of moiré-trapped valley excitons in MoSe₂/WSe₂ heterobilayers. *Nature* 567, 66-70.
- Shen, Y., Wu, H., 2012. Interlayer shear effect on multilayer graphene subjected to bending. *Appl. Phys. Lett.* 100, 101909.
- Shenoy, V.B., Gracias, D.H., 2012. Self-folding thin-film materials: From nanopolyhedra to graphene origami. *MRS Bulletin* 37, 847-854.
- Shim, J., Lui, C.H., Ko, T.Y., Yu, Y.-J., Kim, P., Heinz, T.F., Ryu, S., 2012. Water-gated charge doping of graphene induced by mica substrates. *Nano Lett.* 12, 648-654.
- Shin, B.G., Han, G.H., Yun, S.J., Oh, H.M., Bae, J.J., Song, Y.J., Park, C.Y., Lee, Y.H., 2016. Indirect Bandgap Puddles in Monolayer MoS₂ by Substrate-Induced Local Strain. *Adv. Mater.* 28, 9378-9384.
- Song, Y., Mandelli, D., Hod, O., Urbakh, M., Ma, M., Zheng, Q., 2018. Robust microscale superlubricity in graphite/hexagonal boron nitride layered heterojunctions. *Nat. Mater.* 17, 894-899.
- Style, R.W., Jagota, A., Hui, C.Y., Dufresne, E.R., 2017. Elastocapillarity: Surface Tension and the Mechanics of Soft Solids. *Annu. Rev. Condens. Matter* 8, 99-118.
- Sun, Y., Liu, K., 2019. Strain engineering in functional 2-dimensional materials. *J. Appl. Phys.* 125, 082402.
- Sunku, S., Ni, G., Jiang, B., Yoo, H., Sternbach, A., McLeod, A., Stauber, T., Xiong, L., Taniguchi, T., Watanabe, K., 2018. Photonic crystals for nano-light in moiré graphene superlattices. *Science* 362, 1153-1156.
- Tapasztó, L., Dumitrică, T., Kim, S.J., Nemes-Incze, P., Hwang, C., Biró, L.P., 2012. Breakdown of continuum mechanics for nanometre-wavelength rippling of graphene. *Nat. Phys.* 8, 739-742.
- Tawfick, S., De Volder, M., Hart, A.J., 2011. Structurally programmed capillary folding of carbon nanotube assemblies. *Langmuir* 27, 6389-6394.
- Tedeschi, D., Blundo, E., Felici, M., Pettinari, G., Liu, B., Yildirim, T., Petroni, E., Zhang, C., Zhu, Y., Sennato, S., 2019. Controlled Micro/Nanodome Formation in Proton-Irradiated Bulk Transition-Metal Dichalcogenides. *Adv. Mater.* 31, 1903795.
- Temmen, M., Ochedowski, O., Schleberger, M., Reichling, M., Bollmann, T., 2014. Hydration layers trapped between graphene and a hydrophilic substrate. *New J. Phys.* 16, 053039.
- Timoshenko, S.P., Gere, J.M., 2009. *Theory of elastic stability*. Courier Dover Publications.
- Timoshenko, S.P., Woinowsky-Krieger, S., 1959. *Theory of plates and shells*. McGraw-hill.
- Tomori, H., Kanda, A., Goto, H., Ootuka, Y., Tsukagoshi, K., Moriyama, S., Watanabe, E., Tsuya, D., 2011. Introducing nonuniform strain to graphene using dielectric nanopillars. *Appl. Phys. Express* 4, 075102.
- Torres, J., Zhu, Y., Liu, P., Lim, S.C., Yun, M., 2018. Adhesion energies of 2D graphene and MoS₂ to silicon and metal substrates. *physica status solidi (a)* 215, 1700512.
- Tu, Q., Spanopoulos, I., Yasaei, P., Stoumpos, C.C., Kanatzidis, M.G., Shekhawat, G.S., Dravid, V.P., 2018. Stretching and Breaking of Ultrathin 2D Hybrid Organic-Inorganic Perovskites. *ACS Nano* 12, 10347-10354.

- Uwanno, T., Hattori, Y., Taniguchi, T., Watanabe, K., Nagashio, K., 2015. Fully dry PMMA transfer of graphene on h-BN using a heating/cooling system. *2D Mater.* 2, 041002.
- Vasu, K., Prestat, E., Abraham, J., Dix, J., Kashtiban, R., Beheshtian, J., Sloan, J., Carbone, P., Neek-Amal, M., Haigh, S., 2016. Van der Waals pressure and its effect on trapped interlayer molecules. *Nat. Commun.* 7, 12168.
- Vella, D., 2019. Buffering by buckling as a route for elastic deformation. *Nat. Rev. Phys.* 1, 425-436.
- Vella, D., Adda-Bedia, M., Cerda, E., 2010. Capillary wrinkling of elastic membranes. *Soft Matter* 6, 5778-5782.
- Vella, D., Bico, J., Boudaoud, A., Roman, B., Reis, P.M., 2009. The macroscopic delamination of thin films from elastic substrates. *Proc. Natl. Acad. Sci. U. S. A.* 106, 10901-10906.
- Vella, D., Davidovitch, B., 2017. Indentation metrology of clamped, ultra-thin elastic sheets. *Soft Matter* 13, 2264-2278.
- Vella, D., Davidovitch, B., 2018. Regimes of wrinkling in an indented floating elastic sheet. *Phys. Rev. E* 98, 013003.
- Vella, D., Ebrahimi, H., Vaziri, A., Davidovitch, B., 2015. Wrinkling reveals a new isometry of pressurized elastic shells. *EPL (Europhysics Letters)* 112, 24007.
- Wan, K.-T., Guo, S., Dillard, D.A., 2003. A theoretical and numerical study of a thin clamped circular film under an external load in the presence of a tensile residual stress. *Thin Solid Films* 425, 150-162.
- Wang, B., Cunnig, B.V., Kim, N.Y., Kargar, F., Park, S.Y., Li, Z., Joshi, S.R., Peng, L., Modepalli, V., Chen, X., 2019a. Ultrastiff, Strong, and Highly Thermally Conductive Crystalline Graphitic Films with Mixed Stacking Order. *Adv. Mater.* 31, 1903039.
- Wang, B., Huang, M., Kim, N.Y., Cunnig, B.V., Huang, Y., Qu, D., Chen, X., Jin, S., Biswal, M., Zhang, X., Lee, S.H., Lim, H., Yoo, W.J., Lee, Z., Ruoff, R.S., 2017a. Controlled Folding of Single Crystal Graphene. *Nano Lett.* 17, 1467-1473.
- Wang, B., Li, Z., Wang, C., Signetti, S., Cunnig, B.V., Wu, X., Huang, Y., Jiang, Y., Shi, H., Ryu, S., 2018. Folding Large Graphene-on-Polymer Films Yields Laminated Composites with Enhanced Mechanical Performance. *Adv. Mater.* 30, 1707449.
- Wang, D., Chen, G., Li, C., Cheng, M., Yang, W., Wu, S., Xie, G., Zhang, J., Zhao, J., Lu, X., Chen, P., Wang, G., Meng, J., Tang, J., Yang, R., He, C., Liu, D., Shi, D., Watanabe, K., Taniguchi, T., Feng, J., Zhang, Y., Zhang, G., 2016a. Thermally Induced Graphene Rotation on Hexagonal Boron Nitride. *Phys. Rev. Lett.* 116, 126101.
- Wang, G., Dai, Z., Liu, L., Hu, H., Dai, Q., Zhang, Z., 2016b. Tuning the Interfacial Mechanical Behaviors of Monolayer Graphene/PMMA Nanocomposites. *ACS. Appl. Mater. Interfaces* 8, 22554-22562.
- Wang, G., Dai, Z., Wang, Y., Tan, P., Liu, L., Xu, Z., Wei, Y., Huang, R., Zhang, Z., 2017b. Measuring Interlayer Shear Stress in Bilayer Graphene. *Phys. Rev. Lett.* 119, 036101.
- Wang, G., Dai, Z., Xiao, J., Feng, S., Weng, C., Liu, L., Xu, Z., Huang, R., Zhang, Z., 2019b. Bending of Multilayer van der Waals Materials. *Phys. Rev. Lett.* 123, 116101.
- Wang, G., Li, X., Wang, Y., Zheng, Z., Dai, Z., Qi, X., Liu, L., Cheng, Z., Xu, Z., Tan, P., Zhang, Z., 2017d. Interlayer Coupling Behaviors of Boron Doped Multilayer Graphene. *J. Phys. Chem. C* 121, 26034-26043.

- Wang, G., Liu, L., Dai, Z., Liu, Q., Miao, H., Zhang, Z., 2015a. Biaxial compressive behavior of embedded monolayer graphene inside flexible poly (methyl methacrylate) matrix. *Carbon* 86, 69-77.
- Wang, G.R., Gao, E.L., Dai, Z.H., Liu, L.Q., Xu, Z.P., Zhang, Z., 2017e. Degradation and recovery of graphene/polymer interfaces under cyclic mechanical loading. *Compos. Sci. Technol.* 149, 220-227.
- Wang, J., Sorescu, D.C., Jeon, S., Belianinov, A., Kalinin, S.V., Baddorf, A.P., Maksymovych, P., 2016c. Atomic intercalation to measure adhesion of graphene on graphite. *Nat. Commun.* 7, 13263.
- Wang, L., Gao, Y., Wen, B., Han, Z., Taniguchi, T., Watanabe, K., Koshino, M., Hone, J., Dean, C.R., 2015b. Evidence for a fractional fractal quantum Hall effect in graphene superlattices. *Science* 350, 1231-1234.
- Wang, L., Meric, I., Huang, P., Gao, Q., Gao, Y., Tran, H., Taniguchi, T., Watanabe, K., Campos, L., Muller, D., 2013a. One-dimensional electrical contact to a two-dimensional material. *Science* 342, 614-617.
- Wang, P., Gao, W., Cao, Z., Liechti, K.M., Huang, R., 2013b. Numerical analysis of circular graphene bubbles. *J. Appl. Mech.* 80, 040905.
- Wang, P., Gao, W., Wilkerson, J., Liechti, K.M., Huang, R., 2017f. Cavitation of water by volume-controlled stretching. *Extreme Mech. Lett.* 11, 59-67.
- Wang, S.-W., Medina, H., Hong, K.-B., Wu, C.-C., Qu, Y., Manikandan, A., Su, T.-Y., Lee, P.-T., Huang, Z.-Q., Wang, Z., 2017g. Thermally Strained Band Gap Engineering of Transition-Metal Dichalcogenide Bilayers with Enhanced Light–Matter Interaction toward Excellent Photodetectors. *ACS nano* 11, 8768-8776.
- Wang, W., Dai, S., Li, X., Yang, J., Srolovitz, D.J., Zheng, Q., 2015c. Measurement of the cleavage energy of graphite. *Nat. Commun.* 6, 7853.
- Wei, X., Fragneaud, B., Marianetti, C.A., Kysar, J.W., 2009. Nonlinear elastic behavior of graphene: Ab initio calculations to continuum description. *Phys. Rev. B* 80, 205407.
- Wei, X., Kysar, J.W., 2012. Experimental validation of multiscale modeling of indentation of suspended circular graphene membranes. *Int. J. Solids Struct.* 49, 3201-3209.
- Wei, Y., Wang, B., Wu, J., Yang, R., Dunn, M.L., 2013. Bending rigidity and Gaussian bending stiffness of single-layered graphene. *Nano Lett.* 13, 26-30.
- Wei, Y., Yang, R., 2018. Nanomechanics of graphene. *Natl. Sci. Rev.* 6, 324-348.
- Woods, C., Britnell, L., Eckmann, A., Ma, R., Lu, J., Guo, H., Lin, X., Yu, G., Cao, Y., Gorbachev, R., 2014. Commensurate-incommensurate transition in graphene on hexagonal boron nitride. *Nat. Phys.* 10, 451-456.
- Woods, C., Withers, F., Zhu, M., Cao, Y., Yu, G., Kozikov, A., Shalom, M.B., Morozov, S., Van Wijk, M., Fasolino, A., 2016. Macroscopic self-reorientation of interacting two-dimensional crystals. *Nat. Commun.* 7, 10800.
- Wu, W., Wang, J., Ercius, P., Wright, N.C., Leppert-Simenauer, D.M., Burke, R.A., Dubey, M., Dogare, A.M., Pettes, M.T., 2018. Giant Mechano-Optoelectronic Effect in an Atomically Thin Semiconductor. *Nano Lett.* 18, 2351-2357.
- Wu, Y., Wagner, L.K., Aluru, N.R., 2016. Hexagonal boron nitride and water interaction parameters. *J. Chem. Phys.* 144, 164118.

- Xie, S., Tu, L., Han, Y., Huang, L., Kang, K., Lao, K.U., Poddar, P., Park, C., Muller, D.A., DiStasio, R.A., 2018. Coherent, atomically thin transition-metal dichalcogenide superlattices with engineered strain. *Science* 359, 1131-1136.
- Xu, C., Xue, T., Guo, J., Qin, Q., Wu, S., Song, H., Xie, H., 2015. An experimental investigation on the mechanical properties of the interface between large-sized graphene and a flexible substrate. *J. Appl. Phys.* 117, 164301.
- Xu, C., Xue, T., Qiu, W., Kang, Y., 2016. Size Effect of the Interfacial Mechanical Behavior of Graphene on a Stretchable Substrate. *ACS Appl. Mater. Interfaces* 8, 27099-27106.
- Xu, J., Yuan, G., Zhu, Q., Wang, J., Tang, S., Gao, L., 2018. Enhancing the Strength of Graphene by a Denser Grain Boundary. *ACS Nano* 12, 4529-4535.
- Xu, K., Cao, P., Heath, J.R., 2010. Graphene visualizes the first water adlayers on mica at ambient conditions. *Science* 329, 1188-1191.
- Xu, W., Qin, Z., Chen, C.T., Kwag, H.R., Ma, Q., Sarkar, A., Buehler, M.J., Gracias, D.H., 2017. Ultrathin thermoresponsive self-folding 3D graphene. *Sci. Adv.* 3, e1701084.
- Xu, Z., Zheng, Q., 2018. Micro-and nano-mechanics in China: A brief review of recent progress and perspectives. *Sci. China: Phys., Mech. Astron.* 61, 074601.
- Yang, R., Lee, J., Ghosh, S., Tang, H., Sankaran, R.M., Zorman, C.A., Feng, P.X.-L., 2017. Tuning Optical Signatures of Single-and Few-Layer MoS₂ by Blown-Bubble Bulge Straining up to Fracture. *Nano Lett.* 17, 4568-4575.
- Yang, S., Wang, C., Sahin, H., Chen, H., Li, Y., Li, S.-S., Suslu, A., Peeters, F.M., Liu, Q., Li, J., 2015. Tuning the optical, magnetic, and electrical properties of ReSe₂ by nanoscale strain engineering. *Nano Lett.* 15, 1660-1666.
- Yankowitz, M., Chen, S., Polshyn, H., Zhang, Y., Watanabe, K., Taniguchi, T., Graf, D., Young, A.F., Dean, C.R., 2019a. Tuning superconductivity in twisted bilayer graphene. *Science* 363, 1059-1064.
- Yankowitz, M., Jung, J., Laksono, E., Leconte, N., Chittari, B.L., Watanabe, K., Taniguchi, T., Adam, S., Graf, D., Dean, C.R., 2018. Dynamic band-structure tuning of graphene moiré superlattices with pressure. *Nature* 557, 404.
- Yankowitz, M., Ma, Q., Jarillo-Herrero, P., LeRoy, B.J., 2019b. van der Waals heterostructures combining graphene and hexagonal boron nitride. *Nat. Rev. Phys.* 1, 112-125.
- Yankowitz, M., Wang, J.I., Birdwell, A.G., Chen, Y.A., Watanabe, K., Taniguchi, T., Jacquod, P., San-Jose, P., Jarillo-Herrero, P., LeRoy, B.J., 2014. Electric field control of soliton motion and stacking in trilayer graphene. *Nat. Mater.* 13, 786-789.
- Yao, W., Yang, S.A., Niu, Q., 2009. Edge states in graphene: From gapped flat-band to gapless chiral modes. *Phys. Rev. Lett.* 102, 096801.
- Yi, C.L., Zhang, L.Y., Chen, X.M., Wang, X.Q., Ke, C.H., 2019. Nanomechanical Unfolding of Self-Folded Graphene on Flat Substrate. *Exp. Mech.* 59, 381-386.
- Yoo, H., Engelke, R., Carr, S., Fang, S., Zhang, K., Cazeaux, P., Sung, S.H., Hovden, R., Tsen, A.W., Taniguchi, T., Watanabe, K., Yi, G.-C., Kim, M., Luskin, M., Tadmor, E.B., Kaxiras, E., Kim, P., 2019. Atomic and electronic reconstruction at the van der Waals interface in twisted bilayer graphene. *Nat. Mater.* 18, 448-453.

- Yoon, T., Shin, W.C., Kim, T.Y., Mun, J.H., Kim, T.-S., Cho, B.J., 2012. Direct measurement of adhesion energy of monolayer graphene as-grown on copper and its application to renewable transfer process. *Nano Lett.* 12, 1448-1452.
- Yoshida, H., Kaiser, V., Rotenberg, B., Bocquet, L., 2018. Driplons as localized and superfast ripples of water confined between graphene sheets. *Nat. Commun.* 9, 1496.
- Yu, Y., Nam, G.-H., He, Q., Wu, X.-J., Zhang, K., Yang, Z., Chen, J., Ma, Q., Zhao, M., Liu, Z., 2018. High phase-purity 1T'-MoS₂ and 1T'-MoSe₂ layered crystals. *Nat. Chem.* 10, 638.
- Yue, K., Gao, W., Huang, R., Liechti, K.M., 2012. Analytical methods for the mechanics of graphene bubbles. *J. Appl. Phys.* 112, 083512.
- Zamborlini, G., Imam, M., Patera, L.L., Menteş, T.O., Stojić, N.a., Africh, C., Sala, A., Binggeli, N., Comelli, G., Locatelli, A., 2015. Nanobubbles at GPa pressure under graphene. *Nano Lett.* 15, 6162-6169.
- Zang, J., Ryu, S., Pugno, N., Wang, Q., Tu, Q., Buehler, M.J., Zhao, X., 2013. Multifunctionality and control of the crumpling and unfolding of large-area graphene. *Nat. Mater.* 12, 321-325.
- Zelisko, M., Ahmadpoor, F., Gao, H., Sharma, P., 2017. Determining the Gaussian Modulus and Edge Properties of 2D Materials: From Graphene to Lipid Bilayers. *Phys. Rev. Lett.* 119, 068002.
- Zhang, C., Li, M.-Y., Tersoff, J., Han, Y., Su, Y., Li, L.-J., Muller, D.A., Shih, C.-K., 2018a. Strain distributions and their influence on electronic structures of WSe₂-MoS₂ laterally strained heterojunctions. *Nat. Nanotechnol.* 13, 152-158.
- Zhang, D., Wang, Y., Gan, Y., 2013a. Characterization of critically cleaned sapphire single-crystal substrates by atomic force microscopy, XPS and contact angle measurements. *Appl. Surf. Sci.* 274, 405-417.
- Zhang, D.B., Akatyeva, E., Dumitrica, T., 2011. Bending ultrathin graphene at the margins of continuum mechanics. *Phys. Rev. Lett.* 106, 255503.
- Zhang, J., Xiao, J., Meng, X., Monroe, C., Huang, Y., Zuo, J.M., 2010. Free folding of suspended graphene sheets by random mechanical stimulation. *Phys. Rev. Lett.* 104, 166805.
- Zhang, K., Arroyo, M., 2013. Adhesion and friction control localized folding in supported graphene. *J. Appl. Phys.* 113, 193501.
- Zhang, K., Arroyo, M., 2014. Understanding and strain-engineering wrinkle networks in supported graphene through simulations. *J. Mech. Phys. Solids* 72, 61-74.
- Zhang, K., Arroyo, M., 2016. Coexistence of wrinkles and blisters in supported graphene. *Extreme Mech. Lett.* 14, 23-30.
- Zhang, K., Tadmor, E.B., 2018. Structural and electron diffraction scaling of twisted graphene bilayers. *J. Mech. Phys. Solids* 112, 225-238.
- Zhang, Q.T., Yin, H., 2018. Spontaneous buckling-driven periodic delamination of thin films on soft substrates under large compression. *J. Mech. Phys. Solids* 118, 40-57.
- Zhang, X.-F., Liu, S., Shao, X., 2013b. Fluorescence of chemically derived graphene: Effect of self-rolling up and aggregation. *J. Lumin.* 136, 32-37.
- Zhang, X., Wang, X., Miller, J.D., 2015. Wetting of selected fluorite surfaces by water. *Surf. Innovations* 3, 39-48.

- Zhang, Y., Heiranian, M., Janicek, B., Budrikis, Z., Zapperi, S., Huang, P.Y., Johnson, H.T., Aluru, N.R., Lyding, J.W., Mason, N., 2018b. Strain Modulation of Graphene by Nanoscale Substrate Curvatures: A Molecular View. *Nano Lett.* 18, 2098-2104.
- Zhang, Y., Liu, Q., Xu, B., 2018c. Self-Folding Mechanics of Surface Wettability Patterned Graphene Nanoribbons by Liquid Evaporation. *J. Appl. Mech.* 85, 021006.
- Zhao, J., Deng, Q., Ly, T.H., Han, G.H., Sandeep, G., Rummeli, M.H., 2015. Two-dimensional membrane as elastic shell with proof on the folds revealed by three-dimensional atomic mapping. *Nat. Commun.* 6, 8935.
- Zhu, S., Huang, Y., Klimov, N.N., Newell, D.B., Zhitenev, N.B., Strosio, J.A., Solares, S.D., Li, T., 2014. Pseudomagnetic fields in a locally strained graphene drumhead. *Phys. Rev. B* 90, 075426.
- Zong, Z., Chen, C.-L., Dokmeci, M.R., Wan, K.-t., 2010. Direct measurement of graphene adhesion on silicon surface by intercalation of nanoparticles. *J. Appl. Phys.* 107, 026104.